PROTEOSTASIS IN BUDDING YEAST

By

Chuankai Zhou

B.S., Peking University, 2010

Submitted to the graduate degree program in Molecular and Integrative Physiology and the Graduate Faculty of the University of Kansas in partial fulfillment of the requirements for the degree of Doctor of Philosophy.

_____

Rong Li, Ph.D., Co-Chair

_____

John A. Stanford, Ph.D., Co-Chair

_____

Ting Xie, Ph.D.

_____

Partha Kasturi, Ph.D.

_____

Alejandro Sánchez Alvarado, Ph.D.

Date Defended: May 24th, 2016

The dissertation Committee for Chuankai Zhou

certifies that this is the approved version of the following dissertation:

PROTEOSTASIS OF BUDDING YEAST

_____

Rong Li, Ph.D., Co-Chair

_____

John A. Stanford, Ph.D., Co-Chair

Date approved: July 26th, 2016

ABSTRACT

Cells utilize an array of quality control mechanisms to maintain a stable and functional proteome. These protein homeostasis mechanisms counteract the constant challenges of protein damages through an integrated network of chaperones, the ubiquitin-proteasome system and autophagy. Loss of protein homeostasis leads to formation of protein aggregates, a phenomenon underlies aging and the progression of numerous neurodegenerative diseases characterized by the deposition of protein aggregates and mitochondrial dysfunction. During cell division, aggregates formed by damaged proteins are segregated asymmetrically such that the damaged proteins are not inherited by the sibling cell with important biological potentials, such as longevity and stemness. In my studies, I examined the dynamics of protein aggregates, including formation, motility, asymmetric segregation and dissolution, in budding yeast to understand the mechanisms used to maintain a functional proteome in this eukaryotic cell. The results of my thesis have revealed that: 1) the aggregation of cytosolic misfolded proteins requires new polypeptide synthesis and is restricted to the surface of mitochondria and ER, which harbors the majority of active translation sites; 2) the motility of aggregates can be characterized as random walk with confinement cast by the associated organelles; 3) the geometry of bud neck, together with the confinement, largely precludes the leakage of protein aggregates during the polarized growth of daughter cells; 4) Sir2p is not directly involved in the aggregate dynamics; 5) mitochondria contribute to the dissolution of cytosolic aggregates by importing and degrading the proteins trapped in the aggregates. Thus, the sophisticated interactions between different cellular structures influence the dynamics of protein aggregates and the cytosolic proteostasis.

ACKNOWLEDGEMENT

This is my sixth spring in Kansas City since the plane landed here in the summer of 2010. Just like most young students, I joined Li lab with ambitions, however, had no clue what I will end up with after six years. Fortunately, I was surrounded by a group of talented colleagues and mentored by a great scientist that together have allowed me to go through a fruitful PhD training.

I would like to give my deepest thanks to Dr. Rong Li for taking me as her student and mentoring me throughout the years. I learned not only how to carry out projects, but also how to enjoy science, which is the key to keep one's enthusiasm on decoding the secret of nature. Dr. Rong Li's insightful vision and creativity navigated me through the unknown world of projects and protected me from the hidden rocks. Dr. Rong Li also maintained a state-of-art balance between fearless exploration to enjoy science and a productive direction to focus on. The most important part is that she sees the potential and weakness of a young student, protects the potentials and guides me away from the weakness.

I would like to thank my committee members Dr. Alejandro Sánchez Alvarado, Dr. Ting Xie, Dr. John Stanford and Dr. Partha Kasturi for their constructive suggestions during the entire period of my doctoral research. The discussions in the committee meetings and personal meetings helped me to think differently of my projects and appreciate the ongoing research outside of my field.

I would like to thank my collaborators Dr. Brian Slaughter, Dr. Jay Unruh, Dr. Boris Rubinstein and Dr. Amr Eldakak. I have learned a tremendous amount of technologies from all of them. The discussion with them are critical for the progress of my projects. Their inputs had brought the research to a level that I am alone will never reach.

I would like to thank Dr. Kausik Si for providing me the opportunity and resource to finish my last project. Discussion with Dr. Kausik Si has inspired me in my project and my future career. I also want to

thank all the rotation students that I fortunately worked with. Kristen Mickey and Akshay Narkar contributed to the progress of my project. Collaborating with Linhao Ruan, a former rotation student and a close friend, is very productive in the last project (Chapter six). I would like to thank Dr. Michael Wolfe and Dr. Susan Abmayr who helped a lot throughout the years to make sure I am on track.

I would like to thank all the facilities in Stowers Institute that provided a lot of assistance to improve the efficiency of experiments. I am also grateful for the unique research environment created by Jim and Virginia Stowers. I would like to thank the American Heart Association for providing predoctoral research fellowship for my projects.

Finally, I thank my friends and family for their support throughout the years. It will be impossible for me to carry out my projects without the encouragement from my wife Liying Li.

Table of Contents

LIST OF FIGURES

CHAPTER ONE: INTRODUCTION

A functional proteome is critical to all cellular processes. Protein homeostasis, or proteostasis, refers to the state and process of maintaining the balance between expression, folding, modification, translocation and degradation of each protein to ensure proper protein-protein interaction, and consequently the organization of the macromolecules and organelles within a cell. Proteins in a cell are metastable and not only challenged by the crowded cellular environment, but it is also affected by the polymorphism and mutations, mistakes in translation and posttranslational modification as well as environmental stresses. Cells have evolved sophisticated mechanisms to cope with these challenges and actively maintain proteostasis through a network of molecular chaperones, ubiquitin dependent proteasome and autophagy. These mechanisms not only interact with each other in a cell-autonomous manner, but are also integrated as a whole to achieve proteostasis across different tissues to ensure health and lifespan of the organism in metazoans. However, all these mechanisms were challenged by aging and stress. This leads to the accumulation of damaged proteins which not only directly affect the efficiency and fidelity of cellular process but also initiate a cascade of pathological events that culminate in the collapse of proteostasis and development of diseases. These are exemplified by the neurodegenerative diseases, including Alzheimer's, Parkinson's, Huntington's diseases and amyotrophic Lateral Sclerosis, which present a great challenges and burden to healthcare system and pharmaceutical industries. Traditional view of these diseases is centered on the key risky factors that misfold and aggregate in different diseases. However, it is increasingly evident that protein aggregation and amyloid state are generic features that accessible to most of the proteins under appropriate conditions. In this introduction I discuss the basic knowledge that underlie proteostasis, diseases and the cellular mechanisms involved. These previous results form the basis of my thesis study and also point to the future directions.

Proteostasis collapse is a hallmark of aging and the cause of many diseases

All animals, except for a few, experience the process of getting old, a process called aging. This inevitable time-dependent functional decline has attracted curiosity and searching for fountain of youth throughout the history of humankind. Why do we age? Is there a limit to how old we can live? Many aging theories have been proposed to explain these questions, such as programmed longevity, wear and tear theory and free radical theory. However, there are very few testable hypotheses around until M. Klass isolated long-lived mutants of C. elegans for the first time in 1983. This started a new area in aging research and followed by the expanding of our knowledge on the molecular and cellular bases of longevity and aging. The gradual accumulation of cellular damages is widely accepted as the general cause of aging. Consequently, cellular damage can cause degeneration of tissues and their functions as well as provides aberrant growth advantages to certain cells that produce cancer. This conceptual framework has ignited a plethora of studies to test the sources of aging-related damages and the corresponding cellular responses that try to maintain homeostasis. The mechanisms revealed by these efforts were conceptualized into nine hallmarks of aging, including the loss of proteostasis (Lopez-Otin et al., 2013).

Proteins are responsible for most of cellular processes. The wide variety of highly specific structures of proteins come from protein folding that serves to bring domains scattered in 1-D amino acid sequence into close proximity to form functional domains(Vendruscolo et al., 2011). The folding process not only brings the genetic information into life, but also is a risky step that vulnerable to interference from its cellular milieu. Given the sensitivity of protein folding, it is not surprising that aging and a lot age-related diseases are linked to impaired protein folding and cells invest a large portion of its

resource to maintain quality control and protein homeostasis (Gidalevitz et al., 2011). Protein homeostasis involves mechanisms that stabilize and assist protein folding as well as proteolytic degradation of irreversibly damaged ones by proteasomes and autophagy. The causative impact of protein homeostasis on aging has been well supported by a plethora of overexpression studies of different components of chaperones, autophagy and proteasomes, which not only extend the life span of model organisms, but also delay the progress of dystrophic and degenerative pathologies. Moreover, protein homeostasis may stand in the center of longevity signaling network as most of the conserved longevity manipulations rely on the upregulation of partial, if not all, of the protein homeostasis network.

Aging related diseases and their causes.

Alzheimer's disease

Alzheimer's disease (AD) is the foremost example of neurodegenerative disease both in terms of its social impact and the intensity of basic as well as clinical research. AD is a bone fide age-related disease with its etiology manifested after 60s of both sexes, slowly robs its victim of basic brain functions such as memory and language (Selkoe, 2011). Although many similarities exist, AD shouldn't be confused with senile dementia, the progressive cognitive decline happen during normal aging.

The identification of the Aβ molecules as the major component of senile plaque enabled researchers to develop antibodies and revealed innumerable Aβ positive foci in patient brains. One study using Aβ40 and 42 specific antibodies found that Aβ42 deposits in numerous pre-amyloid foci where Abeta40 seems

to mark mature plaques that entangled with neuritic dystrophy and peri-plaque gliosis (Selkoe, 2011). In brain regions that are not manifested in clinical syndromes such as cerebellum contain only Abeta42 positive foci. In the same line, examination of healthy eldly without dementia also showed this kind of pre-amyloid foci, suggesting that these Aβ positive patients are in the early stage of disease progression.

Although Aβ plaque is the diagnostic criteria for AD and the main stream of research, there are many other cellular abnormalities coexist. One such structure is the neurofibrillary tangles (NFT) that consist of mainly hyper-phosphorylated tau. However, these two classic proteinaceous lesions, NFTs and Aβ plaques, can occur independently with many tau dementia that not characterized by Aβ plaques. Nonetheless, reduction of endogenous tau ameliorates the AD symptoms in Tg mice, albeit no change in amyloid plaques and neuritic dystrophy, indicating that tau hyper-phosphorylation and aggregation contribute to the progress of disease (Roberson et al., 2007). This is consistent with the observation that about 70% of sporadic AD is associated with NFT. It appears that NFT formation of wild type tau can follow Aβ accumulation, but not vice versa. This is supported by the study that the dynamic of non-phosphorylated tau temporally follow the clearance and reemerge of Aβ (Oddo et al., 2004).

Aβ comes from a series of proteolytic cleavage of its precursor APP. APP is a transmembrane protein that expression ubiquitously throughout development with its peak at the maturation of nervous system. APP, especially its ectodomain, has many functions including protease inhibition, cell adhesion, radial glial-guided migration, neuritotrophy (Anliker and Muller, 2006). In most tissues, APP is cleaved by several membrane-bound proteases at various sites, producing a set of Aβ peptides that can be detected in cerebrospinal fluid, plasma and cell culture medium. Cleavage by β-secretase and γ-secretase is particular prominent in neurons, which leads to the generation of Aβ 40 and 42, and thus may be related to the vulnerability of brain tissue to Aβ amyloidosis.

Many transgenic mice overexpressing human APP gene were constructed, however, only the APP23 mice from Novartis show neuronal loss in CA1 region of hippocampus, despite that as much as 25% of the neocortex of these mice was filled with Aβ plaque (Calhoun et al., 1998). Many studies have confirmed that morphological and biochemical changes happen well ahead of amyloid plaque deposition, suggesting that the diffusive pre-amyloid species are the major source of neurotoxicity. Indeed, many soluble dimer, oligomer or Aβ have been isolated and shown neurotoxicity when injected, partially through inducing tau hyper-phosphorylation and pathology (Cleary et al., 2005). In the contrast, the injection of insoluble amyloid plaque cores did not impair long-term potentiation (LTP) unless the plaques were solubilized to release dimers (Shankar et al., 2008). The study by Lambert et al. demonstrated that proteins, such as clusterin, coexist with Aβ in plaque may chaperone its self-association and generate more toxic oligomers (Lambert et al., 1998).

Parkinson's disease

Parkinson's disease is a devastating neurodegenerative disease that happens to about 1.2 million Americans. It is a heterogeneous age-related disease that combines both motor and non-motor symptoms. The prodromal symptoms such as constipation and olfactory dysfunction can precede typical motor features such as rest tremor and bradykinesia by more than two decades (Kalia and Lang, 2015). Although dopaminergic neuronal loss in substantia nigra pars compacta (SNpc) is generally known as the major cause of PD, however, this complex disease involves neurotransmitters other than dopamine and regions far beyond the SNpc, including peripheral neuron systems (enteric neurons), vagus nerve and sympathetic neurons (Kalia and Lang, 2015). Progression of PD is characterized by worsening of motor functions and complications in non-motor features. The early motor symptoms associated with

dopamine insufficiency can be symptomatic treated with levodopa, however, the late-stage PD is often associated with treatment-resistant motor and non-motor features such as freezing of gait, dyskinesia, urinary incontinence and dementia (Coelho and Ferreira, 2012).

Age is the greatest risk factor for the development of PD, which was once thought to be caused primarily by environmental toxins such as pesticides and well-water drinking. However, it became clear that genetic factors contribute significantly by themselves or interact with environmental factors (e.g. the risk reduction effect of coffee consumption relies on the polymorphisms in a cytochrome p450 locus) to the risk of PD (Kalia and Lang, 2015). Of that, about 10% of the PD are hereditary cases found in families. The first genetic mutation identified in familiar PD is SNCA that encodes the protein α-synuclein (Polymeropoulos et al., 1997). Although not all of the PD patients examined show inclusion bodies named Lewy body, Lewy body is recognized as a hallmark of PD. The major component of Lewy body is α-synuclein, which also forms oligomers or small aggregates in neuronal processes (Lewy neurites).

How α-synuclein aggregation causes nigral neuron loss and PD is not fully understood. α-synuclein has an important role in pre-synaptic vesicle homeostasis, which could be disrupted by both loss- and gain-of-function associated with α-synuclein mutation and aggregation. It has been proposed that the pathological deposition of α-synuclein in aggregates can lead to neuronal dysfunction by obstructing cellular trafficking and/or disrupting membranes such as mitochondria (Zaltieri et al., 2015). Reciprocally, damaged mitochondrial, which is usually associated with increased burden of ROS generation, can cause post-translational modification and aggregation of α-synuclein (Bosco et al., 2011). Oxidative modification can also come from the metabolic intermediate of dopamine, which partially explains the sensitive of dopaminergic neurons to α-synuclein.

Parkin and PINK1 represent the other two well-studied PD mutations. PINK1 is a kinase localizing to the mitochondrial outer membrane, while Parkin is an E3 ligase that recruited to mitochondrial outer membrane during stress by PINK1. Upon loss of membrane potential, PINK1 accumulates on the mitochondrial surface and recruit Parkin, which in turn ubiquitinates mitochondrial membrane proteins and attracts autophagosome. In addition to Parkin and PINK, DJ1 and CHCHD2 are also implicated in mitochondrial health (Guo, 2012). DJ1 senses oxidation and translocates from cytosol into mitochondrial to protect it from oxidative stress. Mutations in LRRK2 are the most frequent cause of familiar PD, in that they are found in about 4% of familiar PD.

Huntington's disease

Huntington's disease (HD) is one of the nine diseases caused by expansion of CAG repeat coding for glutamine. As one of the classic genetic lesion, HD was first completed described by George Huntington in 1872 and the gene, HTT, responsible for the disease was identified by a consortium of researchers in 1993 (1993). People inherit one or two copies of Htt with more than 35 CAG repeats in its first exon develop classic symptoms such as chorea and gait disturbance (Finkbeiner, 2011). The brain regions affected by HD including the stiatum medium spiny neurons that express dopamine receptor. The length of repeat correlates with the symptomatic age and the severity of the disease, with >50 repeats cause juvenile HD that happen in early life.

The affected neurons in HD show accumulation of nuclear inclusions as well as cytoplasmic aggregates in perinuclear region and dendrites (Finkbeiner, 2011). Inclusion body of mutant Htt is usually blamed to cause cellular dysfunction through sequestering essential metastable proteins as well as inhibiting proteasome function. A model based on in vitro studies proposed that the occasional

failure in releasing these indigestible polyglutamine peptides could “choke” the affected proteasome and cause inhibition (Mitra et al., 2009). Another possible damage caused by oligomerization and aggregation of Htt could be the aberrant depletion of benign polyQ-containing proteins, such as transcriptional factors CBP and TBP (Schaffar et al., 2004). The third model of cytotoxicity associated with the polyQ mutations is the enhancement of a normal function. PolyQ expansions found in spinal bulbar muscular atrophy (SBMA) and spinocerebellar atrophy1 (SCA1) cause neurodegeneration through its normal interacting partners and signaling pathways (Kratter and Finkbeiner, 2010). Nonetheless, expression of a highly potent disaggregase Hsp104 in mice reduced the number of IBs in the brain and extended the lifespan (Vacher et al., 2005).

Protein folding and strategies of quality control.

Historic views of protein folding.

The interest in protein folding can date back to the paper published by Fred Sanger on the primary sequence of insulin in 1951. Since then, more proteins got sequenced and protein biochemists tried to understand how the primary sequence gives rise to a functional protein (Anfinsen, 1973). It was a serendipitous discover in Chris Anfinsen’s lab when they were trying to understand the formation of 4 disulfide bonds within ribonuclease. The ribonuclease randomly formed disulfide bonds, with no enzyme activity, after β-ME and urea were removed. However, ribonuclease regained its enzyme activity when small amount of β-ME was added during the folding step. This unexpected reversibility, together with the later work from his lab on the tertiary structure of RNase, led him to believe that the information for the folding of a protein is contained in its amino acid sequence. However, the in vitro refolding process

usually takes about hours to reach about 8% activity, which is significantly slower than in *in vivo* synthesis that only needs approximately 2min. This discrepancy led them to discover the first "chaperone" in endoplasmic reticulum, which is the disulfide bond isomerase. Addition of this enzyme speeded up the refolding process essentially similar to the *in vivo* synthesis (Schechter, 1995).

At about the same time, people began to study heat shock induced transcriptional and translational adaptation in fly salivary gland. Upon temperature shift, the existing chromosomal puffs faded away, which was accompanied by the emergency of a few new puffs in the chromosome spread (Horwich, 2014). As the puffs of polytene observed in heated drosophila salivary gland can also be induced by the mitochondrial toxins, this observation prompted the speculation that the response is an attempt to adapt to the mitochondrial stress (Leenders and Beckers, 1972). Indeed, enzymatic activities of several mitochondrial enzymes were found to increase after heat shock. However, the cell fractionation suggested that majority of these proteins co-migrated with nuclear fractions (Velazquez et al., 1980). The arrival of cloning and specific antibodies allowed Pelham to specifically express drosophila Hsp70 in mammalian cells and observed expression-dependent stress resistance (Pelham, 1984). These dHsp70 not only shuttled into nucleus following heat shock, they also assisted the recovery of nucleoli, and probably bound to the disrupted RNPs and catalyzed their assembly. The milestone paper published by Pelham and Lewis in the following year established the prescient model that Hsp70 is an ATP dependent chaperone (Lewis and Pelham, 1985). Concurrent data from other studies irrelevant to heat shock also identified similar principle: the clathrin uncoating ATPase was identified to be the constitutively expressed isoform of Hsp70, namely Hsc70 (Ungewickell, 1985). In addition, Hsp70 homolog, BiP, was identified as a binding partner for immunoglobin heavy chain and promoted oligomeric assembly in this case (Haas and Wabl, 1983). Shortly thereafter, Hsp70s were found to be

critical in cross-membrane translocation in ER and mitochondria. Studies by Blobel and Schekman independently reached the same conclusion that yeast SSAs are critical for ER protein translocation (Chirico et al., 1988; Deshaies et al., 1988). Later on the crystal structure of Hsp70 suggested that it prefers the extended conformation of proteins. This is in contrast to another group of HSPs, namely HSP60s, which bind collapsed while still globular substrates and shield the substrates by global enclosure in its central cavity (Bukau and Horwich, 1998).

The bacterial homolog of Hsp60 was first noticed in a search for host genes that required in the phage particle assembly but not incorporated into the final product. GroE mutants were found to be important for the assembly of mutant T4 phage and also caused temperature sensitive growth defect for the host (Georgopoulos et al., 1972; Takano and Kakefuda, 1972). Similar observation was made in chloroplast by John Ellis and colleagues that the newly synthesized large subunits of RuBisCo did not migrate with the holoenzyme, but co-migrated with a 60kD protein in non-denaturing polyacrylamide gel (Barraclough and Ellis, 1980). These two 60kD proteins found in different systems were sequenced and turned out to be evolutionary homologues that were named “chaperonins” (Hemmingsen et al., 1988). Based on the similarity between bacterial and plant chloroplast, as well as the endosymbiotic hypothesis of the origins of mitochondria and chloroplast, chaperonin was predicted to be essential in mitochondria. This was confirmed one year later by Horwich group who discovered the yeast mitochondrial Hsp60 that critical for the folding of imported mitochondrial proteins (Cheng et al., 1989). In addition, this study, together with Ostermann et al. also provided the first evidence for the concept that folding of monomeric mitochondrial protein requires chaperonin to achieve its final conformation (Ostermann et al., 1989). This folding process can be separated into two NEM sensitive steps, binding of the polypeptides to the Hsp60 and the subsequent ATP dependent release of folding product (Ostermann et al., 1989).

Protein folding *in vivo*

Early *in vitro* studies on protein folding revealed several steps took by denatured polypeptides toward their native state. Upon removal of denaturant such as urea, polypeptide collapses in a few milliseconds to form some nucleation centers, which are some secondary structures. These secondary structures then interact with each other as well as the remaining residues to search for the native tertiary structure via a series of kinetic intermediates. This nucleated folding allow polypeptides to reach native states in a biological relevant timescale and avoid the Levinthal's paradox (Anfinsen, 1973). Recent studies provided evidence for the existence of such intermediates and showed that a lot of native like structures already formed, albeit substantial non-native interactions between different secondary structures prevail (Bartlett and Radford, 2009). This step usually takes several minutes and is often confounded with misfolding intermediates with hydrophobic cores exposed that may lead to aggregation. The extent of aggregation depends on the concentration of the free folding polypeptides as well as the temperature. However, the concentration of nascent polypeptides in the cytoplasm of E. coli is about 35μM, surrounded by a cytosol with 340g/L protein (Ellis and Hartl, 1996). Moreover, the co-translational folding casts another layer of complexity as the C-terminal 30 amino acid of the emerging domain are topologically prevented from folding by the ribosome. Because translation is relatively slower than folding, nascent chains are exposed as partially folded, aggregation-prone intermediates. The partially folded intermediates can interact with each other to form either amorphous aggregates or highly ordered, fibrillar aggregates, which are usually toxic and cause diseases (Figure 1-1). Although many proteins can adopt this kind of thermodynamically stable amyloid under *in vitro* conditions, their prevalence in vivo is restricted by the chaperones, indicating that they can become more widespread under circumstance of environmental stress or aging when protein quality control fails. All of those

imply the important role of chaperones in the *de nova* folding of newly translated polypeptides (Hartl, 1996).

In contrast to the *in vitro* refolding of ribonuclease that happened spontaneously, expression of exogenous recombinant proteins in bacteria resulted in the aggregation of recombinant proteins, which can occupy up to 20% of the cellular volume (Williams et al., 1982). In bacteria, the chaperone trigger factor binds to the ribosome large subunit and contacts with the emerging nascent polypeptides. The Hsp70 homologue DnaK interacts with nascent chain subsequently. Trigger factor and DnaK not only assist the *de novo* folding of the nascent polypeptides, they also change the folding kinetics by delaying the folding relative to translation, allowing the entire domain to be fully translated.

In budding yeast, a specific Hsp70 system named ribosome-associated complex (RAC) and another nascent chain associated complex (NAC) cooperate with cytosolic Hsp70/Hsp40 to assist co-translational folding. RAC consists of Ssb1, Ssz1 and zuotin, together with NAC, are the first cytosolic factors to contact with nascent polypeptide (Figure 1-2). Similar to trigger factor, they bind nascent chains and delay premature compaction until the entire domain is present for folding. Cytosolic Hsp70/Hsp40 do not bind ribosome directly, instead they engage in the folding of nascent chain after NAC and RAC. When the Hsp70 was pull down from mammalian cell culture, Beckman et al. found a lot of newly synthesized peptides were co-precipitated with Hsp70 transiently after translation (Beckmann et al., 1990). While after 2hr of chasing period, majority of the pulse labeled newly translated peptides no longer bound to the Hsp70. Moreover, Hsp70 bound the emerging peptides co-translationally as it was co-fractionated with the polysomes. Given that less than 5% of the newly synthesized protein stayed bound to Hsp70 after 2hr chase, Beckman et al. suggested that during physiological condition the newly translated peptides are the major clients for Hsp70.

Chaperones cooperate in vivo to assist *de novo* folding of nascent polypeptides. Two models had been proposed to describe the chaperone-mediated folding. In the first model, evidence from *in vitro* translation system suggested that the nascent polypeptides are released from RAC/NAC into cytosol after translation and engaged in cycles of binding and release of Hsp70/40 or chaperonin until all non-native domains are folded. In each cycle, small amount of proteins reach their native state and the remaining majority rebind to the chaperones (Farr et al., 1997). The second model, however, proposed that the process of *de novo* folding is a highly coordinated reaction due to the processive interaction of different chaperones with nascent polypeptides. The abundance of various chaperones engaged in the *de novo* folding prevents the release of folding intermediates into cytosol under physiological condition. *In vivo* expression of a mutant GroEL trap failed to pull down any nascent polypeptides, indicating that co-translational folding is encapsulated in an enclosed environment without discharging non-native, aggregation sensitive intermediates into bulk cytosol (Thulasiraman et al., 1999).

Transmembrane proteins may use different machineries and mechanisms to achieve their specific topologies and conformation on 2-D lipid membrane. Much less is known on how transmembrane proteins fold into their native state. The complexity comes from the fact that the cytosolic and ER lumen part of a given transmembrane protein are spatially separated in addition to the additional hydrophobic environment of lipid bilayer (Skach, 2009).

Chaperones

Trigger factor

Trigger factor (TF) is an abundant protein with about 50μM in most bacteria (Agashe et al., 2004). This 50kD protein exceeds the concentration of ribosomes *in vivo* (50 vs 30μM). TF exists as

dimer in the free cytosol. Monomer TF binds ribosomal next to the polypeptides exit site with a mean residence time about 15 sec (Kaiser et al., 2006). Ribosome bound TF captures the emerging nascent chain and remains associated with the elongating polypeptides for up to 35sec. New TF enters the cycle and associates with ribosome and nascent chain sequentially. Dissociation of TF from nascent chain is an ATP independent reaction, which could be driven by the tendency of the nascent chain to bury the hydrophobic sites. The sequence preference for TF and how many TF can be found on a nascent polypeptide are unclear.

Two non-exclusive mechanisms have been proposed to explain the chaperone activity of TF *in vivo*. The sequential binding of TF to the elongating nascent chain described above supports the model in which the binding of TF delays the folding until the entire domain emerges from ribosome. On the other hand, the amphiphilic nature of the substrate-binding grove in TF and the holding function of TF for ribosome assembly favor the model that TF acts in a way similar to GroEL/ES by providing folding environment for large domains. Indeed, TF shows higher affinity for the full length folding protein than short peptides and can protect the substrate up to 280 residues from proteolytic degradation in solution (Hoffmann et al., 2006).

Hsp70 and Hsp40

Hsp70s are a group of highly conserved ATPase with molecular weight ~70kD. The Hsp70s are the central organizers of the entire protein homeostasis network, such as protein folding, translocation, degradation and transportation. This versatility of Hsp70s roots from their basic function in binding and release of substrates through ATP-hydrolytic cycle. This basic ATP cycle is tightly regulated by Hsp40 and

nucleotide exchange factor (NEF) (Hartl et al., 2011). Hsp40s are a family of conserved J-domain proteins that found in all Hsp70-mediated functions. In most Hsp40s, the J-domain is coupled to a peptide-binding domain so that Hsp40s can bind both Hsp70 and substrates. By joining different J-domains with various peptide-binding motifs, cells create a highly versatile Hsp70/40 system that not only can prevent the aggregation and catalyze the folding of polypeptides, but also facilitate many specialized cellular functions. One such example is the protein auxilin, which can bind the clathrin coat and recruit cytosolic Hsc70 to catalyze the clathrin uncoating and release of clathrin triskelions (Ungewickell et al., 1995). In addition to the disassembly of clathrin, Hsp70/40 also mediates translocation of proteins across membranes in mitochondria and endoplasmic reticulum.

Although Hsp70s overlap with each other in binding a variety of non-native stretches without obvious consensus in sequence, they show different preference for certain amino acid pattern in the exposed hydrophobic regions. The amino acid pattern recognized by ER luminal Hsp70, namely the BiP, was characterized in details by Gething group (Blond-Elguindi et al., 1993). The pattern recognized by Hsp40 is not well studied. Despite substantial overlap in substrates, Hsp40 differs from Hsp70 significantly in terms of binding specificity. For example, only Hsp40 can recognize the molten-globule state without extended stretch, such as casein that exposes hydrophobic surfaces in its native conformation. In contrast, the reduced carboxy-methylated α-lactalbumin, which has an extended conformation in the absence of denaturant, can only bind to Hsp70 (Langer et al., 1992).

In the ATP-bound state, Hsp70s show high on/off rate for the substrate, allowing the Hsp70 to bind exposed hydrophobic sites. The interaction with Hsp40 stimulates the ATP hydrolysis in Hsp70 and stabilizes its association with substrate by reducing the on/off rate. The nucleotide-exchanging factor facilitates the ADP-ATP exchange, resulting in substrate release(Hartl et al., 2011). This ATP cycle of Hsp70/40 prevents the aggregation of non-native proteins and allows them to fold. Similar function for

Hsp70/40 was observed under stress. *In vitro* experiments demonstrated that Hsp70/40 binds the inactivated luciferase and prevents it from aggregation, which is essential for its reactivation (Schroder et al., 1993). Interestingly, the presence of Hsp70/40 *in vivo* cannot prevent the aggregation of luciferase, indicating specific factors that missing in the *in vitro* system are required for aggregation.

Chaperonins

The name "chaperonin" was coined by John Ellis who described the presence of a factor in chloroplast that binding the Rubisco large subunits (Barraclough and Ellis, 1980). Chaperonin has essential roles in assisting the folding of proteins under both physiological and stress conditions. There are two subgroups of chaperonins: one consists of two stacked seven-subunit rings, exemplified by GroEL, which cooperates with GroES to fold a subset of essential proteins in bacteria, chloroplast and mitochondria; the second group exists in eukaryotic cytosol and consists of two stacked eight- or night-subunit rings, such as TRiC. TRiC contains a lid that functions similarly as the cofactor GroES. GroEL interacts with about 250 different proteins out of the 2,400 bacterial proteome, of which about 85 are obligate substrate for GroEL and many of them are essential proteins. In contrast to GroEL, TRiC appears to have a restricted range of substrate, including actin and tubulin (Hartl, 1996). Interestingly, GroEL can interact with unfolded actin and luciferase, but fails to fold them in the presence of ATP. GroEL maintains the actin in a native-like state that can be recognized and folded into native state by TRiC added into the reaction later (Tian et al., 1995).

In the absence of GroES, GroEL can bind substrates in both sides, with a decreasing affinity towards a series of intermediates ranging from partially folded to extended conformation (Hayer-Hartl et al., 1994). The attachment of GroES causes allosteric alternation in the GroEL and exposes hydrophilic residues in the cavity, which force the substrate to fold. Several monomeric proteins such as DHFR can

reach their native conformations with enzymatic activity inside the GroEL cavity (Mayhew et al., 1996). For the proteins that terminally misfolded and must be degraded, the GroEL may release them after about 20sec at 25°C.

HSP90

Hsp90 is an essential protein that binds a long list of clients. This protein was identified for the first time by co-purification with the first oncogene tyrosine kinase v-src from Ross sarcoma virus transfected chicken cells (Xu and Lindquist, 1993). At the same time, Hsp90 was detected in many nuclear hormone receptor complexes. Kinase and steroid hormone receptors are the best-understood clients for Hsp90 (Taipale et al., 2012). After two decades, its pleiotropic functions have extended to cell cycle progression, telomere maintenance, innate immunity, proteostasis through HSF1, viral assembly, NOS signaling and mitochondrial import, et al(Taipale et al., 2010). However, Hsp90 has little role in nascent chain folding. Instead, it functions downstream of Hsp70s and recognizes a set of metastable proteins in their late stage of folding. Several co-factors have been identified in mediating the processive function between Hsp70 and Hsp90. For example, HOP provides a direct interaction between these two chaperones to allow substrates transfer (Scheufler et al., 2000).

Hsp90 forms dimer through interaction between its C-terminal domains. The N-terminal domain is an ATPase that binds and hydrolyzes ATP. Upon ATP and substrate binding, the N-terminals of the dimer twist around each other and form a molecular clamp. The hydrolysis of ATP releases this conformation and the substrates. The mechanisms used by Hsp90 to recognize this long list of clients remain elusive.

Hsp100

In the early 1990s, proteins trapped in the inclusion body and aggregates were thought to be the end of their journey. With the discovery of Hsp104 in yeast, it became clear that fungi, bacteria and mitochondria can dissolve aggregated formed under stress (Parsell et al., 1991). Hsp104 and its bacterial homologue ClpB are Hsp100 members of the AAA+ superfamily ATPase, defined by the presence of a ~230 amino acid core that comprises conserved walker A and B nucleotide-binding domain (NBD) (Doyle and Wickner, 2009). Hsp104/ClpB extracts and unfolds substrates by threading them through the central cavity, which can be initiated from the ends of a protein or the looped polypeptides regions (Haslberger et al., 2008). Hsp100 solubilizes these fusion proteins without unfolding the stable domains. Measurement of the pulling force using optical tweezer revealed that Hsp100 applies denaturing force up to 20pN on the substrates and unfolds the GFP monomer in two steps (Aubin-Tam et al., 2011).

Hsp100 interacts with Hsp70/40 to dissolve protein aggregates (Parsell et al., 1994). However, it has been difficult to tease out the exact mechanism governing the interplay between these two ATP-dependent chaperones. *In vitro* studies found that Hsp104 alone could remodel yeast prions, with high Hsp104 concentration catalyzed the disassembly of fibers, whereas the low concentration stimulated the fiber formation (Shorter and Lindquist, 2006). The amyloidogenic function of Hsp104 is not ATP hydrolysis dependent yet ATP binding is required. Instead, the disassembly of fiber requires ATP hydrolysis.

The observation of species-specific genetic interaction between Hsp100 and Hsp70/40 suggested a directly physical contact between these two ATPase chaperone systems and argued against sequential actions towards aggregate dissolution (Krzewska et al., 2001). The M domain, which is specific to the Hsp100 subfamily of AAA+ proteins, was shown to regulate ATPase activity as well as mediate species-specific Hsp100-Hsp70 interaction (Oguchi et al., 2012; Seyffer et al., 2012). Hsp70

prefers derepressed state of M-domain and stabilizes a detached conformation that allows further Hsp70 binding and ATPase activation. These results, therefore, consists with a model that M-domain functions as a break for the coordinated ATPase activity upon substrate engagement, which explains the cellular tolerance of Hsp100 overexpression. Deregulation of this mechanism leads to uncontrolled unfolding of native proteins and gains cellular toxicity (Schirmer et al., 2004).

The model that Hsp70 recognizes M-domain as substrate is disproved by the lack of cross-linking between the substrate-binding domain of Hsp70 and Hsp100. Instead, M-domain interacts with the ATPase domain in Hsp70. The interaction surface overlaps with the binding region of nucleotide exchanging factor of Hsp70. As Hsp100 does not activate the nucleotide change in Hsp70, the discharge of substrate from Hsp70 depends on the threading of substrate through Hsp100 (Rosenzweig et al., 2013).

Although it is clear in many experiments that Hsp104 and ClpB behave similarly, some sporadic evidences suggest that Hsp104 evolved from ClpB to be capable of processing prion. Based on sophisticated *in vitro* studies, Destantis et al. proposed an operational model that ATP turnover in Hsp104, but not ClpB, could switch from probabilistic mode upon binding to amorphous aggregates to a coordinated mode when dealing with amyloid fibers (Desantis et al., 2012). However, this unique property of Hsp104 is not consistent with the *in vivo* results in which the ClpB/DnaK/GrpE or ClpB with M-domain from Hsp104 can substitute the Hsp104 in supporting prion propagation (Reidy et al., 2012; Tipton et al., 2008).

Hsp110-Hsp70-Hsp40 system

Metazoan cells lack the Hsp100 family that used by fungi, plant, bacteria, mitochondria and chloroplast to disentangle the aggregated proteins. The cytosol of metazoan cells, instead, contains a different disaggregation system that has been identified as Hsp110-Hsp70-Hsp40 (Ben-Zvi et al., 2004; Shorter, 2011). This early study identified a mysterious disaggregase activity in multiple cell lysates and narrowed down to these three factors. Similar results by another study confirmed the role of Apg2 (Hsp110)-Hsc70-Hjd1 (Hsp40) in dissolving aggregates formed by both chemical and thermal denatured proteins (Rampelt et al., 2012). Although the yeast Hsp110 Sse1 can substitute Apg2 in the tri-chaperone system, the yeast counterparts lack any detectible disaggregase activity under the same *in vitro* condition. The Hsp110s is a subfamily of Hsp70, consisting of three isoforms in human: Hsp105a/HSPH1, Apg-2/HSPH2 and Apg1/HSPH3. While the role of ATPase and typical Hsp70 activity of Hsp110 in the tri-chaperone system is debatable, its NEF activity cannot be replaced *in vitro* by the other two distinct classes of NEFs, namely Bag-type and HspBP1-type (Nillegoda and Bukau, 2015; Rampelt et al., 2012). Together with an *in vivo* study with fly, Mattoo et al. presented compelling data suggesting that Hsp110 is a *bona fide* Hsp70 and they can stimulate nucleotide exchange for each other *in vitro*(Kuo et al., 2013; Mattoo et al., 2013). These results led Mattoo et al. to postulate a “Clamp and Walk” model in which the Hsp110-Hsp70 heterodimer applies power stroke on aggregated peptides through coordinated substrate binding and release. This model was challenged by Bukau group who showed that Hsp110 was dispensable for the Hsp70/heterocomplexed J-protein to unwind aggregates (Nillegoda et al., 2015). The clustered Hsp70s on the surface of aggregates may concentrate and facilitate the unwinding of a given trapped peptide more efficiently than random clamp and walk. Entropic pulling by enclosure of the substrate in Hsp70s can apply 10-20pN on the substrate per Hsp70 (De Los Rios et al., 2006). Coordinated ADP/ATP cycle of clustered Hsp70 can extract and modify the surface of aggregates.

The disaggregation activity of this tri-chaperone system is strong enough that can reactivate luciferase aggregated in the absence of Hsp26 as well as efficiently disentangle α-synuclein amyloid fiber (Gao et al., 2015). However, these results mainly came from *in vitro* assays that the concentration of each component could determine the outcome of each assay. In addition, the size of aggregates used in these *in vitro* assays were much smaller and chemically simpler than *in vivo* ones.

Small HSPs

sHSPs are a family of widespread and poorly conserved chaperones that can be found throughout all kingdoms. Although sHSPs are diverse in sequence and size, they share some common features such as small protein size, α-crystallin domain, formation of oligomer and response to stress conditions by changing conformation and expression (Haslbeck et al., 2005). Two different models of chaperone activity have been identified for sHSPs: sHSPs oligomers expose hydrophobic sites through either dissociation (e.g. Hsp26) or conformational alternation that allows substrate binding (e.g. Hsp26, Hsp42)(Haslbeck et al., 2004) (Figure 1-3). This process can be spontaneous under heat shock or regulated by posttranslational modification that triggered by stress conditions (Koteiche and McHaourab, 2003). The posttranslational modification mechanism allows sHSPs to response to a variety of cellular proteostasis stresses other than heat shock. Several lines of evidence indicate that substrates are recognized by sHSP in their early unfolding stage. The binding could prevent the loss of core structures in substrates and improve the efficiency of subsequent refolding by ATP dependent chaperones (Basha et al., 2012).

The ability to prevent non-native proteins from aggregation, which comes from the binding and shielding of hydrophobic sites, is contradictory to the observations that sHSP is required for aggregate

formation, especially the Hsp42 dependent CytoQ (Miller et al., 2015a). In addition, except for plant and fly mitochondria, most organelles do not contain sHSP, yet are able to form aggregates in these compartments (Basha et al., 2012).

Strategies of protein homeostasis in prokaryotic cells

Unicellular prokaryotic cells usually experience environmental fluctuations frequently. For example, bacteria encounter sudden temperature shift during infection and acid shock in stomach. This type of lifestyle selected a robust protein quality control system to ensure the functionality of its proteome and allow them successfully colonize a new host (Mogk et al., 2011). The chaperones, including TF, DnaK, GroEL and SecB, integrate with each to secure the proper folding and assembly of newly translated proteins. In spite that specific function and substrates have been described for each chaperone, they also show promiscuous binding to many overlapping substrates. For example, GroEL and SecB overexpression can partially rescue the lethality of TF/DnaK double deletion. Upon overproduction, SecB not only binds secretory substrates but also holds cytosolic nascent peptides that can be competed off by TF (Ullers et al., 2004).

Upon environmental shift, such as heat shock, several regulatory circuits fine-tune the expression of protein quality control machineries. Several mRNA and transcription factors serve as thermometer in response to the elevated temperature. On the other hand, indirect titration of chaperones during stress can release the bound transcriptional factors and activate the stress response program. The first RNA thermometer identified is the mRNA encoding for the heat shock transcription factor sigma 32(Morita et al., 1999). This mRNA has very complex secondary hairpins in its 5’ UTR that block the binding of initiation factors and ribosome. Similar structures are also present in the mRNA of

small HSPs, thus the heat shock induce both immediate chaperone capacity as well as transcriptional based adaption (Narberhaus et al., 2006). Alternatively, the inactivation of repressors can also increase the output of chaperone activity. In the indirect titration model, the labile transcription factors such as sigma 32 are sequestered by chaperones or degraded by proteases under physiological condition (Rodriguez et al., 2008).

Under extreme conditions such as the combination of heat shock and oxidative stress, the DnaK is inactivated due to the reduction of ATP/ADP that binds and stabilizes the ATPase domain. Under the same condition, Hsp33 is activated by oxidation and dimerization, binds the misfolded substrates and prevents them from aggregation. Upon removal of the stress factors, DnaK is reactivated while the Hsp33 is inactivated (Winter et al., 2005). In addition to the chaperones, AAA+ protease, such as ClpX/P and Lon, can degrade the misfolded proteins under stress. The mechanism determines the interplay between chaperone and protease is not understood, yet one possibility could be that the substrates fail to fold rapidly are degraded. From an energetic perspective, refolding is more cost effective than degradation and synthesis. Indeed, the chaperones are more abundant than Lon, which could bias the competition towards refolding (Gur and Sauer, 2008; Mogk et al., 2011).

Aggregation of misfolded proteins happens when both chaperone and protease fail to hold the proteome in soluble state under severe conditions. The amount of proteins trapped in the inclusion bodies is about 1-3% of the entire proteome, indicating the sensitivity of the heat shock regulatory circuits in detecting small variation (Winkler et al., 2010). AAA+ chaperone such as ClpB can act on the aggregated proteins and extracts them for refolding. Many AAA+ proteases also possess disaggregation activity *in vitro*. The *in vivo* function of these AAA+ proteases is limited as majority of them, exemplified by Lon protease, are not recruited to the inclusion body (Winkler et al., 2010). The small heat shock proteins co-aggregate with misfolded proteins and keep them competent for disaggregation. The

presence of sHsp during aggregation reduces the size of aggregates up to several orders of magnitude (Mogk et al., 2003; Ratajczak et al., 2009). Although ClpB-DnaK bichaperone system can dissolve aggregates of certain substrates in the absence of sHsp, the incorporation of sHsp facilitates the disaggregation activity and expands the spectrum of substrates.

Another strategy to cope with protein aggregation is the asymmetric segregation of inclusion bodies. In bacteria grown under physiological conditions, time-lapse movies revealed that the inclusion bodies were formed in discrete cellular positions and gradually accumulated in the old pole over cell division (Lindner et al., 2008). The formation of discrete foci throughout the cell was also observed under stress, followed by energy and DnaK-DnaJ dependent coagulation into large pole aggregates (LPA)(Rokney et al., 2009). Although the LPAs preferentially localized to the DNA-free zone in the filamentous mutant of bacteria in this study, the formation of discrete small aggregates were found to overlap with DNA. This is contradictory to the conclusion of a later study that genetic alternations of DNA structure and localization affected the distribution of aggregates (Winkler et al., 2010) (Figure 1-4).

Regardless of the underlying mechanism, the coagulation of small aggregates into LPA facilitates the asymmetric segregation and the rejuvenation of one sibling cell that inherits the new pole after division. The inheritance of LPA by old pole, by unclear mechanism, gradually decreases its fitness over next generations and increases the fitness difference between the old and new poles. By extracting the contribution of old pole to the fitness, LPA was found to cause about 30-40% of the fitness decline in the sibling cell inheriting it (Lindner et al., 2008). The similar fitness segregation between old and new poles was also observed by tracing the poles in time-lapse imaging without labeling, which allowed the authors to demonstrate that two morphologically identical sibling cells generated by fission are functionally asymmetric. Together with the early study in fission yeast and later observation with animal

cells, this study laid the foundation for the existence of asymmetric segregation of aging in cells dividing symmetrically (Barker and Walmsley, 1999; Rujano et al., 2006; Stewart et al., 2005).

Cellular strategies of proteostasis in eukaryotic cells

The inclusion body formation is generally toxic to the bacteria cells, whereas the diverse aggregates in eukaryotic cells are associated with both toxic and beneficial effects. For example, the co-aggregation and sequestration of metastable proteins and chaperones is linked to cellular toxicity. Meanwhile, the formation of amyloid aggregates, especially some aggresomes, can protect cells from the toxicity of soluble oligomeric species (Tanaka et al., 2004). The common feature of aggregation, which is the sequestration of other proteins, can have opposite effects depending on the particular sequestered substrates (functional or toxic) and the type of protein aggregates it forms (Miller et al., 2015d).

The compartmentalization in eukaryotic cells diversifies the deposition sites of aggregates. The specific localization of deposition sites depends on the particular type of aggregate and the stress conditions used to induce aggregation. In budding yeast, the most often used eukaryotic model to study protein aggregation, aggregates can be deposited in INQ (intranuclear quality control compartment), IPOD (insoluble protein deposit) and CytoQ (cytosolic quality control compartment) (Miller et al., 2015c). Aggresome formation was also reported for yeast when 103QP, instead of 103Q, was expressed (Wang et al., 2009). IPOD is a specific deposition site for amyloidogenic proteins and can adopts ring and dot conformation, serving as nucleating site for prion induction (Tyedmers et al., 2010b). The original study that coined the term JUNQ and IPOD is largely disproved by multiple studies: 1) the localization of JUNQ was later found inside nucleus and lack co-localization between INQ and nucleolus and spindle pole

body; 2) the microtubule-based transportation based on the benomyl result was due to the side effects that irrelevant to the microtubule toxicity; 3) the ubiquitination-dependent sorting between IPOD and INQ was found not necessary to distinguish substrates for these two compartments as both ubiquitinated and non-ubiquitinated substrates can populate INQ and cytoQ (Miller et al., 2015b; Shiber et al., 2013).

Similar to the situation in budding yeast, both ubiquitin-dependent and -independent pathways exist to target substrate to aggresome via dynein-mediated transportation. HDAC6 and p62 have been implicated in transporting ubiquitinated substrates to aggresome. HDAC6 is a scaffold protein that binds both ubiquitinated substrates and dynein at the same time, whereas p62 connects ubiquitinated substrates to dynein and autophagy pathway (Kirkin et al., 2009; Komatsu et al., 2007). In addition, the Hsp70 NEF Bag3 interacts with dynein and may allow general Hsp70 substrates to be targeted to the aggresome in ubiquitin-independent manner (Gamerdinger et al., 2009). Furthermore, time-lapse imaging found that the deposition of Htt preceded the accumulation of ubiquitinated substrates in aggresome (Hipp et al., 2012). As in budding yeast, therefore, there is no converged sorting mechanism for protein deposition in specific locus.

Although the signal required for compartment-specific deposition is not clear, Hsp42 and Btn2 are site-specific aggregases in budding yeast. The basic aggregation patterns under heat shock and proteasome inhibition in *Δhsp42* and *Δbtn2* showed that Hsp42 and Btn2 facilitate aggregate deposition in CytoQ and INQ, respectively. The switch of substrate deposition between CytoQ and INQ depends on the status of protein quality control system as mentioned above. The misfolded proteins are partitioned between cytosol and nucleus by the cooperation and competition among Sis1, Hsp42 and Btn2 as well as the balance between the production and dissolution/degradation of substrates (Miller et al., 2015b). Btn2 and Sis1 facilitate the nuclear import of misfolded proteins and thus compete with Hsp42 in

mediating substrate deposition in wild type cells. However, Sis1 and Btn2 are not the only mechanism for nuclear import of misfolded proteins as deletion of both Btn2 and Hsp42 leads to accumulation of diffusive misfolded proteins in the nucleus(Miller et al., 2015a) (Figure 1-5).

The partition of misfolded substrates between CytoQ and INQ may also have different functional consequences in both yeast and animal cells (Schaffar et al., 2004). SOD G93A forms INQ when overexpressed and inhibits the degradation of other INQ substrates (Weisberg et al., 2012). This is partially due to the toxicity of SOD G93A in trapping chaperones and substrate-free proteasomes. Based on the lack of toxicity when SOD G93A was targeted to IPOD by fusing to Htt, Weisberg et al. concluded that toxicity associated with SOD G93A comes after its deposition into INQ and thus the compartmentalization of specific aggregate determines its toxicity. The sensitivity of cells to nuclear localization of toxic aggregates and possible oligomers could be due to the compartment-specific proteostasis as it has been reported that nucleus is less potent in maintain proteostasis than cytosol, ER and peroxisome(Hageman et al., 2007).

To rid themselves of protein aggregates, eukaryotic cells evolved a plethora of machineries that can be grouped into three classes: dissolution, autophagy and asymmetric segregation (Figure 1-6). The dissolution of aggregates has been discussed above with bi-chaperone system (Hsp100-Hsp70-Hsp40) and the recently identified Hsp110-Hsp70-Hsp40 mechanism. Selective autophagy provides an alternative route for aggregate clearance that was coined aggrephage (Stolz et al., 2014). Autophagy was initially described as a non-selective bulk process induced by starvation. However, the basal autophagy is also required for turnover of ubiquitinated substrates in parallel to UPS system as the Atg7 knockout mice accumulate ubiquitinated substrates and form small aggregates labeled by p62(Komatsu et al., 2007).

Autophagy begins with the formation of phagophore, a double-layered crescent membrane, which expands to engulf cytoplasmic material. Phagophore formation is induced by ULK1 kinase in response to the AMPK and mTOR signaling. Downstream signaling activates Atg8 and Atg12, two ubiquitin-like proteins that conjugate phosphatidyl-ethanolamine instead of a protein substrate. The membrane source of phagophore comes from ER, Golgi, mitochondria in mammalian cells (Hailey et al., 2010; Hamasaki et al., 2013). Phagophore membrane is then further propagated through fusing with vesicles from all different sources (Puri et al., 2013).

Selective autophagy under physiological condition relies on cargo-specific receptors that interact with Atg8 through LIR or other domains. The most prevalent signal in animal cells that target substrates to autophagy is ubiquitination (Kirkin et al., 2009). p62 and Nbr1 target ubiquitinated substrates to LC3-autophagosomal membrane. In Htt expressing cells, p62 colocalizes with LC3 and forms a shell around the Htt aggregates under microscope (Bjorkoy et al., 2005). Cue5, the yeast homolog of p62, was recently found to connect ubiquitinated proteins to ATG8. p62 forms oligomers via PB1 domain and likely bridges substrates into a higher-order structure, such as aggresome of damaged proteins and the aggregation of depolarized mitochondria (Geisler et al., 2010; Narendra et al., 2010; Okatsu et al., 2010).

Clearance of protein aggregates by dissolution and autophagy can be hampered under conditions the influx of damaged protein overwhelms the quality control system. In this scenario, asymmetric segregation of protein aggregates serves to prevent the clonal aging induced by toxicity of protein aggregates. Several models have been described to explain the mechanism of asymmetric segregation in budding yeast. One study proposed that protein aggregates associate with actin cables, possibly through a direct interaction of Hsp104p with actin, and ride along the retrograde flow to clear from the bud prior to cell division (Liu et al., 2010). Another model proposed that the attachment of

INQ and IPOD to the nucleus and vacuole, respectively, contributes to the retention of aggregate during cell division (Spokoini et al., 2012). It is thus possible that multiple factors contribute to the asymmetric segregation of protein aggregates (Figure 1-7).

Figures

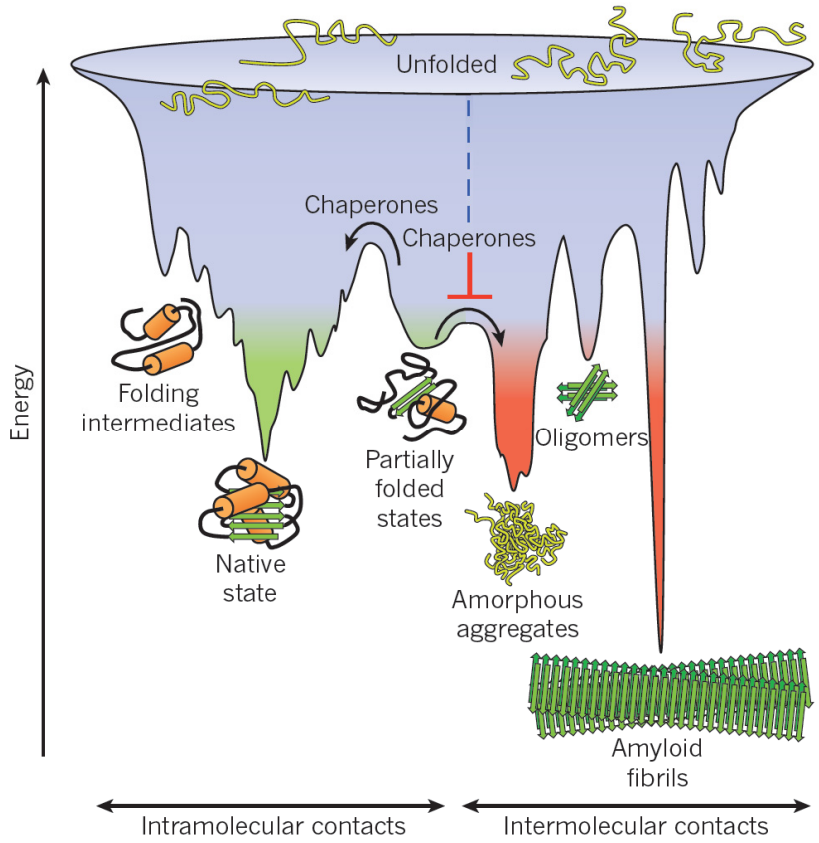

Figure 1-1. Landscape of protein folding pathways (Hartl et al., 2011).

Scheme of the free-energy surface that proteins experienced during folding.

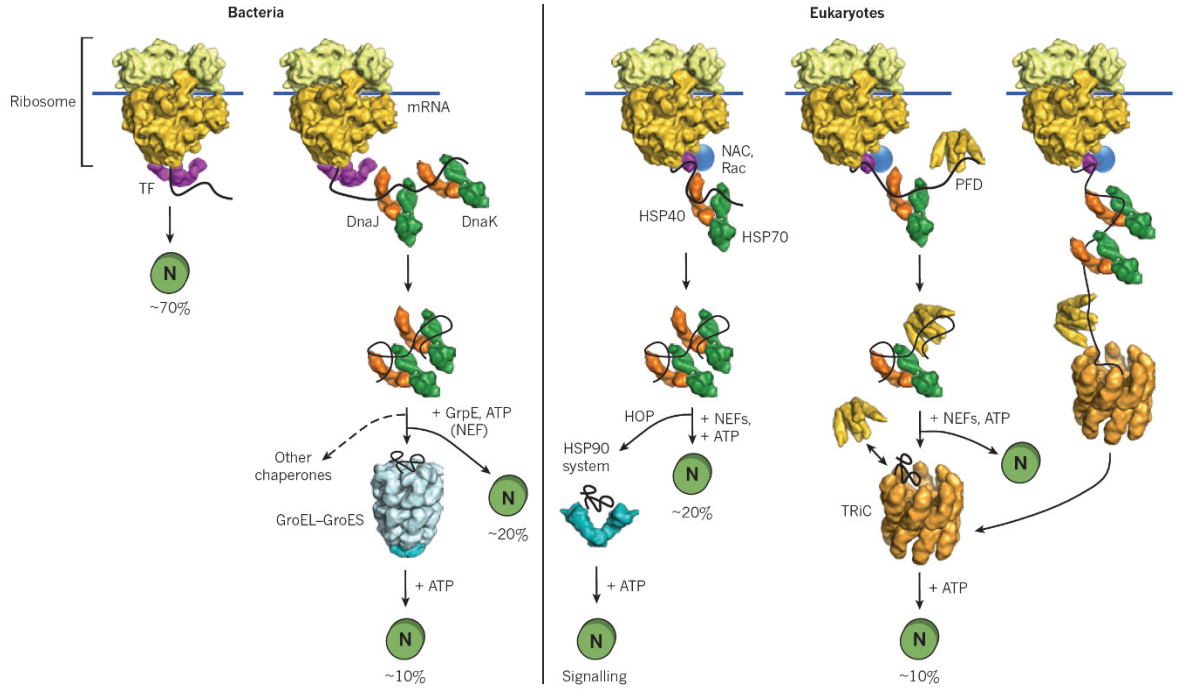

Figure 1-2: Protein folding *in vivo* (Hartl et al., 2011).

In bacteria and eukaryotes, chaperones cooperate with each other in stabilizing nascent polypeptides and assisting the *de novo* folding. The number of interacting substrates is indicated as a percentage of the total proteome.

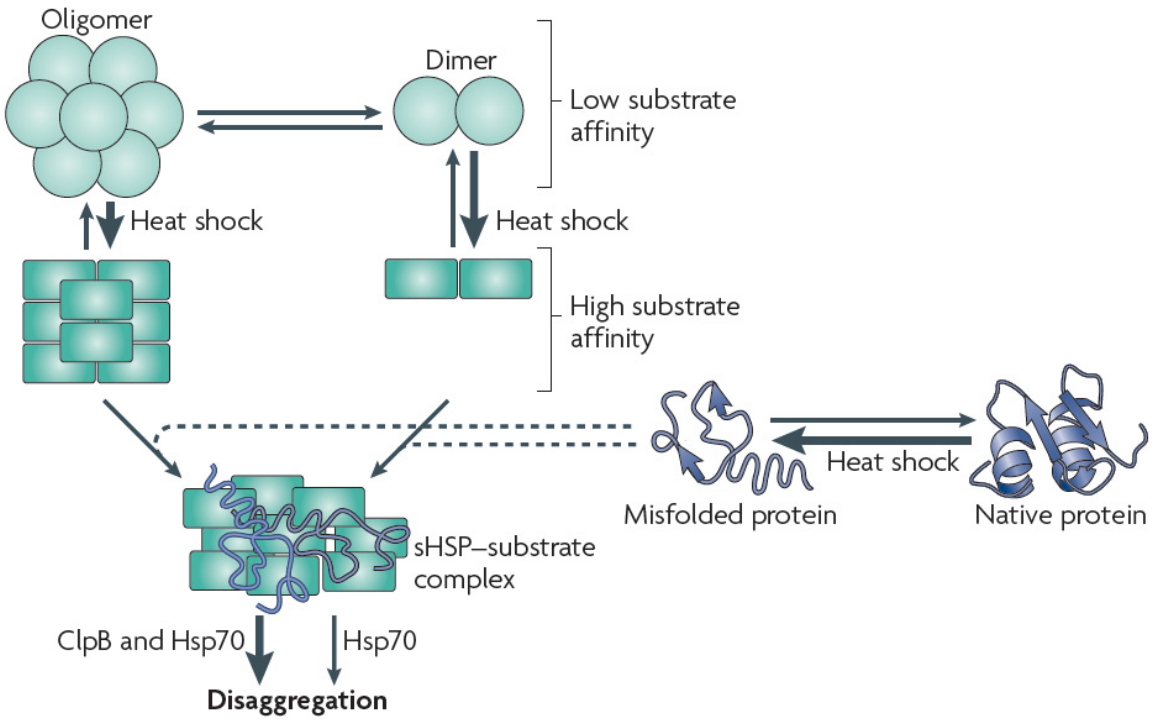

Figure 1-3. Small HSPs and protein aggregation (Tyedmers et al., 2010a).

Small heat shock proteins are in equilibrium between oligomer and subunits. In stress condition, they shift conformation towards the high affinity state, which binds misfolded proteins and maintains them in a competent state for reactivation by ATP dependent chaperones.

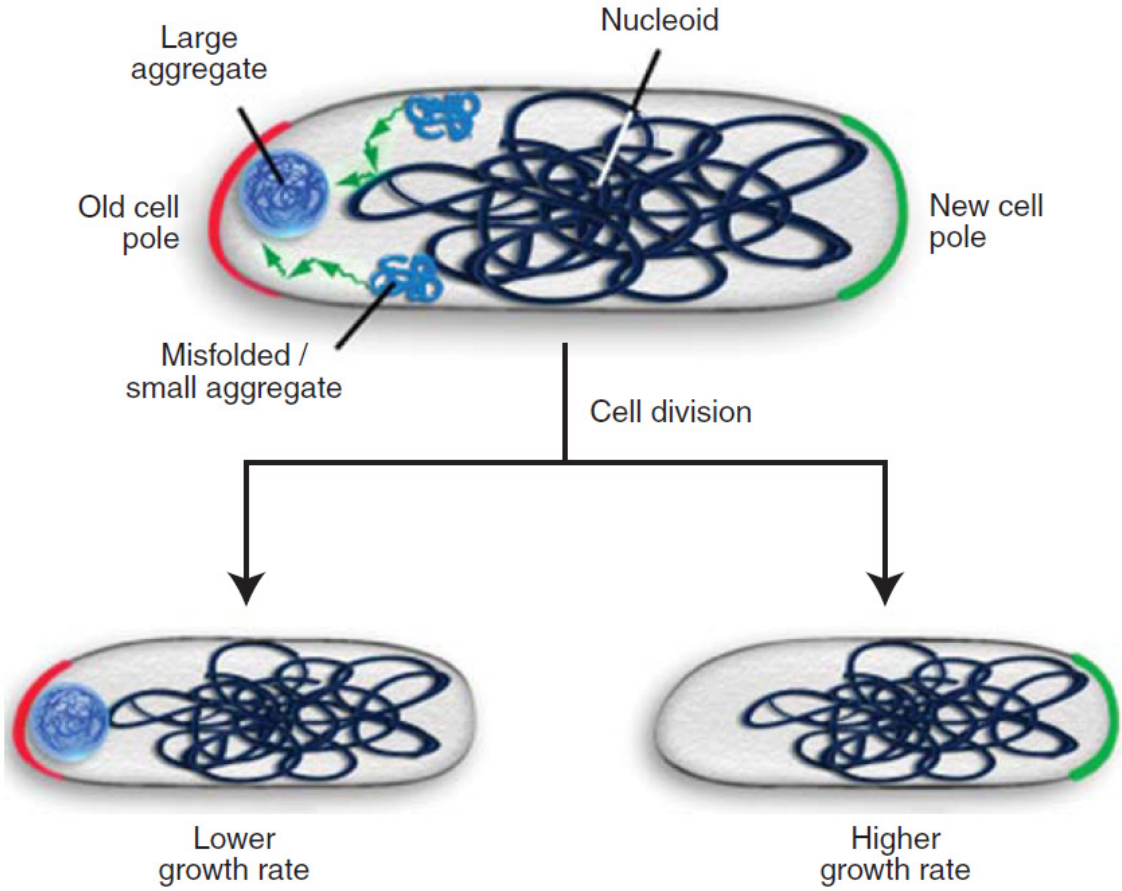

Figure 1-4. The mechanism of aggregation and segregation of misfolded proteins in bacteria (Tyedmers et al., 2010a).

The sequestration and aggregation of misfolded proteins is driven by nucleoid occlusion. The partition of protein aggregate to the old cell pole allows the asymmetric segregation of protein aggregates and cellular fitness through cell division.

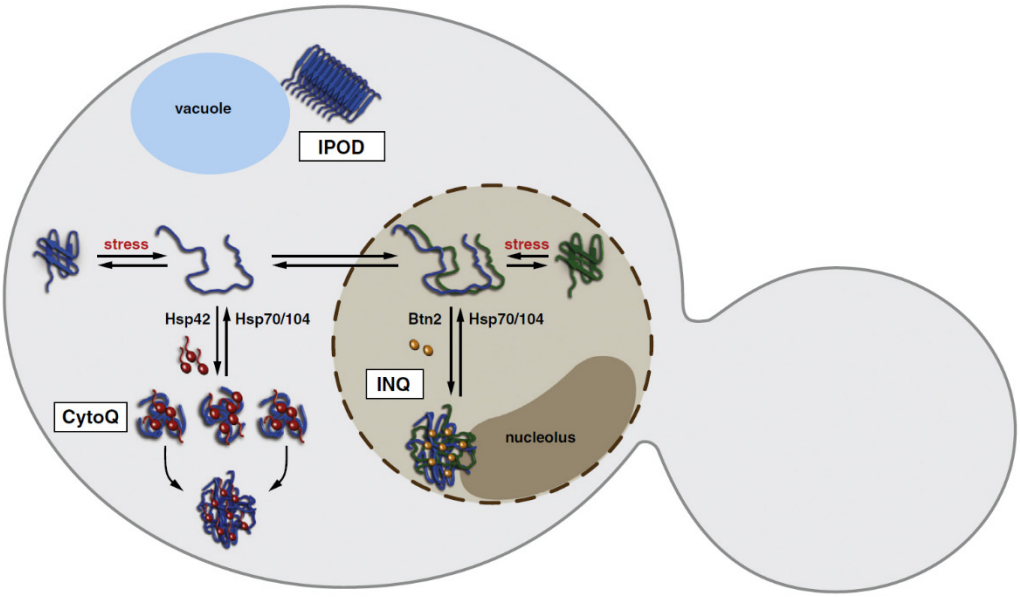

Figure 1-5. INQ, CytoQ and IPOD in yeast(Miller et al., 2015d).

Loss of proteostasis leads to accumulation of damaged proteins and formation of aggregates that deposited at distinct cellular sites.

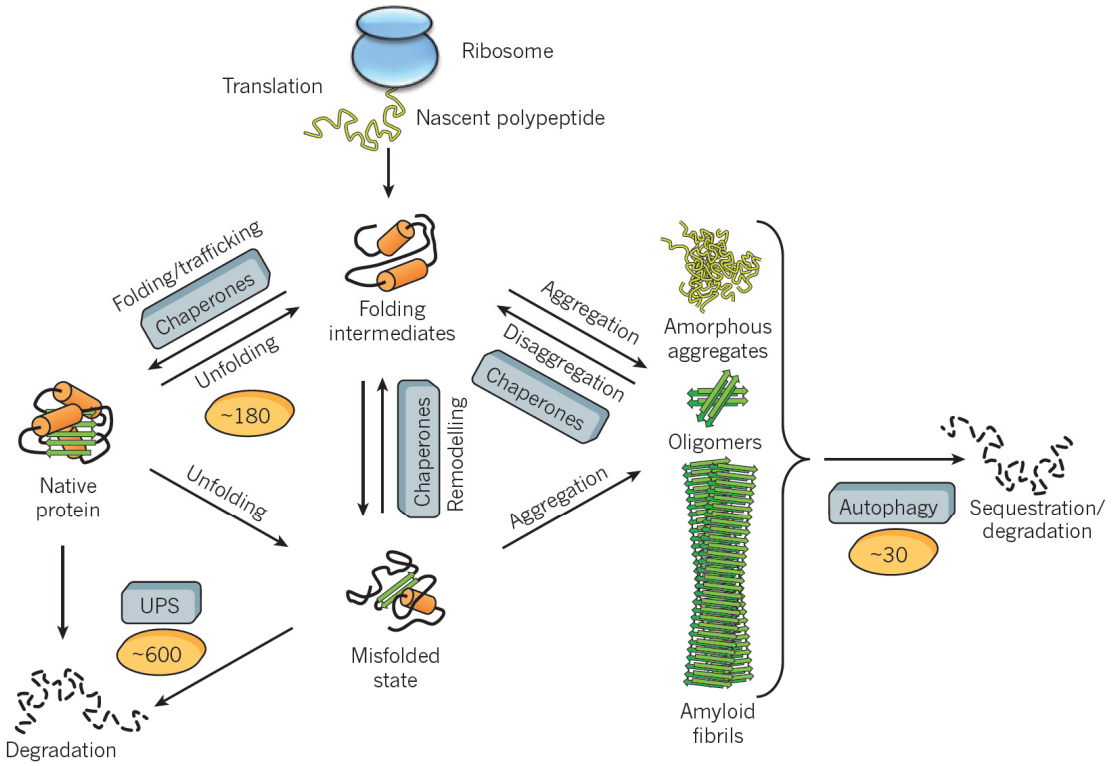

Figure 1-6. Strategies of protein quality control(Hartl et al., 2011).

The folding, refolding and aggregation of proteins are determined by a network of protein quality control factors including chaperones, UPS and autophagy pathway. About 180 different chaperones orchestrate and cooperate with about 600 UPS factors and more than30 autophagy components to prevent accumulation of misfolded proteins and formation of aggregates.

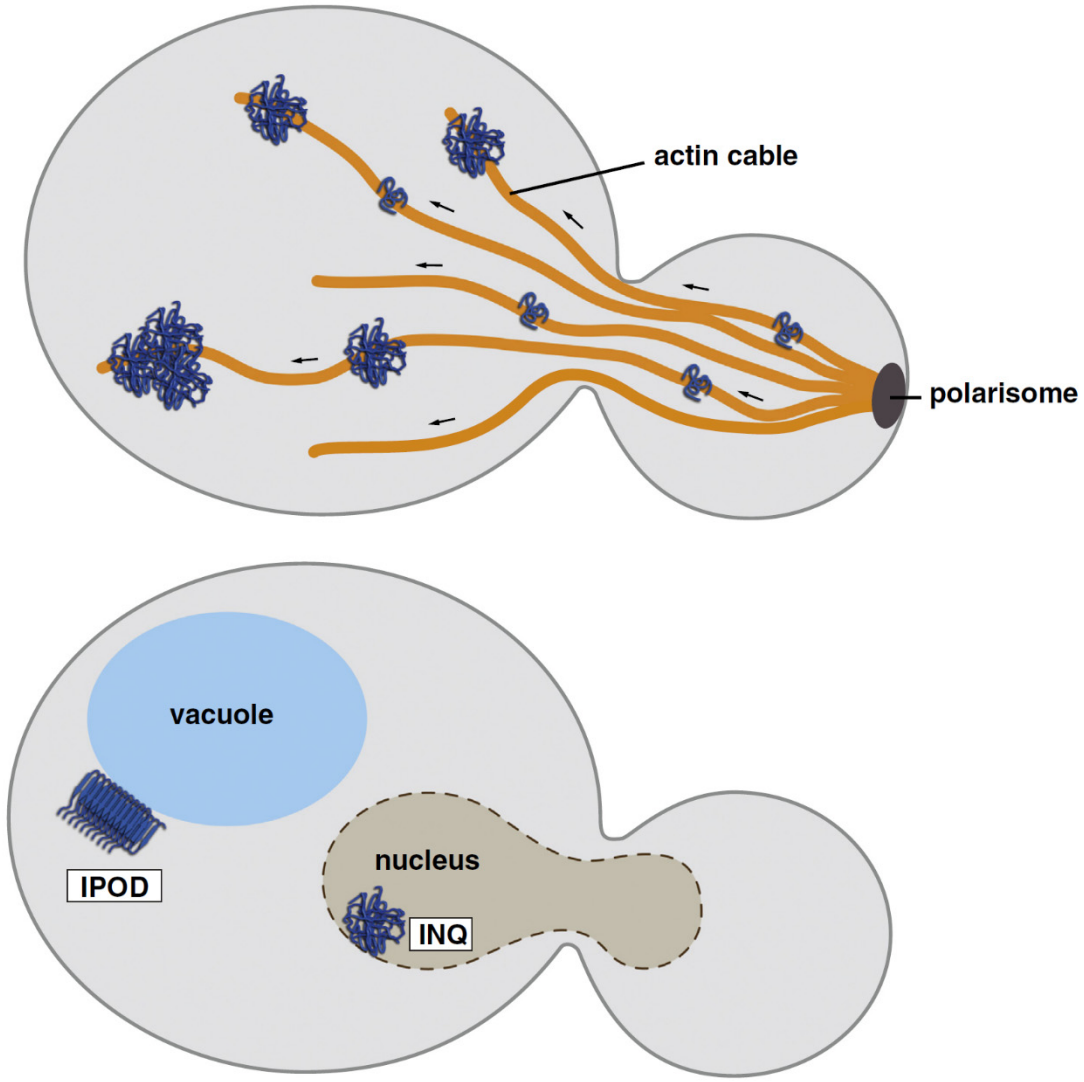

Figure 1-7. Two models of asymmetric inheritance of aggregated proteins in yeast(Miller et al., 2015d).

CHAPTER TWO: MATERIALS AND METHODS

Yeast Strains

Strain	Genotype	Source
RLY4392	*his3Δ1 leu2Δ0 met15Δ0 ura3Δ0*	Steffen et al., Cell 2008.
RLY7022	*HSP104-GFP-HIS3 pSPC42-SPC42-mCHERRY-HIS5/ pRS315 LEU2*	This study
RLY7097	*sir2Δ::kanR*	Giaever et al., Nature 2002.
RLY7110	*HSP104-GFP-HIS3*	Huh et al., 2003.
RLY7167	*sir2Δ::kanR HSP104-GFP-HIS3*	This study
RLY7169	*hsp104Δ::kanR*	This study
RLY7200	*HSP104 Y662A-GFP-HIS3*	This study
RLY7315	*bni1Δ::kanR HSP104-GFP-HIS3*	This study
RLY7316	*bnr1Δ::kanR HSP104-GFP-HIS3*	This study
YBD401	*HSP104-GFP-HIS6*	Liu et al, 2010; Invitrogen;
KY153	*sir2Δ::kanR fob1Δ::Ura3 Nop12Δ::ClonNat HSP104-GFP-HIS3*	This study
KY152	*sir2Δ::kanR fob1Δ::Ura3 Ssf1Δ::ClonNat HSP104-GFP-HIS3*	This study
KY146	*sir2Δ::kanR fob1Δ::Ura3 Hsp104-GFP-HIS3*	This study
KY143	*sir2Δ::kanR Myo2-GFP-HIS3*	This study
	Myo2-GFP-HIS3	Huh et al., 2003
RLY8168	*pRS426-ADH-OLI1-HcRed; DNM1-GFP-HIS3*	This study
RLY8169	*HSP104-GFP-HIS3; trp:: DsRed-HDEL-NatMax*	This study
RLY8170	*HSP104-GFP-HIS3; pRS426-ADH-OLI1-HcRed*	This study
RLY8171	*HSP104-GFP-HIS3; trp:: DsRed-HDEL-NatMax; pYES-mito-BFP*	This study
RLY8172	*HSP104-GFP-HIS3; pESC-URA-Gal-mCherry-UBC9^{ts}*	This study

RLY8173	*trp::p404-GDP-OLI1-HcRed-NatMax;MDM34-GFP-HIS3*	This study
RLY8174	*Δfis1::KanMX; HSP104-GFP-HIS3; pRS426-ADH-OLI1-HcRed*	This study
RLY8175	*Δdnm1::KanMX; HSP104-GFP-HIS3; pRS426-ADH-OLI1-HcRed*	This study
RLY8176	*Δmdv1::KanMX; HSP104-GFP-HIS3; pRS426-ADH-OLI1-HcRed*	This study
RLY8177	*Δfis1::KanMX; HSP104-GFP-HIS3; trp::DsRed-HDEL-NatMax*	This study
RLY8178	*pESC-URA-Gal-GFP-UBC9^{ts}*	This study
RLY8179	*Δrpl42a::NatMX; RPL42B ^{P56Q}-HIS3;HSP104-GFP-URA3*	This study
RLY8180	*MDM34-GFP-HIS; HSP104-mCherry-URA3*	This study
RLY8181	*DNM1-GFP-HIS; HSP104-mCherry-URA3*	This study
RLY8182	*TOM20-mCitrine-HIS3; trp::DsRed-HDEL-NatMa; HSP104-mTur-Ura3;*	This study
RLY8183	*trp::p404-GDP-GFP-Luciferase*	This study
RLY8184	*trp::p404-GDP-OLI1-HcRed-NatMax; ABF2-GFP-HIS3*	This study
RLY8463	*Δfis1::KanMX; HSP104-GFP-HIS3; trp::p404-GDP-OLI1-HcRed-NatMax*	This study
RLY8464	*HSP104-GFP-HIS3; trp::p404-GDP-OLI1-HcRed-NatMax*	This study
RLY8465	*HSP104-GFP-HIS3; pRP1574(EDC3-mCherry-Ura3);*	This study
RLY8466	*HSP104-GFP-HIS3; pRP1661(PUB1-mCherry-Ura3)*	This study
RLY8467	*pRS316-ATG8-GFP; HSP104-mCherry-HIS3*	This study
RLY8468	*ERG11-GFP-HIS3*	(Huh et al., 2003)
RLY8469	*trp::mCherry-Scs2TM-NatMX;Hsp104-GFP-His*	This study
RLY8470	*trp::mCherry-Fis1TM-KanMX;Hsp104-GFP-His*	This study
RLY8471	*leu2::AT1.03-LEU*	This study
RLY8472	*leu2::AT1.03 R122K/R126K-LEU*	This study
RLY2626	*Mat A; ura3-52; his3-Δ200; trp1-1; leu2-3;*	Rancati et al., 2008
RLY8473	*pESC-URA-Gal-GFP-UBC9^{ts}; trp::DsRed-HDEL-NatMax*	This study
RLY8474	*pESC-URA-Gal-GFP-UBC9^{ts}; trp::p404-GDP-OLI1-HcRed-NatMax;*	This study
KaiY 261	*Δhsp104:kan; leu2:: pTDH3-preOLI-HcRed; ura:: pTDH3-preOLI-HcRed*	this study

KaiY 524	*trp::pTDH-KanMX-LucSM-GFP-3xflag*	this study
KaiY 525	*trp::pTDH-KanMX-LucSM-GFP*	this study
KaiY 474	*tim23ts L109P;Hsp104-GFP::Nat*	this study

Hsp104-GFP aggregates clearance assay

Triplicate mid-log cultures (10ml) were heat shocked at 42 ^{o}C for 30min and then shifted back to growth at 42 ^{o}C. Samples were taken every 10 min and fixed in 4% formaldehyde for 25min. Fixation was terminated by washing cells three times with PBS. Imaging was performed on the same day. Aggregates clearance efficiency was calculated as the percentage of buds without aggregates at each time point.

Actin staining and LatA treatment

Cells were fixed with 4% formaldehyde for 2 hr at room temperature with gentle shake. The cells were washed 3 times with PBS and 1 time with PBS+0.2%TX-100. Cells were resuspended in 80µl PBS+0.2%TX-100 and staining with 1.5ul FITC-phalloidin for 40min.

In LatA experiments, mid-log cells were heat shocked and recovered as described in main text. Then 100µg/ml LatA (Invitrogen) or control DMSO was applied to the cells for 10min. 3D time-lapse imaging was performed with present of 100µg/ml LatA (or DMSO control).

Isolation of old cells

Cell populations with advanced replicative age were obtained by magnetic sorting (Chen et al., 2003). Exponentially growing cells were collected and washed twice with ice cold PBS (pH 8.0). $2.5X10^7$ cells were labeled with 1mg/ml Sulfo-NHS-LC Biotin (Pierce) at room temperature for 30 min with gentle shaking. These cells were used as M-cells. The cells were then washed twice with 1ml cold PBS to get rid of free biotin and grown in 500ml YPD for 14-15 hr (OD_{600} was not allowed to exceed 1). The separation of M-cell was carried out by incubating 10^7 M-cell with 20μ anti-biotin microbeads (MACS) in 1ml PBS pH7.2 for 1 hr. Unbounded beads were removed by washing twice with PBS. M-cells were isolated with a magnetic sorter. Successful acquisition of cells with advanced replicative age was verified by staining of buds scars with calcaflour.

Hsp104-GFP aggregates intensity measurements for old cells

Aggregates intensities for old cells were estimated by fitting regions surrounding the aggregates to Gaussian functions with a background parameter to account for diffuse fluorescence. The particle standard deviation was fixed to a value of 0.3 μm determined from fits to the brightest particles. The fitting routine used a Gridsearch algorithm searching over center coordinates with a spacing of 40 nm and fitting amplitude and baseline parameters at each center coordinate with standard linear least squares. Fit regions were identified manually and all fits were performed on sum projections (ImageJ) of the original z stacks so that fitted amplitudes were proportional to the integrated intensity for each aggregate.

STICS measurements of particle motion

As a second, independent method to quantify dynamics of protein aggregates, a variant of

STICS and kICS was used (Berland et al., 1995a; Hebert et al., 2005a; Kolin et al., 2006b). In STICS analysis, the spatio-temporal correlation function is measured from the raw image data as follows:

$$G(\rho,\tau) = \frac{\left\langle \delta I(t+\tau, r+\rho) - \delta I(t,r) \right\rangle_{t,r}}{\left\langle I \right\rangle_{t,r}^{2}}. \quad (1)$$

Here ρ and τ are the spatial and temporal shifts of the correlation function. This function can be quickly calculated using spatial fourier transforms (Berland et al., 1995; Hebert et al., 2005). For randomly diffusing diffraction limited particles, the spatio-temporal correlation function is described as follows:

$$G(\rho,\tau) = G(\tau)\exp\left(\frac{-\rho^2}{\omega_0^2 + 4D\tau}\right) = G(\tau)\exp\left(\frac{-\rho^2}{\omega_0^2 + MSD(\tau)}\right). \quad (2)$$

Here the G(□) term is the traditional correlation function from fluorescence correlation spectroscopy and describes the amplitude of the spatial correlation, but not its spatial extent. The rest of the equation is a Gaussian function essentially identical to the spatial probability function for diffusion convolved with the microscopic point spread function PSF. Here □$_0$ is the "beam waist" of the PSF or two times the spatial standard deviation of the PSF. It is easy to see that the above equation can be extended to anomalous forms of diffusion (Schwille et al., 1999a). If the spatial variance of the above equation is denoted as $\sigma^2(\tau)$ and the variance at τ = 0 is denoted as $\sigma^2(0)$, then the mean squared displacement is given as:

$$MSD(\tau) = 2\left(\sigma^2(\tau) - \sigma^2(0)\right). \quad (3)$$

In order to reduce any effect of changes in Hsp104 expression level over time on the STICS map, the time-series were first detrended by dividing each time point by its average. A weak threshold

was applied to remove signal from the cytosol. These two processes left only aggregates and their motion as the dominating factor in the spread of the spatial cross-correlation over time. A single STICS map was calculated per 256x256 pixel field of view containing approximately between 15 and 30 cells. Each line (corresponding to each time shift) of a circular average of the STICS map was fit to a Gaussian to obtain the variance. The points at □ = 0 were not included in the Gaussian fit so as to avoid the contribution from noise and overall intensity changes. Then equation 3 was used to determine the MSD. Similarly to the tracking data, the first 5 points of the MSD plot were fit to $MSD(\tau) = 4D\tau^{\alpha}$.

3D numerical simulation of aggregate partitioning between mother and bud.

Simulations of particle diffusion through a bud neck were performed using a spherical cell model where "mother" and "bud" spheres were separated by a barrier except at the position of the neck opening. The mother and bud diameters were set to 5 and 4.5 μm respectively and the neck diameter was adjusted as described in the text. 80000 particles were distributed randomly in three dimensions within the mother box before the start of the simulation. At each time step of the simulation, particles were moved from their previous position in each dimension by a distance given by a Gaussian random number with standard deviation $\sqrt{2Dt}$ where D is the diffusion coefficient and *t* is the time step. The diffusion coefficient was set to 0.001 $\mu m^2/s$ for consistency with the diffusion coefficient in aged cells and the time step was set to 5 seconds. This value was chosen because it is small enough to prevent large steps outside of the cell boundary but large enough to allow reasonable simulation time (2000 minutes). Diffusion steps occurring outside of the spheres were reflected back into the spheres. The barrier between mother and bud was enforced by reflecting any diffusion steps that crossed the neck and did not land within the cylinder delineated by the neck opening. Images were created from the simulations by creating a 160 x 160 nm

pixel square corresponding to each particle that was within 1.25 μm of the middle z plane of the simulation. 1D probability density functions for particle position were then created using custom written kymograph tools in ImageJ (NIH, Bethesda, MD). For 2D probability density functions, a sum projection of all particles was created.

Simulation of random walk with confinement and transport components.

Simulations of random diffusion for alpha value distribution analysis and individual trajectory visualization were performed similarly to those described above. Here particle displacements were restricted to two dimensions for consistency with the projected 2D tracking that was performed experimentally. Experimental trajectories are observed for a variable length of time, either due to loss of tracking or disappearance of the particle. We found that the trajectory length distribution was exponential with an average trajectory length of 9.3 frames. In order to match the experimental noise characteristics, our simulated trajectories had lengths specified by an exponential random number with an average of 9.3 frames. Particle positions were updated at each time point as before, but the time between frames was set to 60 seconds, and the diffusion coefficient was set to 0.0005 $\mu m^2/s$ for similarity with that for heat-induced aggregates. In order to simulate restricted motion (sub-diffusion), 30% of the aggregates were not allowed to diffuse more than 0.5 μm from their starting position. Displacements outside of this region were reflected back into the region. In order to simulate transport (super-diffusion), particles were given a 10% probability of transitioning into a "transport" state at each time point. Once in the transport state, the particles moved along a random vector with a linear speed of 0.005 μm/s while still diffusing with a 100 fold reduced diffusion coefficient compared to the non-transport species. Once in the transport state particles were given a 25% chance at each time point of transitioning back out of the transport state.

1D analytical model of aggregate partitioning between mother and bud

Statement of Problem. Dynamics of the aggregates in the yeast cells were cosidered as a constrained random walk, similar to the episomal DNA motion (Gehlen et al., 2011). Simulations were repeated several hundred thousand times and the result was averaged to obtain the distribution of the particles in a region of prescribed geometry. This approach requires long computations and is justified when applied to the problem with complex geometry. When the geometry is simple enough a simpler approximate approach can be used based on numerical and/or analytical solution of the well-known diffusion equation. This approach is justified in an assumption about well-mixing dynamics, i.e., when the averaging of many random trajectories of small number of particles can be effectively replaced by a distribution of very large number of moving particles.

Consider a problem of aggregates dynamics in the budding yeast cell. The geometry is represented by an union of two intersecting spheres of the radii R_1 of mother cell and R_2 of the bud, where $R_1 > R_2$. For simplicity assume that at $t = 0$ all aggregates concentrated in the mother cell and the bud is clean of them, so that the initial aggregates distribution $C(r, t = 0)$ is uniform in the mother compartment and it is zero in the bud.

The dynamics of the particles density is given by the diffusion equation

$$\frac{\partial C}{\partial t} = D\Delta C, \tag{S1}$$

where D denotes the diffusion coefficient and Δ is the Laplacian second order differential operator that in the Cartesian coordinates reads $\Delta = \partial^2/\partial x^2 + \partial^2/\partial y^2 + \partial^2/\partial z^2$. Assume that the mother-bud axis coincides with the x axis, and the center of the mother compartment is in the origin. The region corresponding to the mother compartment is defined as $|r| < R_1$, the corresponding region for the bud

compartment reads $|r - R_{20}| < R_2$, where $R_{20} = \{R_1 + R_2 - \varepsilon, 0, 0\}$; here the maximal size of the overlapping regions ε determines the neck size $d \approx 4R_1^2\varepsilon/(R_1 + R_2)$. The boundary conditions assume no flux of concentration at the cell membrane and reads $n \cdot \nabla C = 0$, where n denotes the normal to the boundary and ∇C is the concentration gradient.

Reduction to 1D Problem. Analysis of 3D numerical solution leads to reduction of the original problem to the 1D version presented below. The equation (S1) converts into

$$\frac{\partial C}{\partial t} = D\frac{\partial^2 C}{\partial x^2}, \tag{S2}$$

that should be solved in the region $-R_1 \le x \le R_1 + 2R_2 - \varepsilon$ subject to the boundary and initial conditions

$$\frac{\partial C}{\partial x}|_{x=-R_1} = \frac{\partial C}{\partial x}|_{x=R_1+2R_2-\varepsilon} = 0, \tag{S3}$$

$$\begin{aligned} &C(x,0) = 1, -R_1 \le x \le R_1, \\ &C(x,0) = 0, R_1 \le x \le R_1 + 2R_2 - \varepsilon. \end{aligned} \tag{S4}$$

Redefining the spatial variable $x \to x - R_1$ and introducing the parameters $L_1 = 2R_1$ and $L_2 = 2R_2 - \varepsilon$ we arrive at the updated boundary and initial conditions

$$\frac{\partial C}{\partial x}|_{x=-L_1} = \frac{\partial C}{\partial x}|_{x=L_2} = 0, \tag{S5}$$

$$\begin{aligned} &C(x,0) = 1, -L_1 \le x \le 0, \\ &C(x,0) = 0, 0 \le x \le L_2. \end{aligned} \tag{S6}$$

Analytical Solution in 1D. The problem (S2, S5, S6) is solved using the separation of variables method (Tikhonov et al., 1990) in which the spatial and temporal dependencies in the solution are separated. As the result the linear partial differential equation (S2) splits into two ordinary linear differential equations.

The solution is written as infinite series

$$C(x,t) = A_0 + \sum_{n=1}^{\infty} A_n \cos\frac{\pi n(x+L_1)}{L_1+L_2}\exp\left(-\frac{\pi^2 n^2 Dt}{(L_1+L_2)^2}\right), \quad \text{(S7)}$$

where the coefficients A_n are given by

$$A_0 = \frac{L_1}{L_1+L_2}, \quad A_n = \frac{2}{\pi n}\sin\frac{\pi n L_1}{L_1+L_2}, (n>0).$$

Qualitative analysis of the solution shows that at large times $Dt >> 1$ the contribution of the summation terms in (S7) rapidly goes to zero for $n > 1$, so that one can use an approximate solution retaining only the first term in the sum

$$C(x,t) \approx \frac{L_1}{L_1+L_2} + \frac{2}{\pi}\sin\frac{\pi L_1}{L_1+L_2}\cos\frac{\pi(x+L_1)}{L_1+L_2}\exp\left(-\frac{\pi^2 Dt}{(L_1+L_2)^2}\right). \quad \text{(S8)}$$

A comparison of the first 20 terms in (S7) and the 3D experimental simulation for a bud neck diameter of 4.25 μm is shown. The 3D simulation distribution resembles the 1D analytical solution. A comparison shows that the 1.25 μm girth constrains diffusion to a great extent. Therefore, the 1D solution overestimates the rate at which particles equilibrate between the mother and bud.

Retention of Particles in the Mother Compartment. Having the exact (S7) and approximate (S8) solution in analytical form we compute the fraction of particles retained in the mother compartment as a function of time. Using the assumption that 3D distribution $C(x,y,z,t)$ is approximated by the 1D solution $C(x,y,z,t) = C(x,t)$ we compute the total number N_m of particles in the mother as integral

$$N_m(t) = \pi\int_{-L_1}^{0} r^2 C(x,t)\,dx, \quad \text{(S9)}$$

where r denotes the radius of the circular cross section orthogonal to the mother-bud axis at position x. The square of the radius is found from geometry as $r^2 = -x(x+L_1)$. The initial particle number $N_m(0)$ equals to the mother compartment volume $N_m(0) = \pi L_1^3/6$. The fraction f of the mother retained particles reads $f(t) = N_m(t)/N_m(0)$ and is computed as

$$f(t) = -\frac{6}{L_1^3}\int_{-L_1}^{0} x(x+L_1)\, C(x,t)\, dx. \tag{S10}$$

Substitution of the exact solution (S7) into (S9) produces the explicit expression

$$f(t) = \nu + \frac{12}{\pi}\sum_{n=1}^{\infty}\frac{\sin a_n}{n a_n^3}\left[2\sin a_n - a_n(1-\cos a_n)\right] e^{-a_n^2 Dt/L_1^2}, \tag{S11}$$

where the parameter a_n is defined as $a_n = n\pi\nu$, and $\nu = L_1/(L_1+L_2)$.

Retaining the first term in the sum in (S10) we find an approximate solution

$$f(t) = \nu + \frac{12}{\pi^4\nu^3}\exp\left(-\frac{\pi^2\nu^2 Dt}{L_1^2}\right)\sin\pi\nu\cdot\left[2\sin\pi\nu - \pi\nu(1+\cos\pi\nu)\right] \tag{S12}$$

It follows from the solution (S11) that the minimal fraction of the particles in the mother compartment equals to $f_{min} = \nu$ and it is reached at equilibration time t_* roughly estimated as $t_* = (L_1+L_2)^2/(\pi D)$.

Qualitative analysis of the particle dynamics and retention implies that the particles exchange between the two compartments leads to leveling off the concentration distribution at the characteristic time t_* inversely proportional to the particles diffusivity and proportional to square of the cell size. The negligible exchange may be assigned to two reasons: initial state is close to the dynamical equilibrium, or the diffusion coefficient is small enough to prevent transfer of aggregates between the compartments.

We analyzed the data on fraction f dynamics for the WT yeast cells and found the value $f = 0.8$ at the time scale of 90 min. The estimate of the diffusion coefficient D based on the aggregates trajectory analysis gives $D = 1.0 \cdot 10^{-3}\ \mu m^2/s$. The characteristic cell size is in the range $2(R_1 + R_2) = 8 - 10\ \mu m$. The estimate of complete relaxation time produces $t_* = 600\ min$. This means that the random walk motion does not affect the aggregate distribution between the mother and the bud.

Actin cable reconstruction assay and actin staining

In actin cable reconstruction assay, 2x10^8 cell/mL mid-log cells were incubated with 100μg/mL LatA (Enzo) for 10min at 30 °C. Then cells were washed three times with fresh YEPD and recover at 30 °C. Samples were taken before LatA treatment, immediately after LatA treatment and various time-points as indicated in figure. We start timing when the cells were washed first time after LatA treatment.

For phalloidin staining of actin cytoskeleton, cells were fixed with 4% formaldehyde for 2 hr at room temperature with gentle shake. Then cells were washed 3 times with PBS and 1 time with PBS+0.2%TX-100. Proper amount of cells were resuspended in 70μl PBS+0.2%TX-100 and staining with 2ul air dried FITC-phalloidin for 40min. Samples were then washed twice with PBS+0.2%TX-100 and once with PBS before subjected to microscopy.

Protocol for *in situ* detection of carbonylated protein

Basically the staining of carbonylated proteins was done as described previously (Aguilaniu *et al.* 2003). Overnight SC-complete culture grew in 30 °C with OD_{600} around 0.8 was diluted to 0.1 OD_{600} and refreshed for 2hr before adding H2O2 to 1mM. After growing for another 2hr with or without H2O2, about 5x10^7

cells were collected and washed with water for three times. Cells were then fixed by 70% ethanol for 45min at room temperature. Cells are washed and treated with reducing buffer as indicated in previous protocol. For spheroplating, cells were resuspended in 500ul PH7.5 digestion buffer and zymolase (Z1004 from US biological) was added to a final concentration of 100U/mL for 5min at 30 degree. DNPH derivation of carbonyl group and the following immunostaining was carried out as previous protocol. Since the recipe of the kit changes overtime and the DNPH is now dissolved in 2N HCl instead of 100% TFA 10 years ago that used in Aguilaniu et al.'s assay. Therefore instead of just trying the DNPH solution from the new kit (S7150, Millipore), we also prepare the DNPH solution and neutralization solution according the old recipe, that is 100mM DNPH dissolved in 100% TFA and 2M tris-base in 30% glycerol (Wang & Powell 2010). After failed with those materials, we also try the 20mM DNPH in 10% TFA as 10xDNPH solution according to another published work (Tessarz *et al.* 2009). In addition to those endeavor, we also tried various time of DNPH derivation arrange from 5min to 30min. We also contacted Dr. Aguilaniu and Dr. Tessarz for suggestion, and Dr. Aguilaniu told me they never succeed with homemade solutions while Dr. Tessarz made all solutions by himself.

Confocal microscopy

Live-cell images were acquired using either a Yokagawa (Tokyo, Japan) CSU-10 spinning disc on the side port of a Carl Zeiss (Jena, Germany) 200m inverted microscope, Perkin Elmer (Waltham, MA) Ultraview VoX system equipped with Zeiss Definite Focus, or a Carl Zeiss LSM-510 Confocor 3 system. 488/561 nm excitation was used to excite GFP/RFPs, and emission was collected through the appropriate filters onto a Hamamatsu C9100-13 EMCCD on the spinning disc systems or the single photon avalanche photodiodes on the Confocor 3. All GFP images were acquired through a 500-550 nm filter. RFP images were acquired with a 580 nm long pass filter on the Confocor 3 and CSU-10, and a

420-475/502-544/582-618/663-691 multiband filter on the Ultraview. All images were acquired in a multi-track, alternating excitation configuration so as to avoid GFP bleedthrough. The CSU-10 and Ultraview systems utilized a 100x 1.45 NA Plan-Apochromat objective while the Confocor 3 utilized a 40x 1.2 NA Plan Apochromatic water emersion objective with a pinhole of one airy unit. Images were acquired using MetaMorph (version 7.0; MDS Analytical Technologies) on CSU-10 spinning disc system, Volocity 6.3 (Perkin Elmer) on Ultraview system and Carl Zeiss AIM software for the LSM 510.

Structured illumination microscopy (SIM) images were acquired on an Applied Precision OMX Blaze microscope (Issaquah, WA, USA) equipped with PCO Edge sCMOS cameras (Kelheim, Germany). The objective used was an Olympus (Center Valley, PA, USA) 60x 1.42NA Plan Apo N oil objective. Image stacks were acquired at 125 nm intervals. Images for mTurquoise2, mCitrine, and DsRed were excited with 440, 514, and 561 nm lasers, respectively, and emission was collected through standard CFP, YFP, and RFP filter sets. SIM reconstruction was performed with the Applied Precision Softworx software package utilizing multi-color optical transfer functions measured with 100 nm blue, green, and red fluospheres in PBS on a coverslip surface (Life Technologies, Carlsbad, CA, USA) following the Applied Precision protocols. Color alignment in the radial plane was performed using the color alignment slide from Applied Precision. Color alignment in the axial direction was performed using 100 nm tetraspeck beads (Life Technologies). 3D reconstruction of SIM images was done with Imaris.

Yeast cells were grown in synthetic complete (SC) or drop-out media containing 2% dextrose overnight at 30 ^{o}C (23 ^{o}C for *prt1*^{ts}). The 4 ml mid-log culture with OD_{600} of roughly 0.5 was transferred to 42 ^{o}C (37 ^{o}C for *prt1*^{ts}) for 6min (or specified). To express mCh-Ubc9^{ts}, GFP-Ubc9^{ts} and mito-BFP, which are under Gal promoter, cells were grown in SC-Ura media containing 2% raffinose to OD_{600}~0.8 and induced by add 2% galactose for 2hr. Gal induction was ceased by adding 2% glucose for 30min at 30 ^{o}C before applying stresses or imaging.

For 3D fluorescence time-lapse imaging, cells were placed on a thin SC (2% dextrose) agarose gel pad to allow for prolonged imaging at room temperature (Tran et al., 2004). 3D image stacks were acquired every minute for 60-90 min or 20sec for high temporal resolution. Bioptechs Objective Heater System was used to heat up the 100x objective in spinning disk and the temperature of lense was monitored by OAKTON infraPro® infrared thermometer. Lens temperature of 37 ^{o}C achieved an aggregation level comparable to 42 ^{o}C in liquid culture. Each z-series was acquired with 0.5 micron step size. For All images processing was performed in the Image J software (NIH, Bethesda, MD). For visualization purposes, images were scaled with bilinear interpolation was used for figures. Photobleach was corrected for GFP channel.

FRET measurement was performed by using the acceptor photobleaching method. Briefly, yeast cells expressing AT1.03 or AT1.03 R122K/R126K were immobilized on a glass slide. A Perkin-Elmer Ultraview spinning disc system with a CSU-X1 Yokogawa disc was used for imaging. A 100X 1.4 NA Plan-apochromatic objective was used, and emission was collected onto a C9100 Hamamatsu Photonics EM-CCD. CFP was excited with a 440 nm laser, and emission was collected through a 456- 484 nm band pass filter. Even though YFP is excited with this laser line, control experiments demonstrated no YFP back-bleedthrough through the 456- 484 nm filter. YFP was illuminated, and photobleached, with a 514 nm laser. Emission of YFP was collected with a 525-575 nm bandpass filter. 5 to 7 images of CFP were acquired before and after bleaching of the YFP with intense 514 nm light. After subtraction of camera background, the average intensity of CFP in a region of interest spanning the cytosol was determined in the 4 images before acceptor bleach (I1), or the 4 images after acceptor bleach (I2). FRET efficiency is reported as 1-(I1/I2).

EM microscopy

Yeast cells grown in YPD with or without heat shock (30 min at 42 °C) were harvested at mid-log phase, vacuum filtered and freezing-fixed in a high pressure freezer (EM PACT I; Leica). An automatic freeze substitution unit (AFS; Leica) was used for the freeze substitution with 0.1% uranyl acetate and 2% glutaraldehyde in acetone. Cells were infiltrated and embedded in embedding resin (Lowicryl HM20; Polysciences) and polymerized at −50°C. Serial ultrathin sections of 50-70 nm thick were cut on an ultramicrotome (Leica), and sections were collected onto formvar/carbon coated slot copper grids (Electron Microscopy Sciences). After staining sections with UA and lead, serial images were collected on a TEM (FEI Tecnai) and 3D reconstruction was done with ImageJ. For immunogold labeling of the GFP-tagged Hsp104, cells were fixed with 2% paraformaldehyde, 0.01% glutaraldehyde in 0.1 M PBS, then infused with 2.3 M sucrose and polyvinypyrrolidone (PVP) in 0.1 M PBS overnight at 4°C. The pellet was frozen on ultracryo stubs in liquid nitrogen and stored in liquid nitrogen until use. Ultracryo sections (70-100nm) were cut using a Leica EM UC6 ultramicrotome (Leica), incubated with an anti-GFP antibody (Invitrogen) followed by 10 nm gold-conjugated antibody labeling. Grids were all viewed with a FEI Tecnai TEM at 80kV.

Drug treatments

Cycloheximide (C4859, Sigma) was added to a final concentration of 100 μg/ml for 15 min at 30 °C before aggregate-inducing stress treatment. MG132 (C2211, Sigma) dissolved in DMSO was added to a final concentration of 80 μM. Anisomycin (A9789, Sigma) dissolved in DMSO was added to a final concentration of 200 μg/ml for 30 min at 30 °C prior to aggregate-inducing stress treatment. A2C (A0760, Sigma) dissolved in H_2O was added to a final concentration of 1 mg/ml for 10 min in 30 °C.

Hydrogen peroxide solution (216763, Sigma) was diluted 10 times in H_2O and added to a final concentration of 0.7 mM at 30 °C. CCCP (C2759, Sigma) was dissolved in ethanol to 20 mM as stock and 25μM was used to treat cells after heat shock for 15min before time-lapse imaging. Antimycin A (A8674, Sigma) was dissolved in ethanol to 10mM and 10μM was used to treat cells after heat shock as CCCP. 2-DG (D6134, Sigma) was dissolved in SC complete media without glucose addition to 1.63 M and 20 mM was used to treat cells after heat shock. KCN (20781, Sigma) and NaN3 (S2002, Sigma) was dissolved in water and added to culture to 1 mM and 0.2 mM, respectively. GdnHCl (Sigma) was dissolved in water and 3mM was used to inhibit Hsp104 activity.

Survival rate assay

Cells were grown overnight at 30^0C in YPD media then refreshed to $O.D_{600}$ of 0.5 prior to use. Standard serial dilutions and hemocytometer cell counter was used to plate an initial equal number of cells on YPD plates for various strains (Borkovich et al., 1989). Cells were subjected to heat shock treatments at 50^0C for 0, 5, 15, 30 minutes and then plated on YPD plates and incubated at 30^0C for 48 hours. In all cases survival rate was calculated with the colony count as previously described (Sanchez et al., 1992). Colony count assay was done using standard automated AxioVision software and also validated manually with visual inspection.

Aggregate dissolution assay

Aggregate dissolution assays were done as described previously (Zhou C. et al, 2011). Briefly, yeast cells were heat shocked 30 min at 42 °C and recovered for 15min at 30 °C (with or without drug) before mounted on an agarose gel-pad slide for 3D time-lapse imaging. The major technical flow is as

follows: after generating masks of the aggregates, cell areas and cytoplasm was created, they were used to calculate the average aggregates region intensity (includes cytosolic background), average cytosolic intensity, and total aggregates area. The average cytosolic intensity was subtracted from the average aggregates region intensity to obtain the corrected average aggregates intensity without cytosolic background. Finally, the total aggregates intensity was calculated by multiplying the corrected average aggregates intensity by the aggregates area and normalized to the initial intensity for comparison between strains or conditions. Aggregates intensities were measured starting at 30 minutes after the start of acquisition because during the early part of the movies aggregates grew in intensity as explained in detail in (Zhou et al., 2011).

Quantification of the amount of aggregates

The fraction of Hsp104-GFP in aggregates was used as an estimation of the amount aggregate since it binds aggregates with high affinity. The method described above for aggregate dissolution was employed to find the total intensity of aggregate-bound and free cytosolic Hsp104-GFP. The percentage of aggregate-bound Hsp104-GFP in each cell was calculated by dividing total intensity of aggregate-bound Hsp104-GFP by the total intensity of Hsp104-GFP of the same cell. Typically more than 80 cells in each sample were processed and the mean percentage of aggregate-bound Hsp104-GFP was calculated. Specifically, yeast culture treated with CHX/anisomycin/DMSO at 30 ^{o}C were followed by heat shock (42 ^{o}C for wild type cells and 37 ^{o}C for *prt1*^{ts} mutant), H_2O_2 and MG132 for indicated time. All analyses were done with customized plugins in Image J.

Detection of active translation sites

Ribopuromycylation method (David A. et al, 2012) was modified here to detect the active translation sites. Actively growing yeast culture (1-2mL, OD_{600}~0.5) was treated with 150μg/mL puromycin (P9620, Sigma) for 30 sec followed by one wash with fresh media containing 100μg/mL CHX. After re-suspension in fresh media containing 100μg/mL CHX for 2 min, paraformaldeyhe was added to 4% and the cells were fixed for 90min at room temperature. Fixation was terminated by washing twice with sorbitol buffer (1.2M sorbitol, 0.1M potassium phosphate, pH 7.5) and cells were digested by 50 μg/ml zymolase 100T (US biology) at 37 °C for 15min in 200μL sorbitol buffer. Cells were spun down by 400g centrifugation for 30sec and then carefully re-suspended in 200μl sorbitol buffer by tapping before applied to poly-D-lysine (P1024, Sigma) coated coverslip for 10 min at room temperature. The coverslip was washed once with sorbitol buffer to remove floating cells and submerged in -20 °C methanol for 6 minutes followed by -20 °C acetone for 30 seconds. After briefly air drying, coverslip was washed 5x with PBS containing 1 mg/ml BSA and labeled with monoclonal anti-puromycin antibody (1:3000 in PBS/BSA, MABE343, Millipore) for 1 hr at room temperature with gentle shaking. After 5x5 min wash with PBS-BSA, the fluorescent secondary antibody was applied for 1 hr at room temperature followed by 5x wash before mounting and imaging. Erg11-GFP (ER marker) signal survived this procedure and no anti-GFP was used.

Fluorescence correlation spectroscopy

FCS measurements were done as described previously (Slaughter B. et al, 2007). Fluorescence correlation spectroscopy (FCS) data was acquired with a Zeiss confocor 3, equipped with single photon

counting avalanche photodiodes and environmental-control chamber. A 40X, 1.2 NA Plan Apochromatic water emersion objective was used, with a pinhole of 1.0 airy units. For examination of GFP, the 488 nm laser line was used, through a HFT 405/488/561 nm main dichroic. A NFT 565 nm emission beam splitter was used, and GFP emission was collected through a 505-540 nm emission filter.

For FCS experiments with heat shock, live yeast cells were immobilized between a glass coverslip and a slide. To allow for molecular brightness comparisons between samples, pre-measured coverslips of thickness 0.179 mm were used, and the correction collar on the 40X water objective was optimized for this coverslip thickness. The temperature inside the chamber was verified at 42 ± 2 °C. At this temperature, GFP-Ubc9 and GFP-Luciferase began to form visible aggregates, which could be observed with an image prior to the FCS run. The location of each FCS run was chosen to avoid visible aggregates. For each cell, 3 to 5 individual FCS runs of 3 to 5 seconds were acquired.

Correlation curves were generated using standard formulas (Macdonald et al., 2014; Slaughter et al., 2011)

$$G(\tau) = \frac{\langle \delta I(t) \cdot \delta I(t+\tau) \rangle}{\langle I(t) \rangle^2}$$

Where I is the intensity in photon counts, and $\delta I(t) = I(t) - \langle I(t) \rangle$).

In this particular case, we used a sampling frequency of 100,000 Hz and a segmented linear detrending with 2 linear segments. For analysis, the average curve for each individual cell was fit, with a fixed GFP blinking time of 250 μs and a blinking fraction of 5%. Correlation curves were fit to a single diffusing

species. $G_{0,}$ which represents the initial amplitude of the correlation curve, was obtained, and is related to the average number of particles in the focal volume by the following:

$$N = \frac{\gamma}{G_0}.$$

We used 0.27 for γ, a focal volume shape factor (Thompson NL.1991). The average molecular brightness ε, represented in counts per second per molecule, is given by

$$\langle \varepsilon \rangle = \frac{I}{N}.$$

Multiple cells were acquired for each time grouping, and data for each strain was acquired with a minimum of two separate experimental replicates.

Co-localization Quantification

Yeast expressing Hsp104-GFP and mito-HcRed (pRS426-ADH-OLI-HcRed) or DsRed-HDEL (YIPlac-DsRed-HDEL-NatMX) were heat-shocked for 6 min at 42 °C. Z-series were acquired with 0.5 micron step size on either of the spinning disk systems. For aggregate-mitochondria association quantification, max projections were made from Z-series and mitochondria-overlapped aggregates were counted to generate the percentage of organelle-bound aggregates. The results generated from max projections were compared with 3D reconstruction. As we did not observed any apparent difference between max-projection and 3D reconstruction, all aggregate-mitochondria association data presented came from quantification done with max projection. For aggregate-ER association, different focal planes of the same cell were analyzed and ER-overlapping aggregates were counted. Small aggregates usually

significantly overlap with ER while big aggregates show partial overlap due to their size and the fact that DsRed-HDEL is a luminal marker.

Organelle Segmentation

Organelles were segmented for random colocalization simulations and distance dependent mobility measurements. Segmentation was performed in ImageJ (NIH, Bethesda, MD). Images were first blurred with a one standard deviation Gaussian filter. Cytoplasmic background was then subtracted with a rolling ball background subtraction with a radius of 5 pixels. For the mitochondria and vacuoles, the image was then segmented with a threshold at 8 times the average intensity of each subtracted time point. Segmented objects were then filtered to remove any objects with less than 5 pixels. Since ER segmentation was performed on structured illumination images which have a different noise and intensity profile, we adjusted the threshold to 10 times the average intensity and omitted the object filtering step.

Aggregate Colocalization Simulations

Simulations were performed to estimate the maximum percentage colocalization of randomly positioned aggregates with thresholded organelles. For each experimental scenario, borders of a randomly selected subset (>8) of cells were first selected with the elliptical selection tool in ImageJ. For ER simulations, single slices were taken from structured illumination images and segmented as discussed above (Organelle Segmentation). For all other organelles, the simulations were run on maximum projections of the z stack. All possible aggregate centers within each of these 2D segmented

representations of the cells were surveyed and positions less than 3 pixels from the nearest segmented mitochondrial pixel were considered "colocalized." This value was used irrespective of image scaling (e.g. for structured illumination this represents a much more stringent criterion) and was chosen to emulate the visual threshold for colocalization. Given the complexity of ER quantification, the simulation was checked by randomly placing simulated aggregates of typical aggregate size on the image and visually quantifying those images. The two methods gave essentially identical colocalization fractions (within 1%).

Particle tracking and calculation of diffusion coefficient

In order to have a more accurate tracking and avoid crosstalk between trajectories of aggregates, 6 min heat shock time-lapse movies were used in this analysis due to fewer and smaller aggregates in cells. Tracking of Hsp104-GFP-associated protein aggregates was accomplished using a custom ImageJ plugin modeled after the MOSAIC ParticleTracker software (Sbalzarini and Koumoutsakos, 2005). The plugin can be downloaded from http://research.stowers.org/imagejplugins. The plugin differs from the MOSAIC plugin only in that it auto-thresholds based on the fraction of the maximum intensity rather than a constant percentage of the brightest pixels. This is crucial for noisy movies in which few aggregates are present. Prior to tracking, max-projection time-series were Gaussian smoothed (sigma = 1 pixel) and a rolling-background subtraction with a width of 5 pixels was applied. The particle diameter for the analysis was 10 pixels. The threshold was set at 15% of the maximum intensity and trajectories with displacement of more than 20 pixels in a single frame were terminated. In order to calculate a MSD plot, only trajectories lasting longer than 4 time points were considered. The MSD was calculated using the equation, $MSD(\tau) = \left\langle \left| r(t+\tau) - r(t) \right|^2 \right\rangle$. The first 4

points were fit to $MSD(\tau) = 4D\tau^{\alpha}$ by fitting for D with linear least squares for all possible values of α between 0.01 and 2 and selecting the α value that minimized the unweighted fit error. Here *D* is the diffusion coefficient and α is a factor indicating non-random diffusion.

In experiments where the mobility of aggregates associated with mitochondria was assessed relative to all others, we utilized the mitochondrial segmentation described above and searched the aggregate tracking data for portions of tracks that remained associated (within 3 pixels, HS-on/H_2O_2-on) or unassociated with mitochondria for more than 4 frames (HS-off/H_2O_2-off). We then performed the same MSD analysis as above for those track segments. Note that these measurements were intended for relative analysis given that the selection of stably associated (or unassociated) tracks biases the result against rapidly moving aggregates that are more likely to transiently (perhaps non-specifically) associate with mitochondria.

Aggregate size and number quantification

For quantitative comparison of the effect of fis1 on aggregate inheritance, it was necessary to quantitate both the number of aggregates per cell as well as the average size (estimated by the average intensity) of aggregate. The number of aggregates per cell was taken directly from the tracking analysis above by dividing the total number of aggregates at the specified time point by the number of cells present in the particular image. This analysis was averaged over at least 3 fields of view. Intensity per aggregate was determined by summing the 10 pixel radius around each tracked aggregate. This was then used for the average aggregate intensity measurement.

Aggregate leakage analysis

To obtain a statistically reliable result of aggregate leakage rate, 30 min HS at 42 °C was applied to RLY8185/8186 to generate more aggregates in mother cells. 3D time-lapse movies of yeast cells subjected to 30 min heat shocked (42 °C) and 15 min recovery (30 °C) were generated and max projections were used for analysis as previous study (Zhou et al., 2011). Each cell in the process of budding during the first 30 min of the 1 hr long movies was visually examined to score the number (≥0) of the aggregates that moved from the mother into bud (MTB). Percentages of cells with at least one MTB (usually only 1 out of more than 7 aggregates in each wild type cell) are shown in figures. Percent of MTB events not associated with bud-oriented mitochondrial extension, calculated by dividing the number of MTB events not associated with bud-oriented mitochondrial extension over total MTB events in each movie, is shown in figure.

Purification of aggregates

240 mL yeast culture (ky524 or ky525) with OD around 0.5 were heat shocked in 42 °C water bath or treated with 0.7mM H_2O_2 for indicated period of time. After heat shock or H2O2, CHX and CCCP were added to prevent aggregate formation and dissolution. Cells were collected by centrifugation at 5,000 g for 2min and the pellets were washed once with water, re-suspended in 1mL 10mM DTT (PH 9.3) 5min at 30 °C. Then the pellets were washed once with sorbitol buffer (PH 7.5, 1.2M Sorbitol), followed by 5min digestion with 0.7mg/mL zymolase100T (US biological) in 1mL zymolase buffer. Zymolase was removed by centrifugation (800 g) and cells were washed twice with zymolase buffer. 800μl ice cold lysis buffer (50mM HEPES PH 7.5, 150mM NaCl, 1mM DTT, 5% glycerol, 1% Triton-X100 and protease

inhibitor cocktail (roche #11836170001) and 10U/mL RNasin plus RNase Inhibitor (N2611)) by pipetting 15-20 times on ice. 2min centrifugation at 800 g was followed by 1min 6,000 g centrifugation to remove cell debris. The supernatant was carefully transferred to the top of sucrose gradient consisting of 650µl 50%, 2mL 20% and 1mL 10% sucrose dissolved in the lysis buffer. Samples were centrifuged at 20,000 g for 16min. 18-gauge needles were used to insert into 20% sucrose fraction from the side of centrifuge tube to collect about 900ul 20% sucrose fraction. The entire 900ul 20% fraction was directly applied to the column prefilled with about 600µl M2 resin (A2220, sigma) and balanced in cold room according to the manufactory instruction. The column was then washed 20 times with 1mL cold wash buffer (1xTBS contain 10U/mL RNasin plus). Then the beads were carefully transferred into a new 2mL tube, gently inverted 10-15time and left on rack for about 5min-10min to separate beads from wash buffer. The supernatant was replaced with fresh wash buffer. The beads were then loaded back to column and incubated with 650µl of 1xTBS supplemented with 2% SDS for 5min on bench before elution.

Mass spectrum analysis

TCA-precipitated pellets were solubilized and digested with Trypsin. Peptide mixtures were loaded on split-triplephase fused-silica micro-capillary columns and placed in-line with linear ion trap mass spectrometers (LTQ, ThermoScientific), coupled with quaternary Agilent 1100 or 1200 series HPLCs. The MS/MS datasets were searched against a database of 11,986 sequences, consisting of 5,816 S. cerevisiae non-redundant proteins. Peptides significantly enriched in LucGFP-3xFlag sample for at least three repeats are selected to generate the dataset as hits. The mitochondrial enrichment was searched against the mitochondrial proteome generated in yeast genome database under GO term “mitochondrion”.

CHAPTER THREE: MOTILITY AND SEGREGATION OF HSP104-ASSOCIATED PROTEIN AGGREGATES IN BUDDING YEAST

Summary

During yeast cell division, aggregates of damaged proteins are segregated asymmetrically between the bud and the mother. It is thought that protein aggregates are cleared from the bud via actin cable-based retrograde transport toward the mother, and that Bni1p formin regulates this transport. Here we examined the dynamics of Hsp104-associated protein aggregates by video microscopy, particle tracking and image correlation analysis. We show that protein aggregates undergo random walk without directional bias. Clearance of heat-induced aggregates from the bud does not depend on formin proteins but occurs mostly through dissolution via Hsp104p chaperon. Aggregates formed naturally in aged cells also exhibit random walk but do not dissolve during observation. Although our data does not disagree with a role for actin or cell polarity in aggregate segregation, modeling suggests that their asymmetric inheritance can be a predictable outcome of aggregates' slow diffusion and the geometry of yeast cells.

Introduction

Budding yeast cells divide asymmetrically to generate a new cell with full proliferative potential, and an ageing mother cell that can be anywhere along a finite replicative life span (20-30 cell divisions under standard laboratory conditions) (Mortimer and Johnston, 1959). This asymmetry in replicative age is correlated with an unequal segregation of ageing determinants along the axis of cell polarity in a dividing yeast cell (Egilmez and Jazwinski, 1989; Sinclair and Guarente, 1997). One class of such ageing

determinants are aggregates formed by damaged proteins. A seminal study demonstrated that aggregates containing carbonylated proteins, which result from oxidative damage in ageing cells, are preferentially retained by the mother during bud formation and cell division (Aguilaniu et al., 2003). Such asymmetric segregation of damaged proteins appears to be dependent on the actin cytoskeleton (Aguilaniu et al., 2003; Knorre et al., 2010; Tessarz et al., 2009). However, the mechanism by which actin regulates asymmetric partitioning of protein aggregates remains elusive.

In a recent study (Liu et al., 2010), segregation of protein aggregates was studied using a model system where heat-induced protein aggregates were labeled with GFP-tagged Hsp104p, a hexameric AAA ATPase-based chaperon known to play a major role in the modification and dissolution of heat denatured protein aggregates (Parsell et al., 1994; Glover and Lindquist, 1998; Bosl et al., 2006; Doyle and Wickner, 2009). This study implicated several proteins that control the assembly of actin cables, most notably the formin family actin nucleating protein Bni1p, in the segregation of Hsp104-containing protein aggregrates. Actin cables are parallel bundles of actin filaments (F-actin), best known for their role in polarized trafficking of membrane and cell wall materials and organelles during polarized growth (Pruyne et al., 2004). During the early stage of bud growth, actin cables are nucleated from Bni1p localized at the tip of the nascent bud (Evangelista et al., 2002; Sagot et al., 2002). Elongation of actin filaments at their barbed ends generates a retrograde flow of actin subunits in the mother-bound direction (Yang and Pon, 2002). It was proposed that the Hsp104p-containing protein aggregates associate with actin cables, possibly through a direct interaction of Hsp104p with actin, and ride along the retrograde flow to clear from the bud prior to cell division (Liu et al., 2010). Supporting this model, time-lapse movies were presented showing movement of single aggregates in the bud across the bud neck into the mother compartment.

A polarized array of actin cables exist during the part of the cell cycle when the cell undergoes rapid polarized growth, but after mitotic entry the actin organization becomes isotropic (Adams and Pringle, 1984; Lew and Reed, 1995; Pruyne and Bretscher, 2000). Thus, an initial question motivating our study was how mitotic cells might rely on the actin retrograde flow to clear protein aggregates from the bud prior to cytokinesis. We used live imaging to observe the dynamics and movement of Hsp104p-containing protein aggregates. Surprisingly, we found a lack of defined directionality in aggregate movement during budding or other cell cycle stages. Instead, heat-induced aggregates exhibit random walk and are largely cleared from the bud via Hsp104p ATPase-dependent dissolution. Interestingly, while actin depolymerization reduced aggregate random movement and the rate of dissolution, formin proteins do not play any detectable positive role in these events. Based on these findings, we propose an alternative model to explain the asymmetric inheritance of protein aggregates during yeast asymmetric cell division.

Results

Heat-induced protein aggregates undergo random walk

We used the same approach as described (Liu et al., 2010) to observe the dynamics of protein aggregates in live yeast cells. Briefly, protein aggregates were induced with a short (30 min) heat shock at 42 ^{o}C and visualized with Hsp104-GFP. As in Liu *et al*, we used the *HSP104-GFP* strain from the yeast genome-wide GFP-tagged strain collection (Huh et al., 2003), where GFP was introduced at the 3' end of the *HSP104* open reading frame in the genome of the S288c strain BY4741. After a brief recovery at 30 ^{o}C following the heat shock, the cells were imaged by acquiring 3-dimensional (3D) time-lapse confocal movies. As shown in Fig.3-1A, the majority of protein aggregates were motile in both the mother and

the bud at all cell cycle stages. Most aggregate movements were confined within the bud or the mother, but bud-to-mother (B>M) or mother-to-bud (M>B) translocation of the aggregates could be observed at low but roughly equal frequencies (Fig.3-1B, C, Fig.3-2), suggesting no directional bias in aggregate motility.

To quantitatively characterize aggregate movement, we performed automated tracking of individual aggregates (Experimental Procedures) (Fig.3-3- left panel). The mean square displacement (MSD) averaged from 1068 traces showed that the aggregate movement can be approximated as random walk with a small amount of confinement (Fig.3-4A). For pure random walk (diffusion), one expects a linear relationship between MSD and time shift ($MSD(\tau) = 4D\tau^{\alpha}$, where $\alpha = 1$), whereas confinement (sub-diffusion) results in a downward trending relationship ($\alpha < 1$) and transport (super-diffusion) results in an upward trending relationship ($\alpha > 1$). Simulations of random walk based on the observed trajectory lengths showed overall similar trajectory profiles as those observed experimentally, including the occasional more linear trajectories (Fig.3-3 – right panel, compared to left panel). As it is possible that a small fraction of transport (or super-diffusion) may be obscured by averaging, we performed 5000 simulations of aggregate movement with the speed and trajectory length distribution similar to those observed in yeast cells for three scenarios: 1) pure random walk; 2) random walk with 10% super-diffusion; 3) random walk with 30% sub-diffusion. The distribution of α values for each population was compared to the experimentally observed distributions (Fig.3-4B). This analysis found that the experimentally observed distribution matches the shape of the predicted distribution from scenario (3), indicating that the experimental data is consistent with a model that does not include transport. Quantification of a values in small-budded cells showed that the mode of aggregate motility at this cellcycle stage is indistinguishable from that of the entire population (Figure 3-4C)

To ensure that the Hsp104-GFP-expressing strain in our collection had not accumulated random mutations that might disrupt the normal behavior of protein aggregates, we obtained and tested the Hsp104-GFP strain used in the previous work (Liu et al., 2010). This strain showed the same aggregate behavior as our Hsp104-GFP strain (Fig.3-5A,B). We also reconstructed a new Hsp104-GFP strain by genomic tagging of *HSP104* in the BY4741 parental wild-type strain. Observation of protein aggregate movement using this strain was again consistent with the above two strains (data not shown).

Hsp104p chaperon-mediated dissolution is the main mechanism of heat-induced aggregate clearance

Aside from the random motion of the protein aggregates described above, another apparent behavior of the aggregates is their dissolution: during the initial segment of the movies (up to ~20 min), the aggregates grew slightly brighter but then underwent gradual reduction in brightness and number during the rest of the 1-1.5 hr movies (Fig.3-6A, arrow) Near the end of the movies, most buds were cleared of aggregates by this means while the mothers had drastically reduced number of aggregates compared to the initial amounts. By acquiring serial confocal slices spanning the entire Z dimension of cells in these movies, we could rule out the possibility that aggregate disappearance was due to movement out of the focal plane. Concomitant with aggregate dissolution, the diffuse cytosolic GFP level rose likely as a result of release of free Hsp104-GFP (Fig.3-6A). To evaluate the contribution of dissolution to aggregate clearance from the bud relative to that from B>M movement, we quantified the likelihood of these events from the time-lapse movies. As shown in Fig.3-6B, in ~95% of the cells observed, aggregate clearance (defined as disappearance of the last aggregate) from the bud occurred via dissolution (red bar), while only ~5% cells lost their last aggregate by B>M movement (blue bar). Furthermore, in nearly all cases of the latter, the observed B>M movement was a single such event per

cell, before which most of the aggregates in the bud were cleared already via dissolution. As previously reported (Liu et al., 2010), we also observed fusion of colliding aggregates in both mother and the bud (Fig.3-6A, red arrowhead), and large aggregates could sometimes be observed to split into smaller aggregates (not shown).

We next tested the possibility that the observed aggregate dissolution is a result of the Hsp104p chaperon activity by using a mutation, *hsp104*^{Y662A}, which does not affect Hsp104p binding to protein aggregates but disrupts the ATPase activity of Hsp104p (Lum et al., 2004). A strain was constructed where the genomic copy of *HSP104* was replaced with *hsp104*^{Y662A}-GFP. This mutant strain exhibited more aggregates than the wild type immediately after heat shock, and the aggregates in the mutant did not show any dissolution throughout the 3 hour time-lapse movie (Fig.3-6C). In fact, quantification showed that the aggregates in *hsp104*^{Y662A}-GFP strain continued to increase in their intensity (Fig.3-5C), consistent with the notion that the Hsp104p chaperon activity plays a major role in the clearance of heat-induced protein aggregates in yeast cells.

Hsp104p and F-Actin, but not Bni1, play a role in the random movement and dissolution of heat-induced aggregates

We observed that, in addition to a lack of dissolution, the movement of protein aggregates was largely abolished in *hsp104*^{Y662A}-GFP cells. As this reduced movement could possibly be due to over-crowding of the aggregates in the mutant cells, we performed another experiment by subjecting the mutant cells to a much shorter (3.5 min) heat shock, which results in an aggregate density similar to that in wild-type cells. In these cells the aggregates still did not dissolve but did exhibit some motility. Quantification from particle tracking data confirmed that the diffusion coefficient (D) for aggregates in the *hsp104*^{Y662A} mutant was reduced compared to the wild type (Fig.3-7A). This observation suggests

that the Hsp104p ATPase activity plays a role in the movement of the aggregates. We next examined the involvement of F-actin in aggregate movement and dissolution by treating cells with latrunculin A (LatA), an inhibitor of actin polymerization. Cells were first subjected to the aforementioned protocol of 30 min heat shock and a brief recovery and then incubated with 100 μM LatA. Time-lapse imaging started 10 min after LatA addition, at which time most of the cellular actin filaments were undetectable by fluorescent phalloidin staining, and the drug was present throughout the subsequent time-lapse imaging. LatA treatment significantly reduced, though did not completely abolish, the diffusion coefficient (D) of protein aggregates (Fig.3-7A). Interestingly, the rate of aggregate dissolution was also visibly reduced (Fig.3-7B), suggesting that actin contributes to but is not absolutely required for the movement and dissolution of heat-induced aggregates.

To examine if formin proteins are involved in the dissolution and movement of protein aggregates, we tagged Hsp104 with GFP in the *bni1Δ* and *bnr1Δ* strains (BY4741 background) and performed 3D time-lapse imaging of heat-induced aggregates. Neither mutant showed defects in B>M movement of aggregates (Fig.3-2A). In fact, we observed a higher fraction of cells in *bni1Δ* than in wild-type cells that exhibited at least 1 (mostly only 1) event of B>M movement. Quantification of the rates of aggregate movement (D) and dissolution showed that neither mutant is defective in these processes (Fig. 3-7). The aggregates showed slightly faster movement in *bnr1Δ* cells and faster dissolution in *bni1Δ* than those processes in wild-type cells, suggesting that Bni1 and Bnr1 may contribute slightly negatively to aggregate dissolution or movement, respectively. Thus, the roles of F-actin in aggregate movement and dissolution appear to be largely independent of the formin proteins. We note that the calculation of aggregate diffusion coefficients in various strains or under the specified conditions was confirmed by the method of spatial temporal image correlations spectroscopy (STICS) analysis (Berland

et al., 1995; Hebert et al., 2005; Kolin et al., 2006) (Fig.3-8, 3-9), which is independent of the particle tracking approaches. The rates calculated using both methods were consistent.

Asymmetric inheritance of protein aggregates during bud formation

During our time-lapse confocal movies, new buds could be observed to form from a number of mother cells in each experiment. In the majority (68%) of such wild-type cells observed, the aggregates were successfully retained in the mother while the bud grew and the new bud was devoid of aggregates throughout the movies (Fig. 3-10A). In the reminder of the population, 1 (2 in rare cases) aggregate moved into the bud from the mother (Fig. 3-10B). In the majority of these cases, the aggregate dissolved after entry into the bud (Fig.3-10B,C, arrow), while in a small fraction the aggregate moved back to the mother. Formin mutant (*bniΔ* and *bnrΔ*) cells undergoing budding during the time-lapse imaging essentially showed similar behavior, that is, the majority of aggregates were retained in the mother (Fig.3-10C), and those occasionally entering the bud most often dissolved.

We next performed time-lapse movies to observe the dynamics and distribution of naturally accumulated Hsp104-positive protein aggregates. Previous work showed that Hsp104p associates with protein aggregates containing carbonylated proteins resulting from oxidative damage in cells of older replicative age (Erjavec et al., 2007). In an exponentially growing population, where most cells are young, Hsp104p-containing aggregates were rarely observed (data not shown). We hence used a magnetic beads-based sorting protocol (Chen et al., 2003) to obtain populations of wild-type and *sirΔ* enriched for older cells (see bud scar staining in Fig.3-11A).

The naturally formed aggregates (Fig.3-11B) do not dissolve during the duration of our observation by time-lapse movies, allowing long tracking of aggregate movement (Fig.3-11C). The individual long traces show nearly linear fitting of MSD with time with a slight downward trend, suggesting that this movement can be described as random walk with slight confinement (Fig.3-11C). The distributions of α values from tracking many aggregates in older wild-type cells were similar to that of heat-induced aggregates (Fig.3-11D). These observations suggest that the dynamics of the Hsp104-associated protein aggregates formed in different ways exhibit the same type of movement.

A recent study investigating the mechanism of asymmetric partitioning of episomal DNA circles reported free diffusive motion of episomes in the nucleoplasm (Gehlen et al., 2011). Using a numerical simulation, they demonstrated that the retention of episomes in the mother can be explained simply by the geometry of the dividing nucleus and the brief window of time in the cell cycle when nuclear division occurs. As the protein aggregates also undergo random motion, a similar explanation may be applied to the preferential retention of aggregates in the mother during cell division. To test this idea, we performed a 3D numerical simulation of pure random walk with the diffusion rate $D = 1.0 \times 10^{-3}\ \mu m^2/s$ computed from particle tracking of natural Hsp104-GFP-containing aggregates in older cells. A yeast cell was represented as two spheres with radius of R1=2.5 μm (mother) and R2=0.85xR1 (bud) connected by a narrow neck with width d=1.25 μm. Starting from an initial distribution of aggregates entirely in the mother, the probability density map after 90 min (a cell cycle) showed maintenance of a biased distribution of aggregates in the mother (Fig.3-12A, top panel). To evaluate the impact of the geometry of yeast cells on this partitioning, the bud neck size was varied in the simulations. Figure 3-12A (bottom panel) shows that increasing bud neck size reduces the asymmetry in aggregate partitioning. Addition of confinement (α=0.50, approximating the average

value in Fig. 3-11D) also enhanced the segregation asymmetry as expected (Fig. 3-12A). Aggregate asymmetric segregation can also be described using a 1D (equivalent to wide open neck) analytical model, which again shows preferential retention of aggregates in the mother even with no confinement (α=1) (Fig.3-13).

Discussion

Based on the analyses described above, we conclude that the clearance of protein aggregates from the bud does not depend on actin cable-mediated retrograde transport. Our conclusion is based on quantification of aggregates movement from time-lapse recording of a large number of cells. Although linear bud-to-mother movement was observed occasionally, mother-to-bud movement of aggregates was observed at a similar frequency, and thus there was no net directionality in aggregate movement along the mother-bud axis. Particle tracking and trajectory analysis showed that the movement of protein aggregates can be described as random walk with a small amount of confinement. Even though some apparently linear trajectories can be observed, these can be recapitulated by random walk simulations using the same diffusion coefficient and trajectory length. We emphasize that although our data does not support a direct role for actin-based retrograde transport in aggregate segregation, the data does not necessarily argue against an involvement for actin cytoskeleton or cell polarity proteins in this process. It is conceivable, for example, that the abnormally wide bud neck in some of the cell polarity mutants could increase the leaking of protein aggregates into the bud, although such effect is likely to be too subtle to observe reliably in our experiments.

Disassembly of actin filaments following LatA treatment partially abrogated aggregates movement and slowed their dissolution. Although it is possible that residual actin filaments remained and were below detection in LatA treated cells, this observation suggests that actin cables, which were no longer present in LatA-treated cells, are not required for the movement or dissolution of heat-induced aggregates. The effect of LatA on aggregate movement or dissolution may also be indirect if the loss of actin filaments induces a high-stress state interfering with aggregate dissolution or motility. Regardless of the mechanism, our observed effect of LatA on aggregate motility does not help explain a positive role for actin in aggregate asymmetric segregation, as based on our model, reduced aggregate diffusive motion would predict their better retention in the mother. The inhibitory effect of actin depolymerization on the Hsp104-dependent aggregate dissolution is consistent with a functional linkage between actin and Hsp104 reported in recent studies (Erjavec et al., 2007; Tessarz et al., 2009).

We did not observe any apparent requirement for the formin protein Bni1p or Bnr1p in the motility or retention of heat-induced protein aggregates in the mother. The experiments performed previously on the retention of protein aggregates relied on quantification of non-synchronized cell populations at different time points during a continuous incubation at high temperature (Liu et al., 2010). Such an assay would not be sufficient for distinguishing between the possibilities of aggregate clearance by dissolution versus by movement. Because the dynamics of new aggregate formation during the prolonged heat exposure were unknown, buds displaying no aggregates might be new buds that formed after the cells had adapted to the heat stress and ceased the formation of new aggregates, rather than reflecting active aggregate clearance from the bud. Additionally, the unbudded cells observed in this assay might not be the new G1 cells after cytokinesis but instead might be arrested cells failing to adapt to the heat stress. By contrast, we directly observed retention of pre-formed aggregates

during new bud formation by time-lapse movies, and we did not observe any defect in this process in the formin mutants.

Finally, based on the observed diffusion rates of protein aggregates, and borrowing the insight from a recent study explaining the asymmetric inheritance of episomal DNA during yeast nuclear division (Gehlen et al., 2011), we propose that the limited mobility and the narrowness of the bud neck ensure that the vast majority of the proteins aggregates accumulated with ageing are retained in the mother during the limited time of a cell cycle. This idea is supported by our 3D simulation as well as a 1D analytical model. This model implies that no additional mechanism may be needed to confer the asymmetric segregation of protein aggregates during yeast cell divisions.

Figures

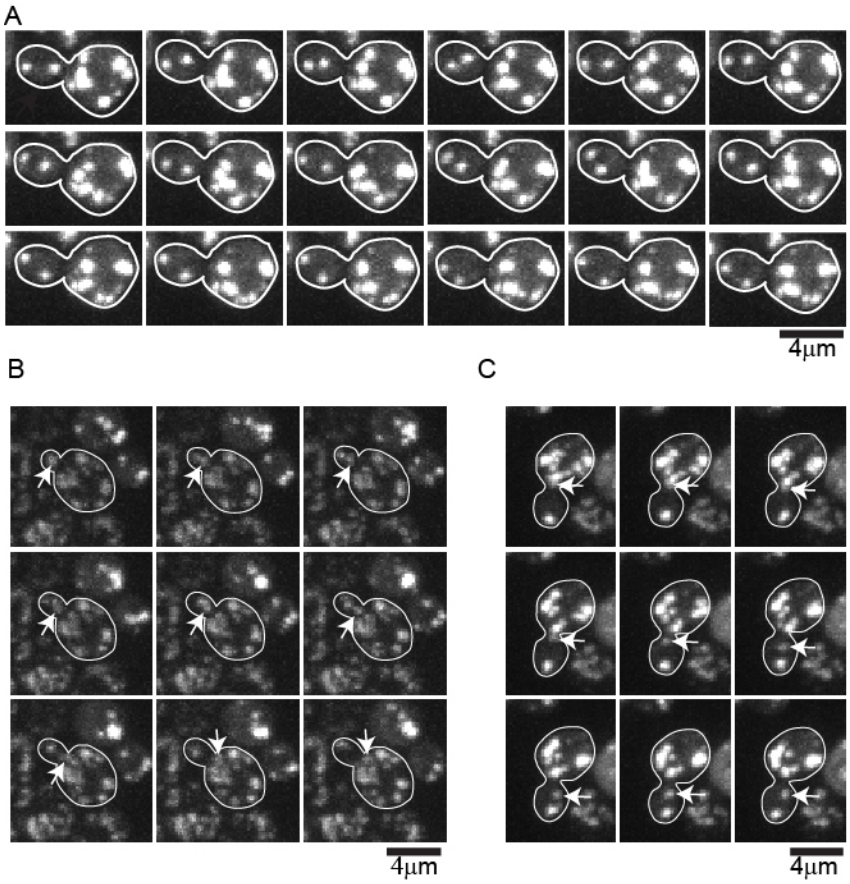

Figure 3-1. 3D time-lapse imaging of heat-induced Hsp104p-containing protein aggregates

A. Observation of Hsp104-GFP-containing aggregate movement in the wild-type BY4741 strain in a representative 3D time-lapse movie. Image stacks were collected and shown at 20s intervals, and are shown as maximum projections.

B. Example of an aggregate (arrow) moving from bud to mother in wild type. Image stacks were collected and shown at 1 min intervals, and are shown as maximum projections.

C. Example of an aggregate (arrow) moving from mother to bud. Image stacks were collected at 1 min intervals, and a maximum projection is shown.

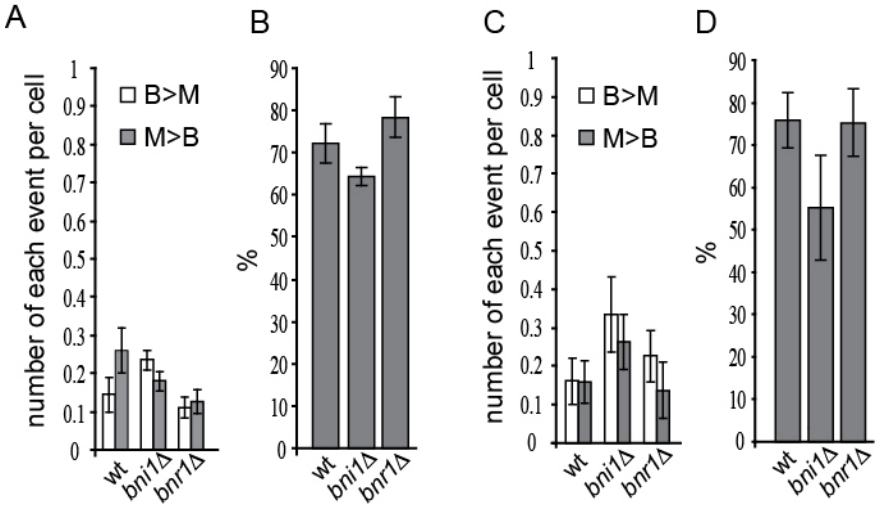

Figure 3-2. The frequency of B>M or M>B movement

A. The frequency of B>M or M>B movement per cell in an exponentially population was calculated by counting the totally number of each type of event divided by the totally number of budded cells observed in each movie. The bar graphs show mean and standard error of the mean (SEM).

B. Percentage of cells in the population in (A) in which no trans-bud neck movement was observed during the 1 hour time lapse movies. Shown are mean and SEM. For both A and B, on average 40 cells/movie from 4-6 movies were quantified for each strain.

C. The frequency of B>M or M>B movement per cell in small budded cells was calculated by counting the totally number of each type of event divided by the totally number of small budded cells observed in each movie. Shown are mean and SEM.

D. Percentage of cells in the population in (C) in which no trans-bud neck movement was observed during the 1 hour time lapse movies. Shown are mean and SEM. For C and D, on average 14 cells/movie from 4-6 movies were quantified for each strain.

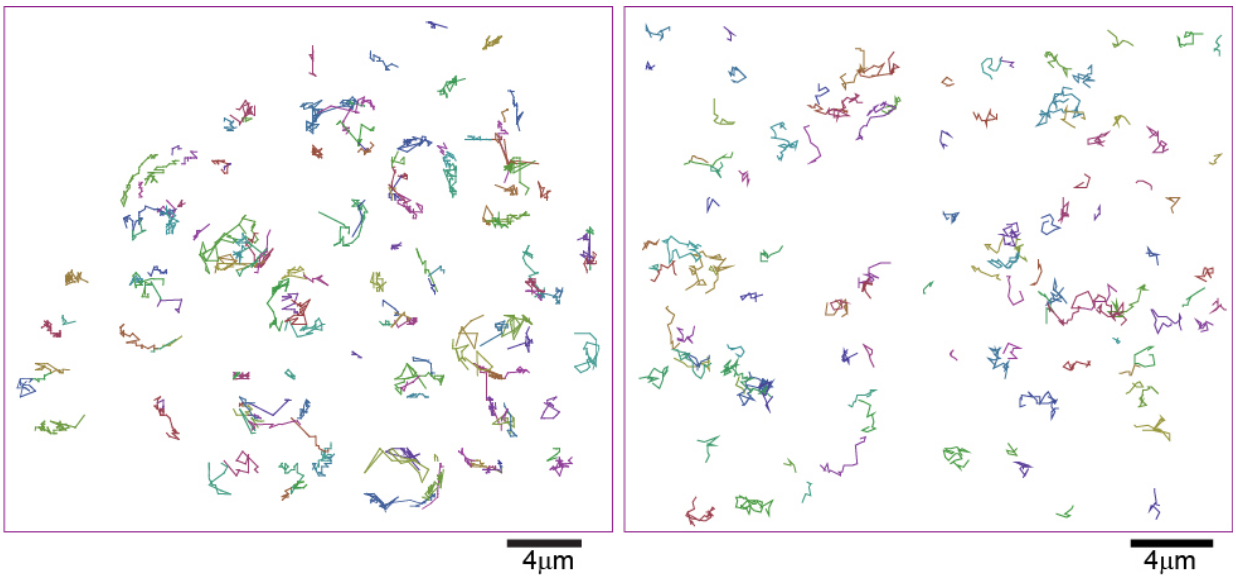

Figure 3-3. Hsp104p-containing protein aggregates undergo random walk

Left panel: A representative field of trajectories from tracking of protein aggregates from 1 hr time-lapse movies. For comparison, the right panel shows a field of simulated trajectories of random walk with observed distribution of trajectory lengths and diffusion coefficient.

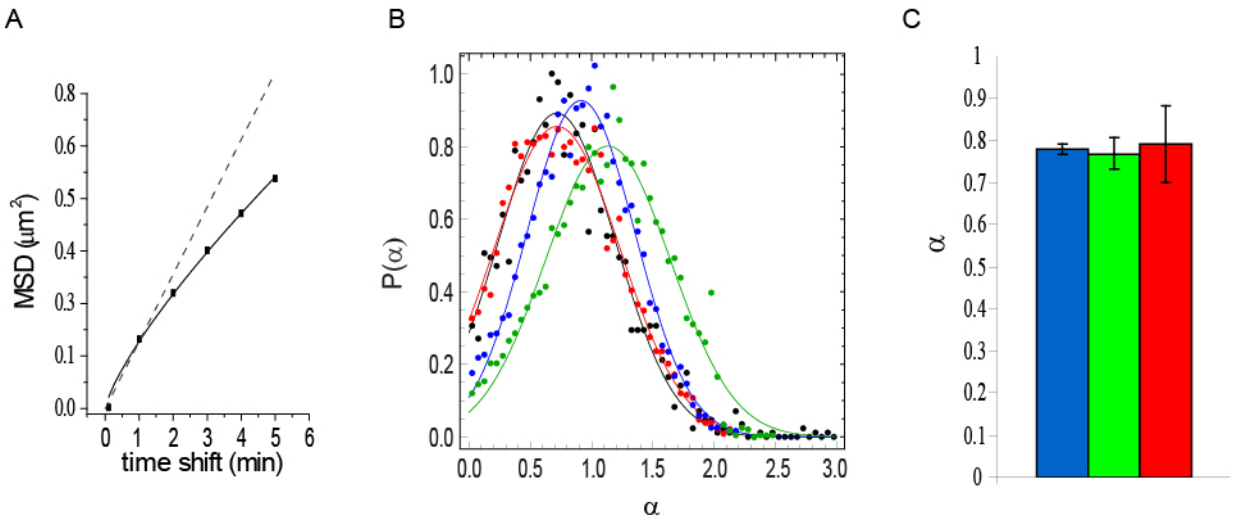

Figure 3-4. Hsp104p-containing protein aggregates undergo random walk

A. A plot of MSD vs time shift, showing that aggregate movement can be characterized as random walk with a small amount of confinement (solid line). Dotted line shows plot expected for pure random walk.

B. α value distributions from 5000 simulations of aggregate movement with the diffusion coefficient and trajectory length distribution similar to those observed in yeast cells for each of the three scenarios: 1) pure random walk (blue); 2) random walk with 10% super-diffusion (green); 3) random walk with 30% sub-diffusion (red). The distribution of α values for each population was compared to the experimentally observed distribution (black), showing the observed is consistent with scenario (3).

C. Comparison of average α values (mean and SEM) from aggregates in different population of cells in 60min 3D time-lapse movie. Blue: aggregates in all the cells in the movies (N=3542); green: all aggregates in the small budded S/G2 cells (N=182); red: aggregates in the buds of the S/G2 cells (N=31). N refers to the number of aggregates.

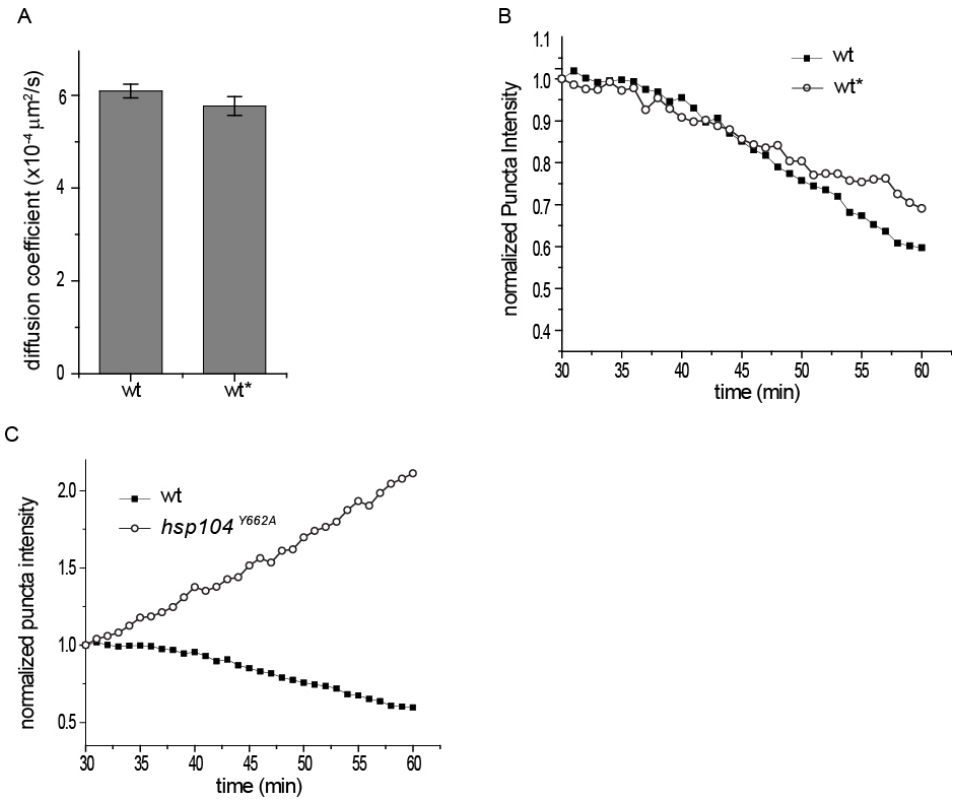

Figure 3-5. Comparison of dissolution kinetics and diffusion coefficients among different strains and conditions (part1).

A. Comparison of diffusion coefficients calculated from aggregate tracking between the two wild type strains. Shown are mean and SEM. More than 1000 aggregates from at least 2 movies/strain were tracked. wt, RLY7110; wt*, YBD401 (Liu et al., 2010).

B. Quantification of aggregate dissolution (see Experimental Procedures) in the two strains in (A). Shown are plots of total aggregate intensity as a function of time from time-lapse movies of a field of cells (50-100 cells per field) starting from the 30 min frame when aggregates in wild type no longer grew in brightness. Each plot is an average from two movies. Black square: RLY7110; open circle: YBD401.

C. Quantification of aggregate dissolution following the same method as in (B) in wild-type (wt) cells and *hsp104* ^{Y662A} cells.

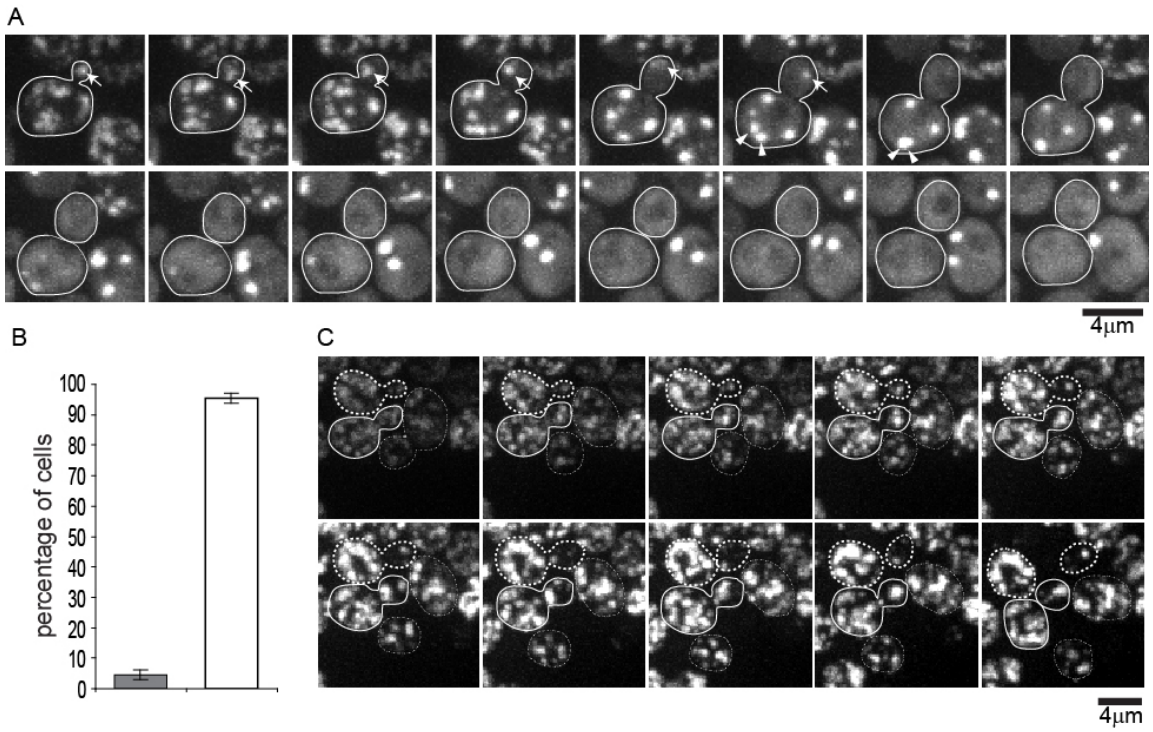

Figure 3-6. Heat-induced aggregates are cleared from the bud through Hsp104p chaperon-mediated dissolution

A. Hsp104-GFP-associated aggregates show gradual clearance through dissolution. The arrow indicates an example of an aggregate dissolving; arrowheads indicate two aggregates fusing and then dissolving. Images stacks were collected at 1 min intervals; the montage shows maximum projections at 6min intervals from a 90 min movie.

B. Comparison of the percentage of cells where the last aggregate was cleared from the bud by dissolution (white bar) to that by bud-to-mother movement (gray bar) in the wild type. On average 47 cells/movie from 5 movies were quantified. Shown are mean and SEM.

C. Aggregate dissolution depends on chaperon activity of Hsp104p. In *hsp104*^{Y662A} mutant cells, the aggregates not only did not dissolve over a representative 3hr movie but also increased in brightness over time. Montage starts from 18 min of the movie and frames (maximum projections) are shown at 18min intervals.

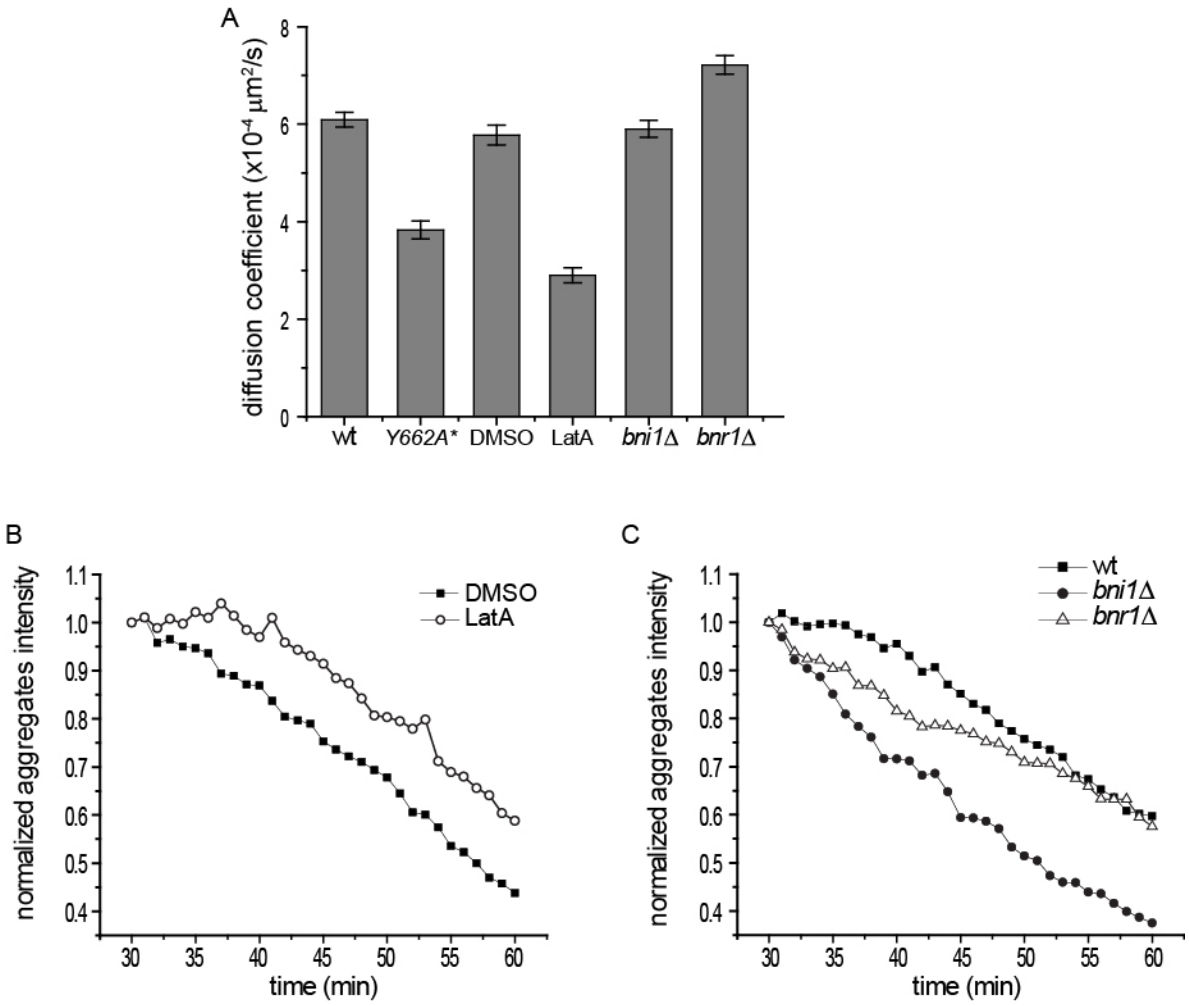

Figure 3-7. Comparison of dissolution kinetics and diffusion coefficients among different strains and conditions (part2).

A. Diffusion coefficient of each strain and condition as indicated quantified from aggregate tracking data (see Experimental Procedures). Shown are mean and SEM. *The quantification for *hsp104*^{Y662A} cells was done from the 3.5 min heat shock experiment to mimic wild-type aggregate density. For each strain or condition, more than 450 (and in many cases over 1000) aggregates from 2-4 movies were tracked and quantified.

B-C: Quantification of aggregate dissolution following the same method as in (fig.3-6) for the same conditions or strains examined in (A).

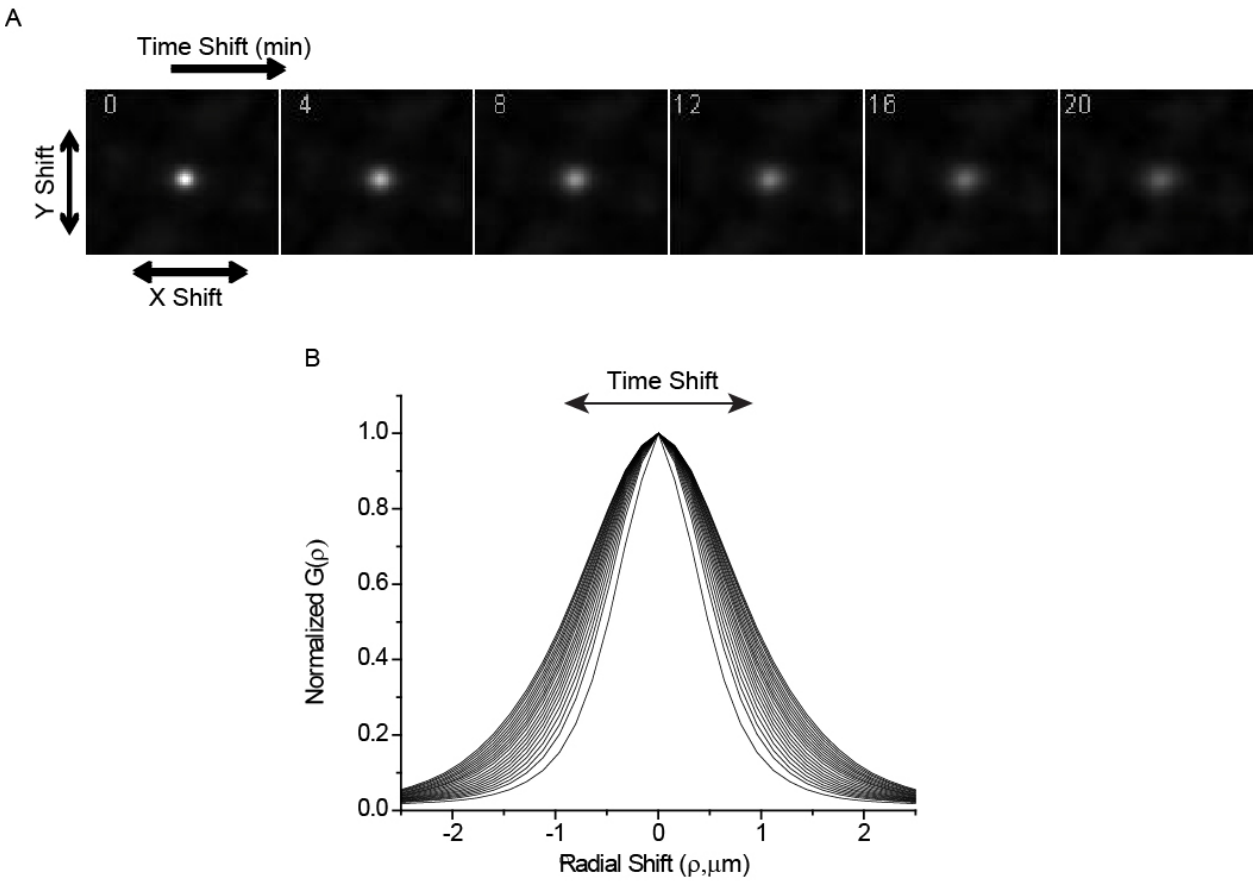

Figure 3-8. STICS Analysis of Aggregate Motility (part1)

A. Following background subtraction (see Extended Experimental Procedures), the decay of the spatial-temporal correlation function as a function of time shift was calculated. A single value was obtained per field of view of cells. Shown are the spatial correlation related to x and y shift as a function of time shift.

B. The spatial correlations were circularly averaged to generate plots of G(r) over radial shift. These plots were fit to Gaussians to quantify the increase in width of the spatial-temporal correlation function over time shift, as the motion of the particles decreases the spatial correlation over time. This increase in width was used to calculate MSD for the particles (see Extended Experimental Procedures). Initial amplitude of G(r) is normalized here to emphasize the increase in width over time shift.

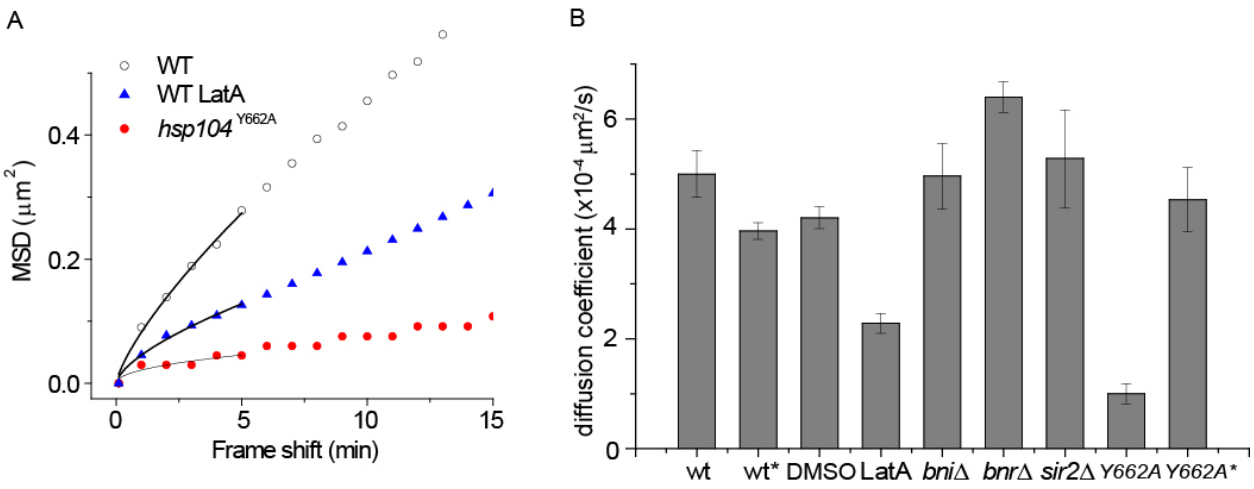

Figure 3-9. STICS Analysis of Aggregate Motility (part2)

A. MSD was calculated from the increase in width as shown in (B) (see Extended Experimental Procedures). Representative MSD plots of STICS results for a single field of view are shown for wild-type (wt), wt + LatA, and *hsp104Y662A* (30 min heat shock).

B. Diffusion coefficients calculated from STICS analysis of different strains and conditions. Y662A*: hsp104 Y662A mutant with 3.5min heat shock. All other strains and conditions were with 30 min heat shock. Each plot shows the mean and SEM of diffusion coefficient calculated from MSD plots from a minimum of 3 fields of view of cells, with each field of view consisting of 20 to 40 cells.

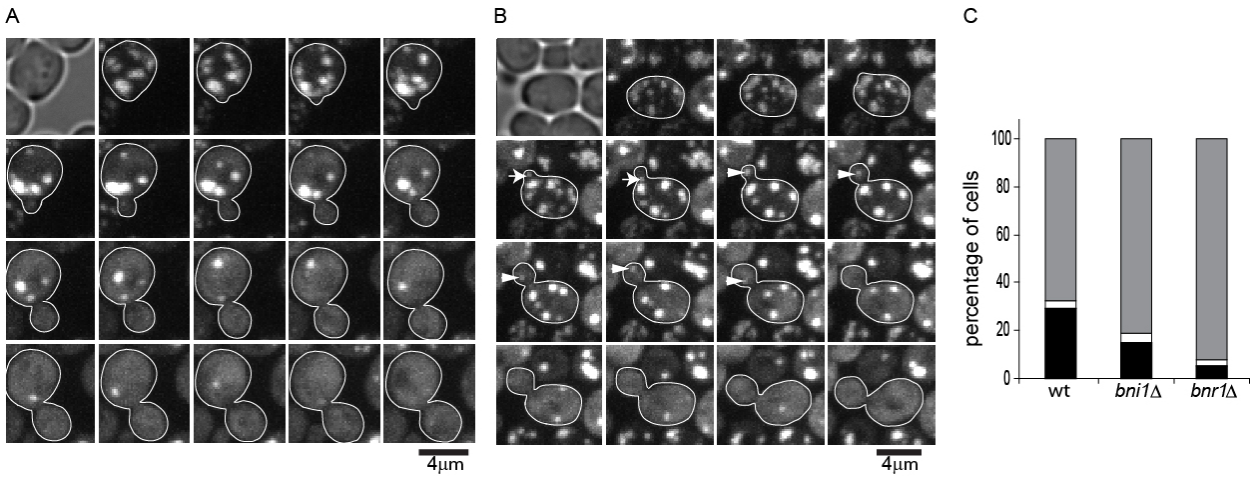

Figure 3-10. Retention of heat-induced protein aggregates in the mother during bud formation.

A. An example of retention of protein aggregates in a wild-type mother cell undergoing budding. Image stacks were collected 1 min intervals; montage is shown as maximum projections every 4 min.

B. Time-lapse images of a cell showing two different fates of aggregates that leaked into the bud from the mother during bud formation. Image stacks were collected 1 min intervals; montage is shown as maximum projections every 4 min. Arrows point to an aggregate that returned to the mother after leakage into the bud; arrowhead points to an aggregate that dissolved after leakage into the bud.

C. Percentages of cells displaying three different types aggregate behavior during new bud formation and growth in three different genetic backgrounds as indicated. Cells either with a tiny bud initially devoid of any aggregates or giving birth to a new bud during the first 30min of 1 hr long 3D time-lapse movies were scored. Gray bar: cells with no aggregates leakage into the bud; black bar: cells in which aggregates leaked into the bud were subsequent cleared by dissolution; white bar: cells in which aggregates leaked into the bud and subsequent moved back to mother. N=108 cells (wt); 74 cells (*bni1Δ*), 133 cells (*bnr1Δ*).

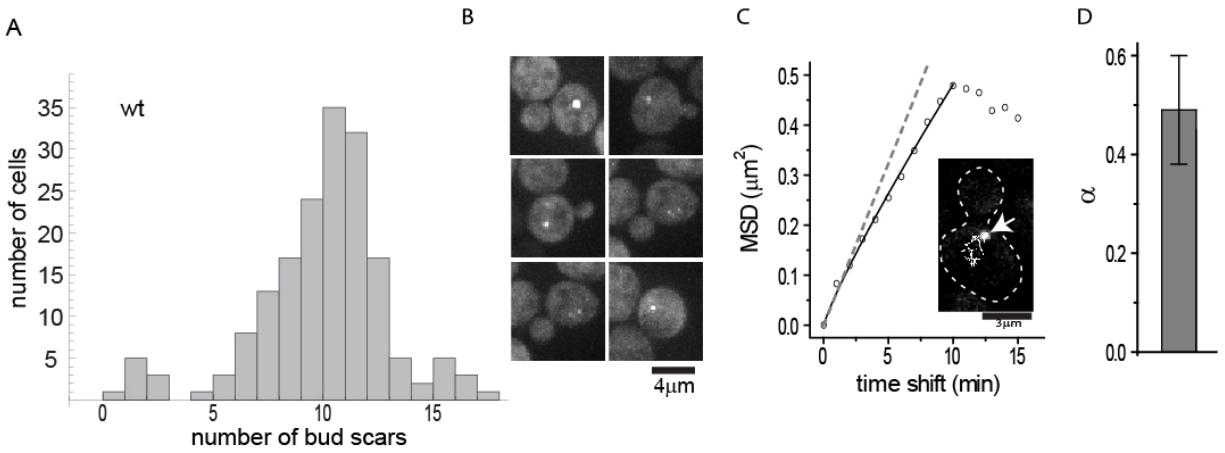

Figure 3-11. Observation of motility and distribution of Hsp104p-containing aggregates in aged wild-type cells.

A. Age distribution of magnetic-beads sorted old wild-type cells determined by bud scar counting (> 170 cells were counted for each population).

B. Representative images showing asymmetric distribution of Hsp104-associated protein aggregates in aged wild-type from the populations in (A). Shown are maximum projections of 3D image stacks.

C. Trajectory (white line in left panel) and MSD (right panel) analysis of an Hsp104-GFP-associated aggregate (arrow) in an old wild-type cell from a 60 min 3D time-lapse movie.

D. Hsp104-GFP-containing protein aggregates in old wild-type exhibit a similar type of movement. Shown are mean and SEM of α values calculated from long aggregate tracks as in (E). n=21 tracks for wild-type aggregates.

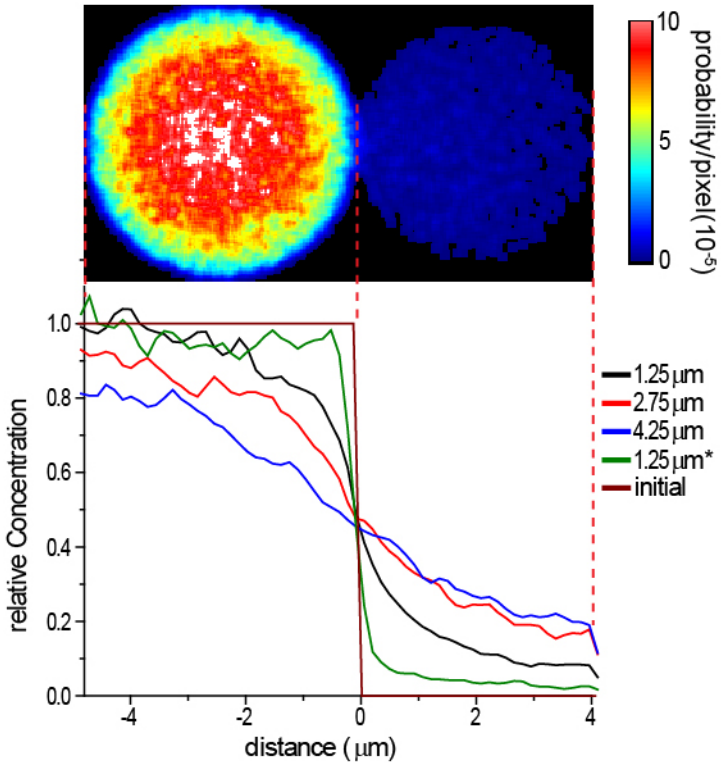

Figure 3-12. 3D numerical simulation of aggregate partitioning between mother and bud during a yeast cell cycle.

Probability density map of protein aggregates after a cell cycle period (90 min) from a 3D numerical simulation of aggregate retention assuming random walk (α =1) (see Experimental Procedures) as a 2D sum projection (top) and lateral profiles of central plane (bottom). Each colored line corresponding to simulation with a particular neck size (diameter) as indicated. The brown line shows the initial distribution at the start of the simulation and the green line shows the 1.25 μm neck size simulation with confined diffusion (α = 0.50, as measured in aged cells).

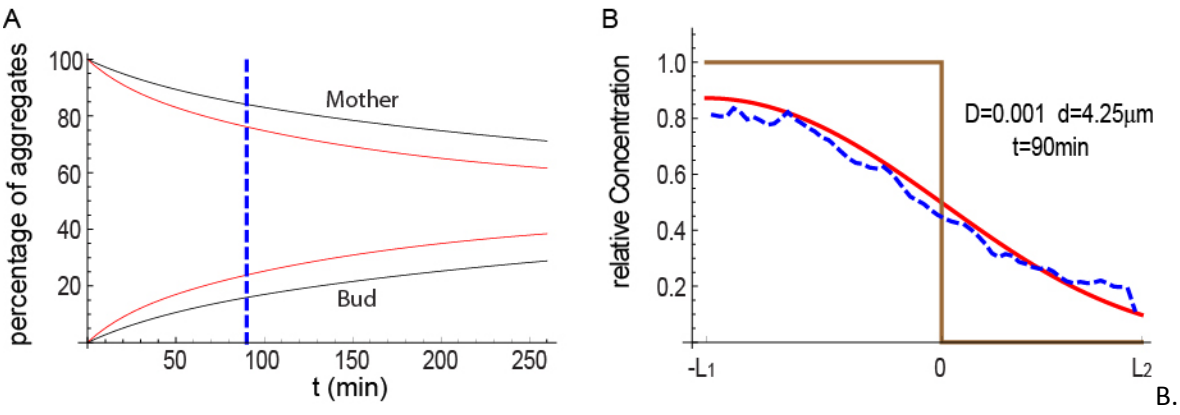

Figure 3-13. 1D analytical model of aggregate partitioning between mother and bud during a yeast cell cycle.

A. Analysis of protein aggregate retention using a 1D analytical solution (Formula S12, see Supplementary Information) for D=0.0005 $\mu m^2/s$ (black) and D=0.001$\mu m^2/s$ (red). The dashed blue line denotes 90 min time point.

B. A comparison of aggregates distribution after 90min in 3D simulation for D=0.001 $\mu m^2/s$ and neck size of 4.25 μm (mimicking open neck, blue dashed curve) to the 1D analytical solution (Formula S7, using 20 terms, see Extended Experimental Procedures) (red solid curve). The brown curve represents the initial aggregates distribution. 0 on x axis is the position of bud neck and mother-bud orientation as in A; L1 and L2 is the length of mother and bud cell, respectively.

CHAPTER FOUR: SIR2 INDEPENDENCE IN THE MOTILITY AND SEGREGATION OF HSP104-ASSOCIATED PROTEIN AGGREGATES IN BUDDING YEAST

Summary

Sir2, the NAD-dependent histone deacetylase in budding yeast, was reported previously to regulate the asymmetry in cellular replicative aging in part by sparing the daughter cell from damaged protein during mitosis. This role was proposed to rely on Sir2's ability to influence actin cable-based transport of protein aggregates from the bud to the mother. Although this retrograde transportation model of protein aggregates was challenged recently, whether Sir2 regulates protein aggregates partitioning remains unclear. By analyzing the dynamics of Hsp104-associated protein aggregates using live-cell microscopy and particle tracking, we found the motility and asymmetric segregation of protein aggregates between the mother and the bud to be unaffected in *sir2Δ* mutant. However, more cells with protein aggregates were found in old *sir2* mutant cell population compared to age-matched wild-type cells, and the average intensity of the aggregates was moderately but significantly higher in the former than the latter. These observations support a role for Sir2 in protein damage control but not in protein damage asymmetry during yeast replicative aging.

Introduction

One of the breakthroughs in modern aging research is the discovery of *SIR2* in a screen searching for genes extending the replicative life span (RLS) of budding yeast (Kennedy et al., 1995). Sir2, a NAD-dependent histone deacetylase, together with other members of the SIR complex, mediates chromatin silencing at mating-type loci, telomere and rDNA (Imai et al., 2000; Kennedy et al., 1997;

Smith et al., 2000). In yeast, *SIR2* deletion results in shortened RLS whereas *SIR2* overexpression was found to extend RLS Sir2 at least in some studies. Although extensive data suggests that Sir2 plays some role in life span modulation, the mechanistic basis of this role has been obscure and even controversial.

One mechanism by which Sir2 regulates RLS is to prevent the Fob1-dependent recombination between rDNA repeats and the formation of extrachromosomal rDNA circles (ERCs)(Defossez et al., 1999; Kaeberlein et al., 1999; Kobayashi et al., 2004), the accumulation of which accelerates aging in yeast (Kaeberlein et al., 1999; Sinclair and Guarente, 1997). Sir2 has also been implicated in life span extension caused by calorie restriction (CR) (Lin et al., 2000). However this notion was challenged based on the finding that CR can cause robust extension of the RLS in *sir2Δfob1Δ* double deletion strain, suggested that *sir2Δ* cells succumb to the elevated level of toxic ERCs and does not live long enough to show the effect of CR (Kaeberlein et al., 2004). This hypothesis receives further support from the study that SIR2 deletion prevents 32 different lifespan-extending mutations and four methods of CR(Delaney et al., 2011). Most recently, Sir2's role in life span determination has been debated in animal models that include *C.elegans* and *D. melanogaster* (Burnett et al., 2011; Viswanathan et al., 2005).

One of the most intriguing functions proposed for SIR2 has been its projected role in the asymmetric segregation of damaged proteins between the progeny of a yeast cell division. An *S. cerevisiae* cell proliferates through polarized growth of a bud from a mother cell and cytokinesis at the end of mitosis divided at the bud neck to generate a new-born bud cell with a full RLS ahead and a mother cells already in the midst of replicative aging. By adopting an immunofluorescence staining-based protocol, it was found that there is a strong bias in the segregation of aggregates of carbonylated proteins, a product of oxidative damage, between the mother and daughter cell even at the first replicative cycle of a virgin cell (Aguilaniu et al., 2003). These carbonylated protein aggregates were subsequently shown to be associated with Hsp104 (Erjavec et al., 2007), a chaperone protein containing

AAA ATPase domain and able to dissociate and refold aggregated proteins. It was proposed that the Hsp104-containing protein aggregates are cleared from the bud to mother through actin cable-mediated retrograde transport, and that Sir2 influences this process by controlling the activity of the CCT chaperonin complex that facilitates actin folding (Liu *et al.* 2010). By observing the motion of Hsp104-associated aggregates using 3D microscopy and particle tracking, we recent came to the conclusion that these protein aggregates undergo restricted random walk without directional bias and the asymmetric segregation of the protein aggregates result from their slow mobility and the geometry of a budding yeast cell (Zhou *et al.* 2011). This conclusion raises a question as to what role Sir2 might be playing in the asymmetric inheritance of protein aggregates.

Here we applied the same microscopy and image analysis methods as employed previously to examine the effect of *sir2Δ* on protein aggregate motility and inheritance. We show that *sir2Δ* has no effect on the motility or asymmetric segregation of Hsp104-associated protein aggregates but appear to increase the severity of protein aggregate formation during replicative aging.

Results

The effect of *sir2Δ* on the motility and dissolution of heat-induced protein aggregates

Previous studies used heat-induced protein aggregates labeled with Hsp104-GFP as a model to study the dynamics of protein aggregates (Liu *et al.* 2010; Zhou *et al.* 2011), as naturally occurring Hsp104-labeled aggregates are rare in an actively dividing yeast cell population, which consists predominantly of young cells. Thus, in this study we first used heat shock to induce protein aggregation in a *sir2Δ* strain expressing Hsp104-GFP from the genomic *HSP104* locus and followed the aggregate

dynamics by 3D time-lapse movies and particle tracking as described previously (Zhou *et al.* 2011). Briefly, Hsp104-GFP strain was heat shocked at 42 ^{o}C for 30 min followed by a brief recovery at 30 ^{o}C before subjected to time-lapse imaging. As previously observed in wild type cells, the Hsp104-GFP-labeled protein aggregates in *sir2Δ* cells were motile but the motility is mostly confined within the mother or the bud with few undergoing mother-to-bud (M>B) or bud-to-mother (B>M) translocation (Fig. 4-1). Quantification of the frequency of bud-to-mother and mother-to-bud translocation of aggregates revealed no bias toward B>M translocation in either an exponentially growing cell population or the population consisting small budded cells in the polarized growth stage (Fig.4-2) of either *SIR2* or *sir2Δ* genotype. We then performed tracking analysis of aggregate movement from the 3D movies. This analysis found the diffusion coefficient of aggregate motion in *sir2Δ* cells to be indistinguishable from that in wild-type cells (Fig.4-2E). These results indicate that Sir2 does not play any observable role in the motility of heat-induced Hsp104 protein aggregates.

We next quantified the rate of aggregate dissolution from the time-lapse movies and found that *sir2Δ* cells have similar aggregate dissolution rate as wild type (Fig.4-3 A, B). As we previously shown that the observed aggregate dissolution was dependent on the chaperone activity of Hsp104, this result also suggests that the chaperone activity was largely unaffected in *sir2Δ*. To assess the role of Sir2p in aggregate clearance in the bud, we performed a time course experiment, where the percentage of buds that contained aggregates was quantified at various time points during the recovery after heat shock. This assay shows that the rates of heat aggregate clearance from the bud were the same between *sir2Δ* and wild-type cells (Fig.4-3C).

During our time-lapse movies, which last 60 min, a number of cells were observed to initiate budding. We observed that in 64% (*SIR2*) and 74% (*sir2Δ*) of these cells the heat-induced protein aggregates were successfully retained in the mother during bud initiation and growth. In the small

fraction of cells where the retention was not fully successful, aggregates that leaked into the growing bud mostly dissolved and only a minute fraction returned to the mother (Fig.4-3D). Taken together the above experiments showed that Sir2 does not play any significant role in the motility, dissolution, or mother retention of heat-induced protein aggregates.

SIR2 deletion does not affect the assembly or organization of actin cables

It is reported previously that Sir2 regulates the activity of the actin chaperonin CCT complex and that cells show abnormal actin cable structure when *sir2* was deleted (Aguilaniu *et al.* 2003; Liu *et al.* 2010). Because actin cables mediate polarized transport and thus play a critical role in yeast polarized growth and bud formation, a defect in actin formation or dynamics in *sir2Δ* could contribute to the reduced RLS in this mutant. To revisit this issue, we stained actin filaments in yeast with Alexa-488 conjugated phalloidin; however, we did not observe any difference in actin cable abundance or organization between the *sir2*Δ and wild type strain (Fig.4-4A). Nor were there any abnormalities in the appearance or distribution of actin patches. We further examined the function of actin cables by utilizing Myo2 as marker for polarized transport. Myo2 is the yeast type V myosin that transports cargoes along actin cables. It is known that actin cables are required for the proper localization of Myo2 at the bud tip (Pruyne et al., 1998). Consistent with a lack of observable actin cable defect, Myo2-GFP in *sir2*Δ cells localizes properly to the bud tip and to neck during cytokinesis as in the wild type (Fig.4-5A).

As it was proposed that *sir2Δ* cells have a reduced concentration of mature actin monomers in *sir2Δ* cell due to an impaired CCT chaperonin activity (Liu *et al.* 2010), we examined whether the reconstruction of actin cables was slower in *sir2Δ* cells. Wild-type and *sir2Δ* cells were first treated with the actin polymerization inhibitor latrunculin A (LatA) to eliminate the existing actin filaments; the cells

were then washed free of the drug and examined for the recovery of actin structures at different time points thereafter. By quantifying the percentage of cells forming visible actin cable at each time point, we found the *sir2Δ* cells reconstruct actin cable as efficiently as the wild type (Fig.4-4B). Based on the above data, we conclude that *sir2Δ* cells do not have any observable defects in actin cable assembly or organization or assembly despite the possible role for Sir2 in the folding of actin monomers.

The effect of *sir2Δ* on the asymmetric segregation of Hsp104-associated protein aggregates in aging cells.

Previous studies reported that the asymmetric segregation of damaged proteins between the mother and bud relies on the activity of Sir2 (Aguilaniu *et al.* 2003; Erjavec *et al.* 2007; Liu *et al.* 2010;). However, the dynamics of the naturally formed Hsp104-associated protein aggregates had not been previously characterized in *sir2Δ* cells. To this end, we used a magnetic sorting protocol to isolate wild-type or *sir2Δ* cells with advanced replicative age (mean replicative age of 8-10). First, in 94% of the aggregate-possessing cells in the aged wild-type population, aggregates (usually 1 or 2 per cell) were observed only in the mother cell but not in the bud (Fig.4-6A, B). Such asymmetry in aggregate distribution was properly preserved in 95% aged *sir2Δ* cells that contained aggregates (Fig. 4-6B). Interestingly, a difference readily apparent between the two strains was that a higher percentage of aged *sir2Δ* cells contained protein aggregates than the aged wild-type cells, where the difference was much smaller comparing the young cells isolated in the same magnetic sorting experiment (Fig.4-6C). Furthermore, the brightness of the Hsp104-GFP aggregates was on average significantly higher in *sir2Δ* cells than in the wild type (Fig.4-6D). These observations shows that Sir2 is not required for the asymmetric distribution of aggregates between the bud and the mother but do suggest that Sir2 plays some role in preventing protein aggregate formation during replicative aging.

Since *sir2Δ* cells accumulate ERCs, which contributes to the reduction in RLS in this mutant (Kaeberlein *et al.* 1999), we ask if the higher load of protein aggregates in aged *sir2Δ* cells was also linked to the accumulation of ERCs by deleting *FOB1*, a gene required for ERC formation. Interestingly, the percentage of aged *fob1Δsir2Δ* cells with Hsp104-GFP-labeled aggregates was similar to that in aged *sir2Δ* cells (Fig.4-7). As it was previously known that the RLS in *fob1Δsir2Δ* cells can be extended upon reduction of 60S ribosomal subunits, we further tested if gene deletion of either Nop12 or Ssf1, two genes involved in 60S ribosomal subunits maturation would reduce protein aggregate formation in aged *fob1Δsir2Δ* cells. Surprisingly, no reduction in Hsp104 aggregates was evident in those triple mutants (Fig. 4-7). This result suggests that the elevated formation of Hsp104 protein aggregates in *sir2Δ* cells is not necessarily correlated with Sir2's function in RLS.

We also performed 3D time-lapse movies and particle tracking to compare the motility of the naturally Hsp104-decorated aggregates in the aged *SIR2* and *sir2Δ* cells. The distributions of α values calculated from the aggregate tracking data in aged wild-type or *sir2Δ* cells were similar and also close to that of heat-induced aggregates reported in previous work (Fig.4-5B). This observation suggests that the dynamics of the Hsp104-associated protein aggregates formed in different ways exhibit similar type of movement and that Sir2 does not play a role in this movement.

Because carbonylated proteins were known to co-localize with Hsp104-decorated aggregates in aged cells (Erjavec *et al.* 2007), we examined the distribution of carbonylated proteins in wild-type and *sir2Δ* strain using the same immunofluorescence staining protocols as described in previous work. Unfortunately, despite extensive trouble shooting (see also experiment procedure), we were unable to observe the expected asymmetric distribution (Aguilaniu *et al.* 2003) of the staining for carbonylated proteins between the mother and the bud even in wild type cells (Fig.4-8A). Staining of aged cells isolated with magnet sorting also showed even distribution between the mother and the bud (data not

shown). The specificity of primary and secondary antibodies was confirmed each time and hydrogen peroxide treatment was used as positive control (Fig.4-8B). It was possible that the alteration in the components of the new carbonylation detecting kit contributed to our failure, but preparing fresh reagents according to the previous recipe (Wang and Powell, 2010) did not solve the problem. As such, we have been unable to confirm our findings on Hsp104-GFP-decorated protein aggregates by the method of immunofluorenscence staining of carbonylated proteins.

Discussion

In summary, our study as described above challenges the previous conclusion on the function of Sir2 in actin cable assembly and asymmetric segregation of protein aggregates. Our results do not support a direct role for Sir2p in the asymmetric segregation of Hsp104p-associated protein aggregates during yeast cell division. The motility and kinetics of aggregate dissolution and clearance from the bud were similar between wild-type and *sir2Δ* cells. Because the *hsp104*^{Y662A} mutant was strongly deficient in aggregate dissolution (Lum *et al.* 2004; Zhou *et al.* 2011), these data also suggest that the Hsp104p chaperon activity is mostly intact in *sir2Δ*. Moreover, the retention of heat aggregates in the mother cell during bud formation was observed in time-lapse movies and appeared to be similarly effective in *sir2Δ* cells as in the wild type.

We considered the possibility that Sir2 may be specifically required for the segregation of the naturally occurring carbonylated protein aggregates in aged cells. As a previous study showed that these aggregates are also associated with Hsp104p (Erjavec et al., 2007), we imaged Hsp104p-containing aggregate in aged cells. However, the distribution and motility of Hsp104p-containing aggregates in the

aged cell population were again indistinguishable between wild-type and *sir2Δ* cells. One possible explanation is that Hsp104 does not associate with all carbonylated protein aggregates in yeast, as supported by the observation that, whereas almost no Hsp104-GFP aggregates are present in young wild-type cells, these young mother cells contain carbonylated proteins (Aguilaniu *et al.* 2003). However, our effort to observe carbonylated proteins using published protocols was unfruitful.

Figures

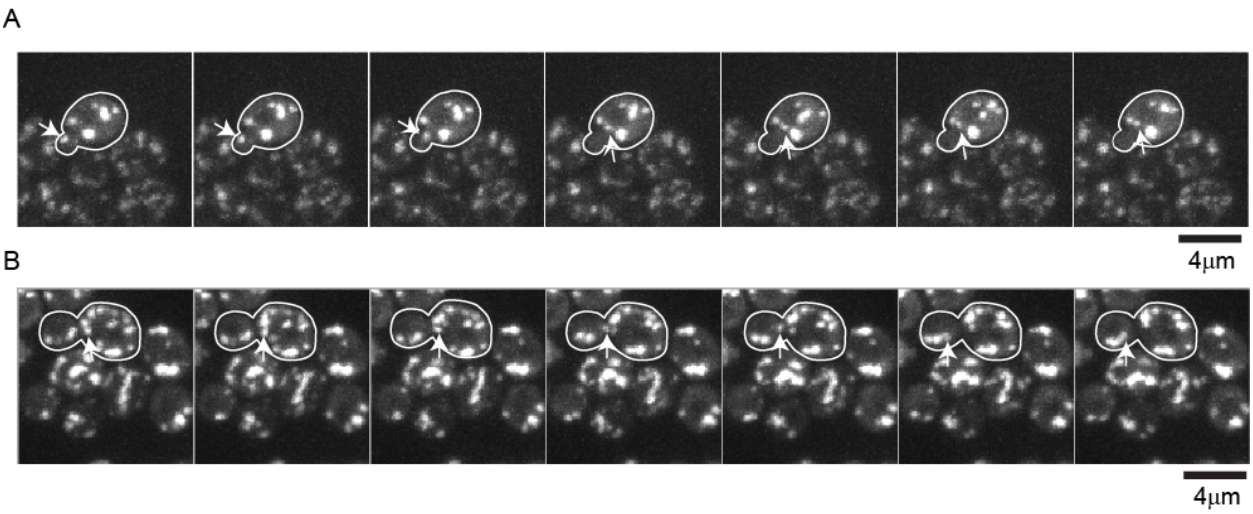

Figure 4-1: Observation of dynamics and distribution of Hsp104p-containing aggregates in wild-type and *sir2Δ* cells.

A. Example of an aggregate (arrow) moving from bud to mother in *sir2Δ* cells. Shown are the maximum projections of Z-stacks collected at 1 min intervals.

B. Example of an aggregate (arrow) moving from mother to bud in *sir2Δ* cells. Shown are the maximum projections of Z-stacks collected at 1 min intervals.

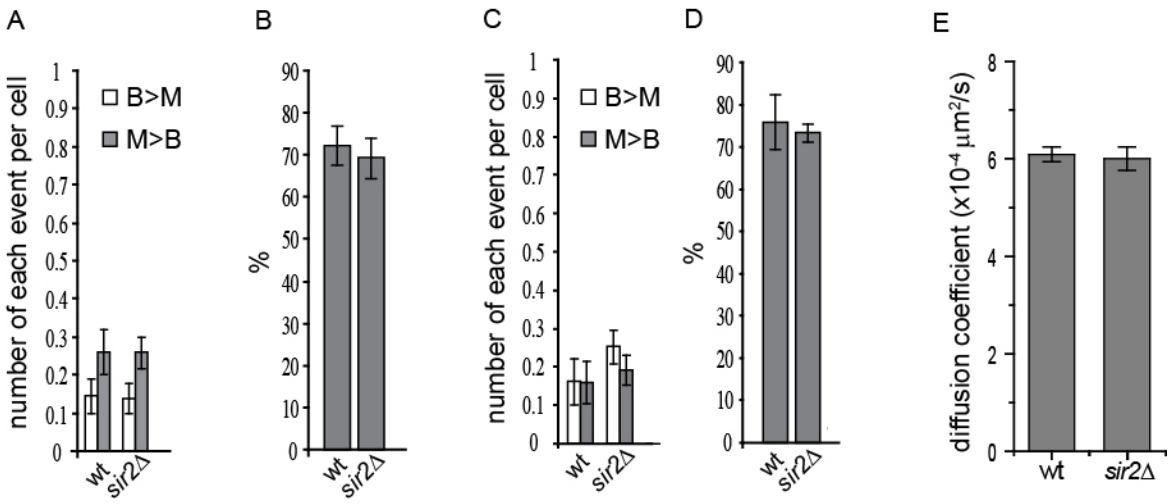

Figure 4-2: Quantification of dynamics and distribution of Hsp104p-containing aggregates in wild-type and *sir2Δ* cells.

A. The frequency of an event as illustrated above the bar graphs per cell was calculated as the totally number of each event divided by the totally number of budded cells in each movie. The bar graphs show average and SEM.

B. Frequency of observing a cell in the population in (A) without any aggregates crossing its bud neck during the 1 hr time-lapse movies. Shown are mean and SEM. For each strain in both (A) and (B), about 40 cells/movie from four to six movies were quantified.

C. The frequency of an event as illustrated above the bar graphs per small budded cell was calculated as the totally number of each event divided by the totally number of small budded cells with bud radius less than one third of its mother in each movie. The bar graphs show average and SEM.

D. Frequency of observing a cell in the population in (C) without any aggregates crossing its bud neck during the 1 hr time-lapse movies. Shown are mean and SEM. For each strain in both (C) and (D), about 40 cells/movie from four to six movies were quantified.

E. Diffusion coefficient of each strain quantified from aggregate tracking analysis (see Experimental Procedures). Shown are mean and SEM of the tracking data from more than 450 aggregates from 2-4 movies for each strain.

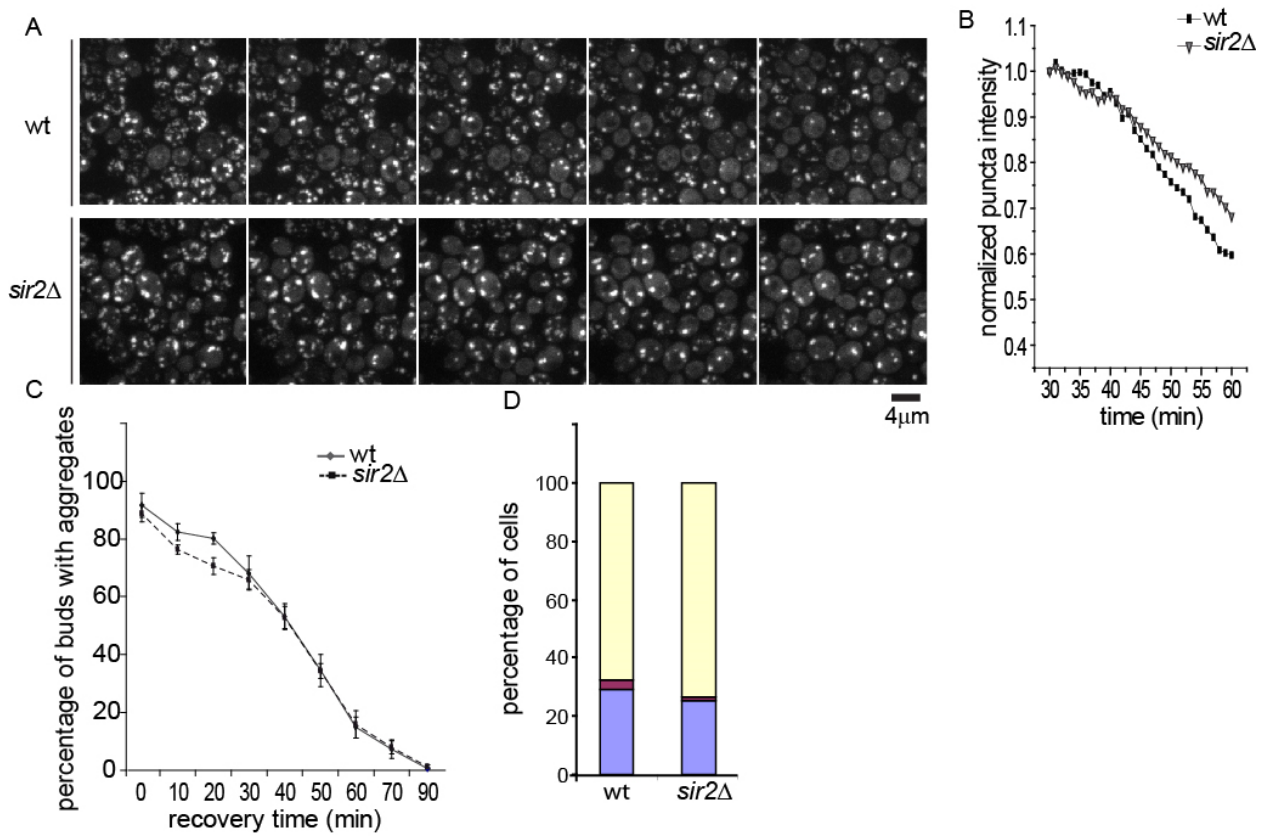

Figure 4-3: Dissolution of Hsp104p-containing aggregates in wild-type and *sir2Δ* cells.

A, B. Example (A) and quantification (B) of aggregates dissolution observed in 3D time-lapse movie. Shown are the maximum projections of Z-stacks collected at 8 min intervals starting from the 30 frame of each movie when there is no longer growth in brightness.

C. *sir2Δ* and wild-type cells exhibited the same rate of aggregate clearance from the bud. After 30min heat shock at 42 °C, cells were recovered in 30 °C and triplicate samples were taken and fixed every 10 min. Z-stack images were taken to score the presence of aggregates in the bud at each time point. Shown are the plots of average and SEM.

D. Percentages of cells displaying three different types aggregate behavior during new bud formation and growth. Cells with a tiny bud initially devoid of any aggregates or giving birth to a new bud during the first 30min of 1 hr long 3D time-lapse movies were scored. Yellow bar: cells with no aggregates leakage into the bud; blue bar: cells in which aggregates leaked into the bud were subsequent cleared by dissolution; red bar: cells in which aggregates leaked into the bud and subsequent moved back to mother. n=108 cells (wt); 68 cells (*sir2Δ*).

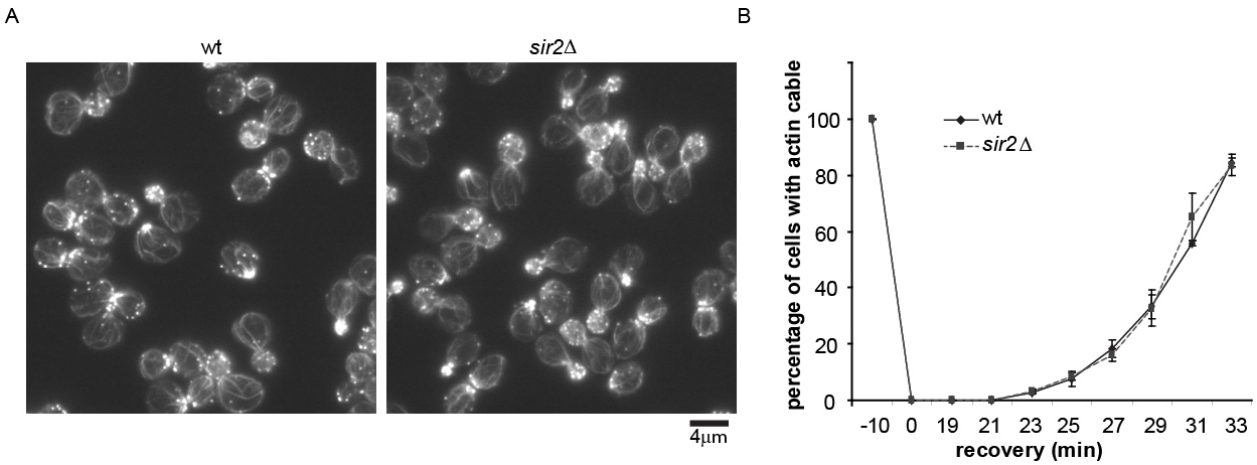

Figure 4-4: *Δsir2* cells have normal structure and function of actin cytoskeleton

A. Actin organization is indistinguishable in *sir2Δ* cells compared to wild type as observed with FITC-phalloidin staining.

B. Actin cables form as efficiently in Δ*sir2* as in wild-type cells. After LatA treatment, cells were washed and recovered in fresh media. Samples were taken, fixed with 4% formaldehyde and stained with FITC-phalloidin. 150-200 cells were scored for the presence of actin cables at each time point. Dotted lines show the average and standard error of the mean (SEM) of three independent repeats of each strain.

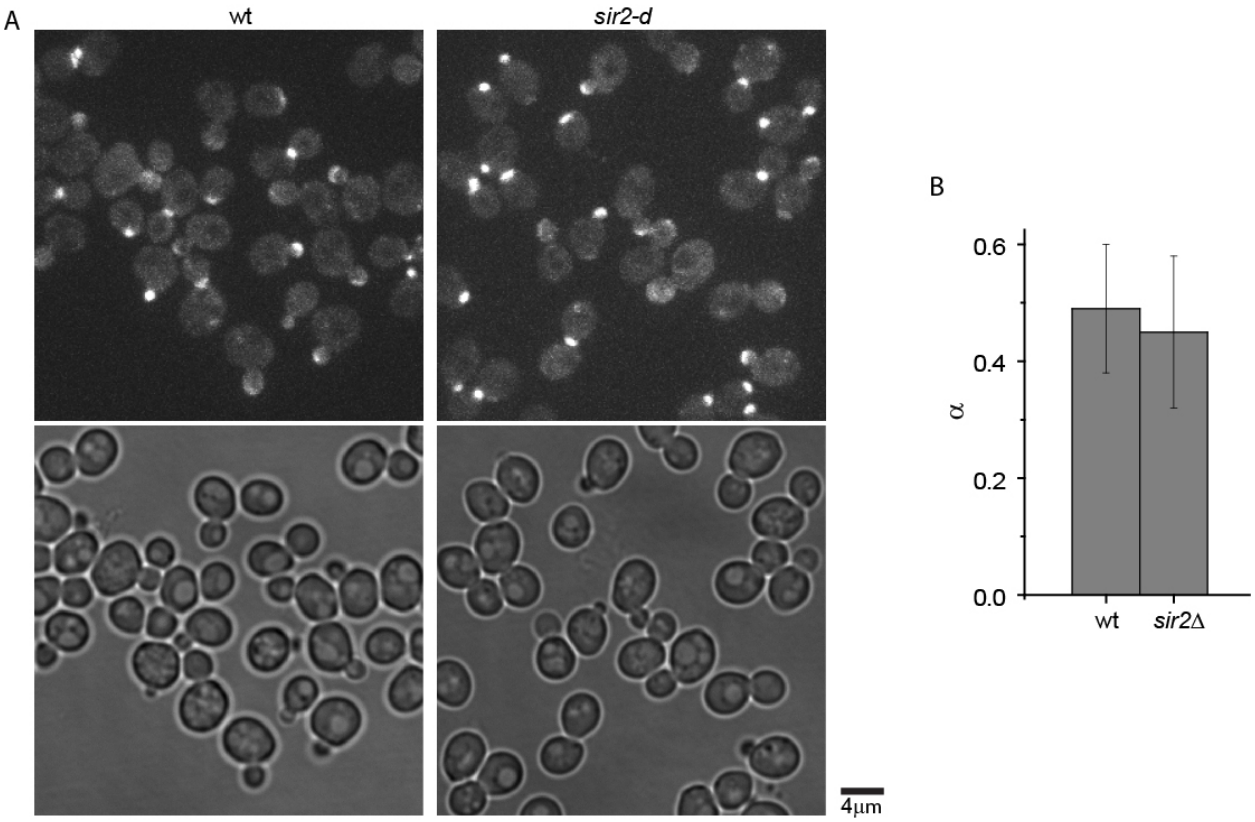

Figure 4-5: *sir2Δ* cells show normal Myo2-GFP localization pattern and aggregate dynamics.

A. The localization of Myo2-GFP in wild type and *sir2Δ* cells. Shown are the maximum projections of Z-stacks. Myo2-GFP localizes to bud tip in nascent bud and bud neck in late cell cycle stage in both wild type and *sir2Δ* strain.

B. Hsp104-GFP-containing protein aggregates in old wild-type and *sir2Δ* cells exhibit a similar type of movement. Shown are distributions of α values calculated from aggregate tracking. Mean and SEM are shown here.

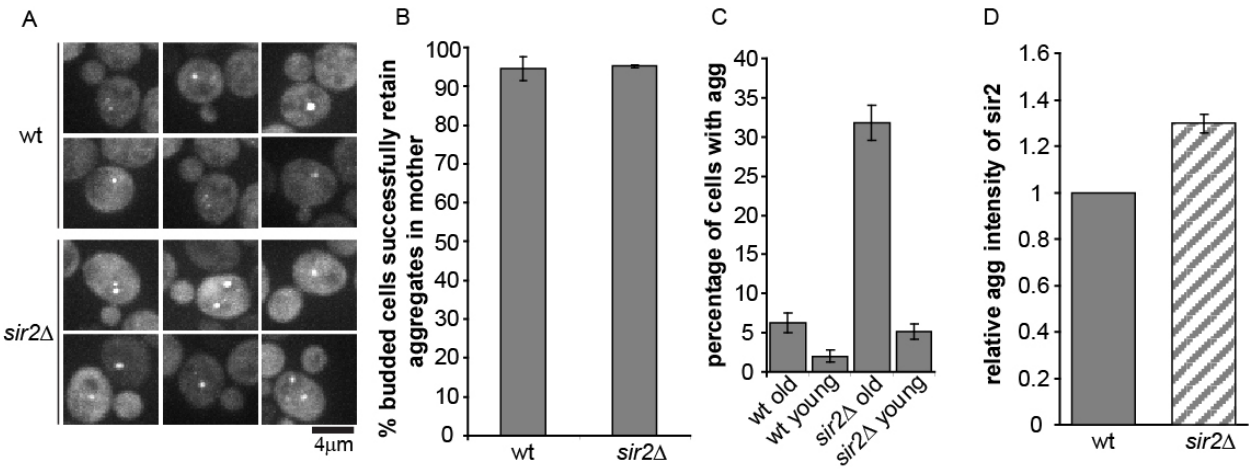

Figure 4-6: The distribution of Hsp104p-containing aggregates in old wild-type and *sir2Δ* cells.

A. Representative images showing asymmetric distribution of Hsp104-associated protein aggregates in magnetic sorted old wild-type and *sir2Δ* cells. Shown are maximum projections of 3D image stacks.

B. Old wild-type and *sir2Δ* cells are equally able to retain Hsp104-GFP-containing aggregates in the mother. Shown are the average and SEM of the percentages of budded cells in which the Hsp104-GFP protein aggregates are perfectly retained in the mother and absent in the bud. For wild type, about 15cells/sorting of four independent sorting are scored; for *sir2Δ*, on average 90cells/ sorting of four repeats are scored.

C. Quantification of percent old *sir2Δ* or wild-type cells that contained Hsp104-GFP-associated aggregates. Shown are average and SEM from four independent sorting experiments with about 200 cells/sorting for all of those four groups.

D. Quantification of aggregates intensity of old wild-type and *sir2Δ* cells (see Experimental Procedures). Shown is the mean and SEM of the fold change of aggregates intensity in *sir2Δ* strain over wild type control in each of four sorting. On average 18 aggregates/sorting for wild type cells and 30 aggregates/sorting for *sir2Δ* cells are measured.

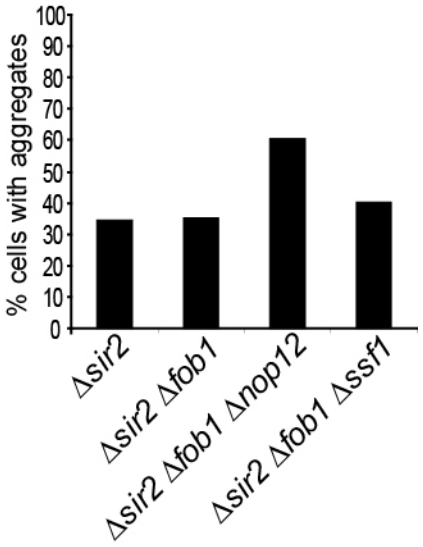

Figure 4-7: RLS can be extended without reducing the Hsp104 aggregates load. More than 250 cells was quantified for each strain

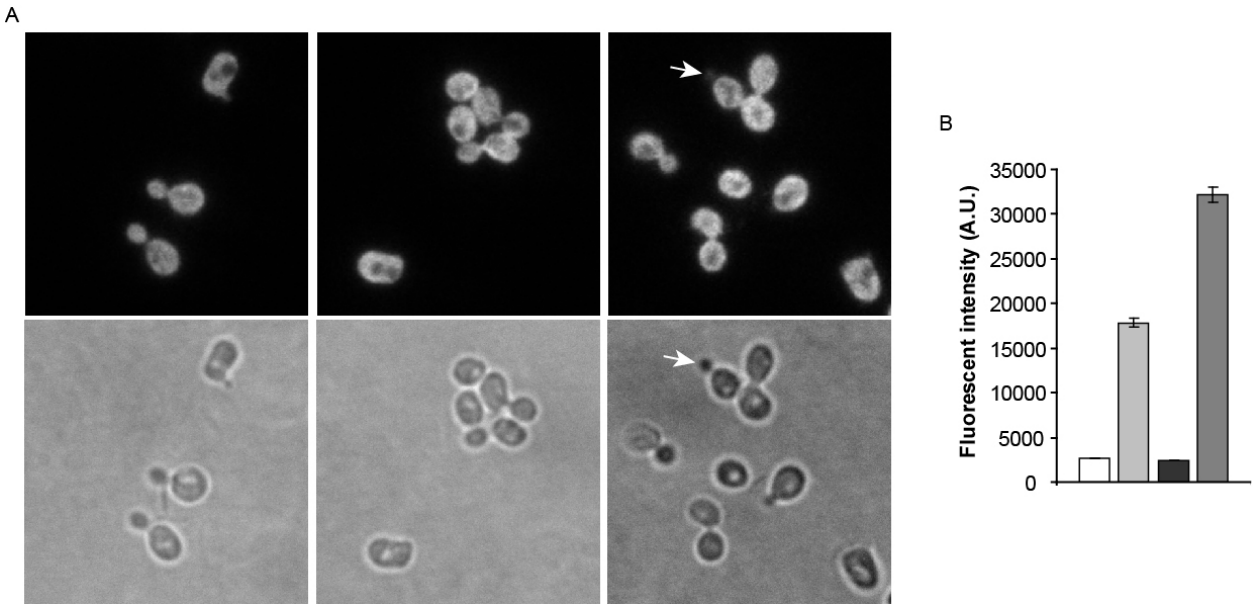

Figure 4-8: *in situ* detection of carbonylated protein showing symmetric pattern of carbonyl signal across mother and bud.

A. Example of *in situ* detection of carbonylated protein using the published protocol (Aguilaniu *et al.* 2003). Wide-field images are taken at a focus plane when most of the cells are illuminated. Arrow points to a cell that is out of the focus plane.

B. Quantification of cytosolic fluorescent intensity in each indicated group. From left to right: cells treated with 10% Trifluoroacetic acid (TFA) as control as control for the specificity of primary antibody; cells treated with DNPH derivation solution; cells treated with DNPH solution but without primary antibody against DNPH as control for the specificity of secondary antibody; cells pre-cultured with 1mM H_2O_2 for 2hr.

CHAPTER FIVE: ORGANELLE-BASED AGGREGATION AND RETENTION OF DAMAGED PROTEINS IN ASYMMETRICALLY DIVIDING YEAST CELLS

Summary

Aggregation of damaged or misfolded proteins is a protective mechanism against proteotoxic stress, abnormalities in which underlie many aging-related diseases. Here we show that in asymmetrically dividing yeast cells aggregation of cytosolic misfolded proteins does not occur spontaneously but requires new polypeptide synthesis and is restricted to the surface of ER, which harbors the majority of active translation sites. Protein aggregates formed on ER are frequently also associated with or are later captured by mitochondria, which greatly constrains aggregate mobility. During mitosis, aggregates are tethered to well-anchored maternal mitochondria, whereas mitochondria acquired by the bud are largely free of aggregates. Disruption of aggregate-mitochondria association resulted in increased mobility and leakage of mother-accumulated aggregates into the bud. Cells with advanced replicative age exhibit gradual decline of aggregates-mitochondria association, likely contributing to their diminished ability to rejuvenate through asymmetric cell division.

Introduction

Formation and intercellular spreading of protein aggregates underlie several aging-related and amyloid diseases (Chiti and Dobson, 2006). Recent data have led to the general view that protein aggregation is a protective mechanism against disrupted protein homeostasis in the presence of acute or chronic stress (Arrasate et al., 2004; Tyedmers et al., 2010a). Because misfolded proteins could interfere with normal biochemical processes or promote denaturation of otherwise properly folded

proteins (Olzscha et al., 2011), aggregation of midfolded proteins and their sequestration into well-confined structures, such as the aggresome, potentially limit the harmful intracellular effect and prevent further spreading through cell division (Rujano et al., 2006; Tyedmers et al., 2010a). In a crowed cytosolic environment, proteins with limited structural stability, especially newly synthesized polypeptides or mutated proteins, may be in a dynamic equilibrium between the folded and misfolded states (Hartl et al., 2011). Misfolded proteins could oligomerize spontaneously once reaching a concentration threshold due to stress (e.g. heat, oxidizing conditions) or impaired proteasome activity, which could grow into visible aggregates (Hartl et al., 2011). On the other hand, the protective role of protein aggregation and the recently revealed involvement of specific factors raise the possibility that aggregate formation may be a highly regulated process that requires energy input and occurs preferentially at specific cellular location (Escusa-Toret et al., 2013; Kawaguchi et al., 2003; Malinovska et al., 2012; Specht et al., 2011).

In the budding yeast *Saccharomyces cerevisiae*, accumulation of damaged proteins and formation of aggregates naturally accompany the process of replicative aging, during which protein aggregates are distributed asymmetrically between the mother cell and the daughter cell (bud) of each division (Liu et al., 2010; Steinkraus et al., 2008; Zhou et al., 2011). Aggregate retention by the mother cell frees the bud of the accumulated damaged products and may contribute to the latter's fully renewed replicative potential (Steinkraus et al., 2008). Protein aggregation can also be induced acutely under a variety of stress conditions or by expression of poorly folded mutant or non-native proteins. When proteasome activity is inhibited, aggregated proteins were shown to be deposited into two compartments: the juxtanuclear quality-control compartment (JUNQ) that recruits ubiquitinated-proteins, and insoluble protein deposit (IPOD) (Kaganovich et al., 2008). A recent study using the model aggregate-forming protein Ubc9^{ts} reported that JUNQ may be the fusion product of small inclusions

termed Q bodies located at the surface of the ER during proteasome inhibition (Escusa-Toret et al., 2013). However, it remains unclear whether these structures represent sites of protein aggregation or later compartmentalization of spontaneously formed aggregates.

Experimentally induced protein aggregates in yeast also segregate asymmetrically and exhibit dynamic properties similar to natural aggregates accumulated during aging (Liu et al., 2010; Spokoini et al., 2012; Zhou et al., 2011). An earlier study of heat-induced aggregates led to a model of retrograde transport along actin cables that actively clears aggregates that in the bud into the mother side (Liu et al., 2010). However, a later study found that the motion of aggregates does not represent active transport but is best characterized as random diffusion with confinement (Zhou et al., 2011). The constrained aggregate diffusion together with the geometry of the dividing yeast cell was predicted to be sufficient for asymmetric retention of damaged proteins. In this study, by tracking the fate of damaged proteins, we show that these proteins rely on new polypeptide synthesis to initiate aggregation. Sites of protein aggregation are predominantly located on the surface of ER, enriched in regions in close contact with or later captured by mitochondria. Such organelle association underlies a mechanism of proteome quality control ensuring asymmetric segregation of proteome damage.

Results

Unstable cytosolic proteins do not aggregate spontaneously in the cytosol during stress

In order to gain general insights into the process of protein aggregation, we employed several different methods to induce protein aggregation in yeast, including heat shock (HS, at 42 ^{o}C), treatment of cells with oxidizing agent H_2O_2, or pulse-feeding cells with azetidine-2-carboxylic acid (A2C), a proline

analog that interferes with protein folding after incorporation into newly translated polypeptides (Liu et al., 2013). These conditions produce proteome-wide aggregation of damaged or misfolded proteins, visualized with green fluorescent protein (GFP)-tagged Hsp104, which binds protein aggregates nonspecifically (Glover and Lindquist, 1998). Hsp104-GFP, produced from the genomic locus possesses wild-type chaperone activity (Zhou et al., 2011) (Fig. 5-2A). We also induced substrate-specific aggregates by expressing mCh-Ubc9^{ts} and GFP-Ubc9^{ts}, respectively representing mCherry- and GFP-tagged Ubc9^{ts}, or GFP-tagged luciferase, a thermally labile protein that aggregate at 42 ^{o}C (Kaganovich et al., 2008; Winkler et al., 2012).

We first asked whether thermal labile proteins aggregate spontaneously in the cytosol or at certain pre-defined sites by performing a sequential aggregate induction experiment (Fig.5-1A). Expression of mCh-Ubc9^{ts} was induced with Gal1 promoter prior to aggregate induction by growing cells in galatose-containing media for 2 hours followed by promoter shutoff. Newly translated polypeptides are particularly prone to aggregation (Hartl et al., 2011; Medicherla and Goldberg, 2008), which can be exacerbated by treating cells transiently (10 min) with A2C (Liu et al., 2013). Numerous aggregates labeled with Hsp104-GFP emerged upon A2C treatment. After A2C washout, we induced aggregation of cytosolic mCh-Ubc9^{ts} by HS and found that aggregates of mCh-Ubc9^{ts} colocalized 100% with Hsp104-GFP-labeled aggregates induced by A2C (Fig.5-1A). A similar result was observed when H_2O_2 was used to induce mCh-Ubc9^{ts} aggregates after A2C treatment (Fig.5-2B). Time-lapse movies showed that during HS mCh-Ubc9^{ts} only accumulated to pre-formed aggregates induced with A2C without forming new aggregates in the cytosol, and concomitantly cytosolic mCh-Ubc9^{ts} fluorescence decreased (Fig.5-1B). To confirm that the aggregated mCh-Ubc9^{ts} came from the pre-existing cytosolic pool, mCherry fluorescence was photobeached prior to HS, and no visible mCh-Ubc9^{ts} aggregates formed (Fig. 5-3A). In addition, when mCh-Ubc9^{ts} aggregates were induced by HS only (without the prior A2C treatment),

mCh-Ubc9^{ts} aggregation, which appeared around 6 min of the HS at 42 ^{o}C, also resided in Hsp104-GFP-labeled aggregates that emerged before accumulating red fluorescence (Fig.5-3B).

To distinguish the possibility that misfolded Ubc9^{ts} first formed invisible soluble oligomers before their incorporation into visible aggregates from that misfolded Ubc9^{ts} monomers are directly incorporated into pre-existing aggregates (Fig.5-4A), we used live-cell fluorescence correlation spectroscopy (Slaughter and Li, 2010) to measure the molecular brightness and thus, the oligomeric state, of diffusing GFP-Ubc9^{ts} species during HS. This analysis showed that the diffusing GFP-Ubc9^{ts} species remained monomeric throughout HS while visible aggregates grew (Fig.5-2C, 5-4B), supporting the scenario that misfolded Ubc9^{ts} monomers do not accumulate as oligomers prior to partitioning into existing aggregates. The FCS experiment was also performed on the other model substrate, GFP-Luciferase, or in the experiment with A2C pretreatment, yielding the same results (Fig.5-4C).

Active translation is required for protein aggregation

We next performed an experiment in which the order of aggregate inductions was reversed (Fig.5-5). Surprisingly, A2C treatment not only increased the intensity of pre-existing aggregates but also induced many new aggregates outside the pre-formed aggregates (Fig.5-5). This raised a possibility that newly synthesized polypeptides initiate aggregate formation. To test this further, we treated cells with cycloheximide (CHX), a translation inhibitor, before induction of protein aggregation. CHX treatment inhibited aggregate formation under all conditions examined (Fig.5-6A, B, and Fig.5-7). CHX did not affect aggregate formation in a CHX-resistant strain (Kawai et al., 1992) (Fig.5-6A). Anisomycin, a translation inhibitor structurally different from CHX (Pestka et al., 1972), *prt1*^{ts}, a temperature-sensitive mutation disrupting translation initiation (Li et al., 2011), and glucose depletion, which is known to

arrest translation (Ashe et al., 2000), also inhibited heat-induced protein aggregation (Fig.5-7). These experiments, however, did not rule out that conditions that inhibit translation (e.g. CHX treatment) may also help "free up" the capacity of chaperone and proteasome systems to prevent the aggregation of native proteins under stress. We therefore blocked chaperone activity by depleting ATP during CHX treatment and HS. The combined treatment with 2- deoxy-d-glucose (2-DG) and antimycin cause over 95% (Serrano, 1977) reduction of cellular ATP by blocking both glycolysis and mitochondrial respiration (Fig.5-8) . However, CHX still fully prevented HS-induced aggregation in ATP-depleted cells (Fig. 5-8), suggesting that CHX suppression of protein aggregation was unlikely to be due to elevated chaperone activity but more likely to be due to a requirement for newly synthesized polypeptides in aggregate initiation.

ER and mitochondria are main organelle hosts for stress-induced protein aggregation

Previous fractionation studies in mammalian cell lines revealed that a large fraction of mRNAs are translated at ER-bound ribosomes (Reid and Nicchitta, 2012). If this is also true in budding yeast, ER could be the main organelle host for protein aggregation under stress. We found, by adapting a puromycin-based assay (David et al., 2012), that ~75% of active translation sites to be associated with ER surface (Fig. 5-9). By using both confocal microscopy and structured illumination microscopy (SIM) with 3D reconstruction, we observed that the vast majority of HS-induced protein aggregates were associated with ER (Fig.5-10A). Under electron microscopy (EM), aggregates formed from HS appeared as electron-dense and amorphous bodies (Fig.5-11) and the association of with ER membrane can be observed (Fig.5-10B). 3D time-lapse movies showed that ~90% of aggregates formed on the surface of ER (Fig.5-10C). This association remained at~90%, much higher than 42% expected for random association simulated using measured aggregate numbers and ER surface area in SIM images, even

though aggregates underwent considerable movement with or along ER. The association of protein aggregation sites with ER was also observed for A2C or H_2O_2-induced ones.

Interestingly, protein aggregates formed under all stress conditions examined also demonstrated extensive association with mitochondria (Fig.5-10, 5-11, 5-12, and 5-13). Time-lapse movies revealed that 60-70% of aggregates initially formed on the surface of and remained continuously associated with mitochondria (Fig.5-12C). Furthermore, many aggregates that were not initially associated were later captured by mitochondria once stress was removed, such that eventually > 85% aggregates were attached to mitochondria (Fig.5-14A). Aggregates did not show prominent association with the rest of the organelles examined (Fig.5-15). Importantly, $Ubc9^{ts}$ aggregates formed under the previously described conditions for IPOD and JUNQ were also found to be associated with ER and mitochondria (Fig.5-14C).

ER and mitochondria are known to have extensive areas of contact. Quantification with tri-color time-lapse confocal microscopy showed that 58$\pm$3% (mean$\pm$SEM, 3 experiments, > 20 cells imaged per experiment) of aggregates emerged initially from regions where ER and mitochondria were juxtaposed, and this fraction increased to nearly 80% of all aggregates due to capture by mitochondria (Fig.5-13). The association of aggregates at or near these organelle contact sites was verified with SIM (Fig.5-11D), as well as with serial sectioning EM with 3D reconstruction (Fig.5-13). However, only a small portion of aggregates showed colocalization with Mdm34 (Fig.5-11E), a component of the well-studied ER-mitochondria encounter structures (ERMES) (Kornmann et al., 2009), possibly because a considerable portion of ER-mitochondrial contact regions are not marked by ERMES components (Kornmann, 2013; Nguyen et al., 2012; Youngman et al., 2004).

Influence of mitochondria on aggregate dynamics

Mitochondria might provide the ATP for the dissolution of protein aggregates. However, electron transport chain poisons, such as cyanide and antimycin, did not affect the kinetics of aggregate dissolution (Fig.5-16A). By contrast, like GdnHCl, which inhibits Hsp104 (Kummer et al., 2013), 2-DG or replacing glucose with glycerol after HS, which prevents cytosolic ATP production, significantly delayed aggregate dissolution, suggesting that glycolysis is the main source of ATP for aggregate dissolution. Interestingly, agents that disrupt mitochondrial membrane potential, such as azide or carbonyl cyanide *m*-chlorophenyl hydrazine (CCCP), did not by themselves induce protein aggregation (data not shown) but strongly blocked aggregate dissolution (Fig.5-16A).

A second effect of mitochondria on aggregates is constraining the latter's mobility. As shown in previous work, aggregates were visibly motile after a short period of recovery (Liu et al., 2010; Zhou et al., 2011). Those aggregates not initially associated with mitochondria exhibited dampened mobility immediately upon capture by mitochondria. The average diffusion coefficient was significantly lower for aggregates attached to mitochondria compared to those that were not (Fig.5-16B). Once attached, the aggregates' motion resembled mostly that of their associated mitochondria. This is most readily observed in H_2O_2-treated cells where mitochondria became mostly immobile. A typical example is shown in Figure 5-16C, where an aggregate exhibited rapid movement until it eventually formed stable attachment to mitochondria and became nearly immobile.

Mitochondria control aggregate asymmetric segregation

Previous studies showed that aggregates are largely retained by the mother during budding and cell division (Liu et al., 2010; Zhou et al., 2011), but it was also known that mitochondria are trafficked

into the bud via actin cables and myosin-V (Altmann et al., 2008; Boldogh et al., 2004). If mitochondrial movement accounts for the motility of associated aggregates, why don't aggregates passively follow mitochondria into the bud? To address this question, we performed 2-color time-lapse imaging of mitochondria and HS aggregates in cells undergoing budding and mitochondria inheritance. Remarkably, the majority of aggregates present in the mother did not follow the mitochondria that entered the bud, but they either underwent dissolution/degradation or remained associated with the mitochondria that were kept in the mother cell and only exhibited confined local mobility (Fig.5-17A). As such, the bud-inherited mitochondria were largely devoid of aggregates. Aggregates that occasionally entered the bud were usually already at the bud neck region and followed the movement of bud-bound mitochondria. This pattern of motility was also observed for foci of Dmn1 and Mdm34 (Fig.5-17B, 5-18A), consistent with previously observed stability of ERMES complex (Nguyen et al., 2012). A similar inheritance pattern was also observed for mitochondrial nucleoids (Fig.5-18B). Note that nucleoids in the mother were overall less anchored than Dmn1 and Mdm34 foci, but the ones entering the bud also often originated from the bud neck region. These observations suggest that some structural assemblies of mitochondria, including the associated protein aggregates, are segregated conservatively during organelle inheritance during yeast asymmetric cell division.

To further test the idea that mitochondria-tethering plays an important role in the asymmetric segregation of protein aggregates, we sought for conditions that could disrupt this association. As mitochondria are known to align with actin cables (Fehrenbacher et al., 2004), we first tested whether treatment with latrunculin A (LatA), an actin inhibitor, would disrupt mitochondria-aggregate association. Although LatA treatment grossly disrupted mitochondrial distribution and morphology, protein aggregates remained bound at a high frequency (Fig.5-14B). We next screened a subset (72) of the yeast non-essential ORF deletion library, encoding mitochondrial outer membrane proteins, and found several mutants showing reduced aggregate-mitochondria association (Fig.5-19A). The strongest

defect was displayed by *Δfis1*, in which only 57% aggregates colocalized with mitochondria, compared to over 85% percent for the wild type (wt) and 45% for simulated random distribution (Fig.5-20A). The association of aggregates with ER was not affected in *Δfis1* (Fig.5-19B). Fis1 is an evolutionarily conserved mitochondrial protein known for its role in yeast mitochondria fission by forming a complex with Mdv1 and Dnm1 (Detmer and Chan, 2007). Both *Δmdv1* and *Δdnm1* showed less severe though statistically significant, defect in aggregate-mitochondria association (Fig.5-20A). However, colocalization was rarely observed between protein aggregates and Dmn1 foci or sites of mitochondrial fission (Fig.5-21). Thus, Fis1 may have a function in aggregate-mitochondria association distinct from its role in mitochondrial fission.

HS-induced protein aggregates in *Δfis1* cells were overall more mobile than those in wt cells (Fig.5-20B). As in wt cells, the mitochondria-free aggregates moved significantly faster than those associated with mitochondria (Fig.5-20C). Accompanying the increased mobility of aggregates, more *Δfis1* cells exhibited mother-to-bud (MTB) leakage of at least one aggregates during bud formation, and this defect was not associated with increased aggregate number or size in the mutant (Fig.5-22). We further classified the MTB-leaking aggregates according to their mitochondrial association in cells with dual labels. In wt cells, the majority of the mitochondrial-associated aggregates stayed in the mother cell, while a small fraction of them (usually near the bud neck) entered the bud with mitochondria and represented 57% of MTB events (Fig. 5-22). Aggregates not associated with mitochondria (~15% of total aggregates) accounted for 43% of MTB leakage, suggesting that free aggregates are much more likely to leak into the bud than mitochondria-associated ones. In *Δfis1* cells, free aggregates represented the majority (73%) of MTB events (Fig.5-22), correlating with the defect in mitochondria-aggregates association.

Gradual loss of mitochondria–aggregate attachments during replicative aging

Since mitochondrial association is required for efficient retention of aggregates in young cells, we examined how this quality control mechanism is affected in old cells with replicative age of 7-10 or 15-17 generations sorted as described (Lindstrom and Gottschling, 2009). Hsp104-GFP-bound aggregates that occurred naturally during the aging process were rare in young cells but could be observed in aged cells. The percentage of aggregates associated with mitochondria showed progressive reduction with increased replicative age (Fig.5-23). This reduced mitochondrial association was not predicted by simulations of random distribution in aged cells. In the 15-17-generation population examined, the observed frequency of aggregate-mitochondria association was reduced to a level close to simulated random distribution (Fig.5-23B). The association of heat-induced aggregates with mitochondria showed similar age-dependent decline (Fig.5-23B, 5-21C).

Discussion

The results described above establish a new framework for protein aggregation under acute stress, from aggregates' initial formation to distribution during asymmetric cell division (summarized in 5-24). Although our findings are consistent with the notion that misfolded proteins of different nature tend to aggregate together, a surprising observation was the requirement for active translation. Our data suggested that nascent translation products play a key role in initiating the sites for protein aggregation. It is known that newly translated polypeptides suffer a prolonged period of sensitivity to stress and environmental changes (Medicherla and Goldberg, 2008), and their high local concentration near sites of protein synthesis could favor aggregate initiation. In contrast to newly synthesized

polypeptides, cytosolic misfolded proteins (Ubc9^{ts} or luciferase at elevated temperature) did not appear to have the ability to initiate aggregation but can be substrates added to existing aggregates.

In vitro biochemical studies have shown that, in addition to intra-protein interactions, agents that discriminately bind to proteins in their folded states (such as proteins' physiological ligands) could also prevent misfolding and aggregation by increasing the energetic barrier between the native and misfolded states (Carpenter et al., 1999). The opposite effect is expected with agents (such as surfactant) having higher affinity to misfolded states. In the cytosol, each protein interacts with a multitude of functional partners, which helps stabilize protein's native states and possibly explains the low likelihood for aggregation, whereas in protein aggregates the misfolded state is favored and stabilized through interaction with other misfolded proteins. Such opposite stabilizing effects on native vs misfolded conformers could drive protein aggregation to proceed like phase separation seeded by newly translated polypeptides enriched near translation sites. It will be interesting to determine if specific types of newly synthesized polypeptides may be particularly potent in aggregate initiating and whether certain components of ER facilitate this process.

Another unexpected finding is the co-involvement of ER and mitochondria in the formation and management of protein aggregates. This may be a consequence of the extensive interaction between these organelles but may also reflect a propensity of aggregates to bind both ER and mitochondria surface components. ER-mitochondria contact sites have been a subject of exciting recent research due to their roles in mediating lipid transfer between the organelles, formation of autophagosomes, and mitochondrial fission (Bockler and Westermann, 2014; Kornmann, 2013). Several interacting proteins that form the ERMES complex were found to be required for ER-mitochondrial interaction, but ERMES themselves only represent a portion of ER-mitochondria contact sites (Kornmann, 2013). Protein

aggregates do not show extensive overlap with ERMES or sites of mitochondrial fission and thus represent another type of interaction bridging these two organelles.

Mitochondria membrane potential, but not mitochondria-dependent ATP production, is required for the dissolution of aggregates. Mitochondrial membrane potential regulates processes such as mitochondrial protein import and calcium homeostasis (Duchen, 2000; Neupert and Herrmann, 2007). A previous study showed that stress conditions can induce hyperpolarization of mitochondrial membrane and this is required for the induction of chaperone expression (Rikhvanov et al., 2005); however, this is unlikely to explain our observed inhibition of aggregate dissolution by uncouplers since Hsp104 induction after HS did not appear to be defective. It is possible that mitochondrial membrane potential contributes to chaperone or proteosome efficiency, or affects aggregate dissolution indirectly through other essential mitochondria-mediated processes.

Asymmetric inheritance, such that aggregated proteins are distributed to only one of the two progeny cells of mitosis, is another clearance mechanism that limits the spreading of proteome damage in a growing population (Bufalino et al., 2013; Rujano et al., 2006; Steinkraus et al., 2008). Our previous study with mathematic modeling proposed that confined slow mobility of aggregates was one of the key reasons for the high-probability of aggregate retention by the mother cell (Unruh et al., 2013; Zhou et al., 2011). While tight association of aggregates with mitochondria, as frequently observed under EM, could explain the observed confinement if mitochondria are relatively immobile, mitochondria in fact are known to undergo rapid and directed extension into the growing bud. What resolves this paradox is the apparent conservative segregation of at least a subset of mitochondrial components. This was evidenced by the retention of not only aggregates but also physiological components of mother mitochondria, such as foci of Dmn1 or Mdm34, or nucleoids that harbor mitochondrial genome, when daughter-bound mitochondria extend rapidly from the bud neck toward the bud tip. This observation

may be consistent with recent studies showing that the volume of mitochondria in the mother cell remains roughly constant while the daughter mitochondrial volume continuously grows throughout the cell cycle and that daughter cells mitochondria are overall "fitter" than mother mitochondria (McFaline-Figueroa et al., 2011; Rafelski et al., 2012).

The increased leakage of mother-born aggregates into the bud in *Δfis1* mutant corroborates the importance of mitochondria tethering as a quality control mechanism for limiting the spreading of damage products to newborn cells. Attaching to mitochondria may also allow irreversible aggregates to be cleared through mitophagy, a catabolic process for removing damaged mitochondria thought to be anti-aging (Kim et al., 2007). However, the association between aggregates and mitochondria appears to decline gradually in aging cells, and this correlates with increasingly abnormal mitochondrial morphology (Fig.7A) (Hughes and Gottschling, 2012). In humans, proteins that form aggregates in several degenerative diseases have also been associated with the mitochondrial membrane (Camilleri et al., 2013; Hashimoto et al., 2003; Pasinelli et al., 2004). Whereas this association could potentially help limit the spreading of disease proteins, it is also known to contribute to mitochondria dysfunction. In cultured mammalian cells, mitochondria were found to be enriched in the aggresome which is partitioned unequally during mitosis (Garcia-Mata et al., 1999; Johnston et al., 1998). Asymmetric partitioning of protein aggregates was also reported recently in asymmetrically dividing *Drosophila* stem cells (Bufalino et al., 2013). It is thus reasonable to speculate that the organelle-based aggregate formation and retention revealed in yeast represents a mechanism of proteome quality control that may also be important during development and aging in metazoans.

Figures

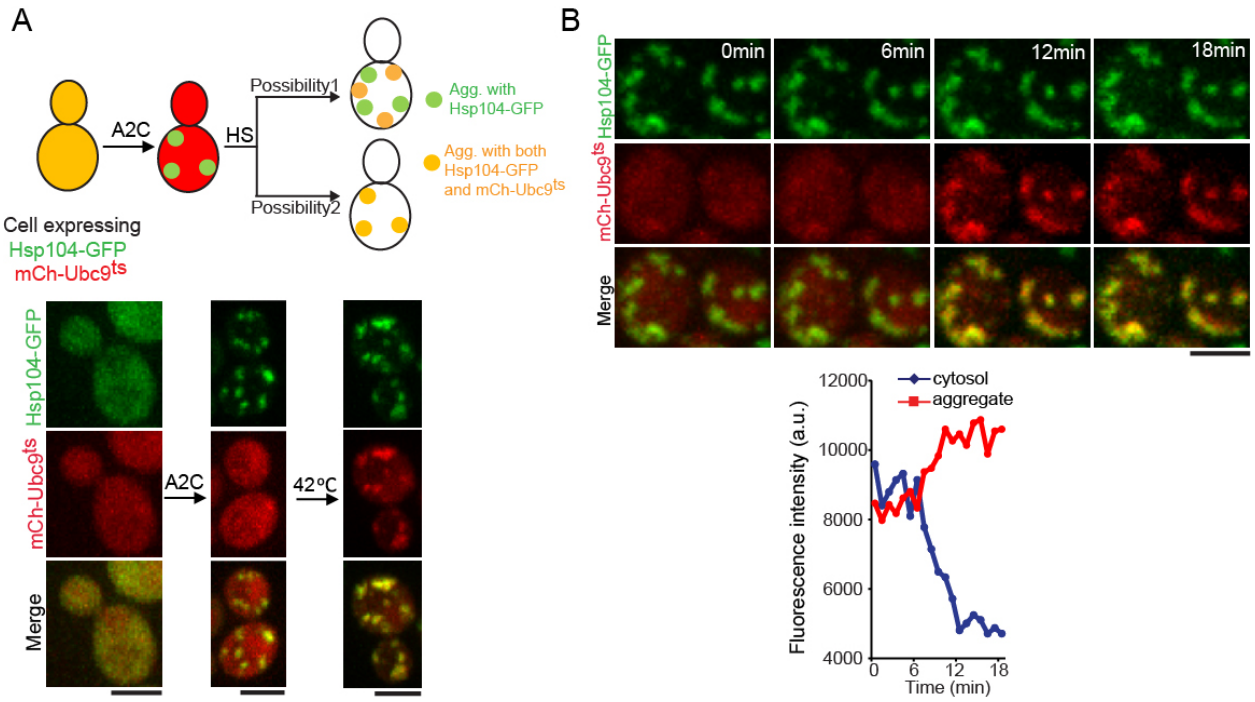

Figure 5-1. Co-aggregation of cytosolic misfolded proteins with newly synthesized polypeptides.

A. Sequential protein aggregation experiment in which cells expressing Hsp104-GFP from its endogenous promoter and mCh-Ubc9^{ts} (briefly induced with Gal1 promoter) were treated for 10 min with A2C. After A2C washed-out, HS or H_2O_2 treatment was applied to induce aggregation of mCh-Ubc9^{ts}. Top: experimental scheme and two possible outcomes; bottom: representative cell images from HS experiment.

B. Up: selected frames from a representative movie showing recruitment of cytosolic mCh-Ubc9^{ts} to pre-existing A2C-induced aggregates (labeled with Hsp104-GFP) during HS. Down: quantification showing gradual depletion of cytosolic mCh-Ubc9^{ts} while aggregate-associated mCh-Ubc9^{ts} signal increased.

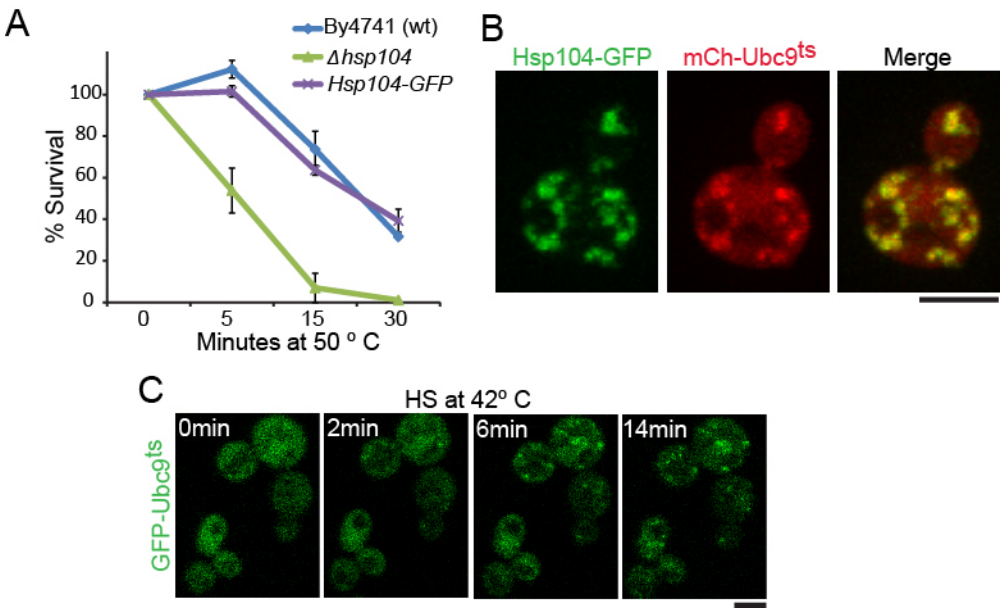

Figure 5-2. Thermotolerance and protein aggregation under stress.

A. Survival rate of different strains as indicated at 50 °C. Survival rate was quantified as percent of colony forming units left after different duration of heat shock at 50 °C. Shown are mean and SEM of three independent repeats.

B. Example images of cells expressing Hsp104-GFP and mCh-Ubc9^{ts} treated with A2C for 10 min, washout, followed by treatment with H_2O_2 (0.7mM for 30 min in 30 °C). Scale bar: 4μm.

C. Representative images of GFP-Ubc9^{ts} aggregate formation at different times during FCS data collection in Figure 5-4B. These are frames of single-plane images from a time-lapse movie taken under conditions identical to the ubc9^{ts}-GFP FCS experiment on the same microscope. Timestamps indicate HS duration. Scale bar: 4μm.

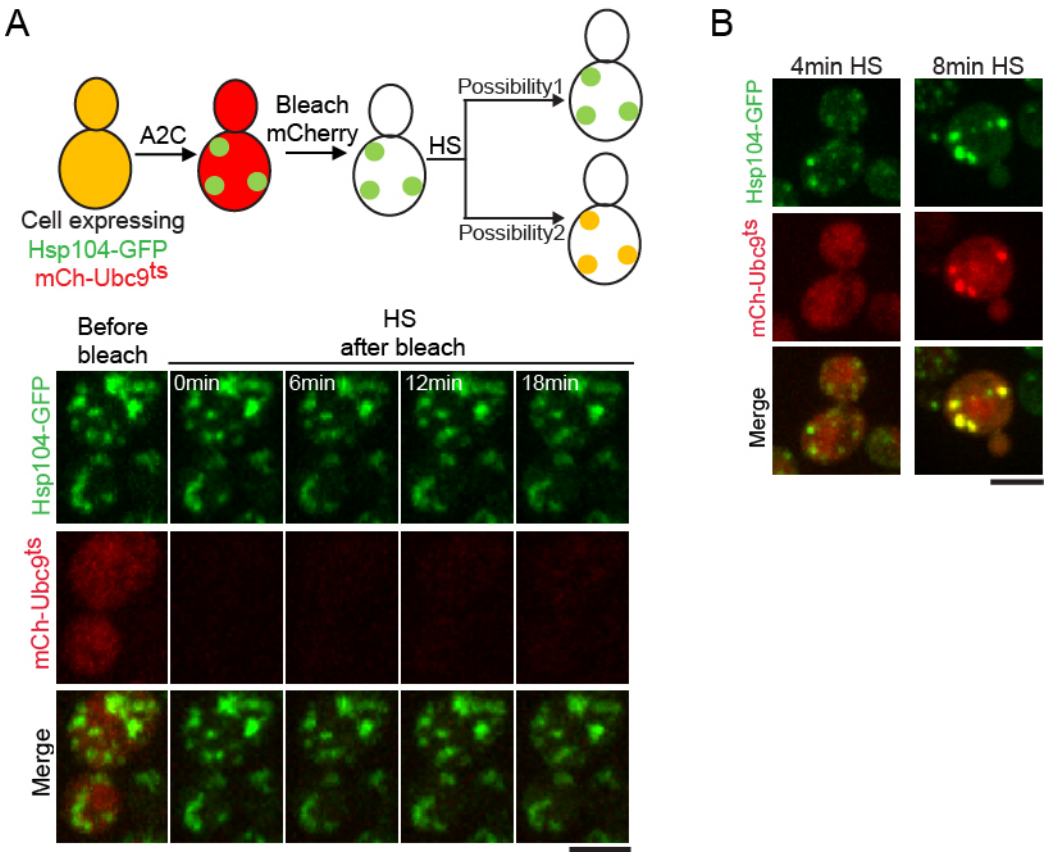

Figure 5-3. Matured proteins form aggregates slower than newly translated peptides.

A. Selected frames from the FRAP experiment where A2C-treated cells with mCh-Ubc9^{ts} photobleached with a 561nm laser before being subjected to HS. Top: experimental scheme with two possible outcomes; bottom: frames from a representative movie showing no accumulation of mCh-Ubc9^{ts} fluorescence into A2C-induced Hsp104-GFP-containing aggregates upon HS.

B. Delayed mCh-Ubc9^{ts} aggregation during heat shock. The culture of same strain as in (A) was heat shocked for indicated time at 42 ^{o}C and representative cells are shown.

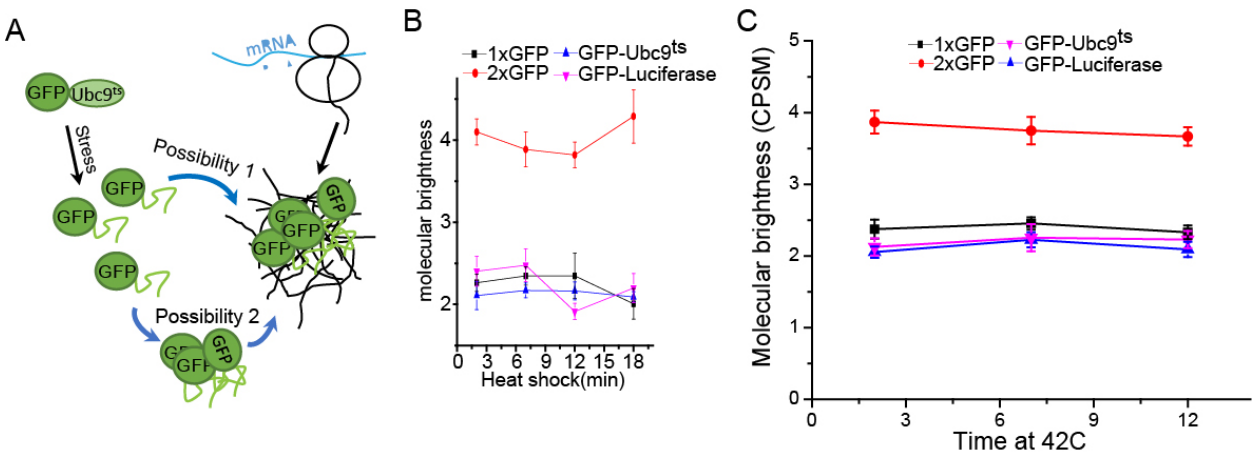

Figure 5-4. FCS data.

A. Two possible pathways leading to recruitment of mCh-Ubc9^{ts} to pre-existing aggregates. Possibility 1: misfolded GFP-Ubc9^{ts} monomers directly add to existing aggregates; Possibility 2: misfolded GFP-Ubc9^{ts} monomers first spontaneously form oligomers and then merge with existing aggregates.

B. Molecular brightness of diffusing GFP-Ubc9^{ts} or GFP-luciferase species as a function of time during 42 ^{o}C HS, as determined by FCS. Plots shown mean and standard error of the mean (SEM) from > 20 FCS runs from at least 9 cells per time point for GFP-Ubc9^{ts} or GFP-luciferase, and > 9 FCS runs from > 3 cells for each time point for 1x and 2xGFP, used as controls for monomer or dimer brightness. Scale bar for all panels: 4μm.

C. Molecular brightness of diffusing GFP-Ubc9^{ts} or GFP-luciferase particles as a function of time during 42 ^{o}C HS after A2C treatment. Briefly, cells were treated with A2C for 10min at 30 ^{o}C followed by washout before heat shock.

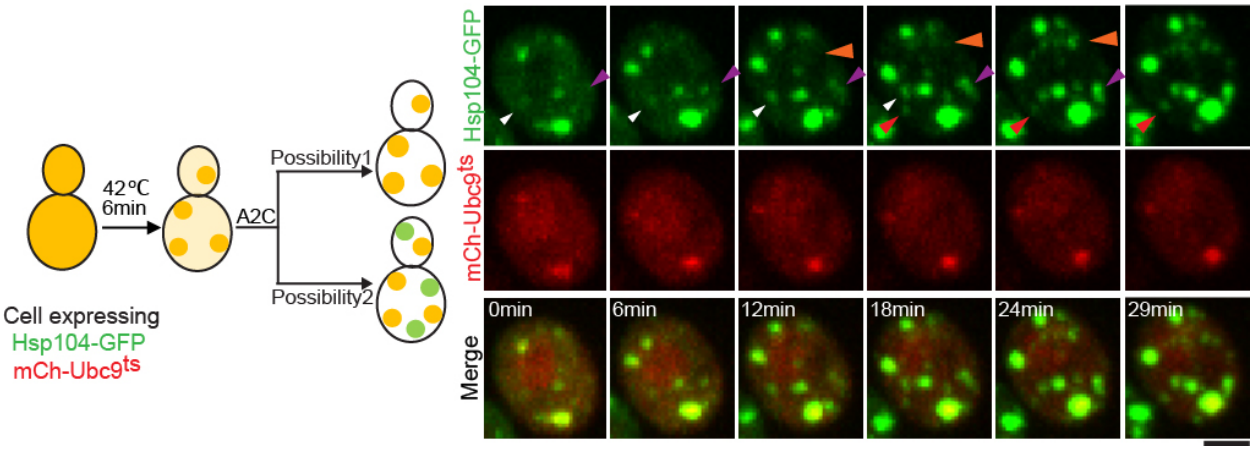

Figure 5-5. Sequential protein aggregation experiment.

Sequential protein aggregation experiment in which cells were first heat-shocked at 42 °C to induce mCh-Ubc9^{ts} aggregates, followed by A2C treatment. Left: schematic and 2 possible outcomes; right: selected frames from a time-lapse movie of A2C induced aggregation. Arrowheads follow new Hsp104-GFP-labeled aggregates outside of existing aggregates.

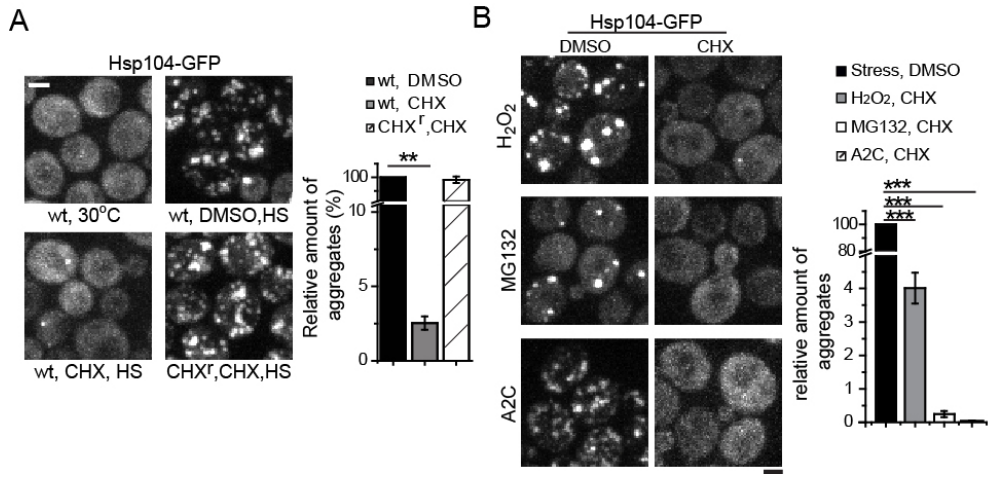

Figure 5-6. Active translation is required for stress-induced protein aggregation.

A. Cycloheximide blocks protein aggregation induced by HS. Left, examples of cells with different treatment as indicated; Right, quantification of aggregate amounts from different treatments. wt, wild type; CHX^r: cycloheximide-resistant strain (*Δrpl42a*; *Rpl42b*^{P56Q}); CHX, cycloheximide; DMSO: solvent control. Histogram show the average (3-4 experiments, > 80 cells per experiment) amount of aggregates per cell normalized to the DMSO control (set at 100%). Error bars show SEM. *** p<0.001, ** p<0.01; * p<0.05.

B. Aggregates induced by indicated stress conditions in the presence or absence of CHX. Left, representative images of cells; Right, quantification of aggregate amount as in B. All scale bars are 2μm.

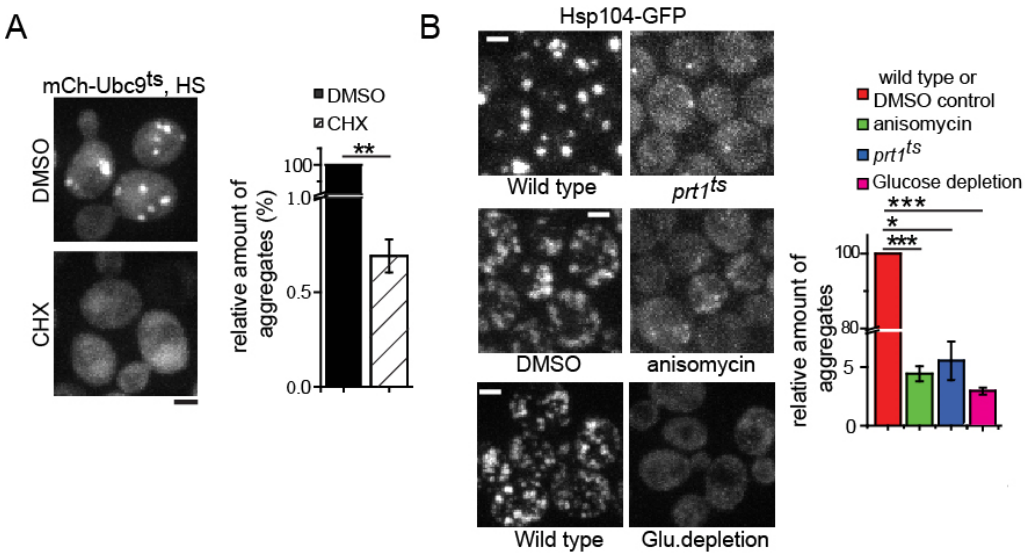

Figure 5-7. Active translation is required for aggregation.

A. Representative images and quantification of mCh-Ubc9^{ts} aggregates in DMSO and CHX treated-cells subjected to HS. Scale bar: 2μm.

B. Example and quantification of aggregates in *prt1*^{ts} mutant and wild-type cells, or wild-type cells pre-treated with anisomycin (30 min) or glucose depletion (10 min) at 30 °C. The amount of aggregates was normalized (as a percentage) to the specific control in each group as shown in the left panel. Scale bars: 2μm. Histograms in (F, G) show the average (from 3-4 experiments, more than 80 cells examined per experiment) amount of aggregates in each cell normalized to DMSO or wild-type control (set at 100%). Error bar: standard error of the mean (SEM). Scale bars: 2μm. *** p<0.001, ** p<0.01; * p<0.05.

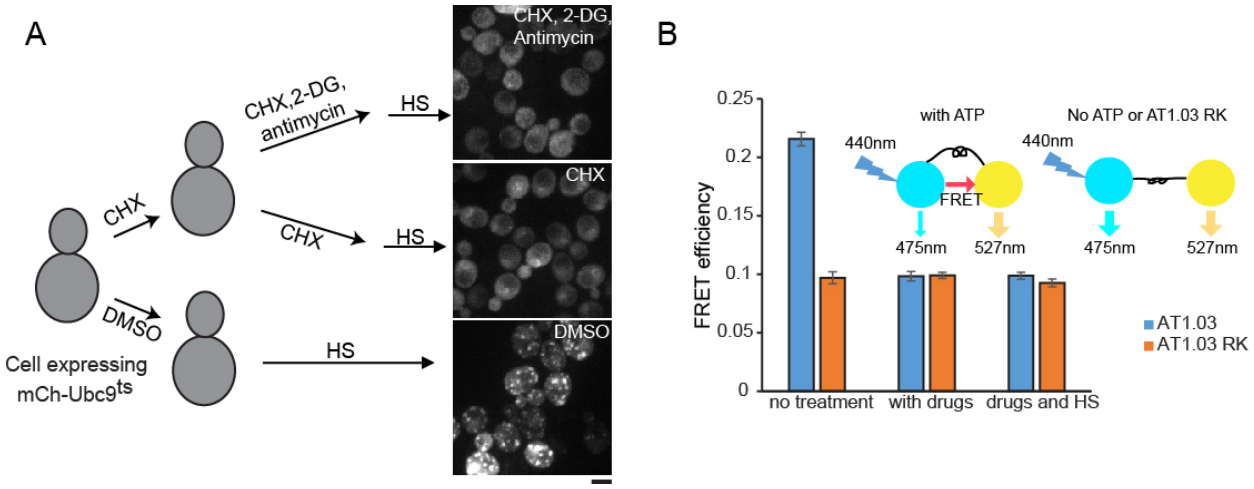

Figure 5-8. Block chaperone activities does not cause protein aggregation during translational inhibition.

A. Experimental scheme and effect of ATP depletion on aggregate formation in cells treated with CHX and heat shock. Cells treated with CHX for 15min followed by glucose depletion by washing and replacing with glucose-free synthetic complete media supplemented with CHX, or CHX and 20mM 2-DG and 18μg/mL antimycin. Cells were incubated in this media for 10 min before heat shock at 42 °C for 15min. A DMSO control for the drug treatments was included in parallel. Representative images are shown for each treatment. Scale bar: 4μm.

B. Verification of ATP depletion with an ATP biosensors. AT1.03 showed a FRET efficiency of ~0.22 in wt cells without any treatment. FRET efficiency dropped to ~0.099 after ATP depletion treatment as described in (A). AT1.03 RK (R122K/R126K) is a negative control for baseline FRET and does not response to ATP concentration less than 10 mM as reported (Imamura et al., 2009). AT1.03 was chose based on its *Kd* and estimated ATP concentration in budding yeast (~2-3 mM) (Ozalp et al., 2010). Cartoon was modified according to Imamura et al., 2009. No treatment, wild type cells express AT1.03 or AT1.03RK without drug treatment; with drugs, AT1.03 or AT1.03RK expressing cells treated with CHX, 2-DG and antimycin as in (A); drug and HS, cells were treated with these three drugs and subjected to HS as in A.

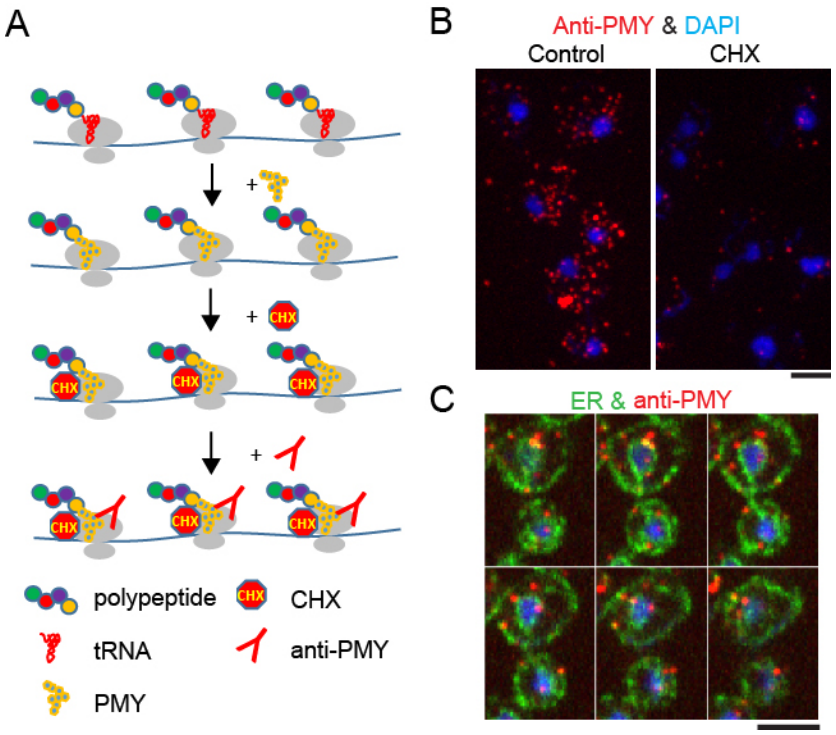

Figure 5-9. Immunostaining for active translation sites

A. Strategy for detecting active translation sites in yeast. The flow chat was modified from David A. et al, 2012. 30 s pulse-labeling of cells with puromycin (PMY) was followed by washout and CHX treatment for 2min before fixation with 4% PFA at room temperature. Active translation sites were visualized with an anti-PMY antibody. See Extended Experimental Procedures for details.

B. The max projection of a representative field of cells with or without 15 min CHX pre-treatment before PMY pulse labeling. CHX pretreatment inhibits the elongation step and reduces the nascent chain puromycylation (Jimenez et al., 1977). Scale bar: 4μm.

C. A representative Z stack of cell showing anti-PMY signal (Red), ER membrane marker (Erg11-GFP) and DAPI (blue). Scale bar: 4μm.

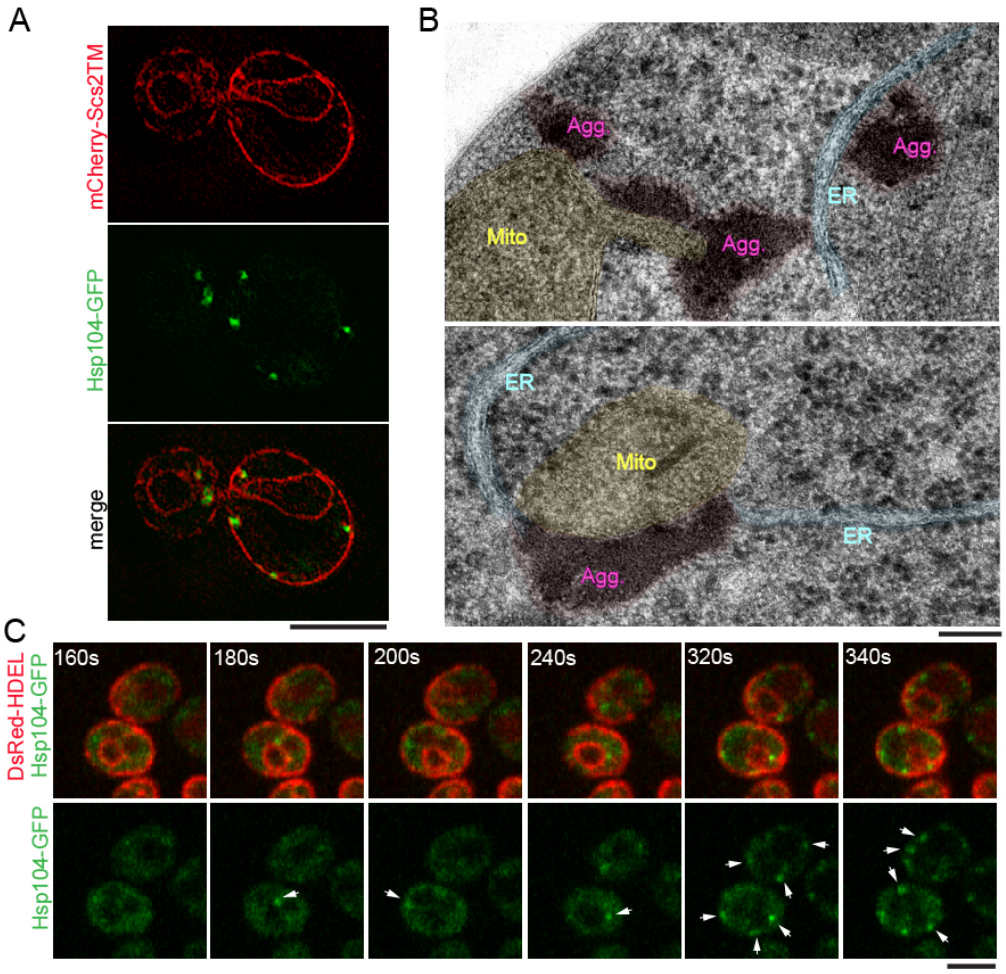

Figure 5-10. ER and mitochondria are main organelle hosts for protein aggregation (Part1).

A. Representative SIM images showing association of protein aggregates (Hsp104-GFP) with ER (mCherry) induced with 6-min HS at 42 ^{o}C.

B. Thin-sectioning EM showing association of protein aggregates (magenta) with ER (blue) and mitochondria (yellow).

C. Fast confocal time-lapse imaging of HS-induced aggregate emergence (Hsp104-GFP) on the surface of ER (DsRed-HDEL). Arrows follow emerging aggregates and the timestamps indicate the time since start of the movie.

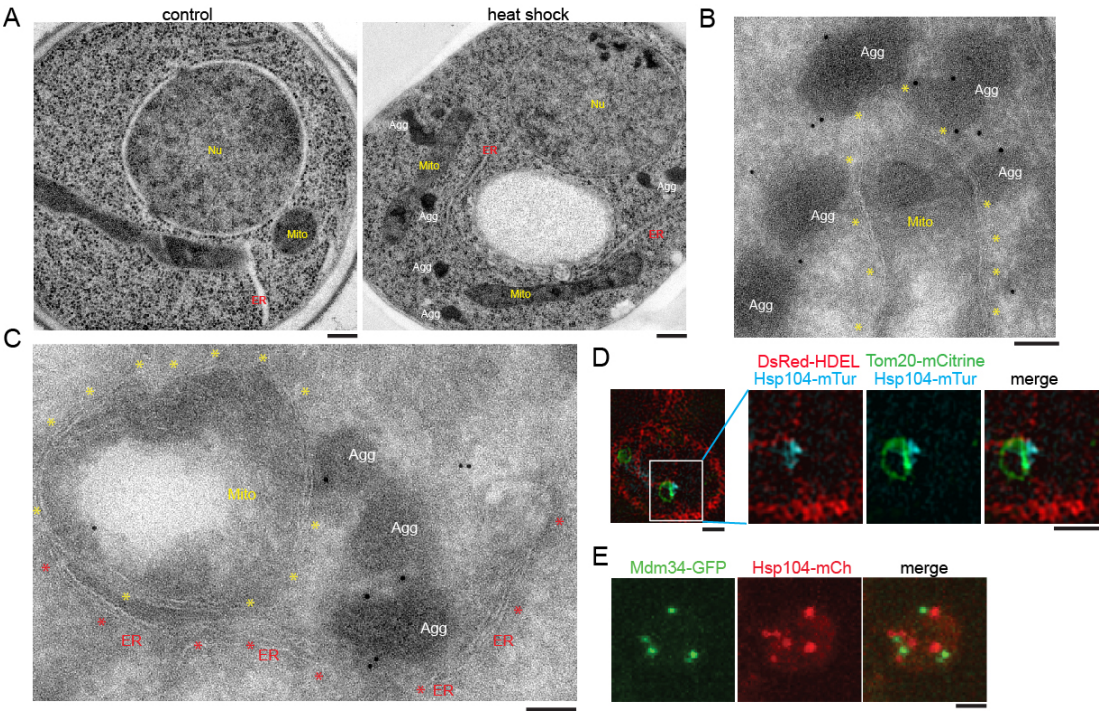

Figure 5-11. ER and mitochondria are main organelle hosts for protein aggregation

E. Representative low-magnification thin-sectioning EM images for control cells and cells treated with HS. Mito, mitochondria; Nu, nucleus; ER, endoplasmic reticulum; Agg, protein aggregates. The same labels are used in other EM images. Scale bar: 200nm.

F, G. Representative immuno-EM images for cells treated with HS. A strong enrichment of gold particles was observed surrounding the electron dense structures labeled as Agg. Colored * help outline the membrane of these organelles. Scale bar: 100nm.

H. A representative tri-color SIM image showing association of Hsp104-labeled aggregates with a site where ER (DsRed-HDEL) and mitochondria (mCitrine-tagged outer membrane protein Tom20) are closely juxtaposed. Scale bar, 1μm.

I. The max projection of a representative cell with ERMES marker (Mdm34-GFP) and aggregates (Hsp104-mCh) induced by 6 min HS at 42 ^{o}C. Scale bar: 2μm.

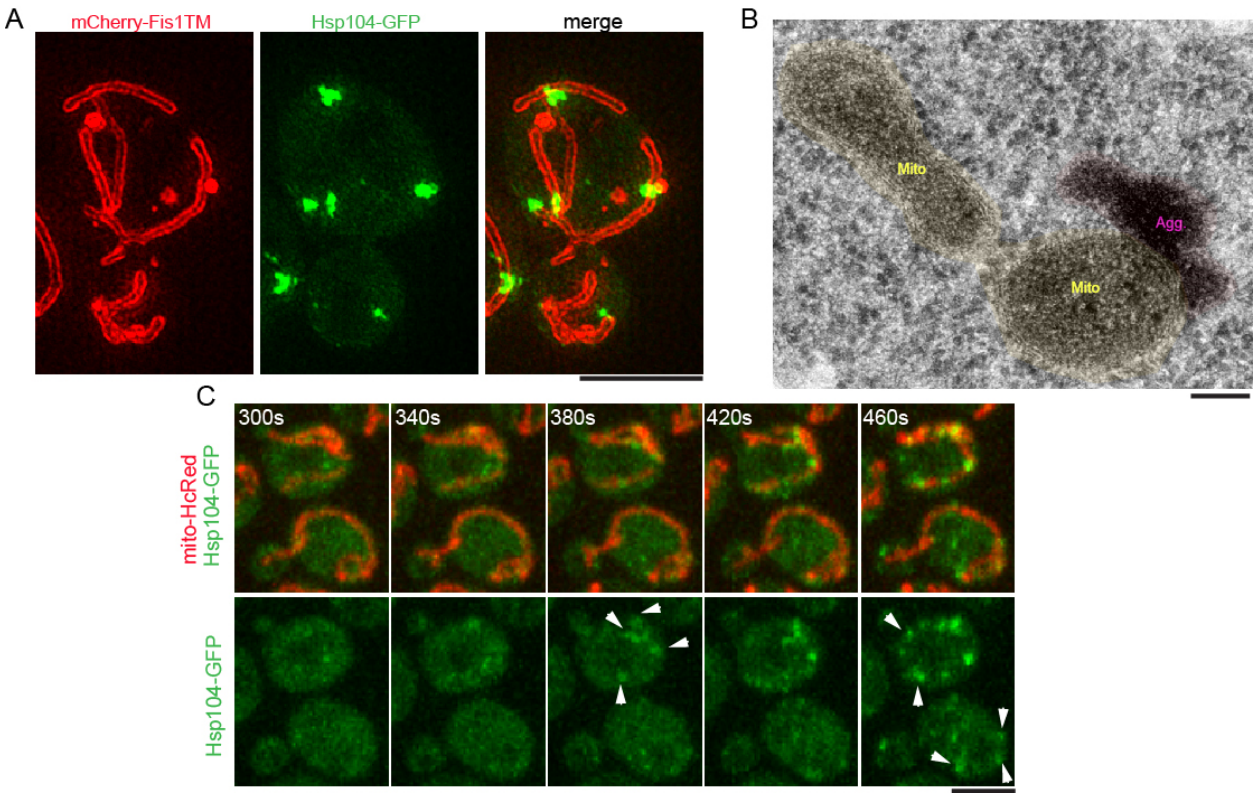

Figure 5-12. ER and mitochondria are main organelle hosts for protein aggregation (Part2).

A. Representative SIM images showing association of HS aggregates (Hsp104-GFP) with mitochondria (labeled with the mitochondria outer membrane marker mCh-Fis1TM). Scale bar: 4μm.

B. Thin-sectioning EM images showing association of protein aggregates (magenta) with mitochondria (yellow). Scale bar: 100 nm.

C. Fast confocal time-lapse images of showing HS-induced aggregates emerging from the surface of mitochondria. Arrow heads follow newly formed aggregates and the timestamps indicate time since the start of the movie. Scale bar: 4μm.

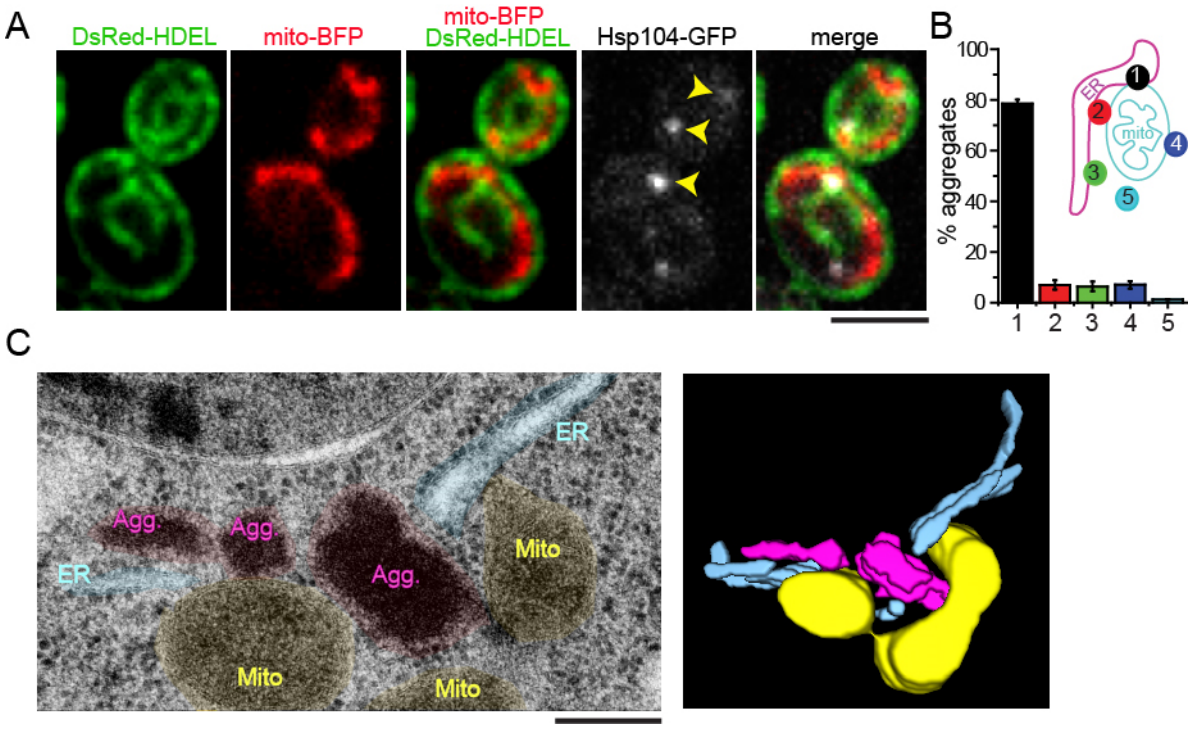

Figure 5-13. ER and mitochondria are main organelle hosts for protein aggregation (Part3).

D. Representative pseudo-colored three-channel confocal images showing simultaneous association of HS-induced aggregates (Hsp104-GFP) with ER (DsRed-HDEL) and mitochondria (mito-BFP). Images were taken after 6 min HS at 42 ^{o}C followed by 10 min recovery at 30 ^{o}C.

E. Percentage of aggregates with illustrated spatial relationship with ER and mitochondria quantified from tri-color confocal microscopy after 6 min of HS and 10 min recovery. Histogram show mean and SEM from 4 experiments of > 100 aggregates examined per experiment.

F. Left: Thin-sectioning EM showing association of protein aggregates (magenta) with ER (blue) and mitochondria (yellow) near organelle contact sites. Right: a plane from of 3D-reconstruction of serial-sections. Scale bars for B, F: 100nm. Scale bars for all other images: 4μm.

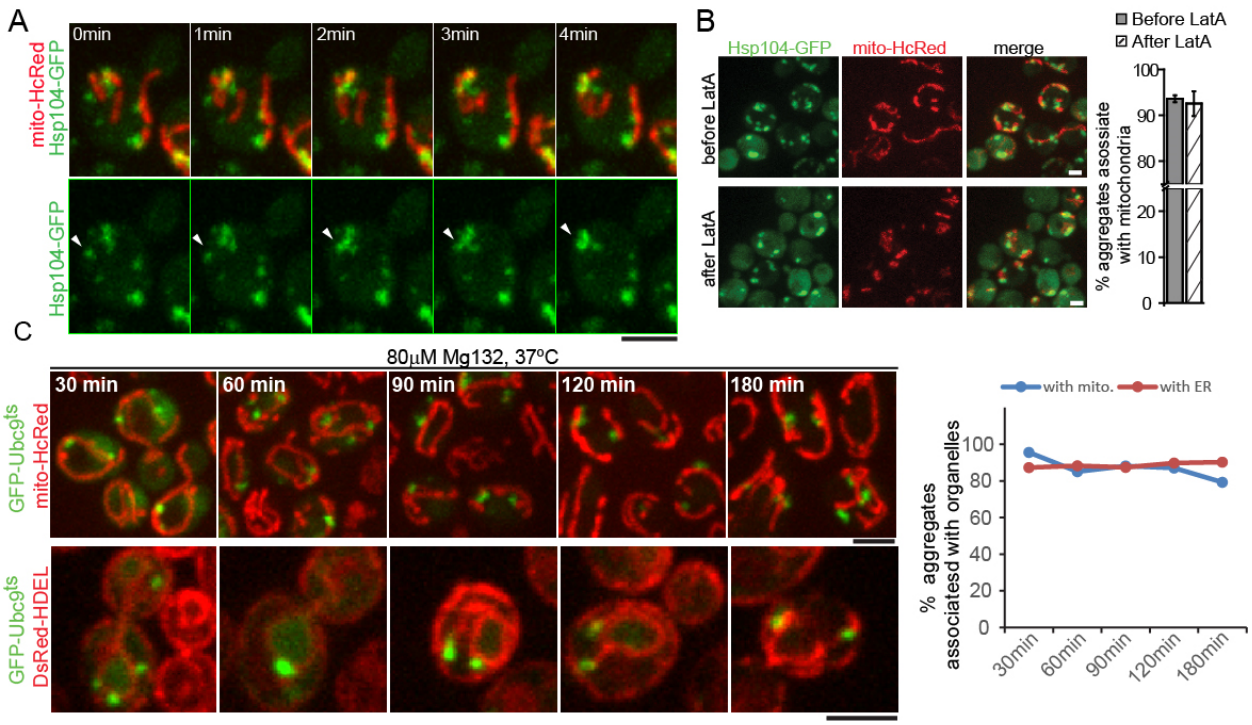

Figure 5-14. Association of protein aggregates induced

A. Montage of a time-lapse movie showing an aggregate (arrowhead) formed away from mitochondria was captured by mitochondria. Cells were heat-shocked for 6 min at 42 °C. Scale bar: 4μm.

B. Cells were heat-shocked for 30 min at 42 °C to induce aggregates and recovered for 45min to allow association of aggregates with mitochondria. 100 μM LatA was then added for 20 min to eliminate actin filaments. Shown are example of cells before and after LatA treatment and the percentage of aggregate-mitochondria association before (gray bar) and after LatA addition (hatched bar). Histograms show mean and SEM from 3 repeats of > 80 aggregates examined per repeat. Scale bars, 2μm.

C. Representative images (left) and quantification (right) of yeast cells at different time points of HS at 37 °C in the presence of Mg132, the previously used condition for IPOD and JUNQ induction (Kaganovich et al., 2008). GFP-Ubc9^{ts} expression was shut-down and Mg132 was added before the temperature shift. With mito, associated with mitochondria; with ER, associated with ER. Scale bars, 4μm.

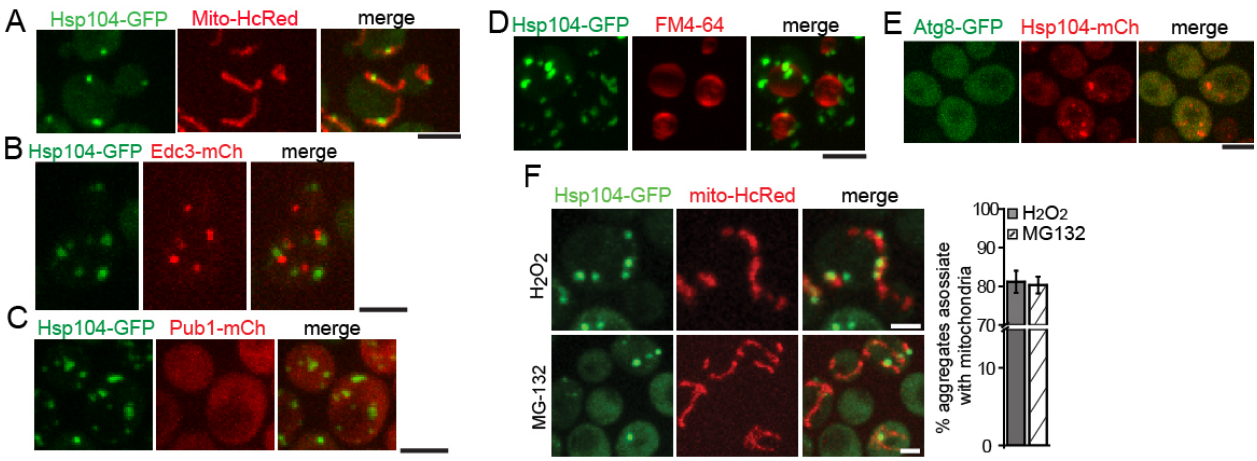

Figure 5-15. Association of protein aggregates induced under diverse stress with different cellular structures

A. Representative confocal images showing association of protein aggregates (labeled with Hsp104-GFP) with mitochondria after 6 min HS at 42 ^{o}C. Scale bar: 4μm.

B-D. Representative images of P-body (Edc3-mCh), stress body marker (Pub1-mCh), vacuole (FM4-64, Invitrogen), autophagosome marker (Atg8-GFP) and aggregates (Hsp104-GFP) induced by 6 min heat shock in 42 ^{o}C. Scale bar: 4μm.

F. Representative images and quantification showing association of protein aggregates (Hsp104-GFP) induced under stress conditions as indicated with mitochondria (mito-HcRed). Scale bar: 2μm.

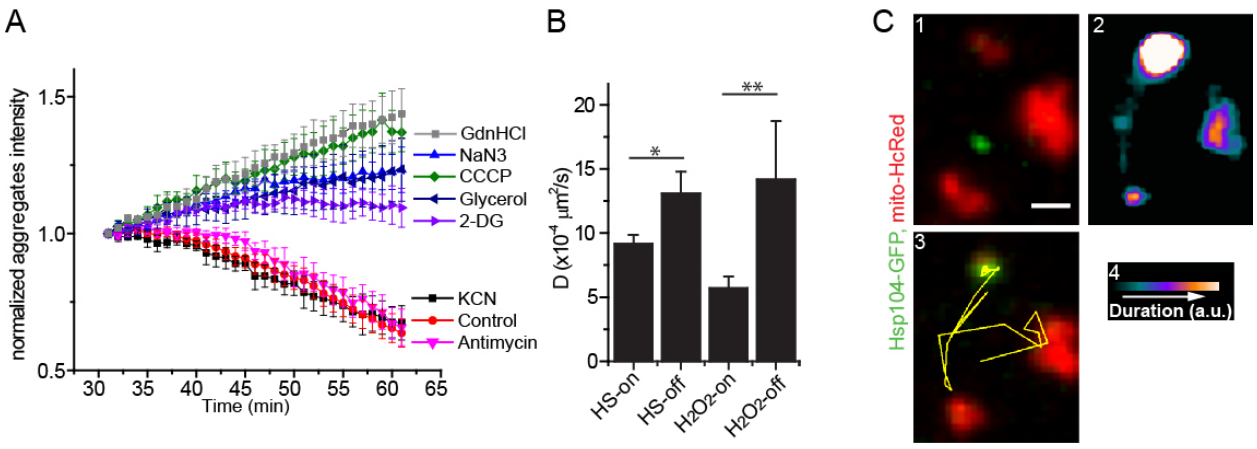

Figure 5-16. Mitochondria play key roles in the dissolution and dynamics of aggregates

A. Quantification of aggregate dissolution kinetics after HS under indicated conditions. Plots are normalized Hsp104-GFP labeled aggregate intensity as a function of time from > 3 movies of a field of cells (50-100 cells per field) starting from the 30 min frame when aggregates in the control no longer grew in brightness. GdnHCl: guanidine hydrochloride; NaN3: sodium azide; CCCP: Carbonyl cyanide m-chlorophenyl hydrazine; 2-DG: 2-deoxy-d-glucose; KCN: potassium cyanide.

B. Diffusion coefficients of aggregates between two different pools of aggregates induced by heat shock or H_2O_2. HS-on or H_2O_2-on: mitochondria-associated aggregates; HS-off or H_2O_2-off: aggregates not associated with mitochondria. > 500 aggregates from 2 movies/strain were tracked.

C. Two frames near the beginning (1) and end (2) of a time-lapse movie tracking the motion of a H_2O_2-induced aggregate (green) relative to mitochondria (red). (2) has the aggregate trajectory (yellow line) superimposed. Heat map in (3) shows duration of aggregate staying at a given location. Scale bar: 1μm.

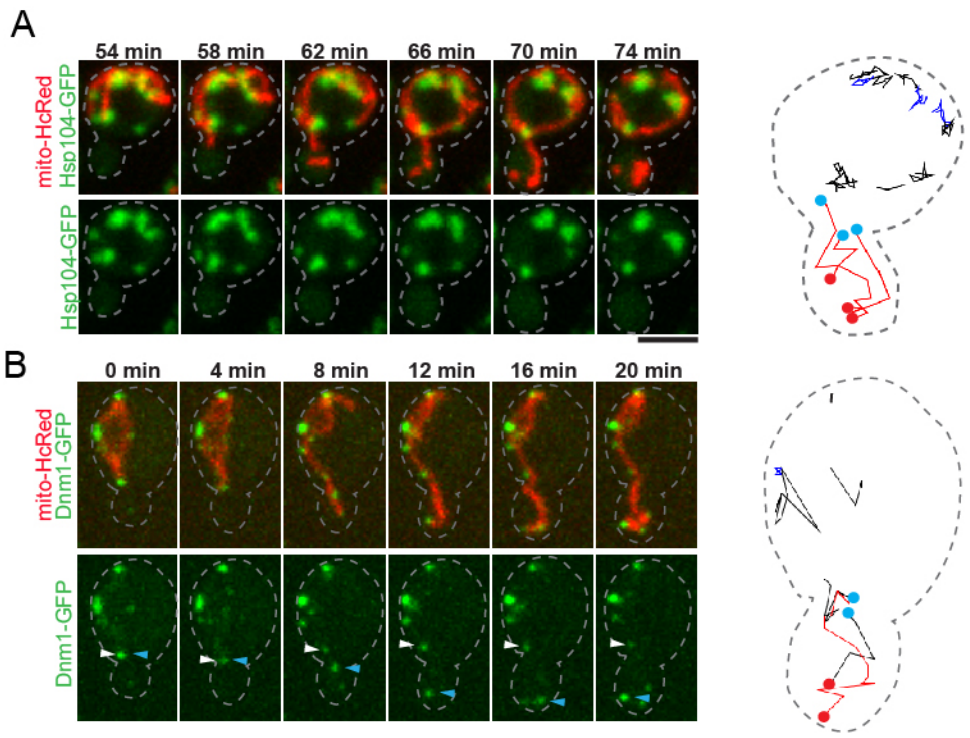

Figure 5-17. Mitochondria confine protein aggregates during asymmetric segregation (Part1)

A. Left: montage of a representative movie showing that mitochondria inheritance does not result in movement of mitochondria-associated aggregates into the bud. Right: trajectories of aggregates (all color except red lines) and mitochondrial tips (red lines) from the same movie. Blue and red dots associated with the more extended tracks represent the beginning and end of these tracks, respectively. Timestamps indicate the time since the start of the movie.

B. Left: montage of a representative movie showing that Dnm1-GFP foci in the mother remain largely stationary as mitochondria extended into the bud. Right: trajectories of Dnm1-GFP foci (black and blue lines) and mitochondrial tips (red lines) from the same movie. Blue arrowhead follows an aggregate moving with mitochondria into the bud; white arrowhead points to one staying in the mother.

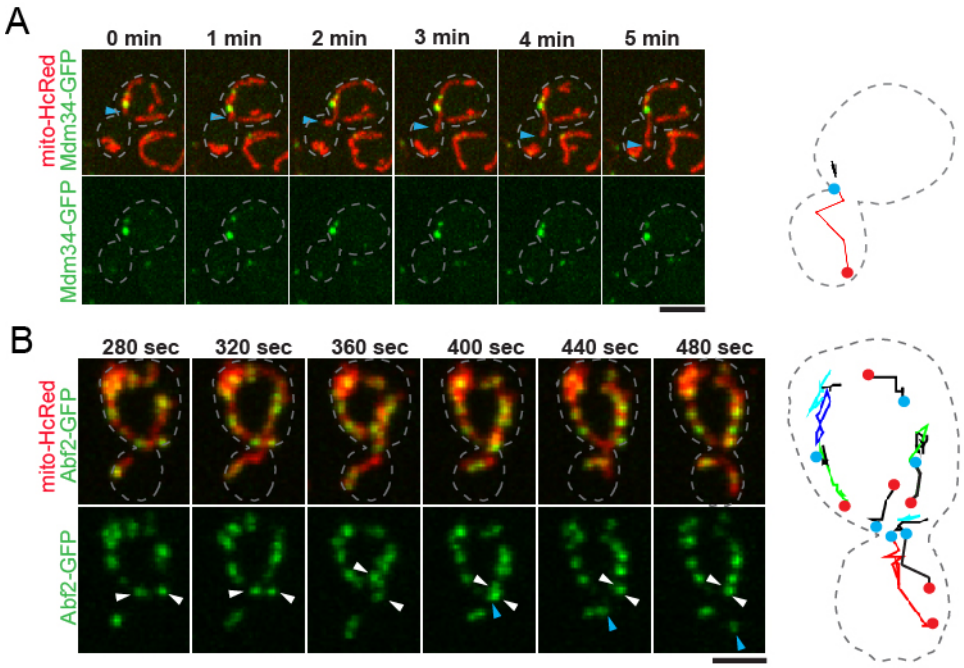

Figure 5-18. Mitochondria confine protein aggregates during asymmetric segregation (Part2)

A. Left: montage of a representative movie showing the extension of mitochondria into bud (blue arrowhead) and the relative immobility of Mdm34-GFP foci in mother cell. Right: trajectories of Mdm34 foci and mitochondrial tip from the same movie.

B. Left: montage of a representative movie showing the restrained motion of mitochondrial nucleoids labeled with Abf2-GFP within mother, contrasting extension of mitochondrial tip into bud. The two white arrowheads follow the front most (near bud neck) maternal nucleoids. Blue arrowheads follow a part of Abf2 foci that split and move into bud with mitochondria. Right: trajectories of nucleoids (all color but red lines) and mitochondrial tip (red lines) from the same movie. See also Movie S8C. All scale bars are 4μm.

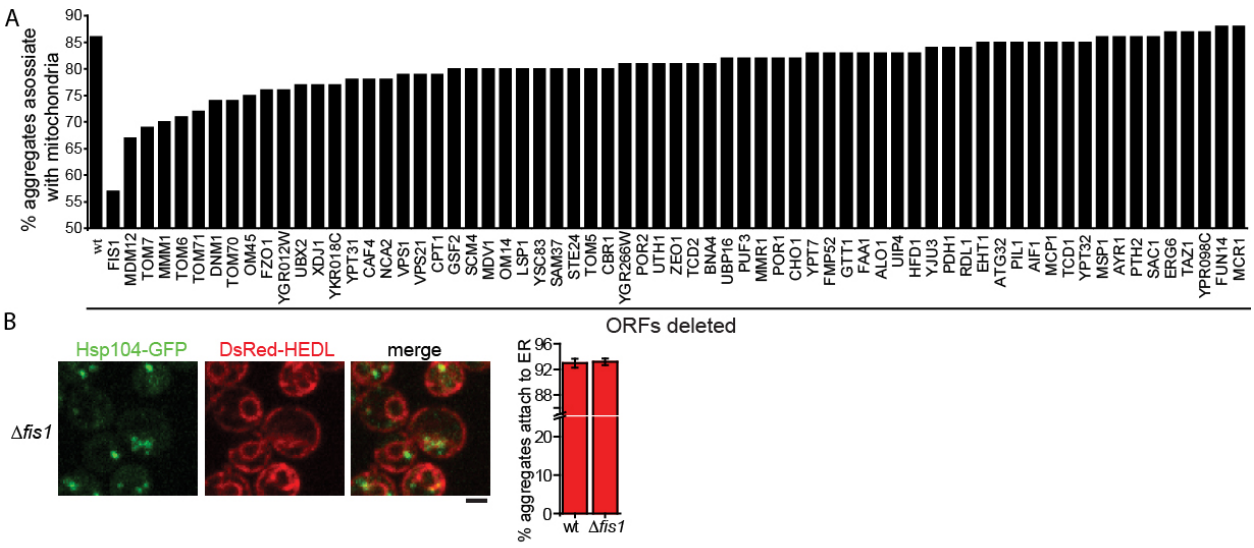

Figure 5-19. Screen for mitochondrial mutants that are defective in aggregate-mitochondria association

A. Screen result for mitochondrial outer membrane proteins important for aggregate-mitochondria association. Percent of aggregates associated with mitochondria in different mutants from the microscopy-based screen. Mutants lacking genes encoding non-essential proteins of mitochondria outer-membrane were chosen for the screen. We note that several mutant strains (*Δgem1, Δmdm10, Δmdm34, Δugo1*) were incorrect in the yeast non-essential gene library and *Δiml2* did not express mito-HcRed well.

B. *Δfis1* does not affect aggregates-ER association. Aggregates-ER association was quantified after 6 min HS. Histograms shows mean and SEM from 3 experiments of >100 aggregates examined per experiment. Scale bars, 2µm.

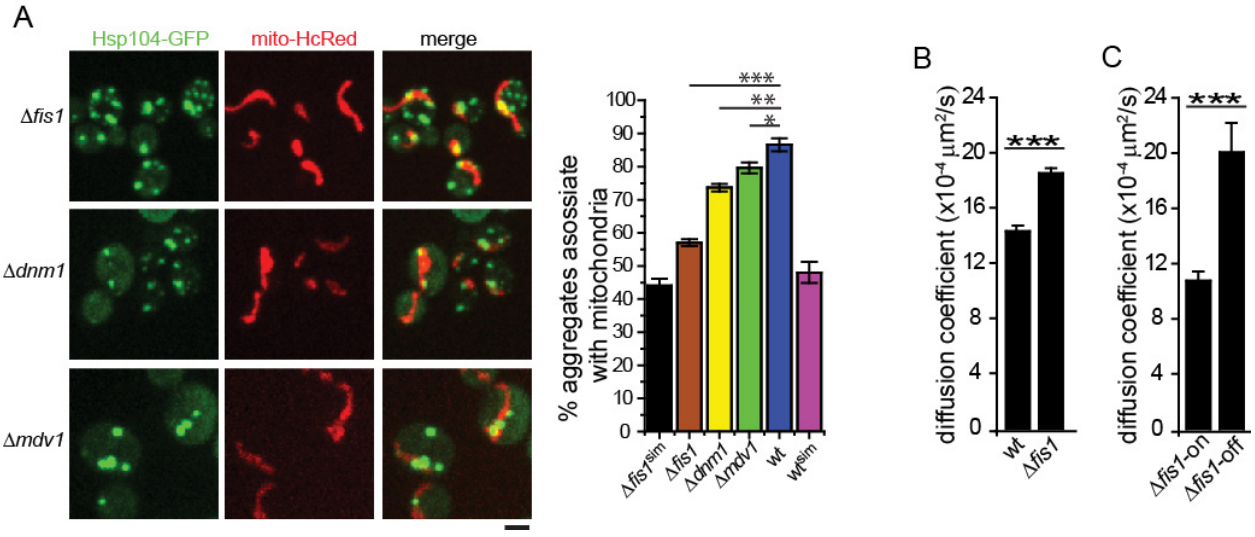

Figure 5-20. Fis1 is important for aggregate-mitochondria association and aggregate dynamics.

A. Representative images and quantification of aggregates-mitochondria colocalization in *Δfis1*, *Δdnm1* and *Δmdv1* cells. *Δfis1*^{SRD} and wt^{SRD}: colocalization from random distribution (SRD) simulated using parameters measured from respective cells. Histogram show mean and SEM from 3-4 experiments with >150 aggregates per experiment. Scale bars: 2µm.

B. Average diffusion coefficients of all aggregates in wt and *Δfis1* mutant. Histogram show mean and SEM of diffusion coefficient calculated from > 100 aggregate trajectories per strain.

C. Diffusion coefficients of aggregates associated (*Δfis1*-on) or not-associated with mitochondria (*Δfis1*-off) in *Δfis1* cells. Histogram show mean and SEM from > 3 movies with > 50 budding cells per movie examined.

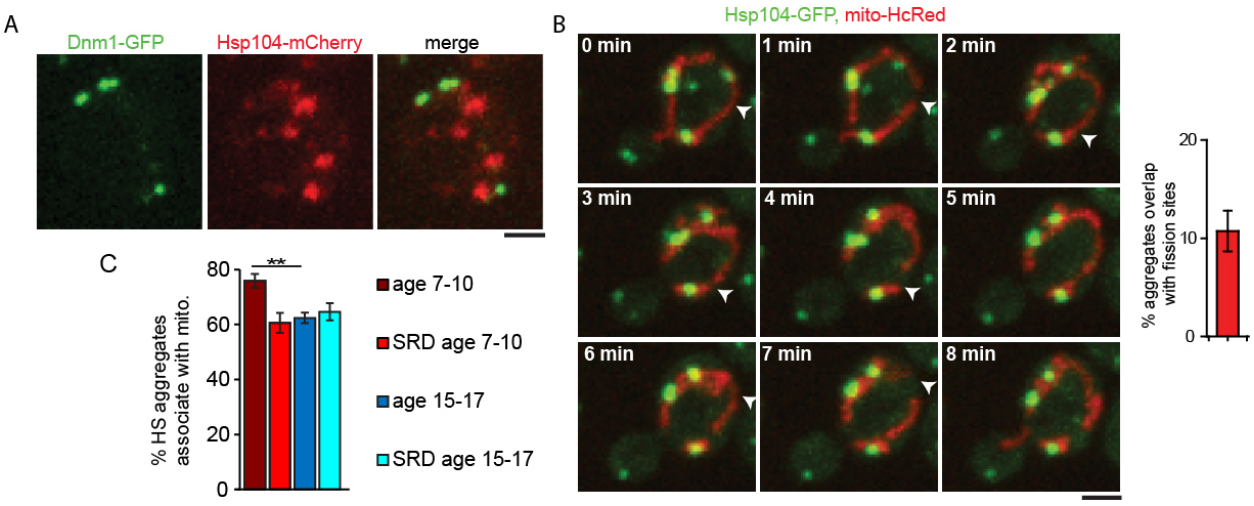

Figure 5-21. Aggregates do not associate with mitochondrial fission sites

A. Representative images and quantification showing a lack of strong colocalization of HS-induced protein aggregates (Hsp104-mCherry) with Dnm1-GFP foci. Scale bars, 2µm.

B. Example of mitochondrial fission sites and percent of aggregates overlapping with fission sites. Arrowheads point to fission events. Right histogram shows mean and SEM of percent of aggregates that overlapped with fission sites. More than 80 fission events per movie were scored and three movies were analyzed. Scale bars, 2µm.

C. Quantification showing gradual decline of mitochondrial association of HS-induced Hsp104-containing aggregates in cells with increasing replicative age. Histograms show mean and SEM of percent aggregates associated with mitochondria from at least 3 experiments with >100 aggregates examined per experiment. SRD age 7-10 and SRD age 15-17: colocalization from simulated random distribution between aggregates and mitochondria using parameters measured from the aged cells.

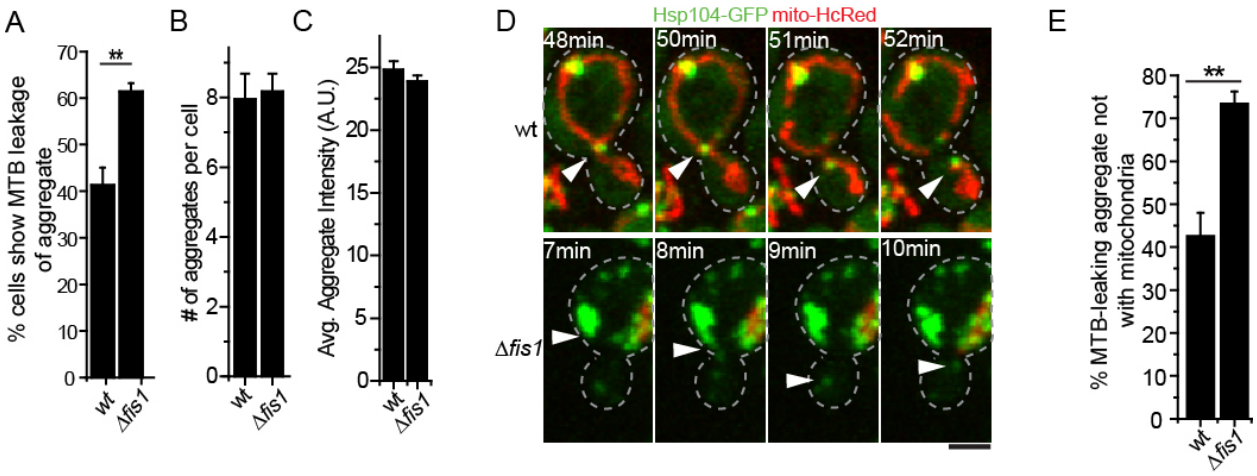

Figure 5-22. Association with mitochondria contributes to mother retention of aggregates.

A. Percentage of cells showing at least one MTB aggregate leakage among all budding cells observed in time-lapses movies. Histograms show mean and SEM from at least three movies.

B. C. Quantification of aggregate number per cell (B) and size (average intensity of aggregates) (C) in *Δfis1* and wt. Histograms show mean and SEM from at least three movies.

D. Montage showing how majority of aggregate leakage occurred in wt and *Δfis1* cells. In wt cells (top), aggregates that leaked into the bud were usually associated with bud-bound mitochondrial extension; in *Δfis1*cells, the majority of leaked aggregates were not associated with bud-bound mitochondrial extension. Arrowheads point to example MTB aggregates. Scale bars: 2μm.

E. Percentage of MTB-leaking aggregates that were not associated with bud-bound mitochondrial extension among all MTB-leaking aggregates in wild type and *Δfis1*. Histogram show mean and SEM from at least three movies with ~30 MTB leakage events per movie observed.

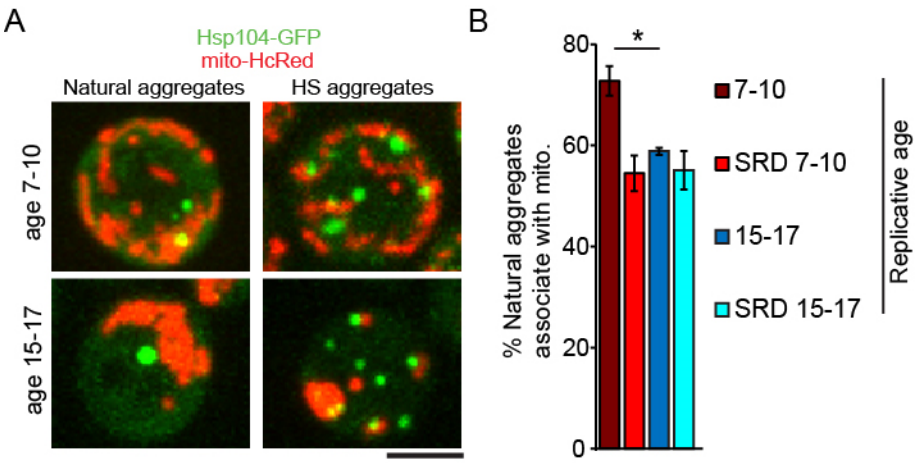

Figure 5-23. Aggregate-mitochondria interaction in aging cells

A. Example images of natural (left panels) or HS-induced (right panels) aggregates, labeled with Hsp104-GFP, in relationship to mitochondria in cells of 7-10 or 15-17 generations old. Scale bar, 4µm.

B. Quantification showing a gradual decline of mitochondrial association of naturally occurring Hsp104-containing aggregates in cells with increasing replicative age. Histograms show mean and SEM from at least 3 experiments with >100 aggregates examined per experiment. SRD: aggregate-mitochondria colocalization from simulated random distribution using parameters measured from the aged cells.

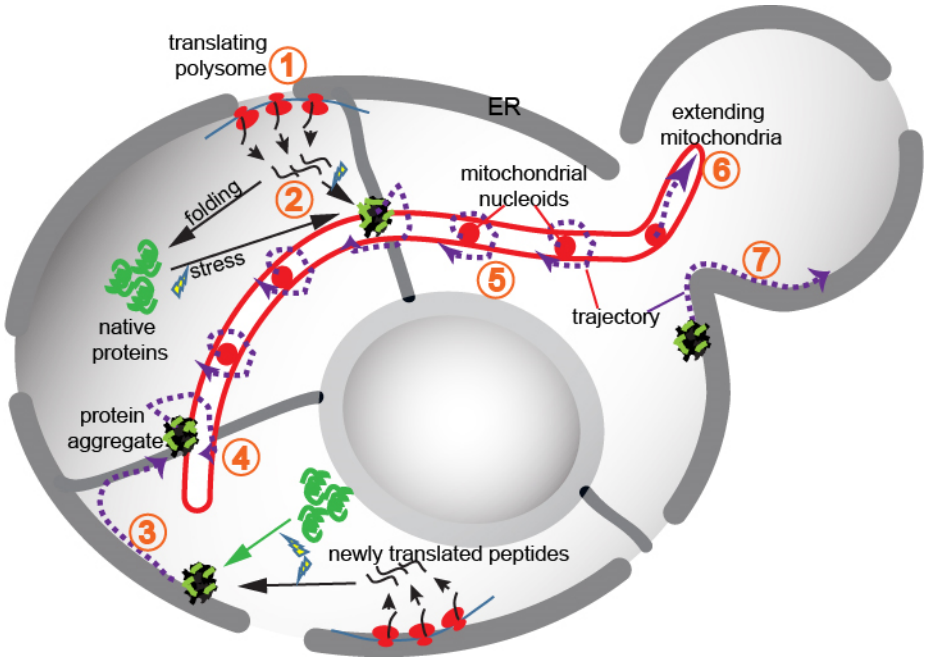

Figure 5-24. Model for organelle-based formation and segregation of protein aggregate

1) Active polysomes, which are enriched on ER, provide the newly translated peptides that either fold into native proteins or misfold and aggregate on ER surface, a process exaggerated under stress. 2) Native proteins aggregate to sites initiated by newly translated peptides on ER, frequently close to mitochondria. 3) Aggregates formed away from mitochondria move along ER and are eventually captured by mitochondria. 4) Association of aggregates at site of ER-mitochondria juxtaposition constrains the mobility of aggregates. 5) During bud formation, stable anchorage of mother mitochondria is also reflected by constrained motion of many mitochondrial components such as nucleoids. 6) Mitochondria that rapidly extend into the bud are likely to acquire these components from either the bud neck region or new assembly. The combination of (5) and (6) explains retention of protein aggregates in the mother during mitochondria inheritance. 7) Disruption of aggregate-mitochondria association by certain mutations or during aging promotes spreading of aggregates into the bud.

CHAPTER SIX: IMPORT OF MISFOLDED PROTEINS INTO MITOCHONDRIA FOR CYTOSOLIC PROTEOSTASIS

Summary

Eukaryotic cells utilize an array of quality control mechanisms to maintain a stable and functional proteome. Loss of protein homeostasis (proteostasis) underlies aging and the progression of neurodegenerative diseases characterized by the deposition of protein aggregates, which is often accompanied by mitochondrial dysfunction. Here we show that mitochondria play a direct role in proteostasis through importing and degradation of misfolded cytosolic proteins. Protein aggregates purified from the cytosol are comprised of both cytosolic proteins and proteins destined for mitochondria. The dissolution of protein aggregates *in vivo* requires mitochondrial import. Surprisingly, in addition to importing mitochondrial proteins, misfolded cytosolic proteins were also imported into mitochondria under both physiological and stress conditions. Import of aggregated proteins under stress is facilitated by the association with mitochondria. Mitochondrial proteases are required for fast dissolution of aggregates and disappearance of imported misfolded proteins.

Introduction

Protein aggregation is a widespread phenomenon in degenerative diseases. Curiously, many of the protein-aggregation diseases, such as Alzheimers, Amyotrophic Lateral Sclerosis (ALS), and Huntington's disease, are also linked with mitochondrial dysfunction. It remains unclear whether and how these major disease manifestations may be linked. It is a common belief that the accumulation of

aggregates enables the consolidation of misfolded or damaged proteins when there is an imbalance in their production and degradation (Arrasate et al., 2004). Cells manage aggregated proteins through a variety of mechanisms that include dissolution, organelle-based retention, and autophagy (Tyedmers et al., 2010a). In asymmetrically dividing yeast cells, protein aggregates formed under stress or during aging are preferentially retained by the mother cell through tethering to mitochondria, while the disaggregase Hsp104 actively dissociate aggregated proteins to garget them for refolding or degradation.

Result

To further investigate the dynamics of aggregated proteins during cellular proteostasis, we developed an affinity-based method, using GFP and Flag-tagged luciferase (Luci-GFP-3xFlag), an aggregation substrate due its inefficient folding in yeast, to purify protein aggregates with the goal of identifying their components by mass spectrometry. After a procedure involving sucrose-gradient fractionation of cytosolic extracts followed by anti-Flag affinity pull-down (Fig.6-1), proteins associated with aggregates were identified by using quantitative Multi-Dimensional Protein Identification Technology (MudPIT) comparing the experimental strain with the control lacking the Flag tag. 330 specific proteins were significantly enriched in aggregates formed after heat shock at 42 ^{o}C for 30 min. This analysis was applied to aggregates purified from cells with increasing time of heat shock and revealed that > 90% aggregated proteins were shared chronologically (Fig. 6-2D). This suggests that the accumulation of aggregates during heat shock comes from gradual aggregation of the same group of proteins. More than 50% of the top 100 hits were verified microscopically by using GFP tagging as forming visible aggregates after heat shock (Fig. 6-2B). Interesting, among the aggregated proteins identified in our study, more than 20% were previously annotated as mitochondrial proteins (Fig. 6-2C, D). A similar

percentage of mitochondrial protein was observed in aggregates purified after H_2O_2 treatment. These results document an enrichment of mitochondrial proteins in extra-mitochondrial (cytosolic) aggregates.

Previous studies found that mitochondria can bind cytosolic protein aggregates and accumulate some non-mitochondrial proteins that are known to form aggregates in the neurodegenerative diseases. Given that a significant portion of aggregates are mitochondrial proteins, we investigated whether mitochondrial import contribute to the dissolution of protein aggregates. To test this, protein aggregates were induced by heat shock and visualized with Hsp104-GFP, the disaggregase that binds aggregates, or Luciferase-GFP (Luc-GFP). We previously showed that such heat-induced aggregates dissolve over time during recovery at the normal temperature (23 ^{o}C). Supporting our hypothesis, cells treated with chlorophenylhydrazone (CCCP), which disrupts mitochondrial membrane potential required for import, failed to dissolve the heat-shock aggregates (Fig.6-3A, B; note that cycloheximide (CHX) was included to prevent *de novo* aggregate formation caused by CCCP). To more specifically disrupt microchondrial import, we used the temperature-sensitive (ts) mutation of *TIM23* (*tim23*^{ts}), encoding the essential subunit of the import complex. *tim23*^{ts} was inactivated during heat shock and delayed aggregate dissolution during the recovery compare to the wild-type strain (Fig. 6-3C). In fact, *tim23ts* cells had normal or even higher membrane potential visualized by the dye Tetramethylrhodamine (TMRM) (Fig.6-3D). These results demonstrate that the dissolution of cytosolic protein aggregates requires active mitochondrial import.

In budding yeast, Hsp104 has been shown to be indispensable for aggregate dissolution. Hence, we investigated the crosstalk between Hsp104 and mitochondrial import on aggregate dissolution. We first confirmed that Hsp104 is essential for aggregate dissolution in the cells experienced 30min heat shock. Surprisingly, *Δhsp104* cells could dissolve aggregates induced by short heat shock (Fig.6-4). These aggregates tightly associated with mitochondria during dissolution and mitochondrial import was required for this Hsp104 -independent dissolution (Fig.6-4). Furthermore, translational inhibition with

CHX dramatically increased this Hsp104-independent dissolution. Even though we cannot rule out the possibility that chaperones other than Hsp104 act upstream of mitochondrial import, yet these results demonstrate that mitochondrial import contributes to the aggregate dissolution independently from Hsp104.

The specificity of mitochondrial import comes from the selectively extended dwelling time of mitochondrial precursors through their binding with the receptors of mitochondrial outer membrane. The binding and dissolution of protein aggregates on the surface of mitochondria may hijack this importing mechanism by acting as receptors for misfolded proteins and enable mitochondria to import aggregated peptides nonspecifically (Fig.6-5A). Thus, the identification of a significant amount of non-mitochondrial protein in the aggregates allowed us to investigate whether the formation of mitochondrial-bound aggregates also facilitate the import of non-mitochondrial proteins. We employed the split GFP system where the polypeptide containing the first 10 β strands of GFP (GFP1-10) was targeted to mitochondria through linkage with a mitochondrial matrix-targeting peptide (MTS), while the 11th β strand of GFP (GFP11) was linked with an aggregate protein (Fig.6-5A). Of note, mCherry was also included in the first construct, as MTS-mCherry-GFP1-10, in order to visualize its proper targeting to mitochondria. As predicted, most of these non-mitochondrial proteins, exemplified by Prt3p, did not show split GFP signal as did by mitochondrial protein Gpx5p (Fig.6-5B). We next examined several non-mitochondrial proteins found in aggregates by the proteomics analysis (Fig.6-6, 6-9). Before heat shock, these proteins tagged with GFP11 showed very limited mitochondria GFP signal; however, they gained access to the mitochondrial matrix, as indicated by the increase of GFP fluorescence, after stress in a mitochondrial import dependent manner as CCCP treatment abolished this effect (Fig.6-6). To investigate the mechanism further, we focused on the LucSM as a model protein. Aggregate formation seemed to facilitate this process as many cytosolic proteins that were not found in the aggregates, such as Mcm6p,

Not3p and Ppt1p, also failed to show mitochondrial split GFP signal after stress (Fig.6-7). Interestingly, CHX treatment during heat shock, which inhibits aggregate formation, blocked the stress-induced mitochondrial translocation of misfolded proteins (fig. 6-6B). The aggregate-mitochondria association was also critical for the import of aggregated non-mitochondrial proteins as demonstrated by the reduction of split GFP signal in the *Δfis1* cells, where the aggregate-mitochondria association was partially disrupted (Fig.6-8A).

The split GFP signal of the aggregation substrates gradually disappeared in a time course consistent with the dissolution of cytosolic aggregate (Fig.6-6). These observations suggest that the aggregation substrates imported into mitochondria are gradually degraded. To further elucidate this mitochondria-based proteostasis mechanism, we tested individual deletions of 14 genes encoding mitochondrial proteases, processing peptidases or oligopeptidases for their effects on the disappearance of the split GFP signal in mitochondria or dissolution of heat-induced cytosolic aggregates. Compare to wild type, most of the deletion strains showed increased split GFP signal for LuciSM after heat shock and delayed disappearance (Fig.6-8C, D). These mutants also showed slower dissolution of cytosolic aggregates labeled by HSP104-GFP, among which deletion of *PIM1*, encoding a LON protease, and *IMP2*, encoding a mitochondrial inner membrane peptidase, showed the most significant disturbance (Fig.6-8B). These results suggest that the mitochondrial proteolysis system plays a role in the dissolution of cytosolic aggregates likely through degradation of imported misfolded or damaged proteins

The above findings revealed a direct role for mitochondrial import and proteases in cytosolic proteostasis under stress; however, some of the aggregate proteins that was identified in our study and in also a previous study dubbed as super aggregators, referring to their tendency to aggregate without stress, showed prominent split GFP signal in mitochondrial even without heat shock (Fig.6-9A, B). This suggests that mitochondria import and degrade unstably folded cytosolic proteins even under

physiological conditions. To test this more directly, we fused GFP11 to wild-type luciferase (Luci-WT), and two mutants, Luci-SM and Luci-DM, with increasing structural instability due to the presence of single (SM) and double (DM) mutations, respectively. Some split GFP signal was found for all three proteins in mitochondria in normally growing cells, but the amount of signal increased with increasing structural instability of luciferase (Fig.6-9D, 6-6B, 6-10). Interestingly, split GFP signal for the instable cytosolic proteins was much higher in cells with compromised activity of Hsp70s (Fig.6-9C, 6-8D). As misfolded proteins are also targeted by chaperones, these observations suggest that this mitochondria-mediated protein homeostasis (mitostasis) may complement chaperones in handling misfolded cytosolic proteins under both physiological and stress conditions.

Discussion

Taken together, our results demonstrate that mitochondria are guardians of cytosolic proteostasis through importing and degradation of misfolded proteins under both physiological and stress conditions, in addition to physically tethering protein aggregates for asymmetric retention during cell division. We coin this mechanism of proteome quality control mito-stasis. This mechanism may be particular crucial under stress conditions when the amount of damaged proteins in the cytosol overwhelms chaperone and the proteasome systems, such that the formation of proteins aggregates captured on the surface of mitochondria facilitates the import of aggregated polypeptides into mitochondria to enable degradation by mitochondrial proteases. Our findings provide a potential explanation for the link between protein aggregation and mitochondrial defects in degenerative diseases. The gradual decline in mitochondrial activity in aging or disease could lead to loss of membrane potential, or import or degradation capacity, which would impede proteostasis in the cytosol leading to accumulation of protein aggregates. Alternatively, defects in other proteostasis mechanisms, such as those involving chaperones or the

proteasome, could result in an overabundance of misfolded cellular proteins inside the mitochondria, thus overwhelming the mitochondria and leading to mitochondrial dysfunction. We envision that these two opposing processes could in fact coexist, forming a positive feedback loop to precipitate a stable disease state and continual degeneration.

Figures

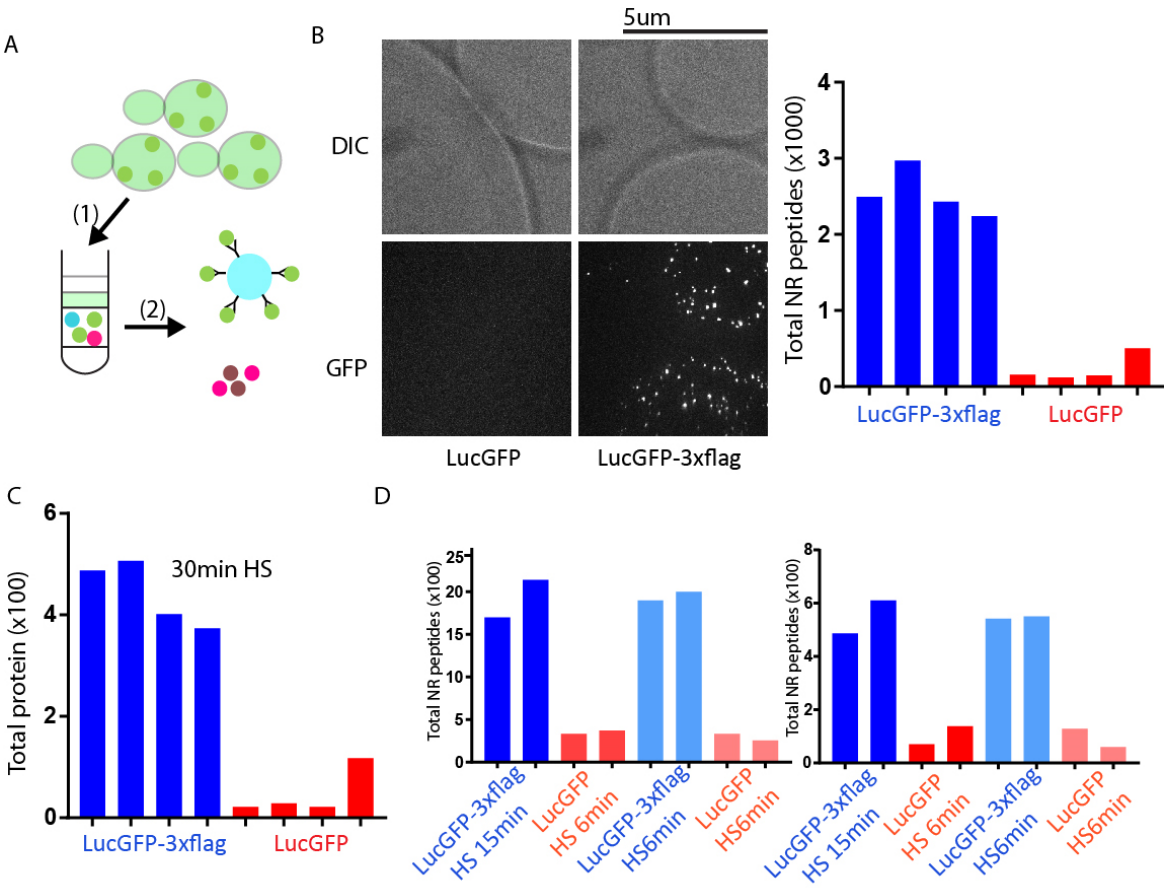

Figure 6-1. Purification and mass spectrum analysis of protein aggregates

A. Pipeline of aggregate purification. Yeast cells expressing LucGFP-3xFlag or LucGFP were stressed by either heat shock or H_2O_2 to induce aggregate formation decorated by LucGFP (green dots). Cell lysate were then applied to sucrose gradient centrifugation to separate LucGFP monomers from the LucGFP aggregates. The fraction enriched with protein aggregates went through the anti-flag column to separate LucGFP-3xflag aggregates (green dots) from other cellular debris (colored dots).

B. Left: Representative images of anti-flag resin and associated aggregates in different experiments. Right: number of peptides identified by mass spectrum of four independent repeats of both LucGFP-3xFlag (Blue) and LucGFP (Red). Scale bar, 5um.

C. Number of proteins identified by mass spectrum of four independent repeats of both LucGFP-3xFlag (Blue) and LucGFP (Red).

D. Number of peptides and proteins identified by mass spectrum of four independent repeats of both LucGFP-3xFlag (Blue) and LucGFP (Red).

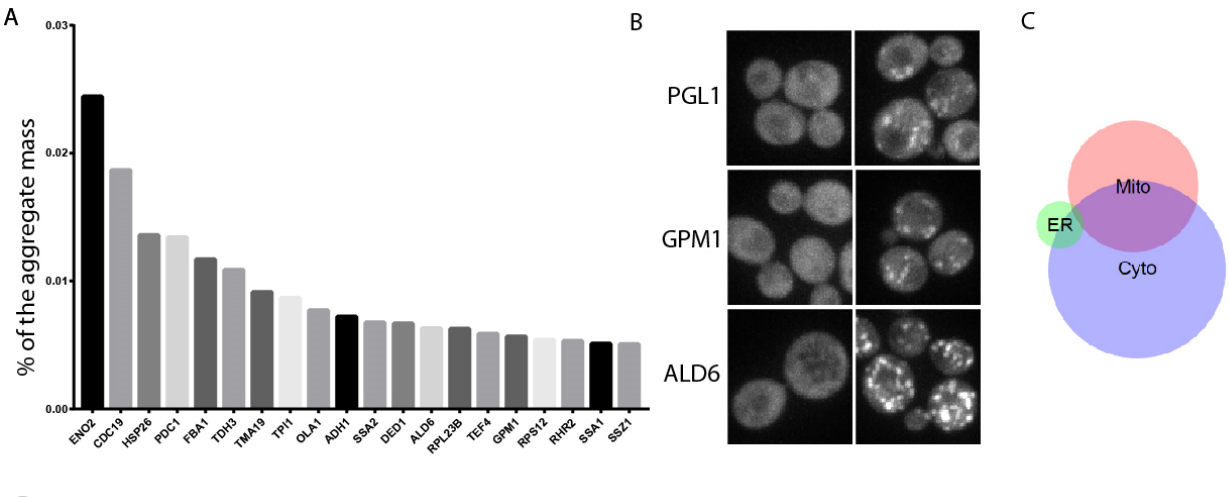

D

	6min HS	15min HS	30min_p2	30min_p1	H2O2_40min	H2O2_70min
specific proteins	396	369	436	562	108	163
Total Overlap with 30minP1(proteins)	315	308	368	562	73	107
percentage overlap with 30min P1	0.92118	0.93036	0.94918	1	0.73344	0.70676
Mitochondrial proteins	82	72	87	122	16	28

Figure 6-2. Mass spectrum analysis of protein aggregates

A. The top 20 hits identified by mass spectrum.

B. Representative images of the hits that form aggregates after 30min heat shock. Scale bar, 5um.

C. Relative amount of mitochondrial protein, cytosolic protein and ER proteins identified in the aggregates.

D. Overlapping hits between aggregates induced under different conditions. Specific proteins were counted by extract the common proteins found in both LucGFP-3XFlag samples and their corresponding LucGFP control samples.

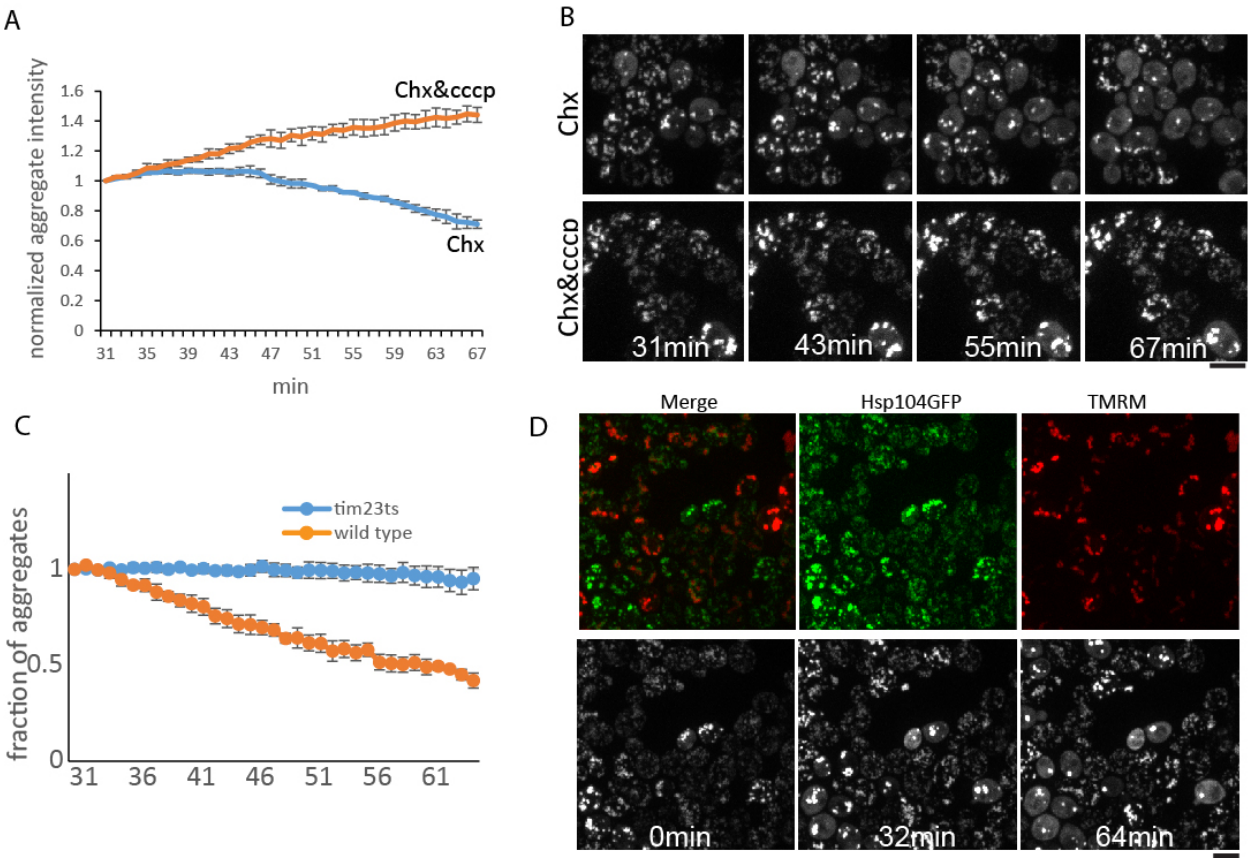

Figure 6-3. Mitochondrial import is important for aggregate dissolution *in vivo*.

A. Quantification of aggregate dissolution in wild type strain with/without CCCP treatment. CHX is included to preclude further aggregation induced by CCCP treatment. Shown are plots of total aggregate intensity as a function of time from time-lapse movies starting from the 30 min frame when aggregates in wild-type no longer grew in brightness. Shown are means and SEM of at least 3 movies for each condition.

B. Representative images of the cells undergo aggregate dissolution in (A). Scale bar, 5um.

C. Quantification of aggregate dissolution following the same method as in (A) in wild-type (orange) and *tim23*^{ts} cells (Blue). Shown are means and SEM of at least 3 movies for each condition.

D. Representative images of *tim23*^{ts} cells from the movies used in (C). TMRM (red) was used to demonstrate the membrane potential of these cells. Scale bar, 5um.

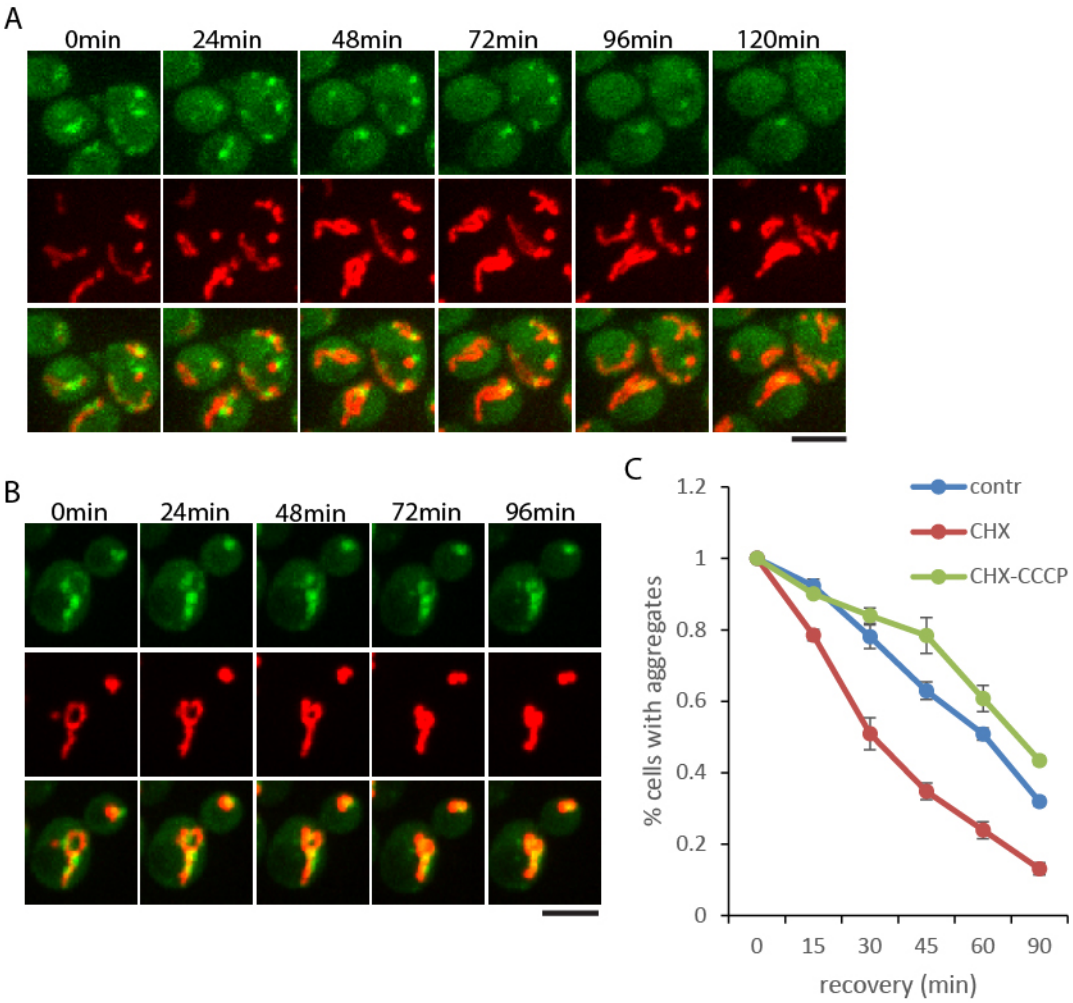

Figure 6-4. Mitochondrial import is important for Hsp104-independent aggregate dissolution *in vivo*

A. Selected frames from a representative movie showing dissolution of aggregates in *Δhsp104* cells. Aggregates were induced by 6.5min heat shock and labeled by LucYFP. The same strain and heat shock condition were used in (A) and (B). Scale bar, 5um.

B. Selected frames from a representative movie showing lack of aggregate dissolution in *Δhsp104* cells treated with CCCP. Scale bar, 5um.

C. Quantification of aggregate dissolution of *Δhsp104* cells under the indicated conditions. Shown are mean and SEM of normalized aggregate intensity as a function of time from >3 movies. Green, cells treated with CHX and CCCP; blue, control cells without drugs; red, cells treated with CHX.

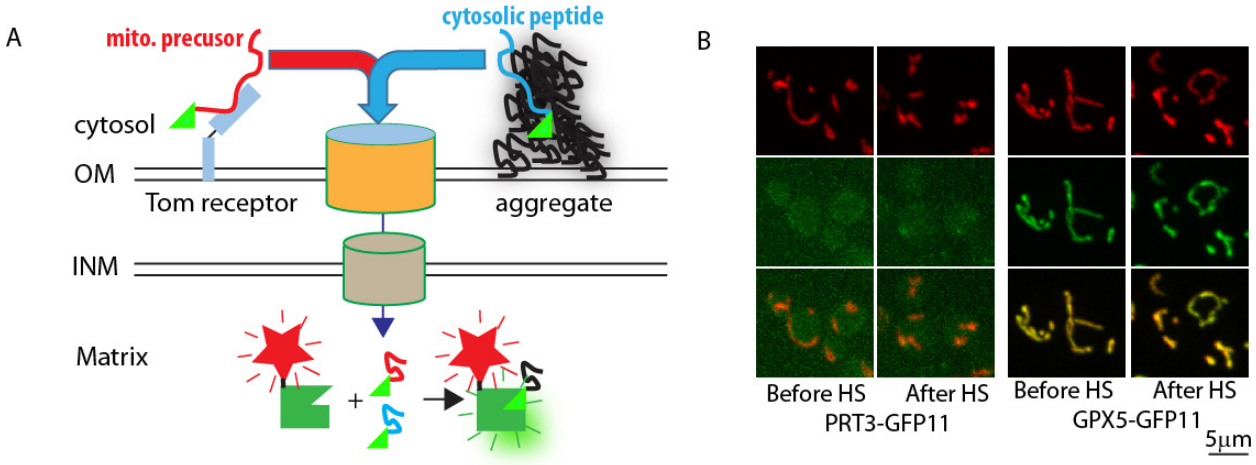

Figure 6-5. Illustration and controls for the splitGFP assay.

A. Schematic diagram showing the possible fate of misfolded peptides in the mitochondria-associated aggregates. The selectivity of mitochondrial import is largely implemented by the Tom receptors which preferentially bind and kinetically restrict mitochondrial precursors on the surface of mitochondria. Similarly, mitochondria-association of aggregates nonspecifically restrict the denatured cytosolic proteins to the mitochondrial surface and facilitate their import. The localization of specific protein labeled with GFP fragment (GFP11, light green triangle) can be traced by the splitGFP assay in which the complement GFP fragment (GFP1-10) fused to mCherry (red star) is expressed in the mitochondrial matrix.

B. Negative and positive controls for the splitGFP assay. PRT3 is a cytosolic protein that not found in the aggregates while GPX5 is a mitochondrial proteins localized in the matrix. Scale bar, 5um.

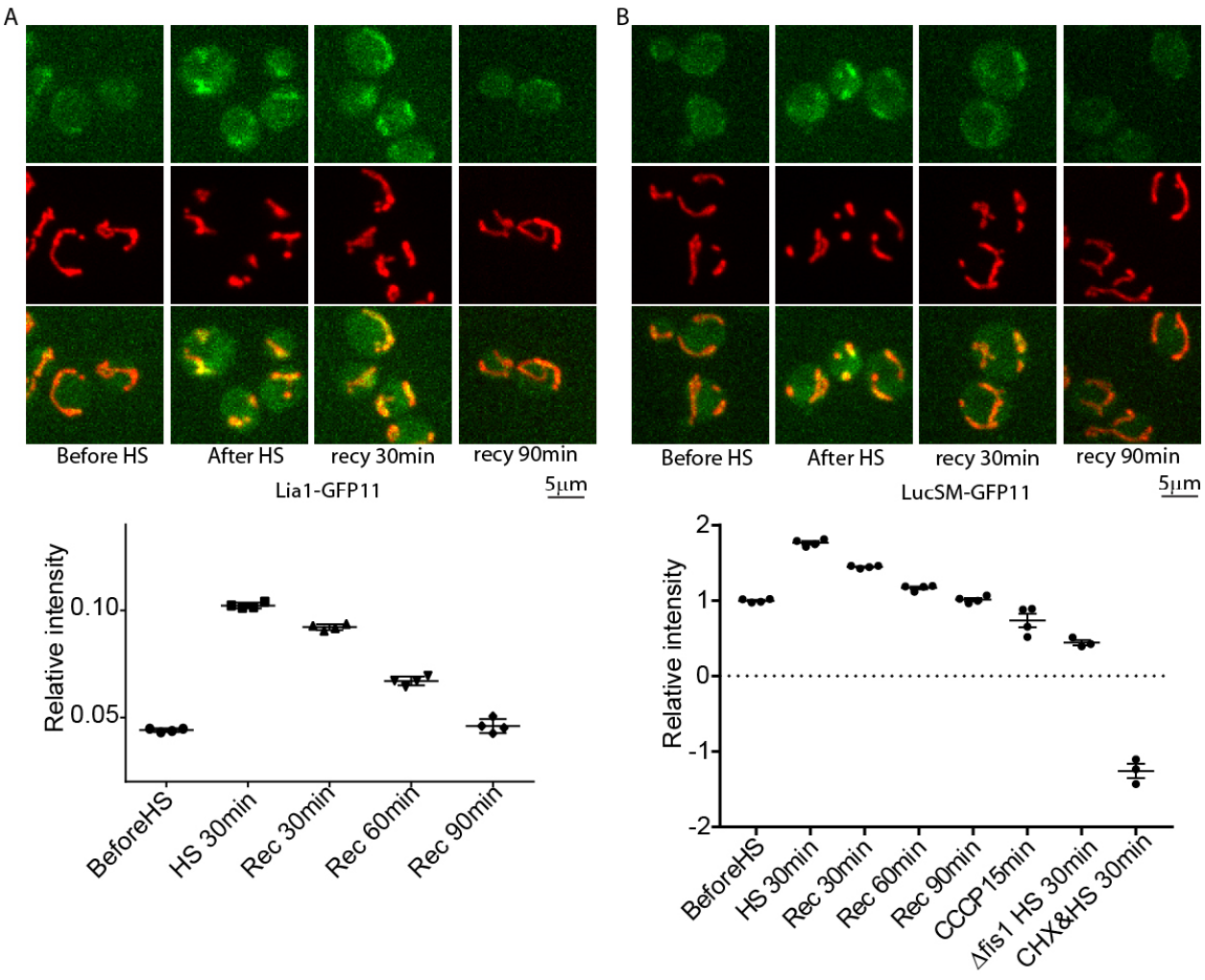

Figure 6-6. Mitochondria import aggregated cytosolic proteins

A, B. Heat shock induced translocation of misfolded cytosolic proteins into mitochondrial matrix. Top, representative images of the cells expressing cytosolic protein Lia1 and LucSM fused to GFP11 before and after heat shock. The SplitGFP signal increased after 30min heat shock and gradually diminished during 90min recovery. HS, heat shock; recy, recovery in 30C after heat shock. Bottom, GFP signals were quantified by FACS and the background was subtracted using control strain without GFP11. GFP signal was normalized to its corresponding mCherry. Shown are the mean and SEM of more than 3 independent experiments, with each time-point normalized to the mean value of samples before HS for (B). CCCP 15min, cells treated with CCCP; *Δfis1* HS 30min, 30min HS applied to the *Δfis1* background. CHX&HS 30min, 30min HS applied to the cells treated with CHX. Scale bar, 5um.

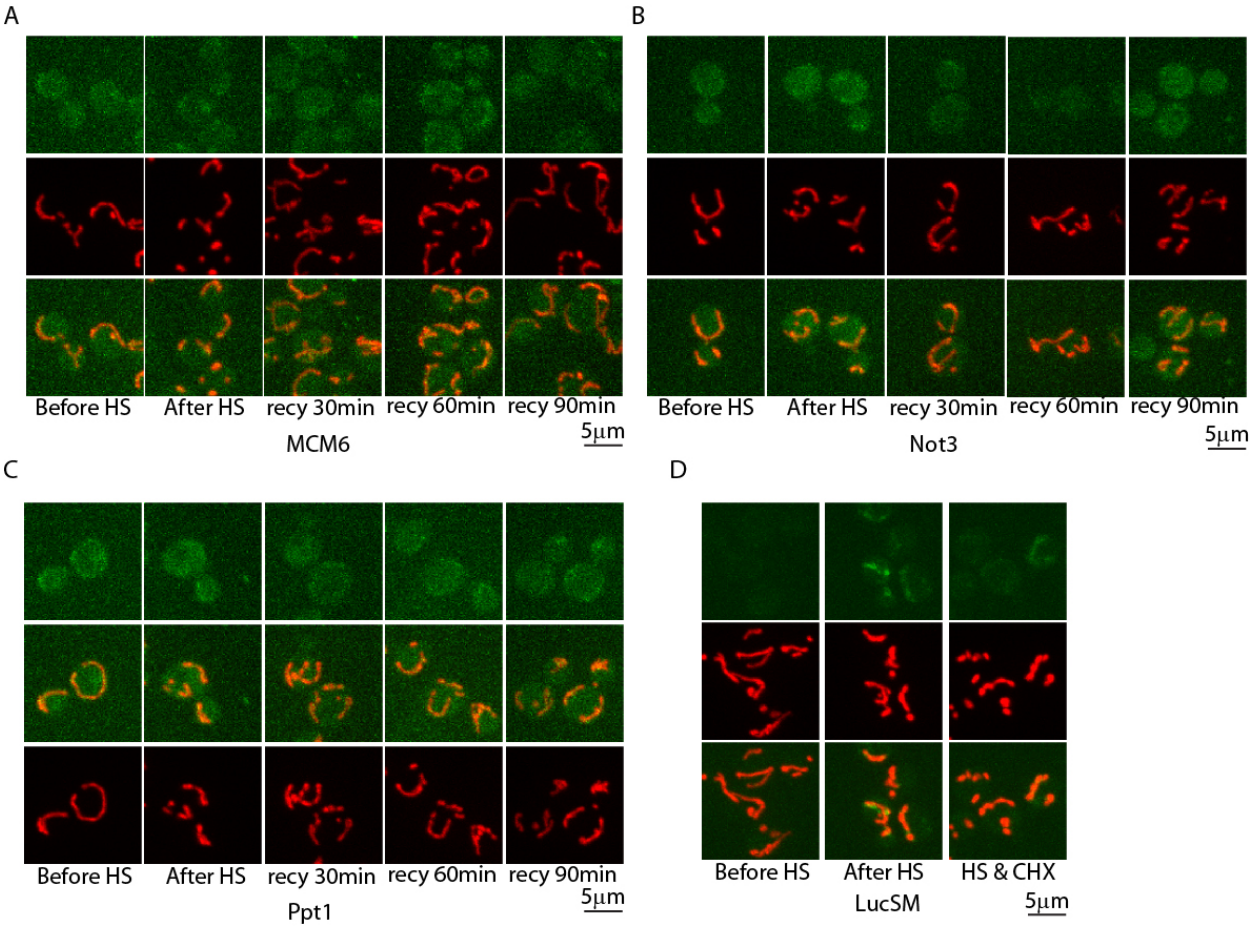

Figure 6-7. Lack of mitochondrial translocation of the cytosolic proteins that not found in the aggregates

Representative images of the cells expressing cytosolic protein Mcm6p-, Not3p- and Ppt1p- GFP11 before and after heat shock. Scale bar, 5um.

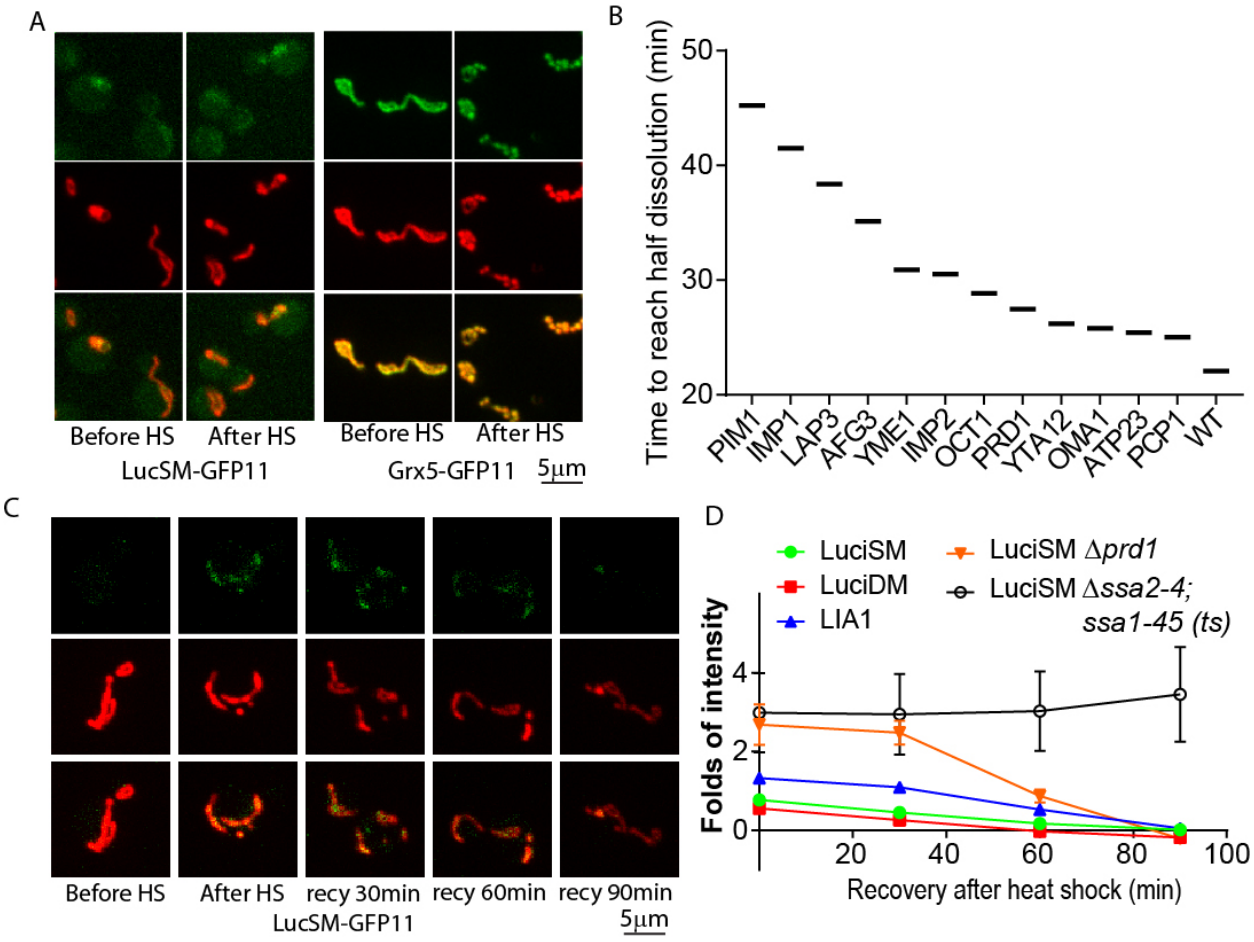

Figure 6-8. Aggregated cytosolic proteins are imported and degraded by mitochondria.

A. Fis1 deletion abolished the heat shock induced mitochondrial translocation of LucSM. Grx5-GFP11 served as control to exclude the possible mitochondrial import defect associated with Fis1 knockout. Scale bar, 5um.

B. Aggregate dissolution in mutant strains lacking specific mitochondrial proteases. The time to dissolve half of the aggregates was averaged from three movies of each strain.

C. Representative images of LucSM-GFP11 expressing *Δprd1* cells before and after heat shock. Scale bar, 5um.

D. Dynamics of splitGFP signal of different strains after heat shock. Cells were heat shocked for 30min and the splitGFP signal were quantified in different time-points. The splitGFP signal of each strain was normalized to its corresponding signal before heat shock.

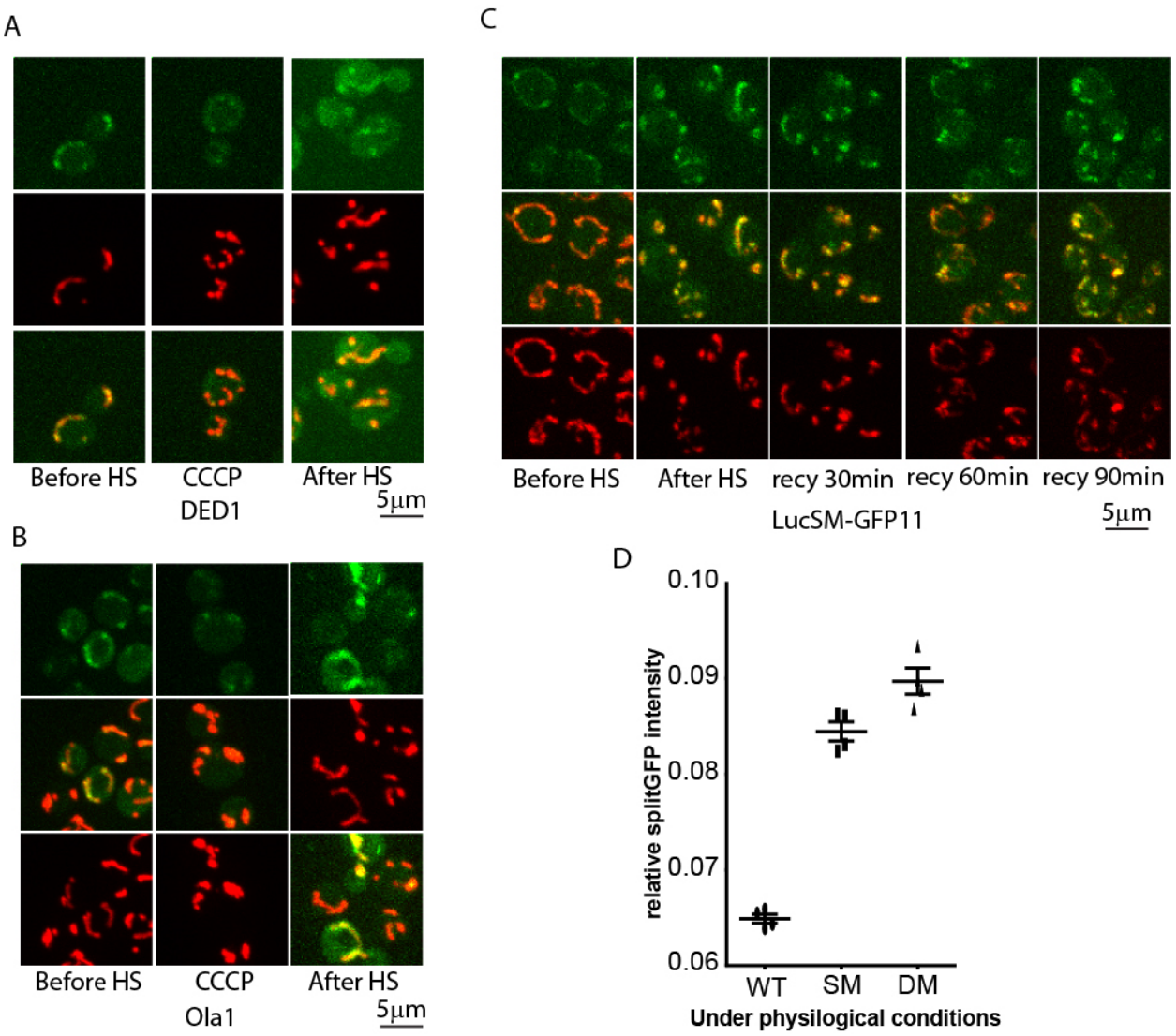

Figure 6-9. Mitochondrial import is part of cytosolic protein homeostasis network.

A, B. Representative images of the cells expressing Ded1p- or Ola1p-GFP11 that treated with different conditions. Scale bar, 5um.

C. Representative images of LucSM-GFP11 expressed in SSA1-4 mutant cells before and after heat shock. In this strain, SSA2, SSA3 and SSA4 are deleted whereas SSA1 bears a temperature sensitive mutation. Scale bar, 5um.

D. SplitGFP signal of LucWT, LucSM and LucDM without stress. GFP signals were quantitified by FACS and the background was subtracted using control strain without GFP11. GFP signal was normalized to its corresponding mCherry signal. Shown are the mean and SEM of more than 3 independent experiments.

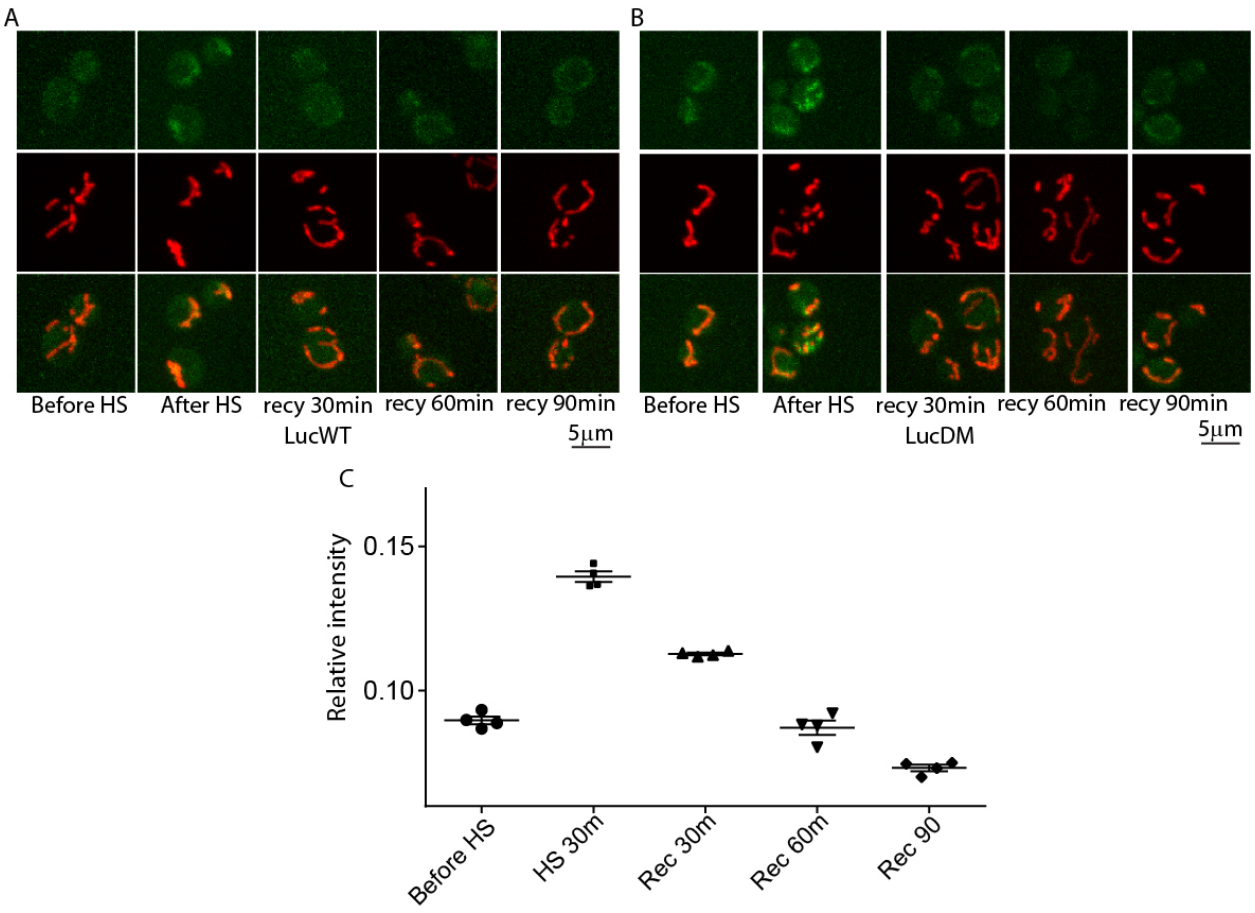

Figure 6-10. Trans-localization of cytosolic proteins into mitochondria after heat shock

A, B. Representative images of the cells expressing cytosolic protein luciferaseWT-GFP11 or luciferaseDM-GFP 11 before and after heat shock. Scale bar, 5um.

C. SplitGFP signal of LucDM at different time-points. GFP signals were quantitified by FACS and the background was subtracted using control strain without GFP11. GFP signal was normalized to it corresponding mCherry signal. Shown are the mean and SEM of more than 3 independent experiments.

CHAPTER SEVEN: CONCLUSIONS

My thesis studies started with the aim to answer how the asymmetric segregation of proteome damages is achieved in budding yeast. The results described above reveal a sophisticated mechanism involving, but not restricted to, cellular geometry, organelle-based confinement and features of aggregate motility that together keep the protein aggregates from entering the growing daughter cells. These results also establish a new framework for aggregate formation and dissolution *in vivo*: 1) nascent translation products play a key role in initiating the sites for protein aggregation, which happens on the surface of mitochondria and ER; 2) the association of aggregates on the surface of mitochondria facilitates the mitochondrial import and degradation of cytosolic proteins that misfolded and trapped in the aggregates. It is known that newly translated polypeptides suffer a prolonged period of sensitivity to stress and environmental changes (Medicherla and Goldberg, 2008), and their high local concentration near sites of protein synthesis could favor aggregate initiation. Since mitochondrial import and the downstream protease mediated degradation are evolutionary conserved mitochondrial functions, thus the new role of mitochondria in cytosolic proteostasis seems to be a conserved mechanism. Indeed, our lab recent found that instable cytosolic proteins were imported by mitochondria similar to the phenomenon discovered in yeast.

Proteome damages contribute to both aging and many neurodegenerative diseases as described in the introduction. Cells have evolved a sophisticated network of proteostasis to counteract the proteome damages caused by intrinsic metabolism and environmental insults. When the accumulation of damaged proteins exceeds the capacity of quality control system, aggregation of misfolded proteins serves to minimize the aberrant interactions between these

malignant species and metastable hub proteins that are essential for survival(Olzscha et al., 2011). The aggregates not only concentrate the misfolded proteins, but also compete with newly translated peptides for chaperones. This could be deleterious for the growing daughter cells as the active assembly of cellular structures, such as clathrin-based endocytosis, are sensitive to the cytosolic chaperones activities. The slow motility of aggregates and special cellular geometry, together with the organelle-based confinement, largely restrict the probability of leaking aggregate. This could be part of the rejuvenation process underneath the observed asymmetric segregation of aging between mother and daughter cells. Although the cellular geometry is specific to budding yeast, the organelle-based anchoring is universal for protein aggregates as in animal cells where the small aggregates are transported along microtubules to form aggresome at MTOC. The aggresome is entangled with mitochondria under electron microscope. The mitochondria and ER from mother cells are restricted from entering daughter cell (Clay et al., 2014; Zhou et al., 2014). Recently, the asymmetric segregation of mitochondria between sibling cells was also found in stem cells (Katajisto et al., 2015). In both yeast and stem cells, the daughter cells that maintain youth or stemness usually inherit mitochondria that are overall "fitter" than their sibling cells (McFaline-Figueroa et al., 2011). Therefore it will be important to learn how the asymmetric segregation of different organelles are coupled.

Protein aggregation was thought as a spontaneous process driving by the increased concentration of misfolded proteins in a crowd cytosol. This conclusion was reached, similar to the Anfinsen's dogma, mainly based on the *in vitro* aggregation of purified model proteins, such as luciferase and GFP. The crowd effect in cytosol not only predisposes proteins to aggregate, but was also co-evolved by the increased strength of protein folding through molecular interactions that strongly augment the energy barrier between folding states. This principle has

been revealed by the *in vitro* biochemical studies that, in addition to intra-protein interactions, agents that discriminately bind to proteins in their folded states (such as proteins' physiological ligands) could also prevent misfolding and aggregation by increasing the energetic barrier between the native and misfolded states (Carpenter et al., 1999). The opposite effect is expected with agents (such as surfactant) having higher affinity to misfolded states. In the cytosol, each protein interacts with a multitude of functional partners, which helps stabilize protein's native states and possibly explains the low likelihood for aggregation, whereas in protein aggregates the misfolded state is favored and stabilized through interaction with other misfolded proteins. Such opposite stabilizing effects on native vs misfolded conformers could drive protein aggregation to proceed like phase separation seeded by newly translated polypeptides enriched near translation sites. Molecular chaperone refers to the proteins that transiently interact but are not a part of the end product of protein complex. This concept also describes the general feature of a functional proteome where molecular interaction is prevailing between proteins, RNA/DNA, lipid et al.

The role of newly translated peptides in initiating aggregation could also be a general principle for not only the amorphous aggregates formed under stress conditions, but also the stable amyloid aggregates and prions that propagate in devastating diseases. Given the flexibility of newly translated peptides, which lack the energy barriers conferred by native folding and molecular interactions, it is highly possible that the amyloid/prion conversion is achieved on the newly translated peptides before they reach the alternative folding states. This is consistent with the observation that overexpression of amyloid precursors can increase the spontaneous prion conversion in budding yeast.

The formation of proteins aggregates on the surface of organelles connects the biology behind aggregates and organelles together. The asymmetric segregation of aggregates and

mitochondria as well as the mitochondrial import mediated cytosolic proteostasis (mito-stasis) are two small pieces of the entire picture awaiting to be unveiled in the future. My on-going works also begin to reveal the molecular mechanism that mediates the aggregate-mitochondria association. Consistent with a role of mitochondrial import in aggregate dissolution, the mitochondrial import receptor Tom70 and Tom20 seem to anchor aggregates on the surface of mitochondria. These findings provide a potential explanation for the link between protein aggregation and mitochondrial defects in degenerative diseases. The gradual accumulation of proteomic damages and the decline in mitochondrial fitness in aging or disease could in fact coexist, forming a positive feedback loop to precipitate a stable disease state and continual degeneration. Future work will reveal whether proteostasis or mitochondrial defect starts this degenerative cycle.

BIBLIOGRAPHY

(1993). A novel gene containing a trinucleotide repeat that is expanded and unstable on Huntington's disease chromosomes. The Huntington's Disease Collaborative Research Group. Cell *72*, 971-983.

Adams, A.E., and Pringle, J.R. (1984). Relationship of actin and tubulin distribution to bud growth in wild-type and morphogenetic-mutant Saccharomyces cerevisiae. J Cell Biol *98*, 934-945.

Agashe, V.R., Guha, S., Chang, H.C., Genevaux, P., Hayer-Hartl, M., Stemp, M., Georgopoulos, C., Hartl, F.U., and Barral, J.M. (2004). Function of trigger factor and DnaK in multidomain protein folding: increase in yield at the expense of folding speed. Cell *117*, 199-209.

Aguilaniu, H., Gustafsson, L., Rigoulet, M., and Nystrom, T. (2003). Asymmetric inheritance of oxidatively damaged proteins during cytokinesis. Science *299*, 1751-1753.

Altmann, K., Frank, M., Neumann, D., Jakobs, S., and Westermann, B. (2008). The class V myosin motor protein, Myo2, plays a major role in mitochondrial motility in Saccharomyces cerevisiae. J Cell Biol *181*, 119-130.

Anfinsen, C.B. (1973). Principles that govern the folding of protein chains. Science *181*, 223-230.

Anliker, B., and Muller, U. (2006). The functions of mammalian amyloid precursor protein and related amyloid precursor-like proteins. Neuro-degenerative diseases *3*, 239-246.

Arrasate, M., Mitra, S., Schweitzer, E.S., Segal, M.R., and Finkbeiner, S. (2004). Inclusion body formation reduces levels of mutant huntingtin and the risk of neuronal death. Nature *431*, 805-810.

Ashe, M.P., De Long, S.K., and Sachs, A.B. (2000). Glucose depletion rapidly inhibits translation initiation in yeast. Mol Biol Cell *11*, 833-848.

Aubin-Tam, M.E., Olivares, A.O., Sauer, R.T., Baker, T.A., and Lang, M.J. (2011). Single-molecule protein unfolding and translocation by an ATP-fueled proteolytic machine. Cell *145*, 257-267.

Barker, M.G., and Walmsley, R.M. (1999). Replicative ageing in the fission yeast Schizosaccharomyces pombe. Yeast (Chichester, England) *15*, 1511-1518.

Barraclough, R., and Ellis, R.J. (1980). Protein synthesis in chloroplasts. IX. Assembly of newly-synthesized large subunits into ribulose bisphosphate carboxylase in isolated intact pea chloroplasts. Biochim Biophys Acta *608*, 19-31.

Bartlett, A.I., and Radford, S.E. (2009). An expanding arsenal of experimental methods yields an explosion of insights into protein folding mechanisms. Nat Struct Mol Biol *16*, 582-588.

Basha, E., O'Neill, H., and Vierling, E. (2012). Small heat shock proteins and alpha-crystallins: dynamic proteins with flexible functions. Trends Biochem Sci *37*, 106-117.

Beckmann, R.P., Mizzen, L.E., and Welch, W.J. (1990). Interaction of Hsp 70 with newly synthesized proteins: implications for protein folding and assembly. Science *248*, 850-854.

Ben-Zvi, A., De Los Rios, P., Dietler, G., and Goloubinoff, P. (2004). Active solubilization and refolding of stable protein aggregates by cooperative unfolding action of individual hsp70 chaperones. J Biol Chem *279*, 37298-37303.

Berland, K., So, P.T.C., and Gratton, E. (1995a). Two-Photon Fluorescence Correlation Spectroscopy: Method and Application to the Intracellular Environment. Biophys J *68*, 694-701.

Berland, K.M., So, P.T., and Gratton, E. (1995b). Two-photon fluorescence correlation spectroscopy: method and application to the intracellular environment. Biophys J *68*, 694-701.

Bjorkoy, G., Lamark, T., Brech, A., Outzen, H., Perander, M., Overvatn, A., Stenmark, H., and Johansen, T. (2005). p62/SQSTM1 forms protein aggregates degraded by autophagy and has a protective effect on huntingtin-induced cell death. J Cell Biol *171*, 603-614.

Blond-Elguindi, S., Cwirla, S.E., Dower, W.J., Lipshutz, R.J., Sprang, S.R., Sambrook, J.F., and Gething, M.J. (1993). Affinity panning of a library of peptides displayed on bacteriophages reveals the binding specificity of BiP. Cell *75*, 717-728.

Bockler, S., and Westermann, B. (2014). Mitochondrial ER contacts are crucial for mitophagy in yeast. Dev Cell *28*, 450-458.

Boldogh, I.R., Ramcharan, S.L., Yang, H.C., and Pon, L.A. (2004). A type V myosin (Myo2p) and a Rab-like G-protein (Ypt11p) are required for retention of newly inherited mitochondria in yeast cells during cell division. Mol Biol Cell *15*, 3994-4002.

Borkovich, K.A., Farrelly, F.W., Finkelstein, D.B., Taulien, J., and Lindquist, S. (1989). hsp82 is an essential protein that is required in higher concentrations for growth of cells at higher temperatures. Mol Cell Biol *9*, 3919-3930.

Bosco, D.A., LaVoie, M.J., Petsko, G.A., and Ringe, D. (2011). Proteostasis and movement disorders: Parkinson's disease and amyotrophic lateral sclerosis. Cold Spring Harb Perspect Biol *3*, a007500.

Bosl, B., Grimminger, V., and Walter, S. (2006). The molecular chaperone Hsp104--a molecular machine for protein disaggregation. J Struct Biol *156*, 139-148.

Bufalino, M.R., DeVeale, B., and van der Kooy, D. (2013). The asymmetric segregation of damaged proteins is stem cell-type dependent. J Cell Biol *201*, 523-530.

Bukau, B., and Horwich, A.L. (1998). The Hsp70 and Hsp60 chaperone machines. Cell *92*, 351-366.

Burnett, C., Valentini, S., Cabreiro, F., Goss, M., Somogyvari, M., Piper, M.D., Hoddinott, M., Sutphin, G.L., Leko, V., McElwee, J.J*., et al.* (2011). Absence of effects of Sir2 overexpression on lifespan in C. elegans and Drosophila. Nature *477*, 482-485.

Calhoun, M.E., Wiederhold, K.H., Abramowski, D., Phinney, A.L., Probst, A., Sturchler-Pierrat, C., Staufenbiel, M., Sommer, B., and Jucker, M. (1998). Neuron loss in APP transgenic mice. Nature *395*, 755-756.

Camilleri, A., Zarb, C., Caruana, M., Ostermeier, U., Ghio, S., Hogen, T., Schmidt, F., Giese, A., and Vassallo, N. (2013). Mitochondrial membrane permeabilisation by amyloid aggregates and protection by polyphenols. Biochim Biophys Acta *1828*, 2532-2543.

Carpenter, J.F., Kendrick, B.S., Chang, B.S., Manning, M.C., and Randolph, T.W. (1999). Inhibition of stress-induced aggregation of protein therapeutics. Methods Enzymol *309*, 236-255.

Chen, C., Dewaele, S., Braeckman, B., Desmyter, L., Verstraelen, J., Borgonie, G., Vanfleteren, J., and Contreras, R. (2003). A high-throughput screening system for genes extending life-span. Exp Gerontol *38*, 1051-1063.

Cheng, M.Y., Hartl, F.U., Martin, J., Pollock, R.A., Kalousek, F., Neupert, W., Hallberg, E.M., Hallberg, R.L., and Horwich, A.L. (1989). Mitochondrial heat-shock protein hsp60 is essential for assembly of proteins imported into yeast mitochondria. Nature *337*, 620-625.

Chirico, W.J., Waters, M.G., and Blobel, G. (1988). 70K heat shock related proteins stimulate protein translocation into microsomes. Nature *332*, 805-810.

Chiti, F., and Dobson, C.M. (2006). Protein misfolding, functional amyloid, and human disease. Annu Rev Biochem *75*, 333-366.

Clay, L., Caudron, F., Denoth-Lippuner, A., Boettcher, B., Buvelot Frei, S., Snapp, E.L., and Barral, Y. (2014). A sphingolipid-dependent diffusion barrier confines ER stress to the yeast mother cell. Elife *3*, e01883.

Cleary, J.P., Walsh, D.M., Hofmeister, J.J., Shankar, G.M., Kuskowski, M.A., Selkoe, D.J., and Ashe, K.H. (2005). Natural oligomers of the amyloid-beta protein specifically disrupt cognitive function. Nature neuroscience *8*, 79-84.

Coelho, M., and Ferreira, J.J. (2012). Late-stage Parkinson disease. Nature reviews Neurology *8*, 435-442.

David, A., Dolan, B.P., Hickman, H.D., Knowlton, J.J., Clavarino, G., Pierre, P., Bennink, J.R., and Yewdell, J.W. (2012). Nuclear translation visualized by ribosome-bound nascent chain puromycylation. J Cell Biol *197*, 45-57.

De Los Rios, P., Ben-Zvi, A., Slutsky, O., Azem, A., and Goloubinoff, P. (2006). Hsp70 chaperones accelerate protein translocation and the unfolding of stable protein aggregates by entropic pulling. Proc Natl Acad Sci U S A *103*, 6166-6171.

Defossez, P.A., Prusty, R., Kaeberlein, M., Lin, S.J., Ferrigno, P., Silver, P.A., Keil, R.L., and Guarente, L. (1999). Elimination of replication block protein Fob1 extends the life span of yeast mother cells. Mol Cell *3*, 447-455.

Delaney, J.R., Sutphin, G.L., Dulken, B., Sim, S., Kim, J.R., Robison, B., Schleit, J., Murakami, C.J., Carr, D., An, E.H.*, et al.* (2011). Sir2 deletion prevents lifespan extension in 32 long-lived mutants. Aging Cell *10*, 1089-1091.

Desantis, M.E., Leung, E.H., Sweeny, E.A., Jackrel, M.E., Cushman-Nick, M., Neuhaus-Follini, A., Vashist, S., Sochor, M.A., Knight, M.N., and Shorter, J. (2012). Operational plasticity enables hsp104 to disaggregate diverse amyloid and nonamyloid clients. Cell *151*, 778-793.

Deshaies, R.J., Koch, B.D., Werner-Washburne, M., Craig, E.A., and Schekman, R. (1988). A subfamily of stress proteins facilitates translocation of secretory and mitochondrial precursor polypeptides. Nature *332*, 800-805.

Detmer, S.A., and Chan, D.C. (2007). Functions and dysfunctions of mitochondrial dynamics. Nat Rev Mol Cell Biol *8*, 870-879.

Doyle, S.M., and Wickner, S. (2009). Hsp104 and ClpB: protein disaggregating machines. Trends Biochem Sci *34*, 40-48.

Duchen, M.R. (2000). Mitochondria and calcium: from cell signalling to cell death. The Journal of physiology *529 Pt 1*, 57-68.

Egilmez, N.K., and Jazwinski, S.M. (1989). Evidence for the involvement of a cytoplasmic factor in the aging of the yeast Saccharomyces cerevisiae. J Bacteriol *171*, 37-42.

Ellis, R.J., and Hartl, F.U. (1996). Protein folding in the cell: competing models of chaperonin function. FASEB J *10*, 20-26.

Erjavec, N., Larsson, L., Grantham, J., and Nystrom, T. (2007). Accelerated aging and failure to segregate damaged proteins in Sir2 mutants can be suppressed by overproducing the protein aggregation-remodeling factor Hsp104p. Genes Dev *21*, 2410-2421.

Erjavec, N., and Nystrom, T. (2007). Sir2p-dependent protein segregation gives rise to a superior reactive oxygen species management in the progeny of Saccharomyces cerevisiae. Proc Natl Acad Sci U S A *104*, 10877-10881.

Escusa-Toret, S., Vonk, W.I., and Frydman, J. (2013). Spatial sequestration of misfolded proteins by a dynamic chaperone pathway enhances cellular fitness during stress. Nat Cell Biol *15*, 1231-1243.

Evangelista, M., Pruyne, D., Amberg, D.C., Boone, C., and Bretscher, A. (2002). Formins direct Arp2/3-independent actin filament assembly to polarize cell growth in yeast. Nat Cell Biol *4*, 32-41.

Farr, G.W., Scharl, E.C., Schumacher, R.J., Sondek, S., and Horwich, A.L. (1997). Chaperonin-mediated folding in the eukaryotic cytosol proceeds through rounds of release of native and nonnative forms. Cell *89*, 927-937.

Fehrenbacher, K.L., Yang, H.C., Gay, A.C., Huckaba, T.M., and Pon, L.A. (2004). Live cell imaging of mitochondrial movement along actin cables in budding yeast. Curr Biol *14*, 1996-2004.

Finkbeiner, S. (2011). Huntington's Disease. Cold Spring Harb Perspect Biol *3*.

Gamerdinger, M., Hajieva, P., Kaya, A.M., Wolfrum, U., Hartl, F.U., and Behl, C. (2009). Protein quality control during aging involves recruitment of the macroautophagy pathway by BAG3. EMBO J *28*, 889-901.

Gao, X., Carroni, M., Nussbaum-Krammer, C., Mogk, A., Nillegoda, N.B., Szlachcic, A., Guilbride, D.L., Saibil, H.R., Mayer, M.P., and Bukau, B. (2015). Human Hsp70 Disaggregase Reverses Parkinson's-Linked alpha-Synuclein Amyloid Fibrils. Mol Cell *59*, 781-793.

Garcia-Mata, R., Bebok, Z., Sorscher, E.J., and Sztul, E.S. (1999). Characterization and dynamics of aggresome formation by a cytosolic GFP-chimera. J Cell Biol *146*, 1239-1254.

Gehlen, L.R., Nagai, S., Shimada, K., Meister, P., Taddei, A., and Gasser, S.M. (2011). Nuclear geometry and rapid mitosis ensure asymmetric episome segregation in yeast. Curr Biol *21*, 25-33.

Geisler, S., Holmstrom, K.M., Skujat, D., Fiesel, F.C., Rothfuss, O.C., Kahle, P.J., and Springer, W. (2010). PINK1/Parkin-mediated mitophagy is dependent on VDAC1 and p62/SQSTM1. Nat Cell Biol *12*, 119-131.

Georgopoulos, C.P., Hendrix, R.W., Kaiser, A.D., and Wood, W.B. (1972). Role of the host cell in bacteriophage morphogenesis: effects of a bacterial mutation on T4 head assembly. Nature: New biology *239*, 38-41.

Giaever, G., Chu, A.M., Ni, L., Connelly, C., Riles, L., Veronneau, S., Dow, S., Lucau-Danila, A., Anderson, K., Andre, B.*, et al.* (2002). Functional profiling of the Saccharomyces cerevisiae genome. Nature *418*, 387-391.

Gidalevitz, T., Prahlad, V., and Morimoto, R.I. (2011). The stress of protein misfolding: from single cells to multicellular organisms. Cold Spring Harb Perspect Biol *3*.

Glover, J.R., and Lindquist, S. (1998). Hsp104, Hsp70, and Hsp40: a novel chaperone system that rescues previously aggregated proteins. Cell *94*, 73-82.

Guarente, L. (2000). Sir2 links chromatin silencing, metabolism, and aging. Genes Dev *14*, 1021-1026.

Guo, M. (2012). Drosophila as a model to study mitochondrial dysfunction in Parkinson's disease. Cold Spring Harbor perspectives in medicine *2*.

Gur, E., and Sauer, R.T. (2008). Recognition of misfolded proteins by Lon, a AAA(+) protease. Genes Dev *22*, 2267-2277.

Haas, I.G., and Wabl, M. (1983). Immunoglobulin heavy chain binding protein. Nature *306*, 387-389.

Hageman, J., Vos, M.J., van Waarde, M.A., and Kampinga, H.H. (2007). Comparison of intra-organellar chaperone capacity for dealing with stress-induced protein unfolding. J Biol Chem *282*, 34334-34345.

Hailey, D.W., Rambold, A.S., Satpute-Krishnan, P., Mitra, K., Sougrat, R., Kim, P.K., and Lippincott-Schwartz, J. (2010). Mitochondria supply membranes for autophagosome biogenesis during starvation. Cell *141*, 656-667.

Hamasaki, M., Furuta, N., Matsuda, A., Nezu, A., Yamamoto, A., Fujita, N., Oomori, H., Noda, T., Haraguchi, T., Hiraoka, Y.*, et al.* (2013). Autophagosomes form at ER-mitochondria contact sites. Nature *495*, 389-393.

Hartl, F.U. (1996). Molecular chaperones in cellular protein folding. Nature *381*, 571-579.

Hartl, F.U., Bracher, A., and Hayer-Hartl, M. (2011). Molecular chaperones in protein folding and proteostasis. Nature *475*, 324-332.

Hashimoto, M., Rockenstein, E., Crews, L., and Masliah, E. (2003). Role of protein aggregation in mitochondrial dysfunction and neurodegeneration in Alzheimer's and Parkinson's diseases. Neuromolecular Med *4*, 21-36.

Haslbeck, M., Braun, N., Stromer, T., Richter, B., Model, N., Weinkauf, S., and Buchner, J. (2004). Hsp42 is the general small heat shock protein in the cytosol of Saccharomyces cerevisiae. EMBO J *23*, 638-649.

Haslbeck, M., Franzmann, T., Weinfurtner, D., and Buchner, J. (2005). Some like it hot: the structure and function of small heat-shock proteins. Nat Struct Mol Biol *12*, 842-846.

Haslberger, T., Zdanowicz, A., Brand, I., Kirstein, J., Turgay, K., Mogk, A., and Bukau, B. (2008). Protein disaggregation by the AAA+ chaperone ClpB involves partial threading of looped polypeptide segments. Nat Struct Mol Biol *15*, 641-650.

Hayer-Hartl, M.K., Ewbank, J.J., Creighton, T.E., and Hartl, F.U. (1994). Conformational specificity of the chaperonin GroEL for the compact folding intermediates of alpha-lactalbumin. EMBO J *13*, 3192-3202.

Hebert, B., Costantino, S., and Wiseman, P.W. (2005a). Spatiotemporal Image Correlation Spectroscopy (STICS) Theory, Verification, and Application to Protein Velocity Mapping in Living CHO Cells. Biophys J *88*, 3601-3614.

Hebert, B., Costantino, S., and Wiseman, P.W. (2005b). Spatiotemporal image correlation spectroscopy (STICS) theory, verification, and application to protein velocity mapping in living CHO cells. Biophys J *88*, 3601-3614.

Hemmingsen, S.M., Woolford, C., van der Vies, S.M., Tilly, K., Dennis, D.T., Georgopoulos, C.P., Hendrix, R.W., and Ellis, R.J. (1988). Homologous plant and bacterial proteins chaperone oligomeric protein assembly. Nature *333*, 330-334.

Hipp, M.S., Patel, C.N., Bersuker, K., Riley, B.E., Kaiser, S.E., Shaler, T.A., Brandeis, M., and Kopito, R.R. (2012). Indirect inhibition of 26S proteasome activity in a cellular model of Huntington's disease. J Cell Biol *196*, 573-587.

Hoffmann, A., Merz, F., Rutkowska, A., Zachmann-Brand, B., Deuerling, E., and Bukau, B. (2006). Trigger factor forms a protective shield for nascent polypeptides at the ribosome. J Biol Chem *281*, 6539-6545.

Horwich, A.L. (2014). Molecular chaperones in cellular protein folding: the birth of a field. Cell *157*, 285-288.

Hughes, A.L., and Gottschling, D.E. (2012). An early age increase in vacuolar pH limits mitochondrial function and lifespan in yeast. Nature *492*, 261-265.

Huh, W.K., Falvo, J.V., Gerke, L.C., Carroll, A.S., Howson, R.W., Weissman, J.S., and O'Shea, E.K. (2003). Global analysis of protein localization in budding yeast. Nature *425*, 686-691.

Imai, S., Armstrong, C.M., Kaeberlein, M., and Guarente, L. (2000). Transcriptional silencing and longevity protein Sir2 is an NAD-dependent histone deacetylase. Nature *403*, 795-800.

Imamura, H., Nhat, K.P., Togawa, H., Saito, K., Iino, R., Kato-Yamada, Y., Nagai, T., and Noji, H. (2009). Visualization of ATP levels inside single living cells with fluorescence resonance energy transfer-based genetically encoded indicators. Proc Natl Acad Sci U S A *106*, 15651-15656.

Jimenez, A., Carrasco, L., and Vazquez, D. (1977). Enzymic and nonenzymic translocation by yeast polysomes. Site of action of a number of inhibitors. Biochemistry *16*, 4727-4730.

Johnston, J.A., Ward, C.L., and Kopito, R.R. (1998). Aggresomes: a cellular response to misfolded proteins. J Cell Biol *143*, 1883-1898.

Kaeberlein, M., Kirkland, K.T., Fields, S., and Kennedy, B.K. (2004). Sir2-independent life span extension by calorie restriction in yeast. PLoS Biol *2*, E296.

Kaeberlein, M., McVey, M., and Guarente, L. (1999). The SIR2/3/4 complex and SIR2 alone promote longevity in Saccharomyces cerevisiae by two different mechanisms. Genes Dev *13*, 2570-2580.

Kaganovich, D., Kopito, R., and Frydman, J. (2008). Misfolded proteins partition between two distinct quality control compartments. Nature *454*, 1088-1095.

Kaiser, C.M., Chang, H.C., Agashe, V.R., Lakshmipathy, S.K., Etchells, S.A., Hayer-Hartl, M., Hartl, F.U., and Barral, J.M. (2006). Real-time observation of trigger factor function on translating ribosomes. Nature *444*, 455-460.

Kalia, L.V., and Lang, A.E. (2015). Parkinson's disease. Lancet *386*, 896-912.

Katajisto, P., Dohla, J., Chaffer, C.L., Pentinmikko, N., Marjanovic, N., Iqbal, S., Zoncu, R., Chen, W., Weinberg, R.A., and Sabatini, D.M. (2015). Stem cells. Asymmetric apportioning of aged mitochondria between daughter cells is required for stemness. Science *348*, 340-343.

Kawaguchi, Y., Kovacs, J.J., McLaurin, A., Vance, J.M., Ito, A., and Yao, T.P. (2003). The deacetylase HDAC6 regulates aggresome formation and cell viability in response to misfolded protein stress. Cell *115*, 727-738.

Kawai, S., Murao, S., Mochizuki, M., Shibuya, I., Yano, K., and Takagi, M. (1992). Drastic alteration of cycloheximide sensitivity by substitution of one amino acid in the L41 ribosomal protein of yeasts. J Bacteriol *174*, 254-262.

Kennedy, B.K., Austriaco, N.R., Jr., Zhang, J., and Guarente, L. (1995). Mutation in the silencing gene SIR4 can delay aging in S. cerevisiae. Cell *80*, 485-496.

Kennedy, B.K., Gotta, M., Sinclair, D.A., Mills, K., McNabb, D.S., Murthy, M., Pak, S.M., Laroche, T., Gasser, S.M., and Guarente, L. (1997). Redistribution of silencing proteins from telomeres to the nucleolus is associated with extension of life span in S. cerevisiae. Cell *89*, 381-391.

Kim, I., Rodriguez-Enriquez, S., and Lemasters, J.J. (2007). Selective degradation of mitochondria by mitophagy. Arch Biochem Biophys *462*, 245-253.

Kirkin, V., McEwan, D.G., Novak, I., and Dikic, I. (2009). A role for ubiquitin in selective autophagy. Mol Cell *34*, 259-269.

Knorre, D.A., Kulemzina, I.A., Sorokin, M.I., Kochmak, S.A., Bocharova, N.A., Sokolov, S.S., and Severin, F.F. (2010). Sir2-dependent daughter-to-mother transport of the damaged proteins in yeast is required to prevent high stress sensitivity of the daughters. Cell Cycle *9*, 4501-4505.

Kobayashi, T., Horiuchi, T., Tongaonkar, P., Vu, L., and Nomura, M. (2004). SIR2 regulates recombination between different rDNA repeats, but not recombination within individual rRNA genes in yeast. Cell *117*, 441-453.

Kolin, D.L., Ronis, D., and Wiseman, P.W. (2006a). k-Space image correlation spectroscopy: a method for accurate transport measurements independent of fluorophore photophysics. Biophys J *91*, 3061-3075.

Kolin, D.L., Ronis, D., and Wiseman, P.W. (2006b). k-Space Image Correlation Spectroscopy: A Method for Accurate Transport Measurements Independent of Fluorophore Photophysics. Biophys J *91*, 3061-3075.

Komatsu, M., Waguri, S., Koike, M., Sou, Y.S., Ueno, T., Hara, T., Mizushima, N., Iwata, J., Ezaki, J., Murata, S*., et al.* (2007). Homeostatic levels of p62 control cytoplasmic inclusion body formation in autophagy-deficient mice. Cell *131*, 1149-1163.

Kornmann, B. (2013). The molecular hug between the ER and the mitochondria. Curr Opin Cell Biol *25*, 443-448.

Kornmann, B., Currie, E., Collins, S.R., Schuldiner, M., Nunnari, J., Weissman, J.S., and Walter, P. (2009). An ER-mitochondria tethering complex revealed by a synthetic biology screen. Science *325*, 477-481.

Koteiche, H.A., and McHaourab, H.S. (2003). Mechanism of chaperone function in small heat-shock proteins. Phosphorylation-induced activation of two-mode binding in alphaB-crystallin. J Biol Chem *278*, 10361-10367.

Kratter, I.H., and Finkbeiner, S. (2010). PolyQ disease: too many Qs, too much function? Neuron *67*, 897-899.

Krzewska, J., Langer, T., and Liberek, K. (2001). Mitochondrial Hsp78, a member of the Clp/Hsp100 family in Saccharomyces cerevisiae, cooperates with Hsp70 in protein refolding. FEBS Lett *489*, 92-96.

Kummer, E., Oguchi, Y., Seyffer, F., Bukau, B., and Mogk, A. (2013). Mechanism of Hsp104/ClpB inhibition by prion curing Guanidinium hydrochloride. FEBS Lett *587*, 810-817.

Kuo, Y., Ren, S., Lao, U., Edgar, B.A., and Wang, T. (2013). Suppression of polyglutamine protein toxicity by co-expression of a heat-shock protein 40 and a heat-shock protein 110. Cell death & disease *4*, e833.

Lambert, M.P., Barlow, A.K., Chromy, B.A., Edwards, C., Freed, R., Liosatos, M., Morgan, T.E., Rozovsky, I., Trommer, B., Viola, K.L*., et al.* (1998). Diffusible, nonfibrillar ligands derived from Abeta1-42 are potent central nervous system neurotoxins. Proc Natl Acad Sci U S A *95*, 6448-6453.

Langer, T., Lu, C., Echols, H., Flanagan, J., Hayer, M.K., and Hartl, F.U. (1992). Successive action of DnaK, DnaJ and GroEL along the pathway of chaperone-mediated protein folding. Nature *356*, 683-689.

Leenders, H.J., and Beckers, P.J. (1972). The effect of changes in the respiratory metabolism upon genome activity. A correlation between induced gene activity and an increase in activity of a respiratory enzyme. J Cell Biol *55*, 257-265.

Lew, D.J., and Reed, S.I. (1995a). A cell cycle checkpoint monitors cell morphogenesis in budding yeast. J Cell Biol *129*, 739-749.

Lew, D.J., and Reed, S.I. (1995b). Cell cycle control of morphogenesis in budding yeast. Curr Opin Genet Dev *5*, 17-23.

Lewis, M.J., and Pelham, H.R. (1985). Involvement of ATP in the nuclear and nucleolar functions of the 70 kd heat shock protein. EMBO J *4*, 3137-3143.

Li, Z., Vizeacoumar, F.J., Bahr, S., Li, J., Warringer, J., Vizeacoumar, F.S., Min, R., Vandersluis, B., Bellay, J., Devit, M.*, et al.* (2011). Systematic exploration of essential yeast gene function with temperature-sensitive mutants. Nat Biotechnol *29*, 361-367.

Lin, S.J., Defossez, P.A., and Guarente, L. (2000). Requirement of NAD and SIR2 for life-span extension by calorie restriction in Saccharomyces cerevisiae. Science *289*, 2126-2128.

Lindner, A.B., Madden, R., Demarez, A., Stewart, E.J., and Taddei, F. (2008). Asymmetric segregation of protein aggregates is associated with cellular aging and rejuvenation. Proceedings of the National Academy of Sciences of the United States of America *105*, 3076-3081.

Lindstrom, D.L., and Gottschling, D.E. (2009). The mother enrichment program: a genetic system for facile replicative life span analysis in Saccharomyces cerevisiae. Genetics *183*, 413-422, 411SI-413SI.

Liu, B., Han, Y., and Qian, S.B. (2013). Cotranslational response to proteotoxic stress by elongation pausing of ribosomes. Mol Cell *49*, 453-463.

Liu, B., Larsson, L., Caballero, A., Hao, X., Oling, D., Grantham, J., and Nystrom, T. (2010). The polarisome is required for segregation and retrograde transport of protein aggregates. Cell *140*, 257-267.

Longtine, M.S., McKenzie, A., 3rd, Demarini, D.J., Shah, N.G., Wach, A., Brachat, A., Philippsen, P., and Pringle, J.R. (1998). Additional modules for versatile and economical PCR-based gene deletion and modification in Saccharomyces cerevisiae. Yeast *14*, 953-961.

Lopez-Otin, C., Blasco, M.A., Partridge, L., Serrano, M., and Kroemer, G. (2013). The hallmarks of aging. Cell *153*, 1194-1217.

Lum, R., Tkach, J.M., Vierling, E., and Glover, J.R. (2004). Evidence for an unfolding/threading mechanism for protein disaggregation by Saccharomyces cerevisiae Hsp104. J Biol Chem *279*, 29139-29146.

Macdonald, P.J., Johnson, J., Chen, Y., and Mueller, J.D. (2014). Brightness experiments. Methods Mol Biol *1076*, 699-718.

Malinovska, L., Kroschwald, S., Munder, M.C., Richter, D., and Alberti, S. (2012). Molecular chaperones and stress-inducible protein-sorting factors coordinate the spatiotemporal distribution of protein aggregates. Mol Biol Cell *23*, 3041-3056.

Mattoo, R.U., Sharma, S.K., Priya, S., Finka, A., and Goloubinoff, P. (2013). Hsp110 is a bona fide chaperone using ATP to unfold stable misfolded polypeptides and reciprocally collaborate with Hsp70 to solubilize protein aggregates. J Biol Chem *288*, 21399-21411.

Mayhew, M., da Silva, A.C., Martin, J., Erdjument-Bromage, H., Tempst, P., and Hartl, F.U. (1996). Protein folding in the central cavity of the GroEL-GroES chaperonin complex. Nature *379*, 420-426.

McFaline-Figueroa, J.R., Vevea, J., Swayne, T.C., Zhou, C., Liu, C., Leung, G., Boldogh, I.R., and Pon, L.A. (2011). Mitochondrial quality control during inheritance is associated with lifespan and mother-daughter age asymmetry in budding yeast. Aging Cell *10*, 885-895.

Medicherla, B., and Goldberg, A.L. (2008). Heat shock and oxygen radicals stimulate ubiquitin-dependent degradation mainly of newly synthesized proteins. J Cell Biol *182*, 663-673.

Miller, S.B., Ho, C.T., Winkler, J., Khokhrina, M., Neuner, A., Mohamed, M.Y., Guilbride, D.L., Richter, K., Lisby, M., Schiebel, E.*, et al.* (2015a). Compartment-specific aggregases direct distinct nuclear and cytoplasmic aggregate deposition. EMBO J.

Miller, S.B., Ho, C.T., Winkler, J., Khokhrina, M., Neuner, A., Mohamed, M.Y., Guilbride, D.L., Richter, K., Lisby, M., Schiebel, E.*, et al.* (2015b). Compartment-specific aggregases direct distinct nuclear and cytoplasmic aggregate deposition. The EMBO journal *34*, 778-797.

Miller, S.B., Mogk, A., and Bukau, B. (2015c). Spatially organized aggregation of misfolded proteins as cellular stress defense strategy. Journal of molecular biology *427*, 1564-1574.

Miller, S.B., Mogk, A., and Bukau, B. (2015d). Spatially organized aggregation of misfolded proteins as cellular stress defense strategy. J Mol Biol.

Mitra, S., Tsvetkov, A.S., and Finkbeiner, S. (2009). Single neuron ubiquitin-proteasome dynamics accompanying inclusion body formation in huntington disease. J Biol Chem *284*, 4398-4403.

Mogk, A., Huber, D., and Bukau, B. (2011). Integrating protein homeostasis strategies in prokaryotes. Cold Spring Harb Perspect Biol *3*.

Mogk, A., Schlieker, C., Friedrich, K.L., Schonfeld, H.J., Vierling, E., and Bukau, B. (2003). Refolding of substrates bound to small Hsps relies on a disaggregation reaction mediated most efficiently by ClpB/DnaK. J Biol Chem *278*, 31033-31042.

Morita, M.T., Tanaka, Y., Kodama, T.S., Kyogoku, Y., Yanagi, H., and Yura, T. (1999). Translational induction of heat shock transcription factor sigma32: evidence for a built-in RNA thermosensor. Genes Dev *13*, 655-665.

Mortimer, R.K., and Johnston, J.R. (1959). Life span of individual yeast cells. Nature *183*, 1751-1752.

Narberhaus, F., Waldminghaus, T., and Chowdhury, S. (2006). RNA thermometers. FEMS Microbiol Rev *30*, 3-16.

Narendra, D., Kane, L.A., Hauser, D.N., Fearnley, I.M., and Youle, R.J. (2010). p62/SQSTM1 is required for Parkin-induced mitochondrial clustering but not mitophagy; VDAC1 is dispensable for both. Autophagy *6*, 1090-1106.

Neupert, W., and Herrmann, J.M. (2007). Translocation of proteins into mitochondria. Annu Rev Biochem *76*, 723-749.

Nguyen, T.T., Lewandowska, A., Choi, J.Y., Markgraf, D.F., Junker, M., Bilgin, M., Ejsing, C.S., Voelker, D.R., Rapoport, T.A., and Shaw, J.M. (2012). Gem1 and ERMES Do Not Directly Affect Phosphatidylserine

Transport from ER to Mitochondria or Mitochondrial Inheritance. Traffic (Copenhagen, Denmark) *13*, 880-890.

Nillegoda, N.B., and Bukau, B. (2015). Metazoan Hsp70-based protein disaggregases: emergence and mechanisms. Frontiers in molecular biosciences *2*, 57.

Nillegoda, N.B., Kirstein, J., Szlachcic, A., Berynskyy, M., Stank, A., Stengel, F., Arnsburg, K., Gao, X., Scior, A., Aebersold, R*., et al.* (2015). Crucial HSP70 co-chaperone complex unlocks metazoan protein disaggregation. Nature *524*, 247-251.

Oddo, S., Billings, L., Kesslak, J.P., Cribbs, D.H., and LaFerla, F.M. (2004). Abeta immunotherapy leads to clearance of early, but not late, hyperphosphorylated tau aggregates via the proteasome. Neuron *43*, 321-332.

Oguchi, Y., Kummer, E., Seyffer, F., Berynskyy, M., Anstett, B., Zahn, R., Wade, R.C., Mogk, A., and Bukau, B. (2012). A tightly regulated molecular toggle controls AAA+ disaggregase. Nat Struct Mol Biol *19*, 1338-1346.

Okatsu, K., Saisho, K., Shimanuki, M., Nakada, K., Shitara, H., Sou, Y.S., Kimura, M., Sato, S., Hattori, N., Komatsu, M*., et al.* (2010). p62/SQSTM1 cooperates with Parkin for perinuclear clustering of depolarized mitochondria. Genes to cells : devoted to molecular & cellular mechanisms *15*, 887-900.

Olzscha, H., Schermann, S.M., Woerner, A.C., Pinkert, S., Hecht, M.H., Tartaglia, G.G., Vendruscolo, M., Hayer-Hartl, M., Hartl, F.U., and Vabulas, R.M. (2011). Amyloid-like aggregates sequester numerous metastable proteins with essential cellular functions. Cell *144*, 67-78.

Orlandi, I., Bettiga, M., Alberghina, L., Nystrom, T., and Vai, M. (2010). Sir2-dependent asymmetric segregation of damaged proteins in ubp10 null mutants is independent of genomic silencing. Biochim Biophys Acta *1803*, 630-638.

Ostermann, J., Horwich, A.L., Neupert, W., and Hartl, F.U. (1989). Protein folding in mitochondria requires complex formation with hsp60 and ATP hydrolysis. Nature *341*, 125-130.

Ozalp, V.C., Pedersen, T.R., Nielsen, L.J., and Olsen, L.F. (2010). Time-resolved measurements of intracellular ATP in the yeast Saccharomyces cerevisiae using a new type of nanobiosensor. J Biol Chem *285*, 37579-37588.

Parsell, D.A., Kowal, A.S., Singer, M.A., and Lindquist, S. (1994). Protein disaggregation mediated by heat-shock protein Hsp104. Nature *372*, 475-478.

Parsell, D.A., Sanchez, Y., Stitzel, J.D., and Lindquist, S. (1991). Hsp104 is a highly conserved protein with two essential nucleotide-binding sites. Nature *353*, 270-273.

Pasinelli, P., Belford, M.E., Lennon, N., Bacskai, B.J., Hyman, B.T., Trotti, D., and Brown, R.H., Jr. (2004). Amyotrophic lateral sclerosis-associated SOD1 mutant proteins bind and aggregate with Bcl-2 in spinal cord mitochondria. Neuron *43*, 19-30.

Pavelka, N., Rancati, G., Zhu, J., Bradford, W.D., Saraf, A., Florens, L., Sanderson, B.W., Hattem, G.L., and Li, R. (2010). Aneuploidy confers quantitative proteome changes and phenotypic variation in budding yeast. Nature *468*, 321-325.

Pelham, H.R. (1984). Hsp70 accelerates the recovery of nucleolar morphology after heat shock. EMBO J *3*, 3095-3100.

Pestka, S., Rosenfeld, H., Harris, R., and Hintikka, H. (1972). Studies on transfer ribonucleic acid-ribosome complexes. XXI. Effect of antibiotics on peptidyl-puromycin synthesis by mammalian polyribosomes. J Biol Chem *247*, 6895-6900.

Polymeropoulos, M.H., Lavedan, C., Leroy, E., Ide, S.E., Dehejia, A., Dutra, A., Pike, B., Root, H., Rubenstein, J., Boyer, R.*, et al.* (1997). Mutation in the alpha-synuclein gene identified in families with Parkinson's disease. Science *276*, 2045-2047.

Pruyne, D., and Bretscher, A. (2000a). Polarization of cell growth in yeast. J Cell Sci *113 (Pt 4)*, 571-585.

Pruyne, D., and Bretscher, A. (2000b). Polarization of cell growth in yeast. II. The role of the cortical actin cytoskeleton. J Cell Sci *113 (Pt 3)*, 365-375.

Pruyne, D., Legesse-Miller, A., Gao, L., Dong, Y., and Bretscher, A. (2004). Mechanisms of polarized growth and organelle segregation in yeast. Annu Rev Cell Dev Biol *20*, 559-591.

Pruyne, D.W., Schott, D.H., and Bretscher, A. (1998). Tropomyosin-containing actin cables direct the Myo2p-dependent polarized delivery of secretory vesicles in budding yeast. J Cell Biol *143*, 1931-1945.

Puri, C., Renna, M., Bento, C.F., Moreau, K., and Rubinsztein, D.C. (2013). Diverse autophagosome membrane sources coalesce in recycling endosomes. Cell *154*, 1285-1299.

Rafelski, S.M., Viana, M.P., Zhang, Y., Chan, Y.H., Thorn, K.S., Yam, P., Fung, J.C., Li, H., Costa Lda, F., and Marshall, W.F. (2012). Mitochondrial network size scaling in budding yeast. Science *338*, 822-824.

Rampelt, H., Kirstein-Miles, J., Nillegoda, N.B., Chi, K., Scholz, S.R., Morimoto, R.I., and Bukau, B. (2012). Metazoan Hsp70 machines use Hsp110 to power protein disaggregation. The EMBO journal *31*, 4221-4235.

Ratajczak, E., Zietkiewicz, S., and Liberek, K. (2009). Distinct activities of Escherichia coli small heat shock proteins IbpA and IbpB promote efficient protein disaggregation. J Mol Biol *386*, 178-189.

Reid, D.W., and Nicchitta, C.V. (2012). Primary role for endoplasmic reticulum-bound ribosomes in cellular translation identified by ribosome profiling. J Biol Chem *287*, 5518-5527.

Reidy, M., Miot, M., and Masison, D.C. (2012). Prokaryotic chaperones support yeast prions and thermotolerance and define disaggregation machinery interactions. Genetics *192*, 185-193.

Rikhvanov, E.G., Varakina, N.N., Rusaleva, T.M., Rachenko, E.I., Knorre, D.A., and Voinikov, V.K. (2005). Do mitochondria regulate the heat-shock response in Saccharomyces cerevisiae? Curr Genet *48*, 44-59.

Roberson, E.D., Scearce-Levie, K., Palop, J.J., Yan, F., Cheng, I.H., Wu, T., Gerstein, H., Yu, G.Q., and Mucke, L. (2007). Reducing endogenous tau ameliorates amyloid beta-induced deficits in an Alzheimer's disease mouse model. Science *316*, 750-754.

Rodriguez, F., Arsene-Ploetze, F., Rist, W., Rudiger, S., Schneider-Mergener, J., Mayer, M.P., and Bukau, B. (2008). Molecular basis for regulation of the heat shock transcription factor sigma32 by the DnaK and DnaJ chaperones. Mol Cell *32*, 347-358.

Rokney, A., Shagan, M., Kessel, M., Smith, Y., Rosenshine, I., and Oppenheim, A.B. (2009). E. coli transports aggregated proteins to the poles by a specific and energy-dependent process. J Mol Biol *392*, 589-601.

Rosenzweig, R., Moradi, S., Zarrine-Afsar, A., Glover, J.R., and Kay, L.E. (2013). Unraveling the mechanism of protein disaggregation through a ClpB-DnaK interaction. Science *339*, 1080-1083.

Rujano, M.A., Bosveld, F., Salomons, F.A., Dijk, F., van Waarde, M.A., van der Want, J.J., de Vos, R.A., Brunt, E.R., Sibon, O.C., and Kampinga, H.H. (2006). Polarised asymmetric inheritance of accumulated protein damage in higher eukaryotes. PLoS Biol *4*, e417.

Sagot, I., Rodal, A.A., Moseley, J., Goode, B.L., and Pellman, D. (2002). An actin nucleation mechanism mediated by Bni1 and profilin. Nat Cell Biol *4*, 626-631.

Sanchez, Y., Taulien, J., Borkovich, K.A., and Lindquist, S. (1992). Hsp104 is required for tolerance to many forms of stress. EMBO J *11*, 2357-2364.

Sbalzarini, I.F., and Koumoutsakos, P. (2005). Feature point tracking and trajectory analysis for video imaging in cell biology. J Struct Biol *151*, 182-195.

Schaffar, G., Breuer, P., Boteva, R., Behrends, C., Tzvetkov, N., Strippel, N., Sakahira, H., Siegers, K., Hayer-Hartl, M., and Hartl, F.U. (2004). Cellular toxicity of polyglutamine expansion proteins: mechanism of transcription factor deactivation. Mol Cell *15*, 95-105.

Schechter, A.N. (1995). Christian B. Anfinsen 1916-1995. Nat Struct Biol *2*, 621-623.

Scheufler, C., Brinker, A., Bourenkov, G., Pegoraro, S., Moroder, L., Bartunik, H., Hartl, F.U., and Moarefi, I. (2000). Structure of TPR domain-peptide complexes: critical elements in the assembly of the Hsp70-Hsp90 multichaperone machine. Cell *101*, 199-210.

Schirmer, E.C., Homann, O.R., Kowal, A.S., and Lindquist, S. (2004). Dominant gain-of-function mutations in Hsp104p reveal crucial roles for the middle region. Mol Biol Cell *15*, 2061-2072.

Schroder, H., Langer, T., Hartl, F.U., and Bukau, B. (1993). DnaK, DnaJ and GrpE form a cellular chaperone machinery capable of repairing heat-induced protein damage. EMBO J *12*, 4137-4144.

Schwille, P., Korlach, J., and Webb, W.W. (1999a). Fluorescence Correlation Spectroscopy With Single-Molecule Sensitivity on Cell and Model Membranes. Cytometry *36*, 176-182.

Schwille, P., Korlach, J., and Webb, W.W. (1999b). Fluorescence correlation spectroscopy with single-molecule sensitivity on cell and model membranes. Cytometry *36*, 176-182.

Selkoe, D.J. (2011). Alzheimer's disease. Cold Spring Harb Perspect Biol *3*.

Serrano, R. (1977). Energy requirements for maltose transport in yeast. Eur J Biochem *80*, 97-102.

Seyffer, F., Kummer, E., Oguchi, Y., Winkler, J., Kumar, M., Zahn, R., Sourjik, V., Bukau, B., and Mogk, A. (2012). Hsp70 proteins bind Hsp100 regulatory M domains to activate AAA+ disaggregase at aggregate surfaces. Nat Struct Mol Biol *19*, 1347-1355.

Shankar, G.M., Li, S., Mehta, T.H., Garcia-Munoz, A., Shepardson, N.E., Smith, I., Brett, F.M., Farrell, M.A., Rowan, M.J., Lemere, C.A*., et al.* (2008). Amyloid-beta protein dimers isolated directly from Alzheimer's brains impair synaptic plasticity and memory. Nat Med *14*, 837-842.

Shiber, A., Breuer, W., Brandeis, M., and Ravid, T. (2013). Ubiquitin conjugation triggers misfolded protein sequestration into quality control foci when Hsp70 chaperone levels are limiting. Mol Biol Cell *24*, 2076-2087.

Shorter, J. (2011). The mammalian disaggregase machinery: Hsp110 synergizes with Hsp70 and Hsp40 to catalyze protein disaggregation and reactivation in a cell-free system. PLoS One *6*, e26319.

Shorter, J., and Lindquist, S. (2006). Destruction or potentiation of different prions catalyzed by similar Hsp104 remodeling activities. Mol Cell *23*, 425-438.

Sinclair, D.A., and Guarente, L. (1997). Extrachromosomal rDNA circles--a cause of aging in yeast. Cell *91*, 1033-1042.

Skach, W.R. (2009). Cellular mechanisms of membrane protein folding. Nat Struct Mol Biol *16*, 606-612.

Slaughter, B.D., and Li, R. (2010). Toward quantitative "in vivo biochemistry" with fluorescence fluctuation spectroscopy. Mol Biol Cell *21*, 4306-4311.

Slaughter, B.D., Unruh, J.R., and Li, R. (2011). Fluorescence fluctuation spectroscopy and imaging methods for examination of dynamic protein interactions in yeast. Methods Mol Biol *759*, 283-306.

Smith, J.S., Brachmann, C.B., Celic, I., Kenna, M.A., Muhammad, S., Starai, V.J., Avalos, J.L., Escalante-Semerena, J.C., Grubmeyer, C., Wolberger, C*., et al.* (2000). A phylogenetically conserved NAD+-dependent protein deacetylase activity in the Sir2 protein family. Proc Natl Acad Sci U S A *97*, 6658-6663.

Specht, S., Miller, S.B., Mogk, A., and Bukau, B. (2011). Hsp42 is required for sequestration of protein aggregates into deposition sites in Saccharomyces cerevisiae. J Cell Biol *195*, 617-629.

Spokoini, R., Moldavski, O., Nahmias, Y., England, J.L., Schuldiner, M., and Kaganovich, D. (2012). Confinement to organelle-associated inclusion structures mediates asymmetric inheritance of aggregated protein in budding yeast. Cell Rep *2*, 738-747.

Steffen, K.K., MacKay, V.L., Kerr, E.O., Tsuchiya, M., Hu, D., Fox, L.A., Dang, N., Johnston, E.D., Oakes, J.A., Tchao, B.N*., et al.* (2008). Yeast life span extension by depletion of 60s ribosomal subunits is mediated by Gcn4. Cell *133*, 292-302.

Steinkraus, K.A., Kaeberlein, M., and Kennedy, B.K. (2008). Replicative aging in yeast: the means to the end. Annu Rev Cell Dev Biol *24*, 29-54.

Stewart, E.J., Madden, R., Paul, G., and Taddei, F. (2005). Aging and death in an organism that reproduces by morphologically symmetric division. PLoS biology *3*, e45.

Stolz, A., Ernst, A., and Dikic, I. (2014). Cargo recognition and trafficking in selective autophagy. Nat Cell Biol *16*, 495-501.

Taipale, M., Jarosz, D.F., and Lindquist, S. (2010). HSP90 at the hub of protein homeostasis: emerging mechanistic insights. Nat Rev Mol Cell Biol *11*, 515-528.

Taipale, M., Krykbaeva, I., Koeva, M., Kayatekin, C., Westover, K.D., Karras, G.I., and Lindquist, S. (2012). Quantitative analysis of HSP90-client interactions reveals principles of substrate recognition. Cell *150*, 987-1001.

Takano, T., and Kakefuda, T. (1972). Involvement of a bacterial factor in morphogenesis of bacteriophage capsid. Nature: New biology *239*, 34-37.

Tanaka, M., Kim, Y.M., Lee, G., Junn, E., Iwatsubo, T., and Mouradian, M.M. (2004). Aggresomes formed by alpha-synuclein and synphilin-1 are cytoprotective. The Journal of biological chemistry *279*, 4625-4631.

Tessarz, P., Schwarz, M., Mogk, A., and Bukau, B. (2009). The yeast AAA+ chaperone Hsp104 is part of a network that links the actin cytoskeleton with the inheritance of damaged proteins. Mol Cell Biol *29*, 3738-3745.

Thulasiraman, V., Yang, C.F., and Frydman, J. (1999). In vivo newly translated polypeptides are sequestered in a protected folding environment. The EMBO journal *18*, 85-95.

Tian, G., Vainberg, I.E., Tap, W.D., Lewis, S.A., and Cowan, N.J. (1995). Specificity in chaperonin-mediated protein folding. Nature *375*, 250-253.

Tipton, K.A., Verges, K.J., and Weissman, J.S. (2008). In vivo monitoring of the prion replication cycle reveals a critical role for Sis1 in delivering substrates to Hsp104. Mol Cell *32*, 584-591.

Tran, P.T., Paoletti, A., and Chang, F. (2004). Imaging green fluorescent protein fusions in living fission yeast cells. Methods *33*, 220-225.

Tyedmers, J., Mogk, A., and Bukau, B. (2010a). Cellular strategies for controlling protein aggregation. Nat Rev Mol Cell Biol *11*, 777-788.

Tyedmers, J., Treusch, S., Dong, J., McCaffery, J.M., Bevis, B., and Lindquist, S. (2010b). Prion induction involves an ancient system for the sequestration of aggregated proteins and heritable changes in prion fragmentation. Proc Natl Acad Sci U S A *107*, 8633-8638.

Ullers, R.S., Luirink, J., Harms, N., Schwager, F., Georgopoulos, C., and Genevaux, P. (2004). SecB is a bona fide generalized chaperone in Escherichia coli. Proc Natl Acad Sci U S A *101*, 7583-7588.

Ungewickell, E. (1985). The 70-kd mammalian heat shock proteins are structurally and functionally related to the uncoating protein that releases clathrin triskelia from coated vesicles. EMBO J *4*, 3385-3391.

Ungewickell, E., Ungewickell, H., Holstein, S.E., Lindner, R., Prasad, K., Barouch, W., Martin, B., Greene, L.E., and Eisenberg, E. (1995). Role of auxilin in uncoating clathrin-coated vesicles. Nature *378*, 632-635.

Unruh, J.R., Slaughter, B.D., and Li, R. (2013). Quality control: putting protein aggregates in a bind. Curr Biol *23*, R74-76.

Vacher, C., Garcia-Oroz, L., and Rubinsztein, D.C. (2005). Overexpression of yeast hsp104 reduces polyglutamine aggregation and prolongs survival of a transgenic mouse model of Huntington's disease. Hum Mol Genet *14*, 3425-3433.

Velazquez, J.M., DiDomenico, B.J., and Lindquist, S. (1980). Intracellular localization of heat shock proteins in Drosophila. Cell *20*, 679-689.

Vendruscolo, M., Knowles, T.P., and Dobson, C.M. (2011). Protein solubility and protein homeostasis: a generic view of protein misfolding disorders. Cold Spring Harb Perspect Biol *3*.

Viswanathan, M., Kim, S.K., Berdichevsky, A., and Guarente, L. (2005). A role for SIR-2.1 regulation of ER stress response genes in determining C. elegans life span. Dev Cell *9*, 605-615.

Wang, P., and Powell, S.R. (2010). Decreased sensitivity associated with an altered formulation of a commercially available kit for detection of protein carbonyls. Free radical biology & medicine *49*, 119-121.

Wang, Y., Meriin, A.B., Zaarur, N., Romanova, N.V., Chernoff, Y.O., Costello, C.E., and Sherman, M.Y. (2009). Abnormal proteins can form aggresome in yeast: aggresome-targeting signals and components of the machinery. FASEB journal : official publication of the Federation of American Societies for Experimental Biology *23*, 451-463.

Weibezahn, J., Tessarz, P., Schlieker, C., Zahn, R., Maglica, Z., Lee, S., Zentgraf, H., Weber-Ban, E.U., Dougan, D.A., Tsai, F.T.*, et al.* (2004). Thermotolerance requires refolding of aggregated proteins by substrate translocation through the central pore of ClpB. Cell *119*, 653-665.

Weisberg, S.J., Lyakhovetsky, R., Werdiger, A.C., Gitler, A.D., Soen, Y., and Kaganovich, D. (2012). Compartmentalization of superoxide dismutase 1 (SOD1G93A) aggregates determines their toxicity. Proc Natl Acad Sci U S A *109*, 15811-15816.

Williams, D.C., Van Frank, R.M., Muth, W.L., and Burnett, J.P. (1982). Cytoplasmic inclusion bodies in Escherichia coli producing biosynthetic human insulin proteins. Science *215*, 687-689.

Winkler, J., Seybert, A., Konig, L., Pruggnaller, S., Haselmann, U., Sourjik, V., Weiss, M., Frangakis, A.S., Mogk, A., and Bukau, B. (2010). Quantitative and spatio-temporal features of protein aggregation in Escherichia coli and consequences on protein quality control and cellular ageing. EMBO J *29*, 910-923.

Winkler, J., Tyedmers, J., Bukau, B., and Mogk, A. (2012). Hsp70 targets Hsp100 chaperones to substrates for protein disaggregation and prion fragmentation. J Cell Biol *198*, 387-404.

Winter, J., Linke, K., Jatzek, A., and Jakob, U. (2005). Severe oxidative stress causes inactivation of DnaK and activation of the redox-regulated chaperone Hsp33. Mol Cell *17*, 381-392.

Xu, Y., and Lindquist, S. (1993). Heat-shock protein hsp90 governs the activity of pp60v-src kinase. Proc Natl Acad Sci U S A *90*, 7074-7078.

Yang, H.C., and Pon, L.A. (2002). Actin cable dynamics in budding yeast. Proc Natl Acad Sci U S A *99*, 751-756.

Youngman, M.J., Hobbs, A.E., Burgess, S.M., Srinivasan, M., and Jensen, R.E. (2004). Mmm2p, a mitochondrial outer membrane protein required for yeast mitochondrial shape and maintenance of mtDNA nucleoids. J Cell Biol *164*, 677-688.

Zaltieri, M., Longhena, F., Pizzi, M., Missale, C., Spano, P., and Bellucci, A. (2015). Mitochondrial Dysfunction and alpha-Synuclein Synaptic Pathology in Parkinson's Disease: Who's on First? Parkinson's disease *2015*, 108029.

Zhou, C., Slaughter, B.D., Unruh, J.R., Eldakak, A., Rubinstein, B., and Li, R. (2011). Motility and segregation of Hsp104-associated protein aggregates in budding yeast. Cell *147*, 1186-1196.

Zhou, C., Slaughter, B.D., Unruh, J.R., Guo, F., Yu, Z., Mickey, K., Narkar, A., Ross, R.T., McClain, M., and Li, R. (2014). Organelle-based aggregation and retention of damaged proteins in asymmetrically dividing cells. Cell *159*, 530-542.